Low-cost polymer chip for isothermal amplication assay

Garbarino, Francesca

Publication date:
2018

Document Version
Publisher's PDF, also known as Version of record

Ph.D. Thesis

Low-cost polymer chip for isothermal amplification assay

Francesca Garbarino

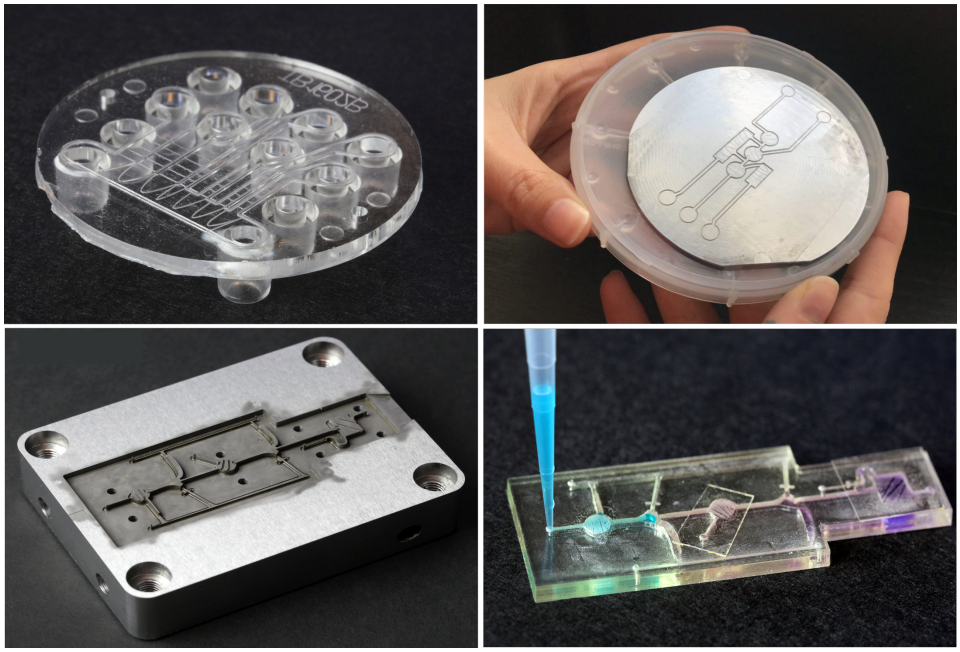

Supervisor: Mikkel Fougt Hansen, Associate Professor

Co-supervisor: Gabriel Khose Antonio Minero, PhD

Department of Micro and Nanotechnology
Technical University of Denmark

14 November 2018

Abstract

There is an increasing need to optimize diagnostics and health care and to develop methods to deliver the care closer to the patient's homes, in order to reduce the load on hospitals and clinics. In developing countries it is a challenge to obtain effective diagnosis and treatment for outbreaks of infectious diseases, such as influenza and tuberculosis, where the latter is causing more deaths than any other infectious disease. Point-of-care systems based on microfluidic devices have the potential to fulfill some of these needs and new technologies based on DNA amplification are continuously emerging and are under implementation on such devices.

For these technologies to be competitive, devices need to be fabricated through low-cost mass-production processes, e.g. by injection moulding. In academia, though, often the fabrication methods are not compatible with industrial mass-production and this can present a significant barrier to the commercialization of developed devices. It is therefore vital to seek a manufacturing process applying industry-level technologies for rapid prototyping of microfluidic devices.

The research presented in this thesis focused on three main topics: First, a microfluidic system was designed that used capillary structures to ensure controlled filling of separate, but connected, fluidic chambers. The filled liquids needed to remain stable under heating to the temperature required for the assay below.

Second, microfluidic chips were fabricated using either injection moulding with shims defined by micromilling combined with ultrasonic welding to seal the chips or by using laser ablation combined with adhesive bonding. The fabricated chips were characterized and the burst pressure of so-called phaseguide structures was studied systematically. At the end of the project, the design of functional prototype chips developed using laser ablation was transferred to a mass-production fabrication process by injection moulding.

Third, an integrated lab-on-a-chip system implementing isothermal rolling circle amplification of synthetic influenza and tuberculosis nucleic acid targets on the chip platform was developed and demonstrated. The assay was run in an automated setup in which magnetic microbeads were used to transport the target between the different assay steps and the amplification products were detected using an optomagnetic readout. Several assay strategies were investigated and quantitative dose-response curves were measured. The results demonstrated the feasibility of performing the complete three-step assay in a low-cost mass-producible multi-chamber device in an automated manner with results that were comparable to those obtained in comparable laboratory assays.

Resumé

Der er et voksende behov for at optimere diagnostik og sundhedspleje og for at udvikle metoder til at få behandling tættere patienters hjem så belastningen af hospitaler og klinikker reduceres. I udviklingslande er det en udfordring at få en effektiv diagnose og behandling ved udbrud af infektionssygdomme som influenza og tuberkulose, hvor tuberkulose forårsager flere dødsfald end nogen anden infektionssygdom. 'Point-of-care' apparater baseret på mikrovæske-systemer har potentialet til at opfylde nogle af disse behov og nye teknologier baseret på DNA amplificering udvikles hele tiden og implementeres i sådanne apparater.

For at disse teknologier er konkurrencedygtige, skal chips fremstilles ved brug af billige masseproduktionsmetoder, såsom sprøjtestøbning. I den akademiske verden, imidlertid, bruges ofte fabrikationsmetoder som er uegnede til masseproduktion og dette kan udgøre en betydelig barriere for kommercialiseringen af de udviklede apparater. Det er derfor vigtigt at søge processer til fremstilling af prototyper af mikrovæske-systemer, som kan omsættes til industriel produktion.

Arbejdet i denne afhandling fokuserede på tre hovedemner: For det første, så blev et mikrovæske-system designet, som brugte kapillær-strukturer til at sikre en kontrolleret fyldning af forbundne væskekamre med adskilte væsker. Væskerne i de enkelte kamre skulle være stabile ved opvarmning til de temperaturer, der var nødvendige for bioanalysen nedenfor.

For det andet, så blev mikrovæske-chips fremstillet ved brug af enten sprøjtestøbning med indsatser defineret med mikrofræsning kombineret med ultralydssvejsning til at forsegle chipsene. De fremstillede chips blev karakteriseret og gennembrudstrykket af såkaldte 'phaseguide' strukturer blev studeret systematisk. Ved afslutningen af projektet blev designet af en funktionel mikrovæske-chip prototype fremstillet ved brug af laserforstøvning overført til masseproduktion ved sprøjtestøbning.

For det tredje, så blev et integreret lab-on-a-chip system designet og demonstreret, som udførte isoterm amplificering af syntetisk DNA fra influenza og tuberkulose ved såkaldt 'rolling circle amplification'. Bioanalysen blev udført i en automatiseret opstilling i hvilken magnetiske mikropartikler blev brugt til at transportere analyten mellem de forskellige analysetrin, og reaktionsprodukterne blev detekteret ved en optomagnetisk udlæsningsteknologi. Flere analysestrategier blev undersøgt og kvantitative målinger af signal vs. analytkoncentration blev udført. Resultaterne demonstrerede at det er muligt at udføre en komplet og automatiseret tre-trins bioanalyse i en billig masseproducerbar multi-kammer chip med resultater som er sammenlignelige med de, der kan opnås i tilsvarende laborato-

rieanalyser.

Preface

This dissertation is written in order to partial fulfill the requirements for obtaining the PhD degree at the Technical University of Denmark (DTU). The work, on which this thesis is based, has been performed at the Department of Micro– and Nanotechnology (DTU Nanotech) in the period from November 2015 to November 2018. The work has been supervised by associate professor Mikkel F. Hansen and postdoctoral researcher Gabriel Khose Antonio Minero.

Francesca Garbarino
Institute of Micro and Nanotechnology
Technical University of Denmark
14 November 2018

Acknowledgements

First, I would like to thank my supervisor Mikkel Fougt Hansen for his extraordinary support during these three years. You are an amazing supervisor, the best that a PhD could ask for. Whenever in doubt, I was always welcome at your door to solve problems and I will never thank you enough for that. I would also like to thank my co-supervisor, Gabriel Khose Antonio Minero for his guidance in the last year of the project. You are an incredible person, ready to advise whenever I needed and always there to guide me in the understanding of biochemistry. Moreover, I would like to thank all the other people in my group, and especially Giovanni Rizzi and Jeppe Fock, for their scientific advice whenever I needed it. I would also like to thank all the master students that have decided to do their thesis in our group, with special thanks to Valentina for her rare kindness and Elisabeta for her wonderful work in the past months. I never could have wished for a better group.

I would further like to thank the many past and present colleagues and above all friends at DTU Nanotech. Especially I would like to thank Andrea, Miriam, Laura, Yasmin for the scientific support we were giving one another if needed and the amazing company both in and out of DTU. Zarmeena and Varadarajan for the pep talks, great company during many conferences in the past three years (and above all for proof-reading this thesis ;)) and Janko, Tano, Abhay and Mina for the good laughs, the many badminton games and wonderful dinners in the past year. I extend my gratitude to all the technical and administrative support I received in Danchip (Claus and Rune) and in Nanotech (Per, Sarah, Louise, Dorthe, Jette, Jesper).

Thanks to my Italian friends for never letting me down even though we see each other rarely. Thank you Giulia, Shuandri, Bonnic, Isa, Benny, Mari, Giuli, Berto and many others.

Huge thanks to my parents, without whom I would not be where I am today. Thank you for always believing in me and supporting me in my decisions, even if it meant going abroad and not seeing you for months and months. Thank you Sara for your constant advice, both knowing me and the academia has made me realize you are the person I look up to. Thank you Andrea for bringing your smile and kindness whenever I see you, let it be Genova, Alessandria, London, Copenhagen, Antibes, Milano and who knows which other cities we will live in.

Many thanks to Edoardo's family (and the soon-to-come little bean) for the good laughs in the past years and for their support too.

Last, but not the least, thank you Edoardo for your never-ending support in the past four years. Thank you for tolerating me in the past months, and for showing what it is really important. I would have never imagined to be where I am today without you.

Francesca Garbarino.

Contents

List of Figures

List of Tables

List of symbols

Symbol	Description
ρ	Mass density
v	Velocity
f_j	Force densities
$-\nabla p$	Pressure gradient
η	Viscosity
L_0	Characteristic length
U_0	Characteristic velocity
Re	Reynolds number
γ	Surface tension
G	Gibbs free energy
T	Temperature
θ_c	Contact angle
θ_W	Wenzel contact angle
r	Roughness of a surface
R_1, R_2	Radii of curvature of the interface
w	Width
h	Height
α	Angle between side and top phaseguide material
β	Expansion angle
φ	Interfacial contact angle to the expanded region
p_burst	Burst pressure
$B(t)$	Magnetic field
I_0	Incoming light intensity
n	MNP density concentration
z	Optical path length

Symbol	Description
$\sigma(\theta)$	Extinction cross-section
ϕ	Phase lag
$V(t)$	Voltage signal
V_{ref}	Reference voltage signal
f	Frequency
V_2'	Real component of second harmonic signal
V_2''	Imaginary component of second harmonic signal
f_{B}	Brownian relaxation frequency
k_{B}	Boltzmann's constant
D_{h}	Hydrodynamic diameter
c	Target concentration
V_{G}	Gas volume
n_{G}	Number of moles of gas
R_{G}	Ideal gas constant
K_{A}	Association constant
n_{H}	Hill coefficient

List of abbreviations

Abbreviation	Description
B_{MNP}	Fraction of bound MNPs
BSA	Bovine serum albumin
CAD	Computer aided design
CO	Capture oligonucleotide
COC	Cycle-olefin polymer
DO	Detection oligonucleotide
EDTA	Ethylenediaminetetraacetic acid
ELISA	Enzyme-linked immunosorbent assay
F_{MNP}	Fraction of free MNPs
PLP	Padlock Probe
ID	Inner diameter
LoC	Lab-on-a-chip
LOD	Limit of detection
μTAS	Micro total analysis system
MMB	Magnetic microbead
MNP	Magnetic nanoparticle
MP	Magnetic particle

Abbreviation	Description
OD	Outer diameter
OM	Optomagnetic
PBS	Phosphate buffered saline
PC	Polycarbonate
PCR	Polymerase chain reaction
PDMS	Polydimethylsiloxane
PMMA	Polymethylmethacrylate
POC	Point-of-care
PP	Polypropylene
PS	Polystyrene
PSA	Pressure sensistive adhesive
PVC	Polyvinyl chloride
RCA	Rolling circle amplification
RCP	Rolling circle product
RPA	Recombinase polymerase amplification
SDG	Sustainable development goal
SPR	Surface plasmon resonance
WHO	World health organization

List of publications

Proceeding	**Burst Pressure of all-polymer phaseguide structures of different heights**, F. Garbarino; K. Kistrup ; G. Rizzi ; M.F. Hansen. The 20th International Conference on Miniaturized Systems for Chemistry and Life Sciences, 9-13 October 2016, Dublin, Ireland. I designed, planned and performed the fabrication of the chips, the experiments and analyzed the data.
Paper I	**Burst pressure of phaseguide structures of different heights in all-polymer microfluidic channels**, F. Garbarino; K. Kistrup ; G. Rizzi ; M.F. Hansen. *Journal of Micromechanics and Microengineering* (ISSN: 0960-1317), vol: 27, issue: 12, 2017. I designed, planned and performed the fabrication of the chips, the experiments and analyzed the data.
Paper II	**DNA handling on magnetic microbeads in RCA assay with optomagnetic detection**, G.A.S. Minero; V. Cangiano; F. Garbarino; J. Fock ; M.F. Hansen. *Submitted manuscript.* I planned the experiments with MMBs together with the main author and performed experiments on melting curve.
Paper III	**Rolling circle amplification and optomagnetic detection integrated on a low-cost polymer chip**, F. Garbarino; G.A.S. Minero; G. Rizzi ; G. Volo; J. Fock ; M.F. Hansen. *Submitted manuscript.* I designed, planned and performed the fabrication of the chips, the experiments and analyzed the data.

List of conference contributions

I	**Burst Pressure of all-polymer phaseguide structures of different heights.** F. Garbarino; K. Kistrup ; G. Rizzi ; M.F. Hansen. The 20th International Conference on Miniaturized Systems for Chemistry and Life Sciences, 9-13 October 2016, Dublin, Ireland. POSTER presentation
II	**Automated rolling circle amplification and optomagnetic product detection in an injection molded all-polymer chip , optimization of amplification temperature.**, F. Garbarino; G.A.S. Minero; J. Fock; G. Rizzi; F. Neumann; N. Madaboosi; P. Asalapuram; M. Nilsson; M.F. Hansen. 43rd International Conference on Micro and Nano Engineering (MNE2017), Sep. 18-22, Braga, Portugal, 2017. ORAL presentation
III	**All-polymer chip with integrated sample handling for molecular diagnostics.** F. Garbarino; G.A.S. Minero; J. Fock; G. Violo; G. Rizzi; M. Nilsson; M.F. Hansen. PRN 2018 - Polymer replication on the nanoscale - 8-9 May 2018, Kgs. Lyngby, Denmark. ORAL presentation
IV	**Magnetic microbead sample handling integrated with optomagnetic nanobead detection.** F. Garbarino; G.A.S. Minero; J. Fock; G. Rizzi; M. Nilsson; M.F. Hansen. 12th International Conference on the Scientific and Clinical Applications of Magnetic Carriers, May 22-26, Copenhagen, Denmark. POSTER presentation
V	**On-chip optomagnetic detection and discrimination of single base mutation in Mycobacterium tuberculosis.** F. Garbarino; G.A.S. Minero; J. Fock; M. Nilsson; M.F. Hansen. Functional DNA Nanotechnology Workshop, Rome, Italy, 6-8 June 2018. ORAL presentation

VI	**Strategies for on-chip DNA processing on magnetic microbeads.** G.A.S. Minero; F. Garbarino; J. Fock; M. Nilsson; M.F. Hansen. 12th International Conference on the Scientific and Clinical Applications of Magnetic Carriers, May 22-26, Copenhagen, Denmark. POSTER presentation
VII	**Optomagnetic sensing and biosensing.** M.F. Hansen; G.A.S. Minero; J. Fock; F. Garbarino; G. Rizzi. 12th International Conference on the Scientific and Clinical Applications of Magnetic Carriers, May 22-26, Copenhagen, Denmark. POSTER presentation
VIII	**Optomagnetic characterization and detection: Inexpensive, fast and sensitive characterization of magnetic nanoparticles and detection of biomolecules.** J. Fock; G.A.S. Minero; ; F. Garbarino; M. Donolato; M.F. Hansen. Micro and Nano Engineering (MNE) 2018, Copenhagen, Denmark, Sep. 24-27, 2018. INVITED TALK

Chapter 1

Introduction

1.1 Societal needs

The World Health Organization (WHO) during their 71st world health assembly held in 2018, has approved an agenda focusing on the third sustainable development goal (SDG) given by the United Nations for the 2019-2023 agenda: *ensure healthy lives and promote well-being for all at all ages* [1], [2]. WHO aims at giving strategic directions and applicable norms for the implementation of those goals worldwide, in low, middle and high income countries. In recent years, the world has witnessed significant improvements in life expectancy; in low-and middle-income countries the driving force is the result of large reductions in children mortality, whereas in high-income countries it is mainly due to declining mortality in the older population [3]. The number of people aged 60 or over, will almost double in 25 years, with 75% of them living in western countries [4], [5]. The increase in the amount of older people in those countries will have a huge impact on an already overburdened healthcare system [4]. For this reason, there is an increasing demand for innovations in health and medical support, but also in the introduction of portable healthcare devices and products which could alleviate hospitals and clinics work, by enhancing the opportunity to perform this testing at home or at the doctor's office [6].

1.2 Point-of-care and microfluidic devices

Since 1990 when Manz *et al.* first described an innovative concept to create miniaturized (or micro) total chemical analysis system (μTAS), scientific research has followed a general trend towards the development of microfabricated microfluidic devices [7]. The development expanded to seek applications in e.g. the medical field, and over the years the concept of μTAS developed into lab-on-a-chip (LOC), to include not only chemical analysis but also laboratory processes with the purpose of creating miniaturized fully automated laboratory systems [8]. Point-of-care (POC) lab-on-a-chip devices have in molecular biology its core application, ranging from diagnostics and genomics analysis [9] to biochemical analysis [10], proteomics [11], biosensors [12] and cell research [13], due to the high throughput and small volumes which are of great advantage when creating portable healthcare devices

[14]–[17]. As expressed by Mark *et al.*, the requirements for an LOC device differ between different market segments.

In the market field of *point-of-care testing*, where my project can be applied, the main requirements are: portability, low-cost instrumentation, high specificity and sensitivity with few false-negatives. Moreover high throughput, small volumes and multiplex capabilities would also be desirable [18], [19]. Also, LOC devices should be disposable for one-time use.
The main advantages of using LOC for medical diagnostics can be summarized as [20], [21]:

- Highly automated process (less need for a technician to run the experiments).
- Shorter time of experiments compared to laboratory techniques.
- Lower sample volumes.
- Small size and portability.
- In some cases the analysis can be performed in parallel on the same device.

There are only few examples of microfluidic systems that have obtained a remarkable market share and between those we can find the glucose meter, pregnancy [22] and drug abuse [23] test strips and cardiac markers [24], [25] (see Fig. 1.1 for the representation of the glucose and pregnancy test devices).

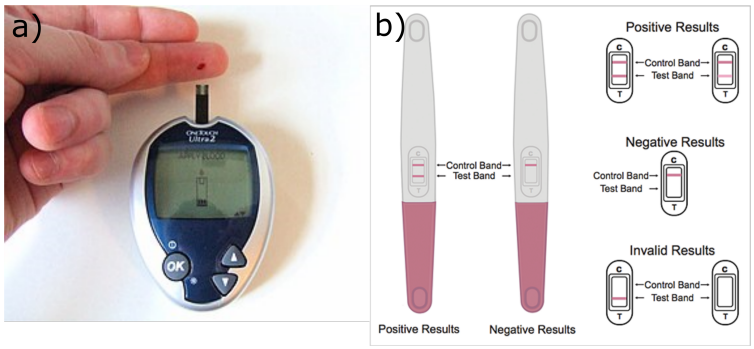

Figure 1.1: (a) Example of a glucose meter and (b) a pregnancy test. In both cases the test-strip used to for the measurements is disposable. Image adapted from [26], [27].

1.2.1 Lab-on-chip technology

Mark *et al.*, define a microfluidic platform (or Lab-on-a-chip system) as *an easily combinable set of microfluidic unit-operations that allow miniaturization within a consistent fabrication technology* [21]. The idea of being able to perform an easy and fast implementation of a biological assay on chip by the study of basic *unit operations* [21], [28] can be summarized as in table 1.1

Table 1.1: Features for the creation of a microfluidic platform. Table adapted from [21].

Microfluidic unit operation	Fabrication technology
Fluid transport	Validated manufacturing
Fluid metering	technology for the whole
Fluid valving	set of fluidic unit
Fluid mixing	operations (prototyping
Separation	and mass fabrication)
Accumulation/Amplification	
Reagent storage	
Incubation	

An LOC system should include at least one or more *unit operations* that could be easily combined together, to establish a specific assay protocol within the given platform. Furthermore it should include one validated *fabrication technology* for the realization of the entire platform [21].

Liquid handling A major aspect to keep in mind when building an LOC, is the ability to obtain an easy-to-use liquid handling. It is considered an important aspect since the final goal of the LOC device is the possibility to perform experiments alone, without the need of a technician. Mark *et al.* divide the liquid aspect of the LOC device in 5 sub-fields, as shown in Fig. 1.2

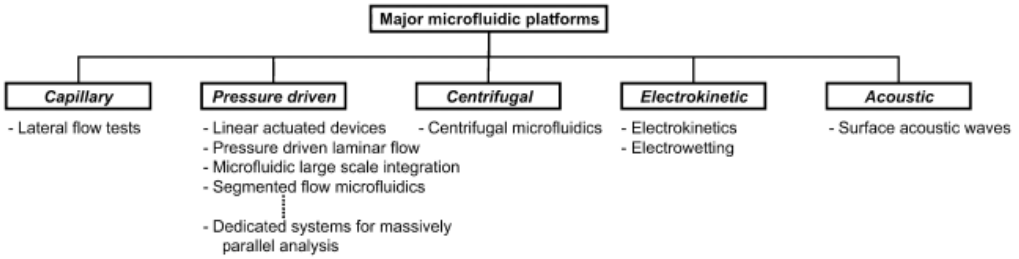

Figure 1.2: Microfluidic platform (or LOC) classified based on the liquid principle. Image adapted from [21].

Each of the sub-fields contains hundreds of examples of LOC devices, which can be found in his review. The *Pressure driven laminar flow* platforms comprise the use of pressure gradients as liquid transport mechanism (in laminar flow). It allows for controllable diffusion mixing, which can be of great advantage e.g. to align cells in continuous flow (flow cytometry) [29], [30], for particle counting and separation [31] among others.
In order to block liquid flow from entering a specific chamber in a LOC system, capillary stop valves were introduced in such devices. They consist of passive non-mechanical valves

operating by surface tension to control the filling of liquid [32]. Similarly, Vulto *et al.* have demonstrated the possibility of creating "flow guidelines", called phaseguides, in order to control the progress of the liquid-air interface [33].

Magnetic beads based technologies Magnetic particles (MPs) have been used for several decades in both manual and automated assays in laboratories. Particles are commonly available in several sizes and with different magnetic properties. Several surface modifications (like the addition of a carboxyl, amino or hydroxyl group) and coatings (protein A, protein G, streptavidin, biotin) are available too. The main advantages consist in their large surface-to-volume ratio, bio-functionalization ability and possibility of manipulation by magnetic fields [34]. These advantages have led to an effort to integrate these magnetic particles in LOC devices [35], [36].
Providing details of all the possible applications would require too much space, but a detailed introduction can be found in the review from Van Reenen *et al.* [34]. In general, for LOC devices, MPs have been applied for mixing fluids, selective capture or labelling of analytes, as means of transport in a static platform and to perform washing steps [34].

1.2.2 Detection

Several detection technologies have been studied for LOC systems, including mechanical [37], electrochemical [38] and optical methods [39]. The fundamental challenge posed for the detection mechanism of these systems, is the ability to be highly sensitive and specific to the target chosen. Pires *et al.* describe the mechanisms and features of the three detection techniques above mentioned, shown in Fig. 1.3 [40].

Method	Mechanism	Features
Electrochemical	Measures changes in conductance, resistance, and/or capacitance at the active surface of the electrodes	(+) Real-time detection (~hundreds seconds range) (+) Low-cost microelectrode fabrication (+) Widely employed in point-of-care (−) Control of ionic concentrations before detection (−) Short shelf life
Mechanical	Detection is based on variations of the resonant frequency or surface stress of the mechanical sensor	(+) Monolithic sensor integration (+) Label-free detection (−) Damping effects in liquid samples (−) Detection generally needs around 30 min (−) Complex fabrication
Optical	Detects variations in light intensity, refractive index sensitivity, or interference pattern	(+) Minimal sample preparation (+) Real-time detection (~hundreds seconds range) (+) Ubiquitous in laboratory (−) Conventional opto-instrumentation is expensive (−) Set-up complexity

Figure 1.3: Summary of the electrochemical, mechanical and optical detection. The (+) sign indicates pros, whereas the (-) indicates cons. Image adapted from [40].

Both electrochemical and mechanical detection techniques are attractive options for the study of LOC devices. However, in both cases there are important drawbacks to consider when creating a microfluidic device. The electrochemical technique can be highly

influenced by temperature, pH and ionic concentrations, which can limit the shelf life of the device [40], [41]. Mechanical sensors, on the other side, can be influenced by mechanical losses associated with viscous damping [40], [41].

Optical detection allows for minimal sample preparation and more importantly its instrumentation ubiquity in the laboratory makes it a good choice when creating lab-on-chip devices. Conventional optical methods include absorbance [42]–[44], fluorescence [19], [45], [46] and surface plasmon resonance (SPR) [47], [48].

Optomagnetic Detection In the project we have used a specific type of optical and magnetic detection called *Optomagnetic Detection*. This detection was pioneered by Mikkel F. Hansen, Marco Donolato and Jeppe Fock [49]–[51]. The technique exploits the rotation ability of magnetic particles in response to an oscillating magnetic field. Fig. 1.4 shows an exemplified version of the technique. The MPs are usually diluted in a solution containing the target that needs to be studied, which is placed along a specific light path. Due to their surface coating, they get attached to the target, which will cause their rotational dynamics to change. We study the extinction cross-section caused by the different rotation mechanism when attached to the target. Fig. 1.4 shows an exemplified version of the technique.

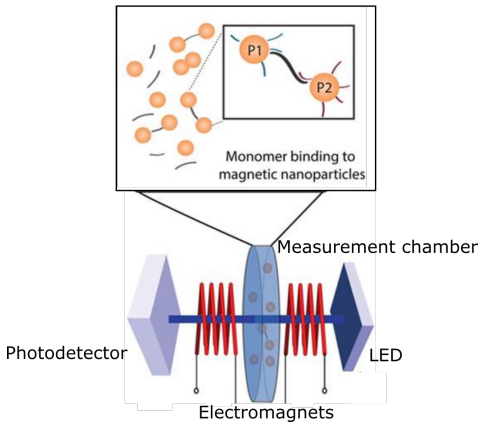

Figure 1.4: Example of the optomagnetic detection technique. Image adapted from [51].

1.2.3 Fabrication technology

Since the early development of microfluidic systems, devices were made in silicon or glass, due to the well established fabrication methods in the semiconductor industry [52], [53]. However, starting from the mid 1990s, polymers began to enter the academic research, due to their low-cost advantage compared to silicon or glass [7]. These materials met the expectations for the creation of a disposable microfluidic device with simplified manufacturing procedures [52]. Also, due to the high variety of polymers available in the market, it was possible to look for the material best suited for the application.
Fabrication of devices using polymers does not require the use of hazardous etching

reagents and the fabrication procedure is relatively easy, which makes them appealing for research labs and not only industry. Tsao [53] defines a 3-step process to select the appropriate material and manufacturing method:

1. Identification of the application needed, and therefore the requirements.
2. Design of the layout of the microfluidic device.
3. Determination of the fabrication strategy and the polymer material, based on the application and requirements of the first step.

It is important to underline that every microfluidic platform is different, therefore it is vital to think carefully about requirements for the specific application needed, because it will in turn affect the choice of material and the fabrication process.

Polymer materials can be divided in three categories: elastomers, thermosets and thermoplastics. The first two types include polydimethylsiloxane (PDMS) and photocurable epoxy SU-8. Their need for curing limits the throughput, not making them appealing for mass production. Thermoplastics on the other hand are well-suited for high volume and low-cost production. They include poly(methyl methacrylate) (PMMA), polycarbonate (PC), polystyrene (PS), polyvinyl chloride (PVC) and the family of cyclic olefin polymers (i.e., cyclic olefin copolymer (COC) and many others). Fabrication procedures for PDMS and thermoplastics are shown in Fig. 1.5.

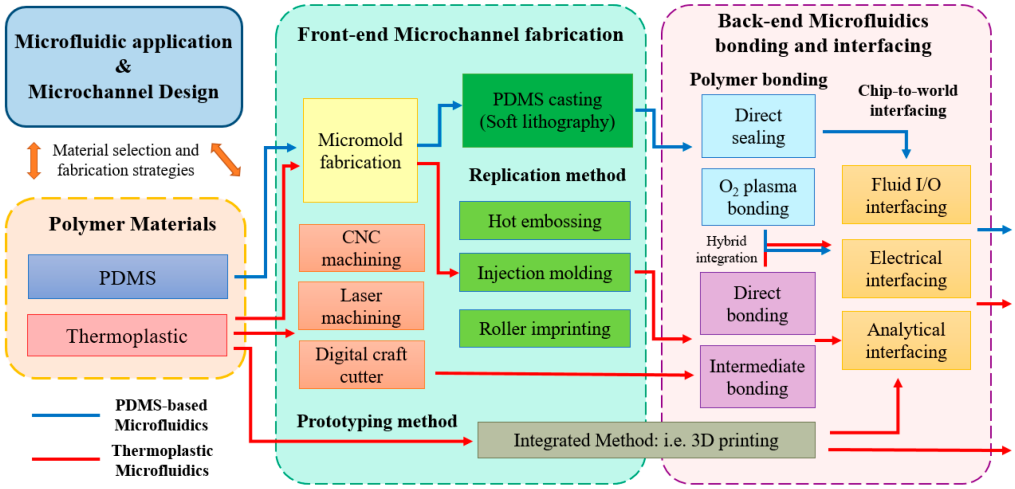

Figure 1.5: Fabrication process chart for PDMS (blue line) and thermoplastics (red line). Image adapted from [53].

Thermoplastic fabrication allows for a variety number of front-end methods, including milling [54] and laser ablation [55]. They can also be fabricated for mass production, with replication processes as hot embossing [56] , roller imprinting [57] and injection moulding [58]. Bonding can be in turn divided in direct bonding such as ultrasonic welding [59], or intermediate bonding which involves the use of an additional material to perform the

bonding. In the project it was only used ultrasonic welding.

1.3 Molecular diagnostics

Molecular diagnostics is a branch of (laboratory) medicine that focuses on the diagnosis of a disease, on the prediction of its course, on the selection of the possible treatments and on the monitoring of the efficacy of therapies [60]. In order to detect the disease, molecular diagnostics uses biological markers, also called biomarkers, traced in the genome of the patient. A biomarker can be defined as *a characteristic that is objectively measured and evaluated as an indicator of normal biological processes, pathogenic processes, or pharmacologic responses to a therapeutic intervention* [61]. In molecular diagnostics it is possible to define three nucleic acid biomarkers:

- microRNA (still under research) for the detection of cancer, such as pancreatic cancer [62].
- RNA for the detection of viruses as dengue, zika [63].
- DNA for the detection of viruses and bacterias, in the latter case research is focusing on study the mutations of bacteria to predict antibiotic resistance [64].

The great importance that these biomarkers have found in recent years lies in their ability to indicate a disease at an early stage (before signs or symptoms), which in turn will impact the treatment given to the patient in the hope to stabilize the disease process [65]. The great sensitivity, specificity, and speed have made molecular assays an attractive alternative to culture or enzyme immunoassay methods as the enzyme-linked immunosorbent assay (ELISA)[66]. These methods can take more than 24 hours to show the final result, causing a delay in the treatment compared to the above mentioned biomarkers [67], [68].
In the field of molecular testing for the study of infectious diseases it is now possible to define qualitative assays that are able to detect a single target, assessing its presence, quantitative assays to monitor and measure the response the presence of viral infections, and multiplexed assays for the detection of at least two or more analytes in the same sample [69]. A basic molecular assay requires normally three steps:

1. extraction and purification of the nucleic acids.
2. the amplification or replication of the target nucleic acid.
3. the detection of the amplified target using the selected method.

In past years researchers have tried to develop "on-chip" solutions, with the aim of integrating and automating the current procedures, to increase the throughput and speed of laboratory tests [70]–[72]. The creation of POC devices to be used in doctor's offices worldwide, could help in the management of pandemic diseases such as Influenza [73] and Tuberculosis among others [74].

1.3.1 DNA amplification

Polymerase chain reaction (PCR) was the first nucleic acid amplification method, making it an essential tool in the detection of DNA sequences [75], [76]. It is still considered the "gold standard" of nucleic acid amplification, but its need to rapid themocycling (heating up to 98°C and cooling down to 60°C rapidly) has made it less attractive for use in point-of-care devices. In contrast to PCR, isothermal amplification methods can be performed at a constant reaction temperature making them easier to perform on-chip. The methods include among others loop-mediated isothermal amplification (LAMP) [77], recombinase polymerase amplification (RPA) [78] and rolling circle amplification (RCA) [79]. The reaction kinetics of these methods varies between exponential (LAMP and RPA) and linear (RCA).

LAMP requires high temperatures (up to 65°C), RPA can be performed low temperatures such as 40°C. Both techniques, as all the exponential amplification techniques, are prone to false-positives, due to the easy contamination and spreading that can occur when handling the solutions.

In contrast, RCA is a more stable method that can amplify the DNA target sequence a thousand fold in 1h. This makes it ideal for applications that require reliable detection at the cost of higher limit of detection (LOD) [80].

In order to start RCA, in a pre-step called "sequence-specific ligation" a circular DNA template gets attached to its complimentary primer [64]. Through the action of an enzyme (phi29 polymerase), this method continuously produces long single-strand DNA concatamer which contains replicated copies of the DNA target. The entire process is shown in Fig. 1.6. The formation of the circular template, prior the RCA, is highly sensitive to sequence mismatches and has been demonstrated to have up to 100% specificity for point mutations[64], [81].

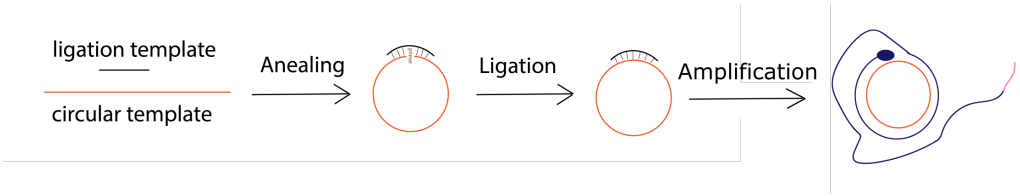

Figure 1.6: Simplified mechanism of pre-amplification step "ligation" and rolling circle amplification . Image adapted from [82].

1.4 Project goals

The goals of this PhD project were:

- To assess manufacturing processes in order to develop a low-cost all-polymer chip with different chambers for on-chip rolling circle amplification assay.

- Integration of bioassay on chip, to make a scalable lab-on-a-chip system for detection of *Influenza virus* and *Mycobacterium tuberculosis* and its antibiotic resistance.

The fabrication part of the project was needed to be kept as simple as possible, in order to be reproduced quite easily. The first part of the project investigated different prototyping techniques for the creation of single use chips, with a focus on injection moulding and CO_2 laser machining. The overall fabrication process should aim at mass-scale production of disposable chips. For the second part of the project, related on the integration of the bioassay on chip, there was a need to make an automated process that a person with a small amount of technical knowledge could use. The creation of an automated setup, together with the use of magnetic beads and external magnets helped develop a lab-on-a-chip device.

1.5 Thesis outline

This thesis describes the design, manufacturing, characterization, and application of different polymers for the creation of single-use polymer chips for a microfluidic system, in particular for the detection of the *Influenza* virus and *Mycobacterium Tuberculosis*. Validation was carried out by comparing the results with reference experiments carried out in our lab.
Chapter 2 provides the necessary theory to understand the project and its results. In particular it focuses on the physics governing microfluidic systems, on the biological knowledge in order to work with DNA sequences and on a brief description of the detection method used in this project.
Chapter 3 gives a description of the fabrication processes and materials applied to manufacture the microfluidic chip systems.
Chapter 4 describes the results obtained in the Conference Proceeding and in Paper I, for the manufacturing of an injection moulded, ultrasonically welded polymer chip and its characterization.
Chapter 5 describes the ongoing process of manufacturing of an injection moulded, ultrasonically welded polymer chip and the struggles faced doing it, which caused a change of the manufacturing process. The integration of RCA and detection on an automated setup is demonstrated.
Chapter 6 presents the most important results obtained over the course of the project and presented in Paper II and III. In this chapter the main focus relied on the integration of the bioassay on chip. A thorough explanation of the setup used is given.
Chapter 7 concludes the thesis by evaluating the project goals and making perspective comments on the feasibility of using polymer chips for assay integration on lab-on-a-chip systems.

Chapter 2

Theory

It is not within the scope of this thesis to perform a thorough analysis of the physical theory pertaining to the subjects. Instead, this chapter presents the needed theoretical background to properly interpret the results. At first, an introduction to the laws regulating liquid flows in microchannels is given. Subsequently the chapter illustrates the needed biological theory to understand the biological assay, and finally, a short explanation on the physics of the detection used in this project is given.

2.1 Liquid in microfluidic devices

The Navier-Stokes equation governs the motion of liquids and can be derived from Newton's second law of motion for fluids. The equation of motion for an incompressible liquid flow is:

$$\rho[\delta_t v + (v \cdot \nabla)v] = \sum_j f_j \tag{2.1}$$

where ρ is the density, v is the velocity and f_j are the force densities comprised of pressure, viscosity and other body forces. Equation (2.1) then can be re-written as:

$$\rho[\delta_t v + (v \cdot \nabla)v] = -\nabla p + \eta \nabla^2 v \tag{2.2}$$

where $-\nabla p$ is the pressure gradient term and $\eta \nabla^2 v$ is the viscosity term. As Henrik Bruus states in his book [83]: *the non-linear term of the equation $\rho(v \cdot \nabla)v$ is responsible for making the mathematical treatment of the equation more complex and difficult.* Therefore, in order to analyze the equation when the non-linear term is negligible, we should use the dimensionless form of the Navier-Stokes equation, where all physical variables are expressed with characteristics scales e.g. L_0 for length and U_0 for velocity. Equation (2.2) thus becomes:

$$Re[\tilde{\delta}_t \tilde{v} + (\tilde{v} \cdot \tilde{\nabla})\tilde{v}] = -\tilde{\nabla}\tilde{p} + \tilde{\nabla}^2 \tilde{v} \tag{2.3}$$

where $\tilde{}$ denotes dimensionless physical variables and

$$Re = \frac{\rho U_0 L_0}{\eta} \tag{2.4}$$

where ρ is the density, U_0 is the velocity of the fluid, L_0 is the characteristic length scale, and η is the viscosity. The characteristic length scale for a rectangular channel is considered the hydraulic diameter, which is equal to $d_\mathrm{h} = 4A/P$, where A is the cross-sectional area of the flow and P is the wetted perimeter of the cross-section. The Reynolds number (Re) describes the ratio between inertial and viscous forces. In systems having a low Reynold's number (Re $\ll$1), the Navier-Stokes equation is reduced to the linear Stokes equation,

$$0 = -\nabla p + \eta \nabla^2 v \tag{2.5}$$

In microfluidic systems where equation (2.5) is valid, turbulence is absent and the flow becomes laminar.
For better understanding of this parameter, I will present a calculation for the Reynold number for one of the channels studied in the project. In Paper I a channel is described with width $W = 1$ mm and height $H = 200$ μm, which is filled with water at a velocity $v = U_0$=1 mm/s. The hydraulic diameter $d_\mathrm{h} = 4A/P = 0.3921$ mm. The kinematic viscosity is given by the ratio between the dynamic viscosity and the density of the liquid and it is equal to $\eta_\mathrm{kin} = \eta/\rho = 0.8926$ mm^2/s.
The Reynolds number will be:

$$\begin{aligned} Re &= \frac{\rho U_0 d_\mathrm{h}}{\eta} \\ &= \frac{U_0 d_\mathrm{h}}{\eta_\mathrm{kin}} \\ &= 0.4393 \end{aligned} \tag{2.6}$$

The result agrees with the above statement of low Reynold's number (Re $\ll$1).

2.2 Surface energy and contact angles

Surface tension and contact angles are fundamental concepts in the theory of microfluidics, and as Bruus [83] states, they allow for understanding the capillary forces that act on two-fluid flows inside microchannels in lab on a chip systems.
Consider a homogeneous liquid. Molecules in the central part of the liquid have exactly the same amount of force pulling them to every side. If we now consider a surface molecule, it has only forces acting upon it toward the liquid. The air – liquid adhesive forces are not comparable to the liquid – liquid cohesive forces, causing the energy of the surface molecules to be higher than those of the bulk. This process is well portrayed in Fig. 2.1

The consequence is the creation at the interface of the surface tension γ defined by the Gibbs free energy (G) per area (A) for fixed pressure (p) and temperature (T):

$$\gamma = \left(\frac{\delta G}{\delta A}\right)_{(p,T)} \tag{2.7}$$

In case of non wetting surface, the system will strive to minimise its total free energy and consequently try to minimise the area of the liquid - air interface [83].

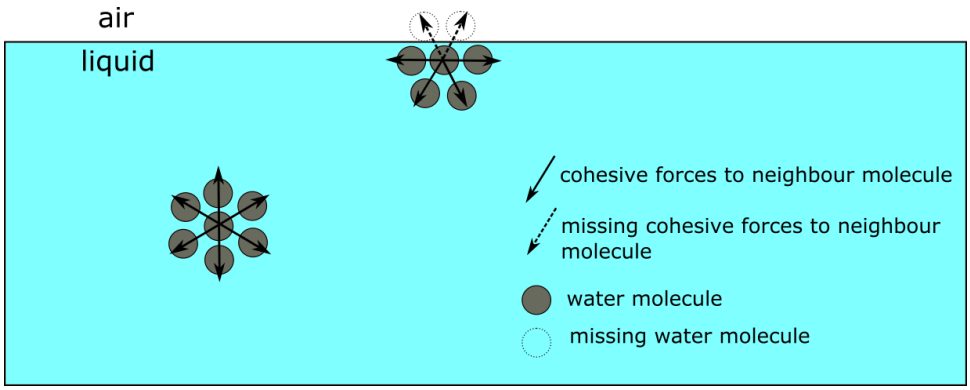

Figure 2.1: Schematic of the surface tension across the liquid-air interface. A molecule in the bulk of the solution will form chemical bonds with neighbouring molecules, whereas a molecule in at the surface will miss some of these chemical bonds. As a consequence, the energy of surface molecules is higher than the bulk ones.

If we now consider a drop of water lying on a surface, as illustrated in Fig. 2.2, and the different surface tensions at the interfaces (liquid-air, solid-liquid and solid-air), the drop will shape itself according to the surface tensions associated with the different interfaces to achieve minimum energy.

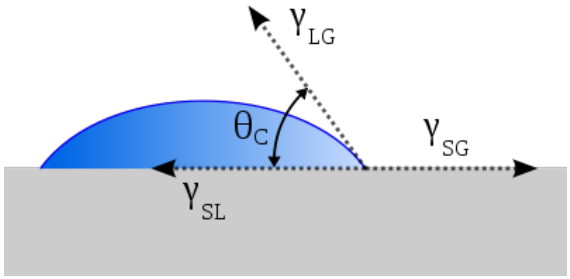

Figure 2.2: Sketch of a drop of water lying on a smooth solid surface. Between the three interface liquid, solid and gas, we will have interfacial tensions as γ_{SL}, γ_{LG} and γ_{SG}. The drop will try to minimise its energy, and depending on the balance of the three energies it will take a certain shape. θ_c is the contact angle. Image adapted from [84].

It is also possible to define the surface tension as a force per unit length. The Young equation can be consequently be re-written for the balance of forces [83], [85]:

$$\gamma_{SG} = \gamma_{SL} + \gamma_{LG} \cos\theta_c \tag{2.8}$$

where γ_{SG}, γ_{SL} , and γ_{LG} are the surface tensions between the different phases and θ_c is the contact angle formed between the surface and liquid phase. Systems with water contact angles $\theta_c < 90°$ are considered hydrophilic and water is expected to (partially) wet the surface of the solid. If $\theta_c > 90°$ the surface is considered hydrophobic.

However in reality, most practical surfaces are rough, with physical and chemical imperfections across the surface of the solid. On such surfaces the only measurable contact angle is the apparent contact angle θ_{ap}, which varies from point to point along the interface of contact between liquid and solid. The apparent contact angle of rough surfaces can be described by the Wenzel law for a completly wetted surface (Fig. 2.3(a)) or the Cassie-Baxter law for a non-wetted surface (Fig. 2.3(b)), if the drop is sufficiently large compared to the roughness scale [86].

The Wenzel law states:

$$\cos\theta_{\mathrm{W}} = r\cos\theta \tag{2.9}$$

In this equation $\cos\theta_{\mathrm{W}}$ is the Wenzel contact angle (the apparent contact angle at the minimum energy), $r > 1$ is the roughness defined as the ratio between the actual area of the surface and the projected area. In this case, as showed in (Fig. 2.3(a)), the liquid has followed the contours of the rough surface. As a consequence it is possible to state that roughness promotes wettability for hydrophilic scenario [85], with a dependence on the chemical properties of the surface.
In case the protrusion of the rough surface are filled with air instead of water, we need to take in consideration the Cassie-Baxter regime:

$$\cos\theta_{\mathrm{CB}} = \phi_{\mathrm{s}}\cos\theta + 1 - \phi_{\mathrm{s}} \tag{2.10}$$

where ϕ_{s} ($\phi_{\mathrm{s}} < 1$) is the fraction of the solid surface area wet by the liquid, $1 - \phi_{\mathrm{s}}$ is the fraction of the air gaps. Also in this case there will be an increase in the contact angle, when the drop bridges the gaps, and it is called superhydrophobicity.

Equations 2.9 and 2.10 can be combined to produce a more general expression for wetting in rough surfaces:

$$\cos\theta_{\mathrm{CB}} = \phi_{\mathrm{s}} r(\cos\theta) + \phi_{\mathrm{s}} - 1 \tag{2.11}$$

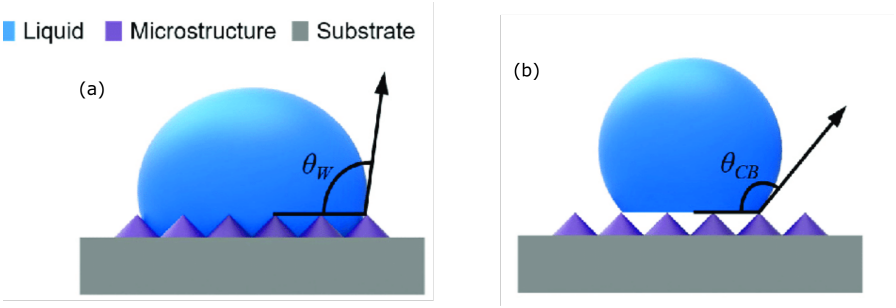

Figure 2.3: Wenzel (a) and Cassie-baxter (b) model of wetting. Image adapted from [87].

2.3 Capillary microvalves and burst pressures

Capillary microvalves rely on the capillary forces dominant in microfluidic systems, which will now be briefly introduced.
An interface between two phases (liquid-gas) with a non-zero surface tension will curve if a pressure difference exists across the interface. This pressure difference can be described by the Young-Laplace equation:

$$\Delta p = \gamma \left(\frac{1}{R_1} + \frac{1}{R_2} \right) \tag{2.12}$$

where γ is the surface tension between the two fluids and R_1 and R_2 are the radii of curvature of the interface.

As demonstrated by Cho [88], in a rectangular microfluidic channel with width, w, and height, h, where a liquid-air interface exists, equation (2.12) can be re-written as:

$$\Delta p = -\gamma \left(\frac{2\cos\theta_{\text{wall}}}{w} + \frac{\cos\theta_{\text{floor}}}{h} \right) \tag{2.13}$$

where θ_{wall} and θ_{floor} are the contact angles between the liquid and side-walls and floor or ceiling of the channel, respectively. Δp denotes the increase in pressure upon passing through the liquid-gas interface, consequently when $\Delta p > 0$ the fluid will spontaneously propagate through the channel, whereas if $\Delta p < 0$ it will not.
A capillary microvalve consists of an abrupt expansion of a microfluidic channel with expansion angle (β), as illustrated in Fig. 2.4, for $\beta > 90°$. Once the interface reaches the expanded region, the interfacial contact angle to the expanded region φ is smaller than the expanded region advancing contact angle θ and the interface is thus pinned as long as $\varphi < \theta + \beta$ [89].

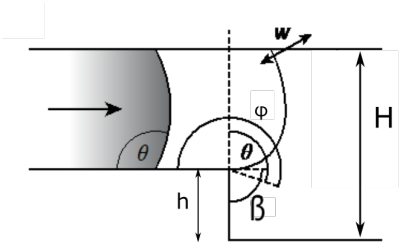

Figure 2.4: Sketch of a geometric capillary microvalve, where pinning is achieved through a sudden change in geometry. θ, β, and φ denote the liquid contact angle with air, expansion angle, and effective contact angle, respectively. w and h denote width and height of the channel. Image adapted from [90].

We can now determine the minimum pressure drop required to advance the interface beyond the expansion with regard to φ, which yields:

$$p_{\text{burst}} = -\gamma \left(\frac{2\cos\theta_{\text{wall}}}{w} + \frac{\cos[\min(\theta + \beta; 180°)]}{h} + \frac{\cos\theta}{h} \right) \tag{2.14}$$

where p_{burst} is the burst pressure of the microvalve and it can be used to predict if a given liquid will be retained or not.

2.3.1 Phaseguides

This section is well described in Paper III and will therefore be summarized.
Under the same basis of the study of capillary microvalves, it is possible to study the pinning pressure for phaseguides. The phaseguide structures are ridges protruding from the channel bottom or top, pinning the liquid meniscus until the pressure exceeds the burst pressure defined by both the geometry of the structure and the wetting properties of the liquid, as stated by Vulto [91] [33]. In his work he defines design rules for phaseguides as shown in Fig. 2.5 and shows the potential of using phaseguides for filling microfluidic structures without bubbles as in Fig. 2.6 .

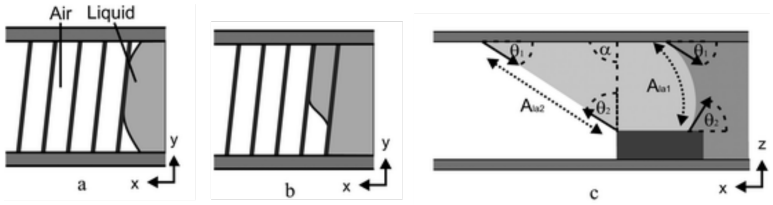

Figure 2.5: Principle of phaseguides as defined by Paul Vulto [33]. (a) and (b) show and advancing liquid jumping over the phaseguide. (c) Schematic representation of pinning effect of the phaseguide: complete pinning will occur when the angle α between the vertical side of the phaseguide and the top material is higher than 180° minus the two contact angles θ_1 and θ_2 of the two materials. Image adapted from [33].

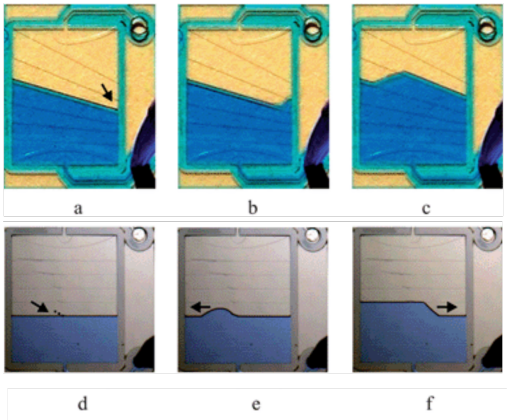

Figure 2.6: Example of two different overflowing methods. (a,d) Show the liquid overflowing phaseguides on two differently shaped predefined position along the phaseguide, at the smallest angle (where the arrow is). (b,e) and (c,f) show the liquid proceeding to fill the entire space until the next phaseguide. Image adapted from [33].

In our project, phaseguides were studied in order to be able to have a controlled filling, without bubbles, of the liquid inside the chambers of the chip. Fig. 2.7 illustrates two different filling processes carried out during the project. Fig. 2.7(a) and (b) show the filling process carried out when characterizing phaseguides in Paper I. The overflow position was selected by designing a centrally placed branch forming an angle α=45° with the straight phaseguide. The liquid overflows as shown in Fig. 2.6(d), (e) and (f), until it reaches the next phaseguide. Fig. 2.7(c) and (d) illustrate the phaseguides designed in Paper III, where the overflowing position is similar to Fig. 2.6(a), (b) and (c). Also in this case the liquid will flow in the gap between phaseguides until it fills the space up completely.

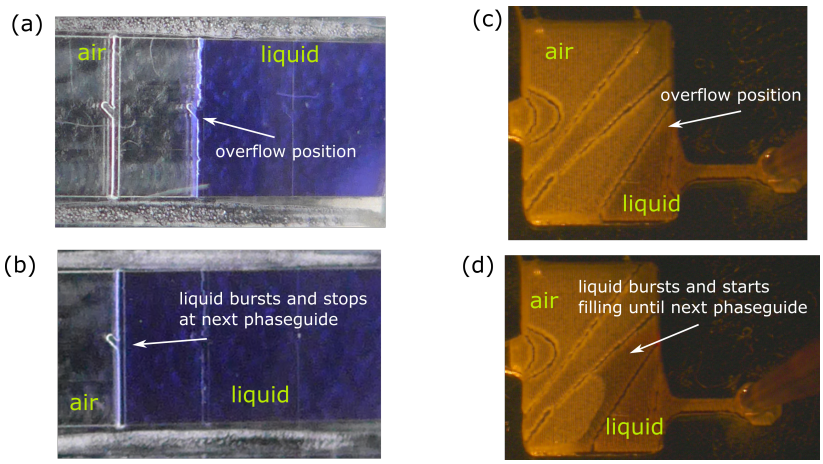

Figure 2.7: Top-views of channels with liquid passing over a phaseguide. (a) Depicts the channels characterized in Paper I, where it is possible to notice the liquid pinning perfectly at each phaseguide. (b) Shows one of the chambers of the chip characterized in Paper III. Also in this case the liquid pins at the first phaseguide, then overflows at the smallest angle and flows in the gap before the next phaseguide.

In the first part of the project, as shown in Fig. 2.8, the channel of width W and height H was formed by a structured injection moulded part sealed by a flat foil, Eq. (2.14) can be written in terms of the contact angles θ_{m} and θ_{f} of the liquid to the moulded part (m) and the foil (f).

In the experimental studies of this project, the interface was observed to always pin at the back edge of the phaseguide in all experiments. At the edge with the expansion, it is possible to define an angle β to horizontal (side-view in Fig. 2.8). Similarly to the theory explained before, the interface is pinned if $\varphi < \theta + \beta$. Consequently, for phaseguides as that in Fig. 2.8, the pressure that we need to apply to overcome the pinning at the edge of the expansion is:

$$p_{\mathrm{pin}} = -\gamma \left(\frac{2\cos\theta_{\mathrm{m}}}{w} + \frac{\cos[\min(\theta_{\mathrm{m}} + \beta; 180°)]}{H - h} + \frac{\cos\theta_{\mathrm{f}}}{H - h} \right) \tag{2.15}$$

A value of $p_{\mathrm{pin}} > 0$ indicates that the liquid-gas interface is pinned at the edge (pinning

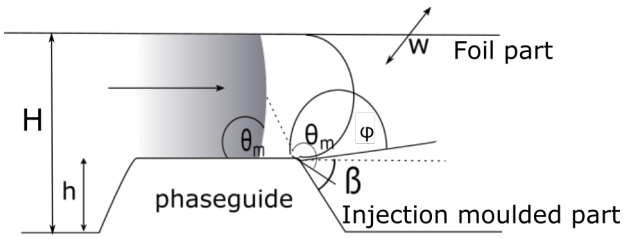

Figure 2.8: Side-view sketch of channel cross-section with a liquid passing over a phaseguide (left to right). The parameters θ_{m}, β, and φ describe the liquid contact angle to the moulded part, the expansion angle, and the effective contact angle, respectively. w and h denote the width of the channel and height of the phaseguide and H denotes the height of the channel. Image adapted from [92].

condition), whereas $p_{\mathrm{pin}} < 0$ indicates that the liquid-gas interface will pass the edge without being pinned.

2.4 Fundamentals of DNA

Deoxyribonucleic acid (DNA) is a molecule composed of two strands that arrange themselves around each other to form the double helix, which carries the genetic instructions used in the growth, development, functioning and reproduction of all known living organisms and many viruses.

The two DNA strands are known as polynucleotides. Each nucleotide is composed of one of four nitrogen-containing nucleobases (cytosine [C], guanine [G], adenine [A] or thymine [T]), a sugar called deoxyribose, and a phosphate group. The nucleotides are bonded together with covalent bonds between the sugar of one nucleotide and the phosphate of the next, resulting in an alternating sugar-phosphate backbone as in Fig. 2.9.

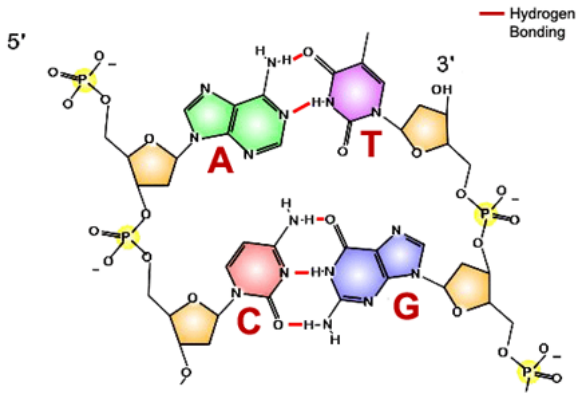

Figure 2.9: Chemical structure of DNA; hydrogen bonds shown as redlines. Image modified from [93].

Directionality or polarity, which is the chemical orientation of a single strand of nucleic acids, is important to keep in mind when handling DNA sequences. Specifically, one must remember the chemical convention for DNA of naming carbon atoms in the nucleotide sugar-ring. The 5'-end of DNA contains a phosphate group attached to the 5' carbon of the ribose ring, and the 3'-end contains a hydroxyl group (-OH), as also illustrated in Fig. 2.9. It is their orientation along the sugar-phosphate backbone that gives directionality to each DNA strand. In a double helix, the direction of the nucleotides in one strand is opposite to their direction in the other strand (antiparallel directionality), in order to allow formation of base pairs called Watson-Crick pairs [94].

The rules of complementary base paring of nucleobases for each strand of a DNA double-helix, are the following:

- adenine (A) bonds to thymine (T), creating two hydrogen bonds.
- cytosine (C) bonds to guanine (G), creating three hydrogen bonds.

These are hydrogen bonds, meaning they can be separated and rejoined relatively easily unlike covalent bonds as shown in Fig. 2.10. A stable initial contact between the two strands with two or three bases has to be made, before the full strand "zipps" together, which is referred as a cooperativity effect.

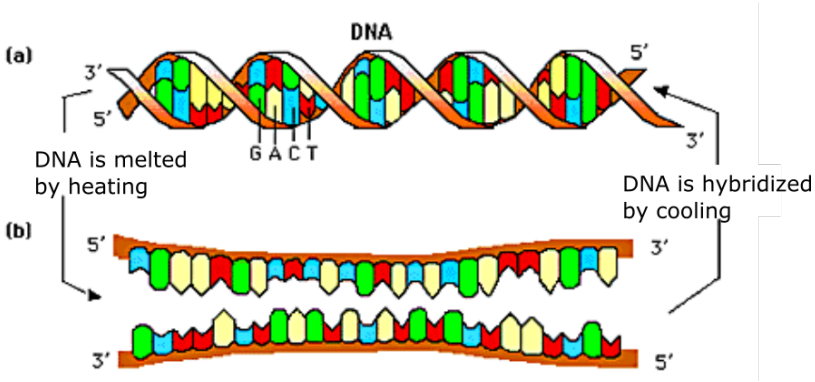

Figure 2.10: Process of melting and hybridizing of a DNA helix. Image modified from [95].

The process in which single stranded DNA anneals to a complementary strand is called hybridization [96]. It is considered to be the basis for many diagnostic applications, which rely on a signal of a labelled probe generated through sequence-specific hybridization with DNA analyte or its amplification product [97]. The association depends on the physical-chemical parameters such as temperature, net charge and base pair composition. In the latter case, association rates of oligomers with high CG content are higher, and therefore more stable, than rates with high AT content.

"Zipping" and "unzipping" of DNA helix has a cooperative effect with a characteristic temperature of transition from an ordered structure (double helix) to randomized DNA coils called melting temperature.

The stability of DNA double helix can be therefore measured by studying the melting temperature, which is referred to the temperature at which 50% of the double stranded molecules are converted into single stranded ones. Consequently, it is both the amount of GC base pairs and the length of the DNA double helix that determine the strength of the association between the two strands of DNA [98], [99]. Lowering the surrounding temperature allows the single-stranded molecules to anneal or hybridize to each other.

Before introducing the next section, it is fundamental to explain the meaning of persistent length and the difference between intramolecular and intermolecular base pairing. The so-called "persistent length" is the critical length for bending of DNA strands. It is considered to be 6 nucleotides. Senior *et al.* [100], illustrate the possibility of creating hairpin-like secondary structures when two complementary arms (each of 6 nucleotides) are joined via a 4 nt loop and self-anneal. Similarly Cederquist [101] has shown the possibility of creating a looped DNA secondary structure with a 22 nucleotide loop.
Intramolecular base pairing implies that two regions of the same single-stranded DNA must be complementary in the opposite direction. Upon such a base-pairing, a secondary structure (double helix) is formed in a way that might terminate in unpaired DNA ends or hairpin-like secondary structures (see Fig. 2.11). The formation of this loop secondary structure depends on the ability of the DNA strand to fold onto itself. If the length of the DNA strand is longer than the persistent length, there is higher probability to form stable secondary structure, whereas the longer DNA hairpin the lesser impact of self-annealing since the DNA strands will be too short to bring the self-complementary parts in a close proximity.

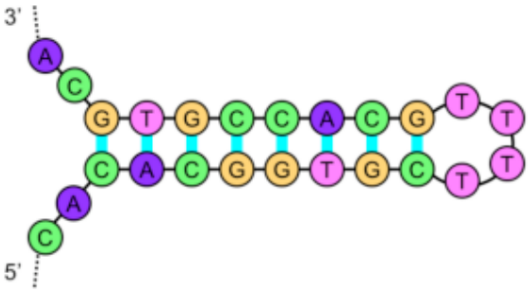

Figure 2.11: DNA hairpin. Image adapted from [102].

The intramolecular bonds have the consequence of slowing down the hybridization between labelled probe and analyte DNA strands, due to the relatively strong competition from the intramolecular bonds. As Gao *et al.* [103] explain, the formation of only three intramolecular bonds can slow hybridization by a factor of two, which may have implications for the design of biosensor using this specific formation of secondary structures.

2.4.1 Sequence specific ligation

Ligation is a process in which two nucleic acid fragments are joined together. It is possible to obtain a template-directed enzyme-free ligation [104], but in our case we have obtained ligation through the action of an enzyme. In our system we use a circularized oligonucleotide probe (from now on referred as padlock probe or PLP), with a length of 90 nt for *Influenza* and 89 nt for *Tuberculosis*. These padlock probes are composed of two target-complementary segments, connected by a DNA loop. The 5′ and 3′ ends of the linear PLPs are brought in proximity upon hybridization to a target sequence [105]. The two ends are joined by the action of a DNA Ligase, creating a circular probe bound to a target. The value of this process lies in its high selectivity, since mismatched probes are poor substrates for ligases, moreover it has been demostrated to have up to 100% specificity for point mutations [64], [81]. The process is shown in Fig. 2.12.

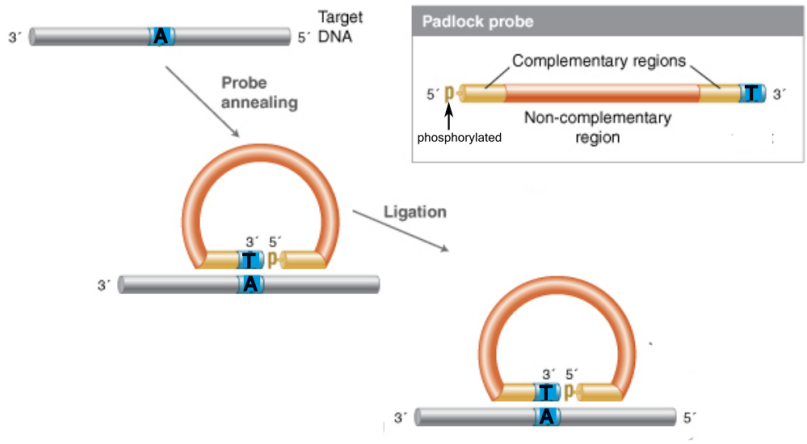

Figure 2.12: A single probe is designed such that the ends of the probes are complementary to the target sequence. When annealed to the desired target, the ends form a nicked structure that can be efficiently ligated if there are no gaps or mismatched base pairs. Image adapted from [106].

It is possible to estimate the melting temperature of a double helix based on its length and the amount of GC base pairs, but since it is a complex calculation it was analyzed with the aid of an online software called "IDT OligoAnalyzer" [107].

The ligation temperature was calculated based on the melting points of the PLP ligating arms: for *Influenza* we obtained 62°C for 5'-terminal and 60°C for 3'-terminal in the ligation buffer (a mixture containing BSA, Tris-HCl, KCl and Triton X-100). For *Tuberculosis* the melting points were: 68.8°C for 5'-terminal and 67°C for 3'-terminal. According to the rule of thumb used in polymerase chain reaction (PCR), the annealing as well as ligation temperature was calculated as 5-10°C lower than the lowest melting point, consequently being 55°C for the *Influenza* and 60°C for the *Tuberculosis* targets.

In our study, both the DNA target and the PLPs were used to hybridize short comple-

mentary sequences of oligonucleotides, referred as capture and detection oligonucleotides (CO and DO), respectively, for different functions which will be elaborated in the following chapters.
The process of finding the right sequence, which could hybridize the DNA strand, has to be carried out along with the study of the intramolecular bonds of the secondary structures of our strands. Fig. 2.13 shows the secondary structures of the *Influenza* DNA Target (Fig. 2.13(A)) and PLP (Fig. 2.13(B)), and *Tuberculosis* DNA Target (Fig. 2.13(C)) and PLP (Fig. 2.13(D)) used in the project.

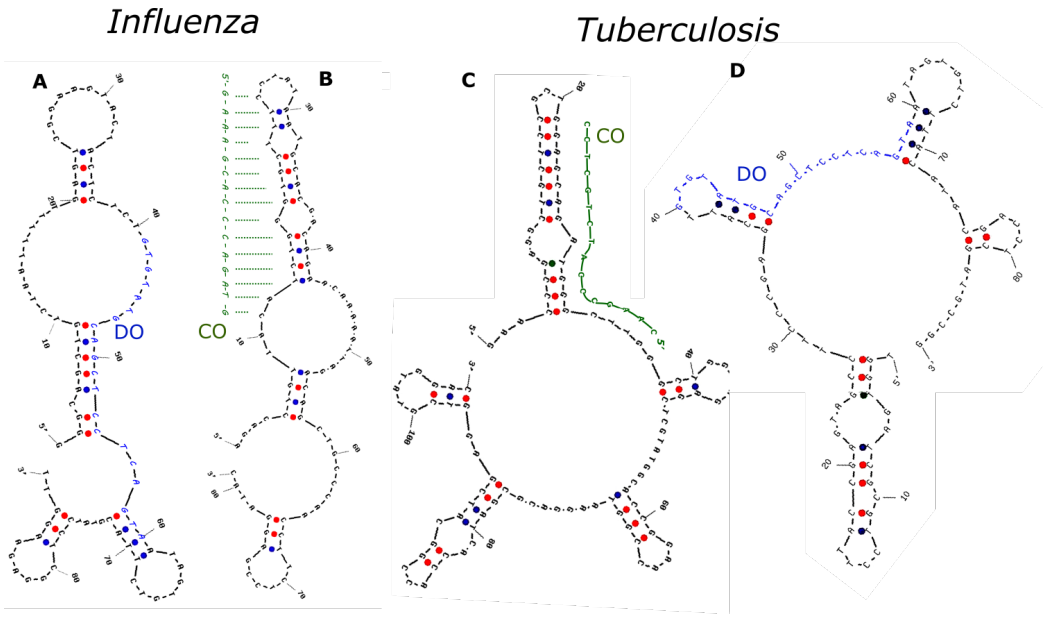

Figure 2.13: Secondary structures of Influenza DNA target (A) and padlock probe (B), and of Tuberculosis DNA Target (C) and padlock probe (D). Image partially adapted from ESI of Paper II.

It is clear from the first look that the both *Influenza* and *Tuberculosis* sequences reveal multiple self annealing spots, above all at the CO binding site (green bases in Fig. 2.13). The blue bases show the DO binding site, which is less problematic thanks to the two unpaired loops of the PLP site.
Due to the strong intramolecular bonds at the CO binding site, there was a need for the melting of those bonds to favour an efficient capture of the DNA Target - PLP conjugates with the CO. The result was obtained by annealing them at 55°C for *Influenza* and at 60°C for *Tuberculosis*. At these temperatures, the intramolecular secondary structures unzips and the CO can bind successfully to the DNA target upon annealing of the complementary DNA strands. Slow cooling of the mixture in thermoshaker (to 30°C during 30 min) was important for CO bridges to form whereas instant cooling of denatured DNA molecules (to 23°C) prevented proper hybridization between the CO and the DNA Target.

2.4.2 Rolling circle amplification (RCA)

Rolling circle amplification is an isothermal amplification technique for molecular diagnostics. Upon sequence specific ligation, where a circular template is formed by annealing and ligation of a padlock probe onto the target, the 3′-end of DNA targets are extended by an enzyme called phi29 polymerase. This enzyme has strong ability to displace newly synthesized DNA copies, by adding nucleotides to a growing line of DNA product (also called rolling circle product or RCP) [81]. This leads to the formation of a long single-stranded DNA concatemer containing repeated copies of the DNA sequence complementary to the PLP as shown in Fig. 2.14.
This amplification technique takes place at 30-40°C and due to the high processivity of the phi29 polymerase, linear amplification can be performed for up to 20 h. After about 30-60 min of RCA, RCA products (RCPs) are coils of DNA with a size of 0.2-1 μm [45].

The amplified DNA sequence has tendency to fold into so-called nanoflowers comprised of DNA wrapped around magnesium pyrophosphate crystals, by-products of amplification. Spatial organization of RCPs is complex and requires further attention since the effective number of binding sites in RCPs can be significantly decreased due to (1) intramolecular folding and (2) co-crystallization of DNA with magnesium pyrophosphate salts.

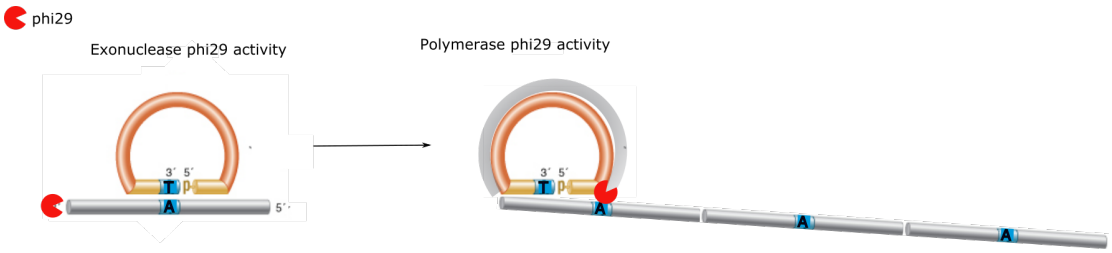

Figure 2.14: Graphic showing the RCA process. The phi29 enzyme first act as exonuclease, removing the single stranded bases from the 3'-end of the DNA Target. Once arrived at the double stranded bases, it starts its polymerase activity by replicating the DNA Target. Image adapted from [106].

2.5 Optomagnetic detection

In order to detect the RCPs, we study the change in the hydrodynamic size of magnetic nanoparticles (MNPs) when they bind to the RCPs. There are several different ways to study the hydrodynamic size, and in this project we use a quite novel and fast method called optomagnetic detection, pioneered in our group by Marco Donolato, Mikkel F. Hansen and Jeppe Fock. The basics of the optomagnetic theory have been extensively reported by Fock *et al.* and Donolato *et al.* [49]–[51]. Here I intend to explain the principles in order to make the results of the next chapters comprehensive.

The optomagnetic technique (from now on called OM technique) probes the second harmonic modulation of light transmitted through a suspension of MNPs in response to

a magnetic field $B(t)$, as illustrated in Fig. 2.15.

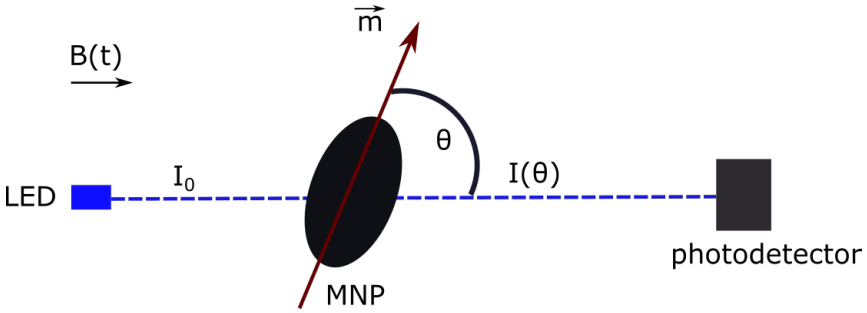

Figure 2.15: Schematic illustration of the principle of the OM technique.

As portrayed in the figure, MNPs have an elongated shape, rather than a spherical one and have a remnant magnetic moment along their longitudinal axis. The Beer-Lambert law describes the intensity of the light, $I(\theta)$, transmitted through a suspenion as:

$$I(\theta) = I_0 \exp\left(-\sigma(\theta) n z\right) \tag{2.16}$$

where I_0 is the intensity of the transmitted light, n is the MNP density concentration, z is the optical path length and $\sigma(\theta)$ is the average extinction cross section of an MNP. The extinction cross section refers to the orientation (angle θ) of the axis of the MNP to the light path axis, and can be written as:

$$\begin{aligned} \sigma(\theta) &= \sigma_{\parallel} \cos^2(\theta) + \sigma_{\perp} \sin^2(\theta) \\ &= (\sigma_{\parallel} - \sigma_{\perp}) \cos^2(\theta) + \sigma_{\perp} \\ &= \Delta\sigma \cos^2(\theta) + \sigma_{\perp} \end{aligned} \tag{2.17}$$

The parameters $\sigma_{\parallel}$ and $\sigma_{\perp}$ are the extinction cross sections of the MNPs, when they are parallel and perpendicularly aligned to the light path. The extinction cross-section can be regarded as the total losses (extinction) of energy from the incident beam due to both absoption and scattering. In our case, both the magnetic field and the light are horizontal as shown in Fig. 2.15, meaning that the parallel cross-section $\sigma_{\parallel}$, will absorb less light compared to the perpendicular one $\sigma_{\perp}$. Therefore $\Delta\sigma$ is expected to be a negative number.

The thermal average of the parameter $\cos^2(\theta)$ can be defined thanks to Boltzmann statistics as $\langle\cos^2(\theta)\rangle = 1/3 + (2 \times \beta^2)/45$, where $\beta = (mB)/(k_{\mathrm{B}}T)$ is the ratio between the magnetic and thermal energies [49]. At low fields $\langle\cos^2(\theta)\rangle = 1/3$.

The signal measured at the photodetector is a voltage $V(t)$ which is normalized with a reference signal V_{ref}, in order to correct for possible variations of the transmitted light. V_{ref} is referred to zero magnetic field and therefore randomly oriented MNPs. The outcome for a thin sample is:

$$\frac{V(t)}{V_{\text{ref}}} \simeq 1 - nz\Delta\sigma\frac{2}{45}(\beta^2) \tag{2.18}$$

In case of an oscillating magnetic field:

$$B(t) = B_0 \sin(2\pi f t) \tag{2.19}$$

the MNPs will show optical extinction depending on their alignment with the magnetic field, based on the frequency f.

If we introduce the oscillating magnetic field $B(t)$ in Eq. (2.18), we can postulate a response of the form:

$$\frac{V(t)}{V_{\text{ref}}} = 1 - \frac{nz\Delta\sigma\frac{2}{45}m^2B_0^2}{(k_{\text{B}}T)^2}\sin^2(2\pi f t - \phi) \tag{2.20}$$

where we have introduced the parameter ϕ, a phase-lag of the MNPs response. By introducing the Pythagorean identities to re-write $\sin^2(2\pi f t - \phi)$, the signal becomes:

$$\begin{aligned}\frac{V(t)}{V_{\text{ref}}} = 1 - \frac{nz\Delta\sigma\frac{2}{45}m^2B_0^2}{(k_{\text{B}}T)^2}&(1 - \cos(2\phi)\cos(4\pi f t) - \sin(2\phi)\sin(4\pi f t) \\ &= V_0 + V_2''\cos(4\pi f t) + V_2'\sin(4\pi f t)\end{aligned} \tag{2.21}$$

The 1st harmonic signal is not observed, due to the square dependence in Eq. (2.20) and thus only the average (or zero'th harmonic) photodetector signal V_0 and the 2nd harmonic signal are considered, which will be used to detect changes in the hydrodynamic size of MNPs. The complex second harmonic signal can be divided in its real ($\sin(4\pi f t)$) component V_2' and imaginary ($\cos(4\pi f t)$) component V_2'' as:

$$V_0' = 1 - \frac{nz\Delta\sigma\frac{2}{45}m^2B_0^2}{(k_{\text{B}}T)^2} \tag{2.22}$$

$$V_2'' = \frac{nz\Delta\sigma\frac{2}{45}m^2B_0^2}{(k_{\text{B}}T)^2}\cos(2\phi) \tag{2.23}$$

$$V_2' = \frac{nz\Delta\sigma\frac{2}{45}m^2B_0^2}{(k_{\text{B}}T)^2}\sin(2\phi) \tag{2.24}$$

We now turn to consider the phase lag ϕ of the response of the particles. The introduction of the magnetic field allows us to study the optical extinction as function of the frequency f. A change in frequency will modify the MNPs ability in aligning with the magnetic field, introducing a phase lag ϕ.
Fig. 2.16 shows the measured signal response for increasing frequencies (2, 25, 107 and 651 Hz).

Clearly, for increasing frequency the phase lag will increase, and in turn the maximum signal amplitude will decrease. The decrease in signal amplitude is due to the change of sign of the magnetic field, before MNPs were able to align.

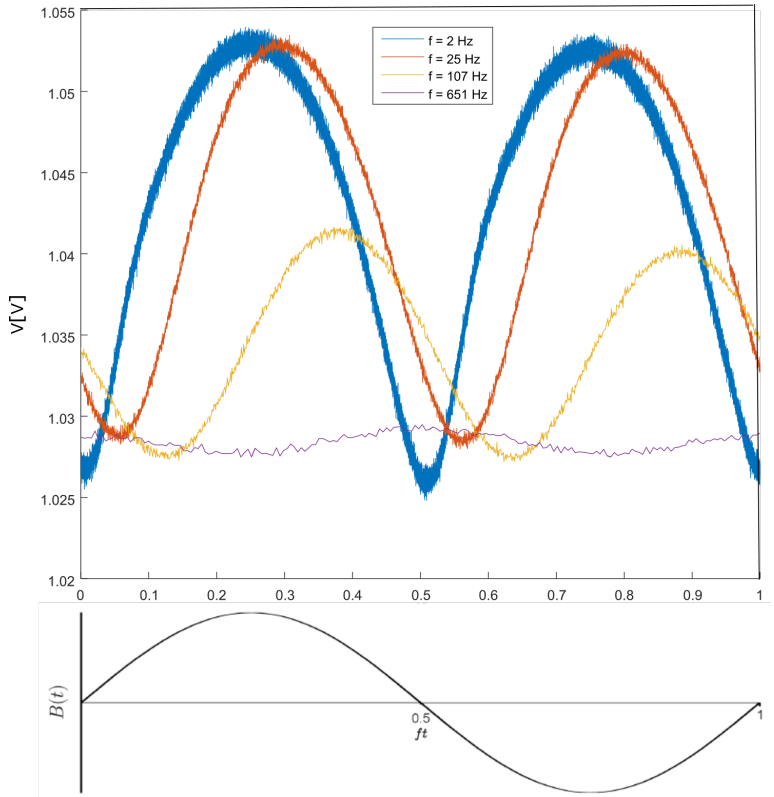

Figure 2.16: Measurements of the photodetector signal at different frequencies with the corresponding oscillating magnetic field. The measurements were done on a suspension of MNPs functionalized with short DNA sequences.

The rotation for the MNPs to align to the magnetic field, in order to reach equilibrium is called Brownian relaxation. The characteristic frequency is:

$$f_{\mathrm{B}} = \frac{k_{\mathrm{B}}T}{\pi^2 \eta(T) D_{\mathrm{h}}^3} \tag{2.25}$$

where k_{B} is the thermal energy, η is the viscosity and D_{h} is the hydrodynamic diameter. Clearly, f_{B} decreases at increasing hydrodynamic sizes. For the 100nm MNPs used for the detection, the Brownian relaxation frequency is equal to 468.38 Hz.

The Brownian relaxation frequency corresponds to the point where V_2' shows a peak-like feature, at approximately $f_p = 1.21 f_{\mathrm{B}}/\sqrt{3} = 0.70 f_{\mathrm{B}}$ and to the point where V_2'' crosses zero [50]. Furthermore $f = f_{\mathrm{B}}$ corresponds to a phase lag of $\phi = \pi/4$. Therefore the peak can be used to determine the Brownian relaxation frequency and consequently also the hydrodynamic size. Fig. 2.17 shows the real, imaginary and phase graphs.

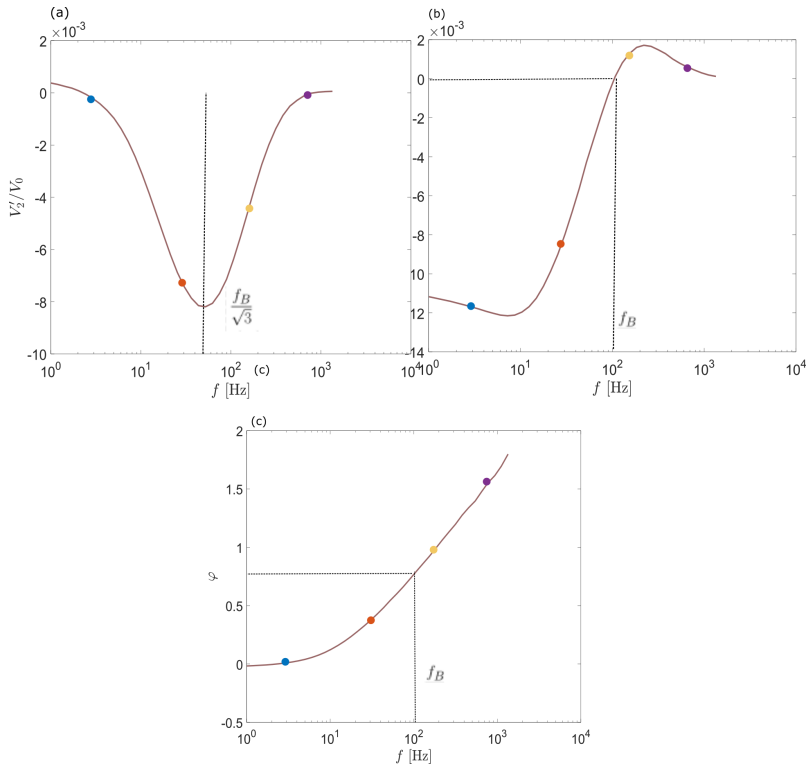

Figure 2.17: (a) Real part , (b) imaginary part and (c) phase lag of the second harmonic signal as function of frequency. The different dots and colors refer to the frequencies studied in Fig. 2.16.

Evaluation of OM spectra In an average experiment, the spectra will show 40 measurements over the course of 30 min, corrisponding to a new spectrum measured every 45 s. The spectra can be seen in Fig. 2.18(a). It can be divided in two areas defined by the two peaks:

- The peak of positive sign at low frequencies associated with clusters of MNPs.
- The peak of negative sign at high frequencies asscociated with free MNPs.

As an example for better understanding, at high DNA concentrations the MNPs will have longer RCPs to attach to, creating more agglutination compared to lower concentrations. As a result, the peak in the high frequencies (turn-off) will lower the amplitude as more free MNPs disappear from the light guide. In contrast, the peak at low frequencies (turn-on) will increase due to the increase in bound particles. Basically, the magnitudes of those peaks change as more free MNPs agglutinate.

The study in the project is carried out analyzing the turn-off signal, with a range of frequencies 50-1000Hz. We detected the binding of MNPs to the rolling circle products (RCPs) via the depletion of unbound MNPs, as shown in Fig. 2.19(a) and (b).

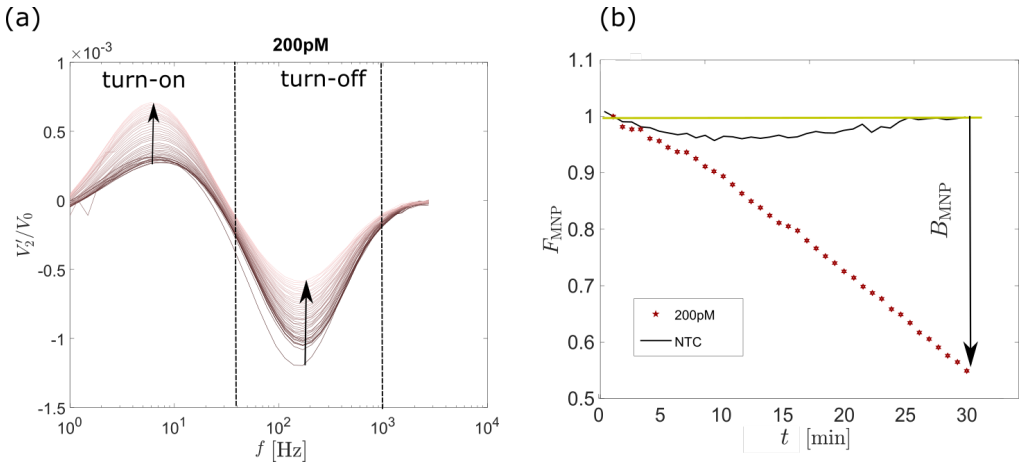

Figure 2.18: (a) Measurement of the normalized real part of the second harmonic. (b) Depleted signal on time. The arrow shows the parameter taken in consideration for our studies, which is the amount of bound MNPs. Measurements was carried at 56°C with a target concentration of 200pM for a period of 30 min. The arrows intend to show the growth profile of the curve over time. Image adapted from Paper III.

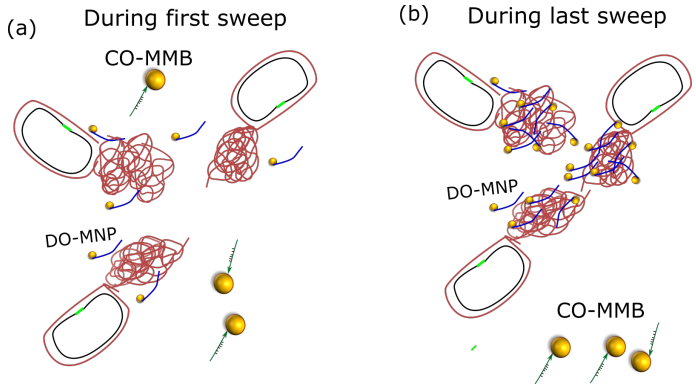

Figure 2.19: (a) Sketch of the situation during the initial sweep. The RCPs detach from the CO-MMB, leaving the RCPs free to move in the chamber. (b) Shows the sketch of what happens during the following sweeps, with the DO-MNPs slowly binding to the RCPs.

The signal over time of Fig. 2.18(b) shows the fraction of free MNPs for two target concentrations: a negative template (black line) and 200pM (brown dots). The higher the concentration, the lower the signal will be, since more MNPs will be bound to the RCPs. Time is also an important factor since more beads will bind to the RCPs over the time. For the NTC sample, the signal depletion due to unspecific interactions was found to be about 3-5%. We can define the fraction of free MNPs (F_{MNP}) in the 40th spectrum as the ratio between the free MNP signal in the 40th spectrum to the first spectrum after the temperature stabilized. Both first and 40th second harmonic signals are normalized

with the zero'th harmonic of the same sweep. The normalization is carried out in order to compensate for variations of the incoming light.

$$F_{\mathrm{MNP}} = \frac{\sum_{f=50\ \mathrm{Hz}}^{1000\ \mathrm{Hz}} V_2'(f,40)/V_0(f,40)}{\sum_{f=50\ \mathrm{Hz}}^{1000\ \mathrm{Hz}} V_2'(f,1)/V_0(f,1)}. \tag{2.26}$$

In the dose response curve we show the fraction of the bound MNPs, as illustrated with the arrow in Fig. 2.18(b), which can be calculated as:

$$B_{\mathrm{MNP}} = 1 - F_{\mathrm{MNP}} \tag{2.27}$$

The results are then portrayed in a dose-response method, where the average from multiple measurements of the depletion of the turn-off signal is calculated for different target concentrations and plotted in a single graph. The time frame at which it is calculated in this project is 20 or 30 min.

Chapter 3

Chip fabrication methods

An important aspect of the project lies in the ability to rapidly create chip prototypes for mass production, in order to be as commercially relevant as possible. The fabrication method chosen for this project evolved over time, with a main focus on injection moulding for the first year and half. Due to some technical problems, it was then chosen to shift towards a faster design prototyping method such as CO_2 Laser for the following year. Finally, thanks to a collaboration with the Mechanical Department at DTU, in the last six months of the project it was possible to shift back again to injection moulding. The reasons that made me take the decision of changing from one fabrication method to another will be described in this chapter.
Kistrup *et al.* [90] demonstrated the possibility of obtaining mass produced finished chips in two (full) working days using micromilling and laser machining as prototyping methods, injection moulding as fabrication method and ultrasonic welding for bonding. The process was used in this project too, and will be explained in the following sections.

3.1 CO_2 laser machining and adhesive bonding

Infrared laser ablation is a material removing fabrication method, which uses heat from the laser beam to ablate the material itself. Its high flexibility together with the possibility of changing the design make this method an important tool for micromachining [108] [109].
The laser machine used is an Epilog Mini 18 Laser, with 45×30 cm^2 work area, a wavelength of 10.6 μm that hits the surface perpendicularly and is focused with the aid of lenses and a mechanical plunger. To control the laser, a vector graphics editor was used (CorelDraw). The machine was operated in two different modes of laser processing: vector cutting, to cut through polymer layers, and raster engraving, to ablate cavities in a layer. In the first one the graphic file consisted of vectors (lines and curves), and once imported in the software the lines were traced vector by vector by the laser and cut. Raster engraving consisted of removing the material pixel by pixel by the laser. In this way, it was possible to create protrusions by removing pixel by pixel only the material around them. The parameters to be chosen were the speed, power and resolution of the laser.

In our case the chip was made of three layers of different heights, as illustrated in Fig. 3.1. Parts 2 and 4 refer to the pressure sensitive adhesive tape (PSA), which is applied to part 3 and was used to bond the parts together (see next section).

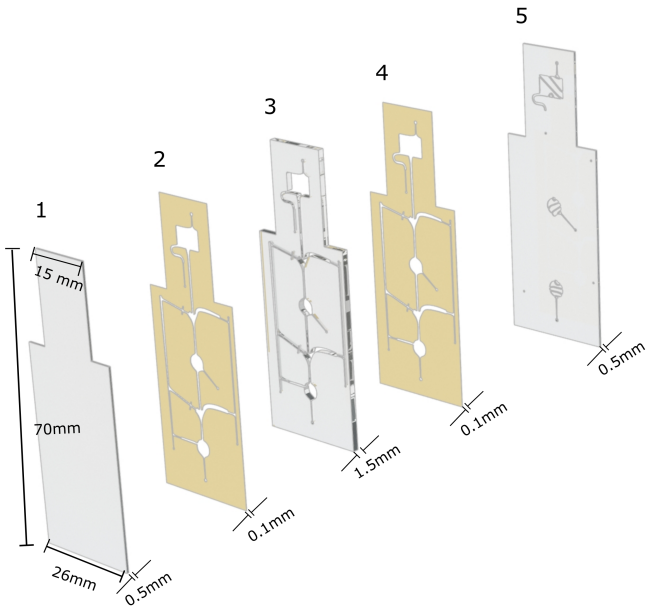

Figure 3.1: Exploded view of the chip layers where parts (1,3,5) consist of the PMMA layers of the chip. Parts (2,4) are the PSA foils. Image adapted from Paper III.

3.1.1 Pressure sensitive adhesive bonding

In order to bond the different chip layers together, a P/O Weber manual 2-column laboratory press, model PW 10 H was used. The machine consisted of two plates (columns) which could be moved through the use of a lever. The chip parts were put together (creating a square of 10 cm) and placed between the two plates at room temperature. A pressure of 20 kN was applied for one minute, allowing the pressure sensitive adhesive to form a bond between layers, after which the chip was ready for the final cut.

3.2 Injection moulding

Injection moulding was the main technique adopted to fabricate chips mainly for its ability to outperform one-step manufacturing methods when talking about mass production. Morevoer, the possibility of manufacturing in (full) 3D allows us to fabricate interconnected chambers and channels for liquids [110].
In this section I will focus on explaining the different steps needed for this specific fabrication method, the process flow chart, with every step, can be seen in Fig. 3.2.

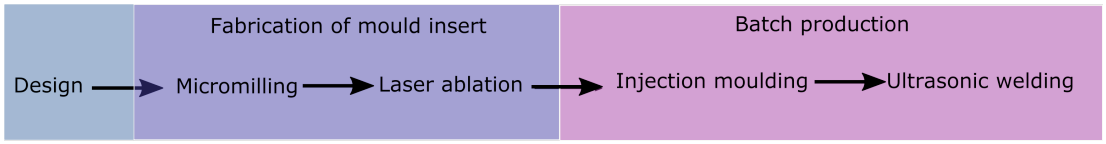

Figure 3.2: Chip development scheme employed for a part of this PhD project.

3.2.1 Materials

The aim of this project was the creation of a low-cost single-use polymer chip, to carry out a specific amplification bioassay. The detection technique used is the optomagnetic detection. This technique uses an LED to send the light through the polymer chip and for this reason the chip should be transparent. Moreover, the polymer should be compatible with the fabrication processes explained above. Therefore, we chose to use a thermoplastic cycle-olefine copolymer (COC), based also on the previous study carried out in the PolyNano project by Kasper Kistrup [90].
Due to a major issue in the demoulding step of the injection moulding process, a short part of the project was done with the use of polypropylene (PP), which had better properties for demoulding [111]. However, the PP grade available at our department (PP grade RF366MO) was very opaque, making it a poor choice for the optomagnetic detection. Poly(methyl methacrylate) or PMMA, a transparent polymer, was the polymer selected for fabricating with CO_2 Laser.

3.2.2 CAD softwares

Computer-aided design (CAD) was used in this project to design the different chips studied. It is an efficient method to draw and modify designs and is widely supported for a series of machines, thanks to the possibility of exporting the design in different formats. In this project Inventor Professional 2016 was the main CAD software used, while SolidWorks 2017 was used to carry on the project collaboration with the Mechanical Department (see subsection 3.2.7).

3.2.3 Micromilling

Milling inserts (or shims) to be placed inside the injection moulding were designed using Autodesk Inventor Professional 2016 and converted in G-code through HSM Express, a CAD/CAM programming tool for Inventor. The fabrication was done on a three-axis Mini-Mill frame fitted with a Nakanishi E3000C spindle and controller (Minitech Machinery, Georgia). The shim (see an example in Fig. 3.3(a)) was created using a 100 mm square-shaped, 2 mm thick 2017 aluminum alloy, which was fixed to the machine with the use of a circular holder screwed to the top of the workplace and filled with oil (see an example in Fig. 3.3(b)). The aluminum square was then micromilled with flat-end mills ranging from 2 mm - 0.5mm, and 0.05 mm engraving tools, to 1.35 mm thick discs ($\varnothing$= 85 mm), to fit in the mould of the injection moulding machine. Thicker or thinner discs were not allowed, creating a height constraint in the fabrication process. Due to this inconvenience,

a maximum height for walls was suggested to be around 200 μm, since deeper cuts once filled with polymer would create more adhesion during the demoulding process.

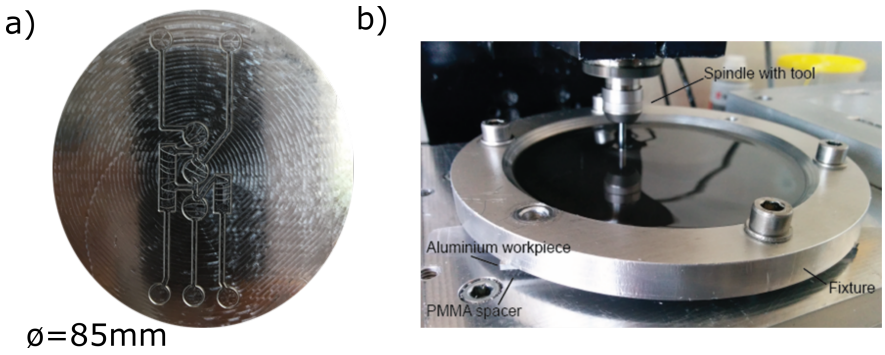

Figure 3.3: (a) Example of a shim created with micromilling. (b) Picture of the micromilling setup, with circular holder screwed to the work area and filled with oil.

3.2.4 Laser modification of the mould insert - creation of energy directors

After the shim was created, a post-processing step was applied to all shims, carried out at DTU Danchip on a microSTRUCT vario (3D-Micromack AG, Chemnitz, Germany) equipped with a Fuego 1064nm, 50W picosecond laser. The shim was placed on the chuck inside the machine. The task was created by uploading a job file (designed on CAD) containing the pattern to be drawn. The pattern, shown in figure Fig. 3.4, was created as an offset of the contour of the chip, by drawing 10 parallel lines (10 μm spacing), repeated 10 times at 50% power, 1000 mm/s speed and focus plane 1.3 mm above the surface [112]. Before the pattern was created, an alignment step was carried out. This allowed the creation of energy directors, pyramid-shaped protrusions introduced at the point of contact of the two polymer parts that need to be fused together (see Fig. 3.5).

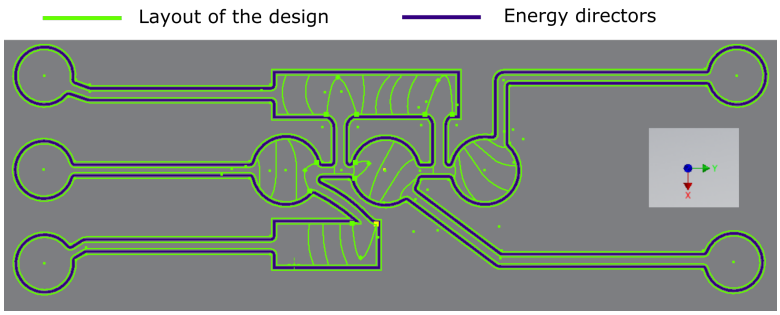

Figure 3.4: Sketch showing an example of the pattern of the energy directors. The green lines define the contour of the layout of the chip, the thick blue line is in reality 10 lines (10 μm spacing).

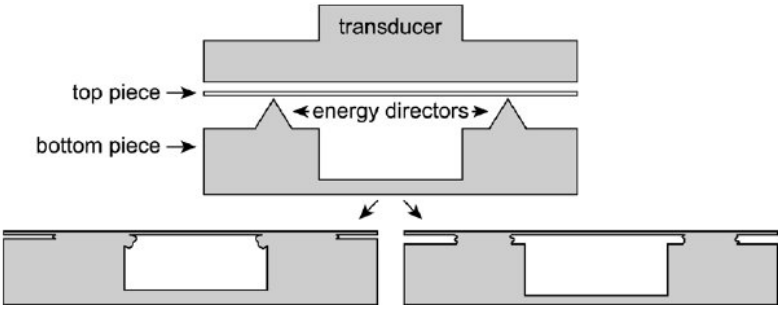

Figure 3.5: Example of what an energy director looks like and its function. Image adapted from [90].

3.2.5 Technical specifications of the injection moulding

A detailed description of injection moulding can be found in [113]. Here I will focus on explaining a few technical details of the process chosen for a better understanding of the outcome. A schematic of the machine is depicted in Fig. 3.6. The injection moulding carried out in this project was mainly performed at DTU Danchip on an Engel Victory 80/45 Tech hydraulic machine (ENGEL, Schwertberg, Austria).

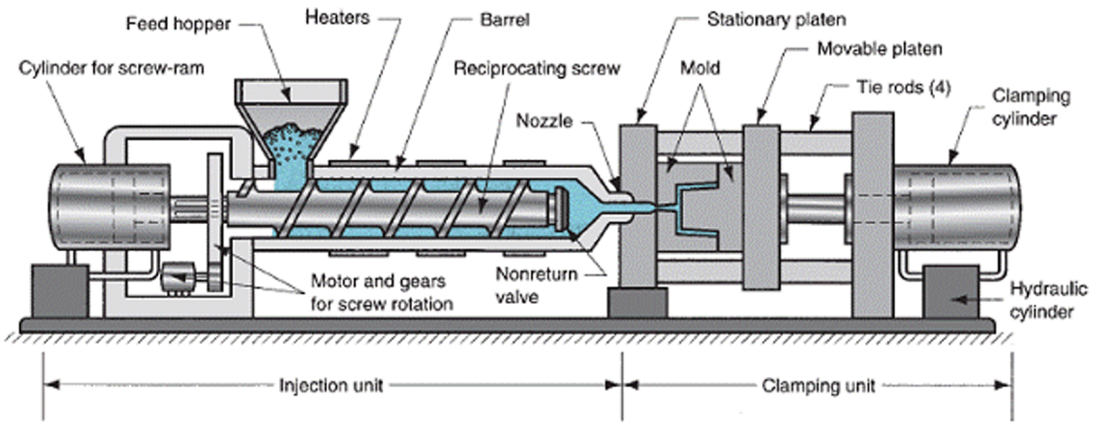

Figure 3.6: Schematic of the injection moulding machine with detailed names of the different parts. The image was adapted from [114].

In order to obtain a mass production of chips, a sequence of five steps termed injection moulding cycle has to happen carefully, after having placed the shim inside the machine:

1. The moulds close and the empty part between the molds is filled at high pressure with molten polymer coming from the barrel and heated up through heaters.

2. The pressure is held for a specific time (depending on the process) to ensure a complete filling over the shim.

3. The pressure is then reduced to a lower pressure called holding pressure where the mould is cooled down.

4. When the polymer right after the nozzle has solidified, the temperature is lowered even more since there is no risk for the polymer to flow out of the mould.

5. Once the polymer is sufficiently solid, the mould opened and the process of demoulding begins. The moulded part is pushed out of the mould by ejector pins.

The parameters to be chosen once the process is started are: heaters and moulds temperatures, pressure, holding and cooling time.
To make the process and the mould part more understandable, Fig. 3.7 illustrates schematic example of the process just described.

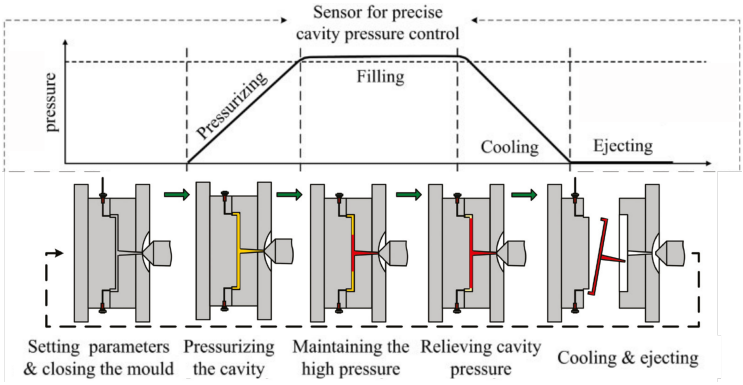

Figure 3.7: Example of a mould and fabricated product. Image adapted from [115].

It is vital to keep in mind that the injection moulding at Danchip department was designed in order to have high flexibility in the creation of different types of chip. In order to achieve this high flexibility, the moulds were created so that it was possible to change only a small part (from now on called "tool") to obtain different shapes of polymer chips. In a normal injection moulding, this would not be the case, but it would require the change of the entire mould (comprised of steel casing, ejector pins etc). The availability at DTU Danchip in regard of fabrication of chips with different outlines are: a luer disc tool (⌀50 mm) featuring 12 luer-locks connectors [116], a microscope slide tool and a flat microscope slide tool (both 26×76 mm^2). In Fig. 3.8 it is possible to see an example of a polymer chip in luer format (part (a) of the figure) and microscope slide format (part (b) of the figure).

Demoulding problems The ejector pins, which should push the chip out of the tool, are in a suited position for the luer disc, however miss out the bottom part the microscope slide. This is of course due to the fact that to make the change of tool faster, the idea was to keep the mould (steel casing and ejector pins) the same, while only changing the part relative to the shape of the chip. This downside is shown in figure Fig. 3.8. In both parts (a) and (b) of the figure, it is possible to notice the holes left by the ejector pins

during the demoulding process (red circles enlight the holes for better comprehension). It is clear that in the case of the microscope slide, the ejector pins are not enough and not placed in a suitable position. A correct positioning would make the ejector pins in both the middle and bottom part of the chip. As a consequence, the demoulding of this specific design introduces a degree of uncertainty, making the realization of the microscope slides more challenging with certain polymers.
In our case, problem arose when trying to fabricate chips in the microscope slide format with the COC TOPAS due to post-molding shrinkage. For COCs it typically falls in low values between 0.4% and 0.7%. Shrinkage is slightly greater in the flow direction rather than in the transverse direction, so very flat parts can be moulded. Due to the low shrinkage of this specific polymer, draft angles should be included during the design process [117]. In our case draft angles of 2° and 5° were included, but the malpositioning of the ejector pins was still the major issue in the demoulding process of the COC. Due to all the above-mentioned, there was a need for the use of a new easy-to-demould polymer.

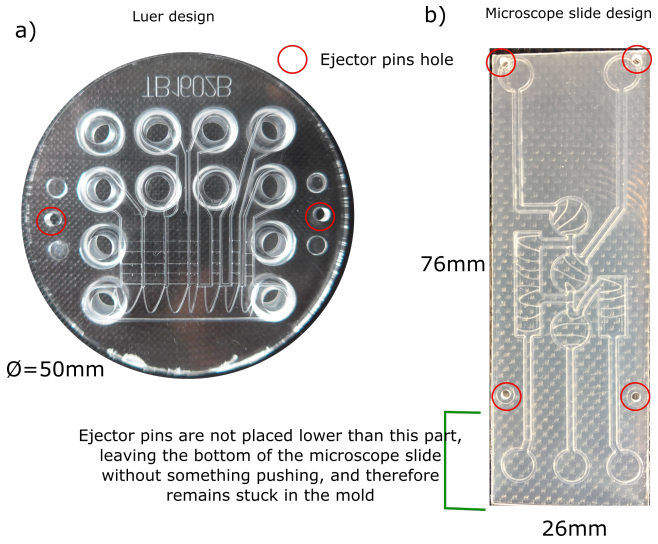

Figure 3.8: (a) Shows a chip created with the luer disc tool. (b) Shows a chip created with the microscope slide tool.

3.2.6 Ultrasonic Welding

The fabrication process used in this PhD project was mainly based on the previous work carried out by former PhD students Kasper Kistrup and Esben Poulsen, who pioneered a technical innovation to create energy directors for ultrasonic welding [90], [112].
The equipment at our department is a Telsonic USP4700 20kHz ultrasonic welder (Telsonic, Erlangen, Germany). It uses ultrasonic vibrations, of frequencies ranging from 15 to 70 kHz, to the parts that need to be connected. These vibrations heat the two parts, specifically in the points of contact (i.e. energy directors), causing them to melt locally and therefore welding them together (see figure Fig. 3.9 for the schematic of the machine).

The ultrasonic welding process used in this project requires the use of a welding delay.

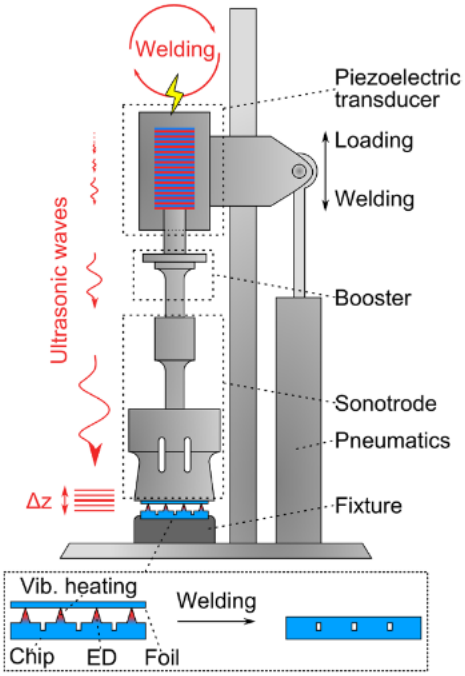

Figure 3.9: Schematic of the ultrasonic welding machine. The image is adapted from Poulsen *et al.* [112].

Initially, the sonotrode part is held up by the pneumatics, and once the part to be welded is placed on the workplace, the pneumatics are switched to down pressure position while the machine begins to move down slowly to approach the parts (phase 1 in Fig. 3.10). Once the sonotrode bottom touches the top part of the chip, the machine changes the pneumatic from down pressure to weld pressure. After a preset delay the generator sends a high-frequency alternating current to the piezoelectric transducer (phase 2 in Fig. 3.10). The piezoeletric reacts by expanding and contracting, creating ultrasonic waves (phase 3 in Fig. 3.10). The energy is then transmitted through the sonotrode to the chip parts, more specifically reaching the contact points between the two parts, which melt and fuse the two parts together as illustrated in phase 4 of Fig. 3.10. The process stops after a hold time, the sonotrode is retracted and the newly formed chip can be taken out. The entire process requires around 10 s. The parameters to be chosen are the delay time, energy, amplitude, weld pressure and hold time.

Limitations of injection moulding at our Department Aside from the demoulding problems that arose during injection moulding of COC polymer at our department, another important factor that limited the achievement of the project goal was the thickness constraint of the injection moulding machine. As stated in section 3.2.3, the shim to introduce in the injection moulding could only be 1.35 mm thick. Consequently, the

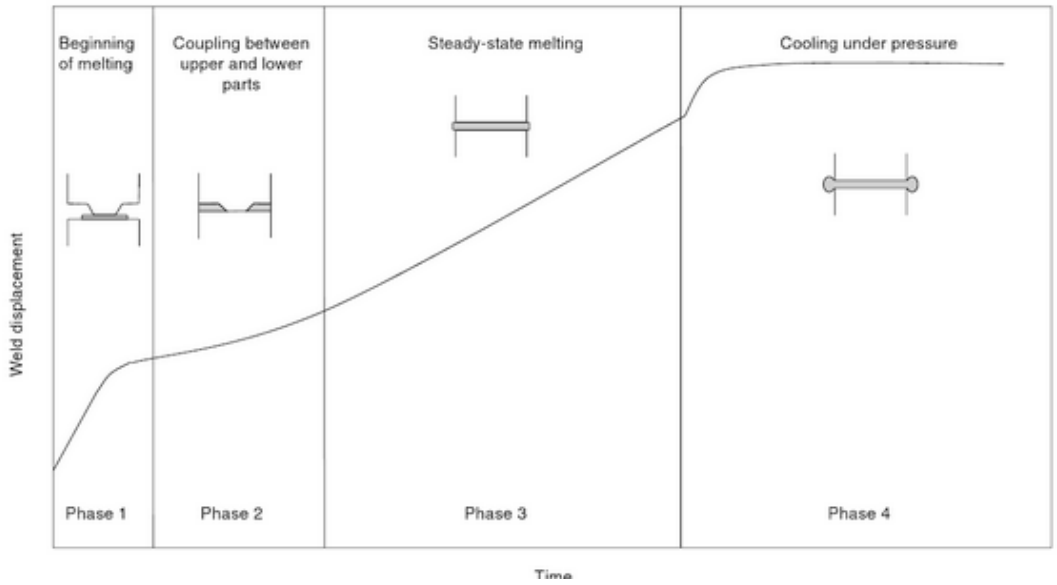

Figure 3.10: Ultrasonic welding process. The image is adapted from Throughton *et al.* [118].

maximum height suggested for the chip walls is around 200 μm, because deeper cavities would make the demoulding close to impossible. Also, in regards of process parameters, it is vital to keep the shim thickness to a certain height to maintain mechanical stability. The wall thickness is of a great relevance when the chip is used with optomagnetic detection. This method, uses a LED and a light guide ($\varnothing$5 mm) to shine the light through the polymer chip. In our case, it is vital that the light shines from the side of the chip rather than from the top/bottom, since in the latter case it would interfere with the heating of the chip itself. In order to shine the light from the side, the thickness of the chip has to be in a range of 2 or 3 mm, similar to the size of the light guide. This called for the need of a new method of fabrication of chips.

3.2.7 Externally fabricated injection moulded chips

Due to the previously mentioned limitations, it was decided to collaborate with the Mechanical Department at DTU, for mass production of chips. The requirement was the creation of an entire mould and two mould inserts, specific for our design. In order to obtain the desired design the first step of the process was to transfer the CO_2 Laser design into SolidWorks 2017, as required by the Mechanical Dept. Several meetings took place to finalize chip design, an essential step to create the mould insert design shown in figure Fig. 3.11, representing the top part of the chip. A similar mould insert was created, simply with a flat design. Also in this case, a post processing step for the creation of energy directors occurred before injection moulding the chip.

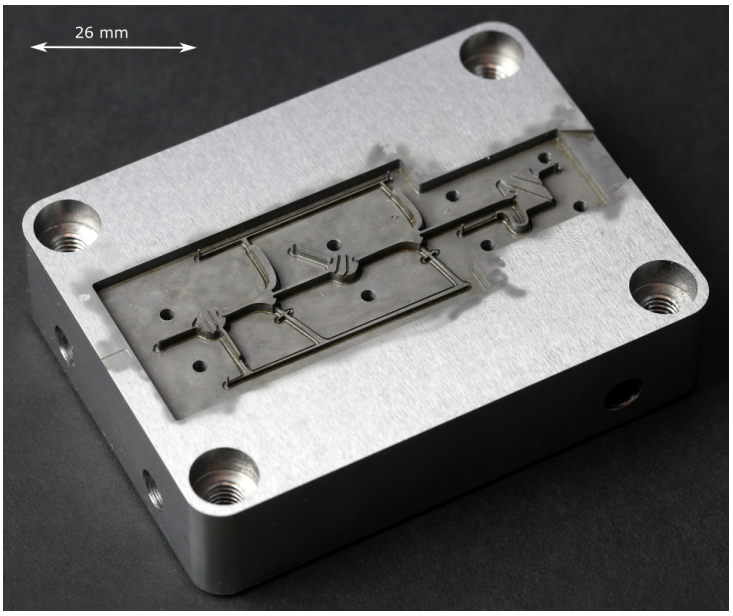

Figure 3.11: Picture of the mould insert created at the Mechanical Department of DTU. The design replicates the one developed using the CO_2 Laser.

Chapter 4

Injection moulded chip for the study of capillary burst pressures

This chapter discusses the fabrication and testing of an all-polymer injection moulded chip for the study of capillary burst pressures. The chapter starts with a description of the limitations of microfluidic devices and the objective, followed by the chip fabrication techniques and its characterization. Finally, the burst pressure measurements are described together with the results. The knowledge obtained in this study, was of great importance for the subsequent chapters.

4.1 Introduction and objectives

A lab-on-a-chip is a class of devices that integrates and automates multiple laboratory techniques into a system that fits on a chip of a few square centimetres in size. The main advantage, but also drawback, of these systems is the high surface-to-volume ratio, causing capillary forces to dominate over inertial ones. Another well-known issue is the occurrence and trapping of air bubbles at undesired locations. In order to solve these problems, Vulto *et al.* presented an attractive structure that allowed control of the wetting and filling of microfluidic devices: phaseguides structures [91]. The phaseguide structures are ridges protruding from either the channel bottom or top, pinning the liquid meniscus until the pressure exceeds the burst pressure defined by the geometry of the structure and the wetting properties of the liquid. The burst pressure is tuned by varying the angle between the phaseguide ridge and the sidewall of the channel or by introducing kinks or branches in the phaseguide structure [119], [120]. By use of phaseguide structures, passive liquid valving and the controlled and bubble-free liquid filling of microfluidic chambers of arbitrary shape was demonstrated [33].

The objective of this part of the project was the creation of a lab-on-a-chip system, that could allow filling of liquids without the risk of trapping air bubbles. The creation of bubbles inside the chambers of a chip, would not only influence any biological reaction happening inside them, but would also interfere with the specific type of optical detection used in this project. Until now, in the main studies cited above, the fabrication was carried

out using photolithography, which leads to well-defined structures with the flaw of being kept of the same height, to keep the fabrication simple. In our case, we have investigated the burst pressure of two different liquids in microfluidic structures, with phaseguides defined by milling and fabricated by injection moulding, allowing a simpler modification of the height of the structure while maintaining a constant geometry. The knowledge obtained in this study enables simple tuning of liquid spreading in different channels, with the use of phaseguides of different heights.

4.1.1 Mould description

The tool chosen was the luer disc, which was defined as a ⌀50 mm disc featuring 12 luer-locks. The shim was defined as the negative counterpart of the design. The layout of the shim included seven channels in parallel, each with its own luer-fitted inlet (as illustrated in Fig. 4.1(b)). Each channel had a height of $H = 200$ μm and contained a sequence of five phaseguides of increasing nominal heights: h_{nom}= 20 μm , 40 μm , 60 μm , 80 μm and 100 μm. All phaseguides were straight and orthogonal to the channel length (90°). One of the channels, of width W=1 mm, did not feature any branches on the phaseguides. The remaining six channels, three of W=1 mm and three of W=3 mm, contained phaseguides with a centrally placed branch forming an angle of α= 45° 60° or 75° (see Fig. 4.1(a)). The overall chip structure, including the luer inlets, is illustrated in Fig. 4.1(b) and (c).

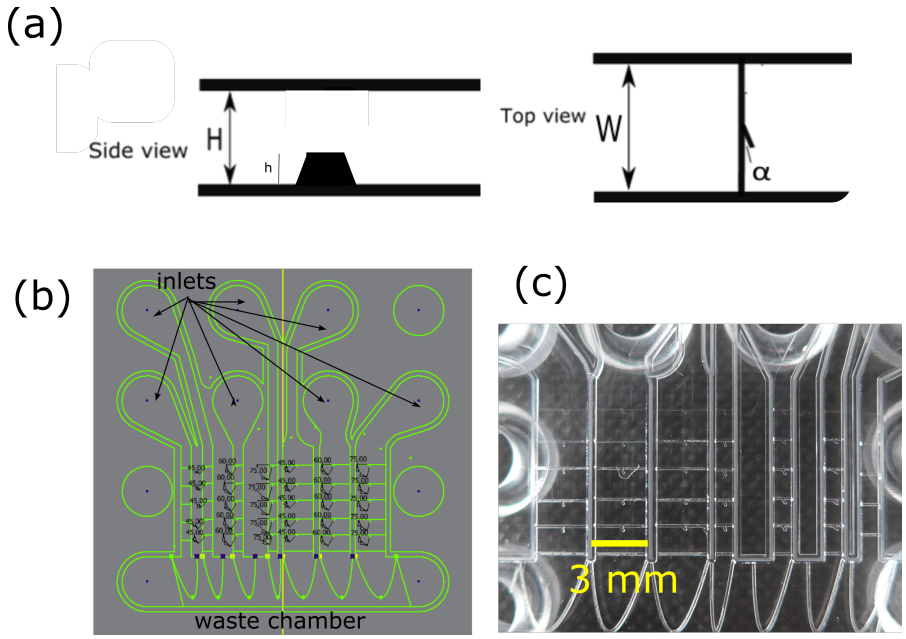

Figure 4.1: (a) Side and top views of a channel (heighth H, width W) with a 90° phaseguide (height h) and a centrally placed branch at an angle α. (b) Layout of the seven channels of the chip, showing the connection from the inlets to the outlets (waste chamber). (c) Picture of the real chip prior to ultrasonic welding, showing the layout of the chip. Image adapted from Garbarino *et al.* [92].

The shim was designed and milled as expressed in the previous chapter, using a 3 mm flat end for the initial rough milling, a 0.5 mm flat end for the countouring of the layout of the design, a 0.05 mm engraving tool with opening angle = 15° for phaseguides (DIXI polytool 7009, art 976370, 30°) and a 2 mm flat end for the cut out of the circular shim from the aluminum square.

4.2 Methods

4.2.1 Fabrication of chips

The all polymer chip consisted of two parts: a main part in COC polymer (TOPAS grade 5013L-10), fabricated by injection moulding and a 0.254 mm COC foil (TOPAS grade 5013S-04), both from TOPAS Advanced Polymers GmbH, Frankfurt, Germany. Injection moulding was carried out at the Danchip department. In this case the luer mould insert was chosen, which featured the negative counterpart of the channel layout on one side and the luer design on the other. The machine ran an isothermal program with the following parameters:

- Heaters: $T_{Heater1}$=240°C, $T_{Heater2}$=250°C, $T_{Heater3}$=260°C, $T_{Heater4}$=270°C.
- Mould: $T_{MouldFront}$=120°C, $T_{MouldBack}$=120°C.
- Injection moulding pressure and time: 1766 bar for 5 s
- Cooling time: 5 s

4.2.2 Characterization methods

Characterization methods were described in detail in Paper I, and will only be briefly summarized.

Test liquids Two different liquids were used in experiments, as shown in Table 4.1. MilliQ and PBST-BSA as a representative buffer for analysis of biological samples. To facilitate visualization of the liquids in the channels, Brilliant Blue R dye was added to both solutions.

Table 4.1: Buffers and reagents composition

Buffer name	Composition	Density
Water	Millipore MilliQ lab water system	998 kg/m3
PBST-BSA	mixture of phosphate buffer saline containing 0.01 % (V/V) of surfactant Tween 20 and 0.1% (V/V) of protein bovine serum albumin, (Sigma Aldrich)	1005 kg/m3

Burst pressure measurements Hydrostatic burst pressures were determined by using a custom built setup (as shown in Fig. 4.2). Experiments were performed by raising one end of a peroxide cured silicone tubing (OD= 10 mm, ID=6 mm), filled with one of the test liquids at time, connected to the chip on one end and to a Thorlabs LTS150 motorized stage (Thorlabs, Newton, NJ, USA) moving in the vertical direction (Δz) on the other side. In the experiments, the chips were mounted with the luer connectors facing downwards. An experiment was performed by first adjusting Δz in a way that the liquid level in the open end of the tube matched the top of the channel. The tubing was then raised at 1 mm/s while carefully monitoring the position of the liquid meniscus in the channel. When the liquid burst through a phaseguide, the stage was immediately paused and the position noted. Subsequently, the stage motion was re-engaged to study the burst pressure of the next phaseguide. Measurements were performed on three different chips, which were rinsed and dried before conducting another set of measurements. The applied burst pressure was determined as $p_{\text{burst}} = \rho g \Delta z$ where ρ is the density of the liquid, $g = 9.82$ mm/s^2 is the gravitational acceleration.

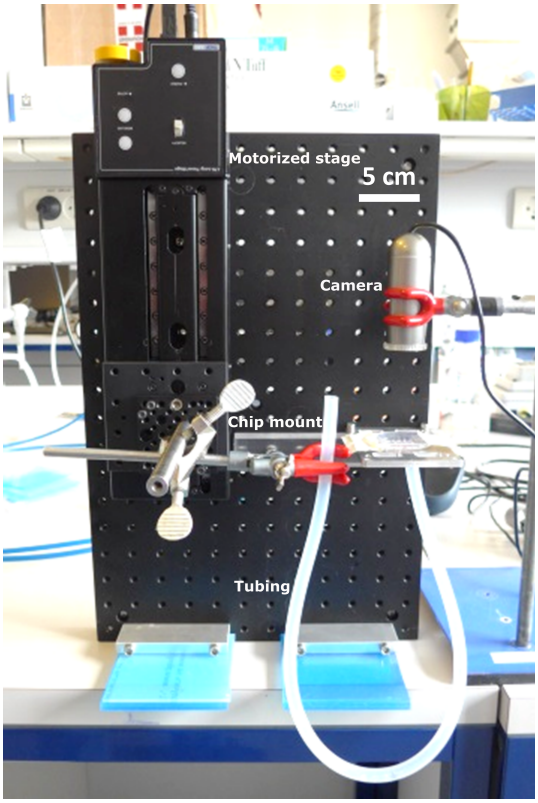

Figure 4.2: Setup used for the experiments. The chip was mounted with the luer connectors facing downwards with one end of a tube attached to the luer. Experiments were performed by increasing the height of the open end of the tube while monitoring the position of the liquid meniscus in the chip. Image adapted from [92].

Channel sealing with Ultrasonic Welding An important aspect in order to characterize the fabrication technique, was the feasibility of the bonding using ultrasonic welding. For this reason, chips were filled with PBST-BSA (mixed with blue dye to aid visualization) and an investigation of the sealing by energy directors was performed using microscopy. PBST-BSA was chosen as liquid because it is able to spontaneously fill any gaps by capillary forces, due to its low contact angle (83°, thus hydrophilic). Fig. 4.3 illustrates the results of this study, after having checked the chips with a microscope (LEICA MZFLIII Stereomicroscope, equipped with a Sony DFW-X710 camera). Fig. 4.3(a) shows a top view of the four 1 mm wide channels of the chip, none of which show leakage. Fig. 4.3(b) shows a zoom-in on one of the 1 mm wide channels. The area containing the welded energy directors can be observed as the two 200 μm wide bands along either side of the channel. The sharp transition between inside and outside of the channel, clearly defines the two regions and indicates that the welding has left either no gap or a gap of negligible size in the region between the channel and the welded energy directors. Results were in agreement with a previous study of energy directors and ultrasonic welding made by the same method [121].

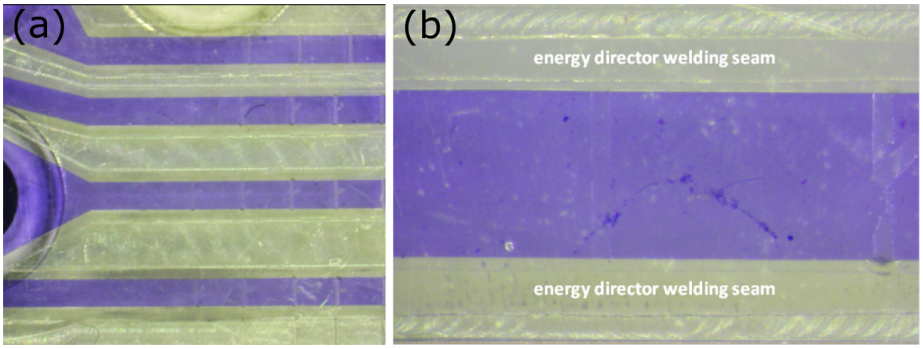

Figure 4.3: Pictures of the injection moulded chip sealed by ultrasonic welding filled with blue-dyed PBST-BSA in the 1 mm wide channels. (a) Shows an overview of four sealed 1 mm wide channels. (b) Shows a zoom-in on one of the 1 mm wide channels. The energy director welding seams are visible as bands along the channel. Image adapted from Garbarino *et al.* [92].

4.3 Results

This section highlights the burst pressure results focusing on the measurements regarding PBST-BSA and channel width W=1 mm, which are of more importance for the second half of the project. The other results are presented in Paper I.

4.3.1 Phaseguides height

All channel and phaseguide geometries were investigated by confocal microscopy to verify their dimensions. The channel width W and height H were found to correspond to their

nominal values, and similarly the lateral geometries of the phaseguide branches matched those of the design. The heights of the phaseguide ridges were investigated at DTU Danchip by using a stylus profilometer (Stylus profiler - Tencor alpha step). The Stylus profilometer uses a moving probe to detect along the surface of the sample, acquiring its surface height. Analysis of the profiles (illustrated in Fig. 4.4) showed that the measured values of phaseguides height h were systematically 12 μm lower than their nominal values h_{nom}, meaning that the actual five values of h in the sequence of phaseguides were h=8μm, 28μm, 48μm, 68μm and 88μm. This deviation was attributed to an offset in the z-zeroing of the engraving tool during the micromilling fabrication of the shim. The measured values were used in the plots and the analysis in the next section.

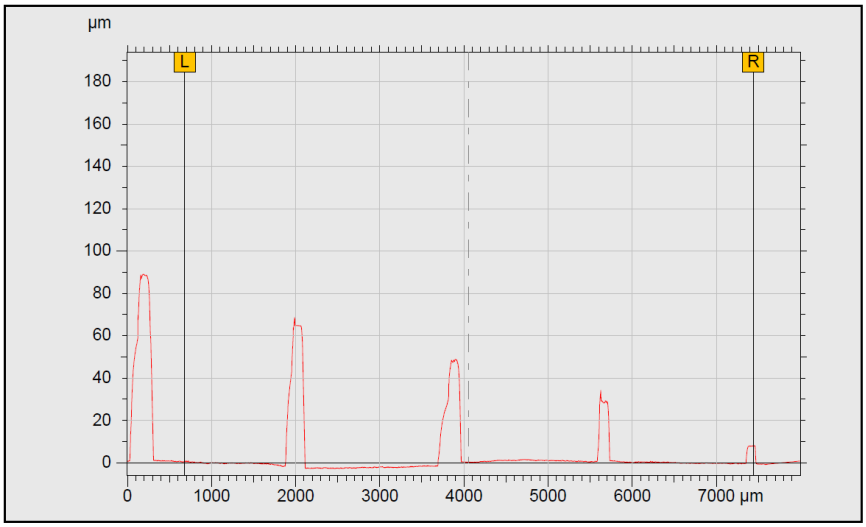

Figure 4.4: Result of stylus profilometer scan along injection moulded channel with W = 1 mm over phaseguides without a branch and nominal heights of of h_{nom}=100 μm, 80 μm, 60 μm, 40 μm, and 20 μm. The measured values are found to be offset by -12 μm due to an offset in the z-zeroing of the engraving tool used for the fabrication. Image adapted from Garbarino *et al.* [92].

4.3.2 Burst pressures

In order to characterize the ability of the capillary microvalves to stop fluid flow, we decided to measure their hydrostatic burst pressure. Section 2.3 covered the theory for capillary microvalves and phaseguides. Briefly, each phaseguide can be thought of as a capillary microvalve and is based on a channel that forms a 75° expansion towards the main chip part, causing the liquid to pin at the expansion point, due to the now larger contact angle associated with the triple contact line at this position (see Fig. 2.4 for a schematic of a capillary microvalve, and Fig. 2.8 for a schematic of a phaseguide). The measured burst pressures were related to burst pressures estimated using equation 2.15. The results are shown in Fig. 4.5.

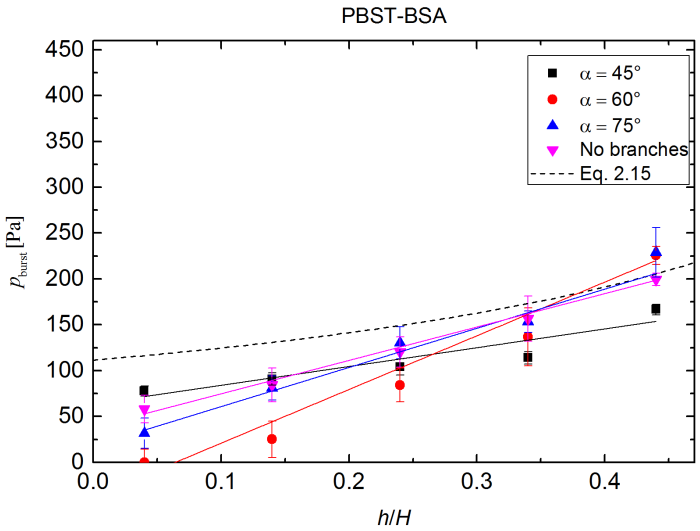

Figure 4.5: Burst pressure p_{burst} measured as function of h/H for phaseguides with and one without branches at the indicated angles for W=1 mm, studied with the PBST-BSA solution. Error bars refer to the standard deviation of the mean (n=3). Solid lines are linear fits of each dataset. The dashed line is a plot of Eq. (2.15) using the measured values of contact angles and liquid-air surface tension given in the text. Image adapted from Garbarino *et al.* [92].

The graph depicts measured values of p_{burst} for PBST-BSA in a channel with W = 1 mm as function of h/H for a phaseguide without a branch and for phaseguides with branches having values of α. Note, that a pressure of 100 Pa corresponds to a liquid column with a height of about 10 mm. The values of p_{burst} were observed to increase systematically in an approximately linear trend from around 0 Pa for h= 8μm to 250 Pa for h=88 μm.
The slope for α=45° was observed to be lower compared to phaseguides with α higher than 45°. The lines are linear fits of $p_{\text{burst}} = p_0 + p_{\text{slope}} \times (h/H)$ to the data. It should be noted that the PBST-BSA measurements were performed on three different chips (n=3), and that the behaviour changed irreversibly once a channel had been primed with the PBST-BSA solution. Specifically the study of the modification of the surface wettability showed that the polymer chip contact angle lowered from 83° to 65°, after an overnight exposure to PBST-BSA. For this reason, repeated measurements on the same chip were not performed for PBST-BSA.

4.4 Summary

In conclusion, we were able to create an injection moulded and ultrasonically welded polymer chip with integrated phaseguide structures. Micromilling introduces a level of uncertainty due to the zeroing of the tools, which can be avoided using a 5-axis Milling machine rather than a 3-axis one as in our project. The fabrication method used in this part of the project is compatible with low-cost mass production of chips, which was one of the main goals of the project. This result enabled us to move forward in the project, focusing on the integration of the biological assay on chip, as explained in the subsequent chapter.

Chapter 5

Automated RCA and detection in injection moulded chip

This chapter discusses our first approach to implement rolling circle amplification (RCA) on a chip. The chapter starts with the chip fabrication techniques with a focus on the choice of material to use, followed by the explanation of the setup to carry out experiments. Finally, RCA and detection on a multi-chambered chip is demonstrated, via the optimization of the RCA temperature. This work was presented at the International conference on Micro and Nano Engineering (MNE2017) as an oral presentation and partially refers to conference contribution II.

5.1 Objective

The objective of this part of the project was the creation of a lab-on-a-chip device, designed for the automation of an isothermal RCA assay. In this chapter, the manufacturing method for the fabrication of chips was injection moulding, with the choice of polypropylene (PP). On-chip RCA and optomagnetic readout of RCPs are demonstrated. The work demonstrates integration of the optomagnetic readout, with a multichamber injection moulded chip.

5.2 Methods

5.2.1 Assay requirements

The assay comprises sequence specific ligation followed by isothermal RCA. In this first chip, the use of microbeads as means of transport between chambers was not yet implemented, so the idea was to carry out both RCA and detection on chip in the same chamber. Moreover in the initial setup, there was only the possibility of heating the entire chip at the same temperature, meaning that ligation had to be performed off-chip in a thermoshaker, otherwise the polymerase enzyme for RCA would have been inactivated.

5.2.2 Mould description and fabrication

The injection moulded all polymer chip was developed at our department, following the process flow explained in section 3.2.
The shim was designed and milled using a 3 mm flat end for the initial rough milling, a 0.5 mm flat end (with a 2° draft) for the countouring of the layout of the design, a 0.05 mm engraving tool with opening angle = 15° for phaseguides (DIXI polytool 7009, art 976370, 30°) and a 2 mm flat end for the cut out of the circular shim from the aluminum square.

Injection moulding was carried out at the Danchip department. The machine allows for two interchangeable tools. In this case, the microscope slide mould tool was chosen for the top part, which featured the negative counterpart of the channel layout on one side. For the bottom part, it was used the flat microscope slide tool. There are two main reasons for deciding to change the tool: the luer tool has 12 luer-locks protruding from the outer part of the chip, which would interfere with the heating of the assay inside the chambers, secondly the microscope slide format enabled the creation of designs where the inlet/outlets can be decided and are not forced by the position of the luers. Similarly, the amount of "free space" where the design in the luer tool can be created is quite minimal compared to the slide format.

The machine ran an isothermal program, using PP, with the following parameters for both top and bottom parts:

- Heaters: $T_{Heater1}$=210°C, $T_{Heater2}$=225°C, $T_{Heater3}$=235°C, $T_{Heater4}$=245°C.
- Mould: $T_{MouldFront}$=50°C, $T_{MouldBack}$=50°C.
- Injection moulding pressure and time: 750 bar for 15 s
- Cooling time: 5 s

The shim layout of the top part of the chip featured three circular chambers (⌀5 mm) of height $H = 200$ μm with a sequence of phaseguides of height $h = 60$ μm to control and enable filling of each chamber with a different liquid from the inlets (see the layout in Fig. 5.1(a)).

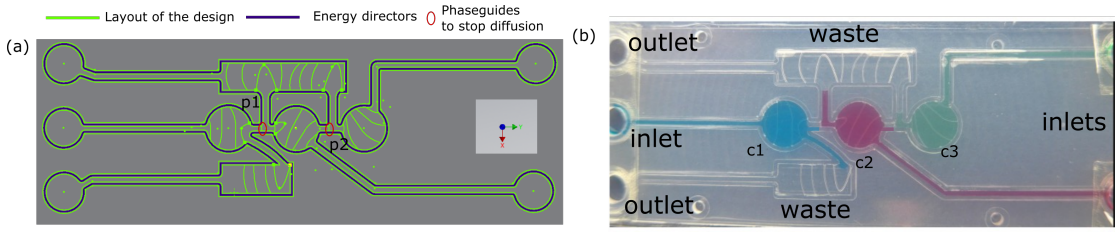

Figure 5.1: (a) Layout of the design (green lines), with energy directors (blue lines) and a focus on the two phaseguides to stop diffusion (p1 and p2, red holes). (b) Photograph of the injection moulded and ultrasonically welded three chambered chip, filled with dyed liquids. The chip format is 26 × 76 mm^2.

Each chamber was connected to a waste chamber, which was then connected to an outlet. The three chambers enabled future integration of the complete assay on the chip, but in this work they were filled with the same liquid.
The bottom part was of the same size as the top one, but completely flat. No design was needed for this part, since the tool chosen (flat microscope slide) had already the specific outline needed.
The outcome of the filling can be seen in Fig. 5.1(b). The picture shows almost no diffusion between the different chambers, thanks to the phaseguides positioned in the channels between them.
The filling process was the following:

- fill c1 until the first phaseguide in the connecting channel (p1) and seal with tape.
- fill c2 until both p2 and p1, and seal with tape.
- fill c3 until p2, and seal with tape.

5.2.3 Material

The choice of material was an important factor, after the demoulding problems that occurred in the first part of the project with the use of COC polymer Topas (see section 3.2.5 for the detailed explanation). In short, the demoulding process was not optimized for the microscope slide format, due mainly to a malpositioning of the ejector pins in the mould. Therefore, it was decided to use polypropylene (PP grade RF366MO, Borealis AG, Austria). PP is designed for high-speed injection moulding and contains nucleating and antistatic additives.
The improved processability, even at low melt temperatures, allows for faster cycle times, making it a good choice for injection moulding process [111].

5.2.4 Automated setup

The automation and measurement setup was designed and built by former Post-Doc of our group Giovanni Rizzi and consists of a motorized stage (LTS 150, Thorlabs, Newton, New Jersey) that shifts between (1) a heater bed regulated by a Peltier element and (2) a custom made position for transmission OM measurements ($\lambda = 405$ nm LED, photodetector, two electromagnets) under the fixed chip position (Fig. 5.2).
The chip position was fixed thanks to a chip holder, for easy fitting and release of the chip. After loading the chip with RCA mixture, the inlets and outlets were sealed using tape. The chip was then placed in position (1) at temperature T_{RCA} and RCA was performed for 20 min followed by quick cooling to 25°C. Then, the motor stage shifted horizontally, bringing position (2) underneath the measurement chamber, where the optomagnetic spectra were recorded.
The entire procedure was automated in LabVIEW, with each cycle (from loading the chip on the setup to the last measurement) lasting around 30 min.

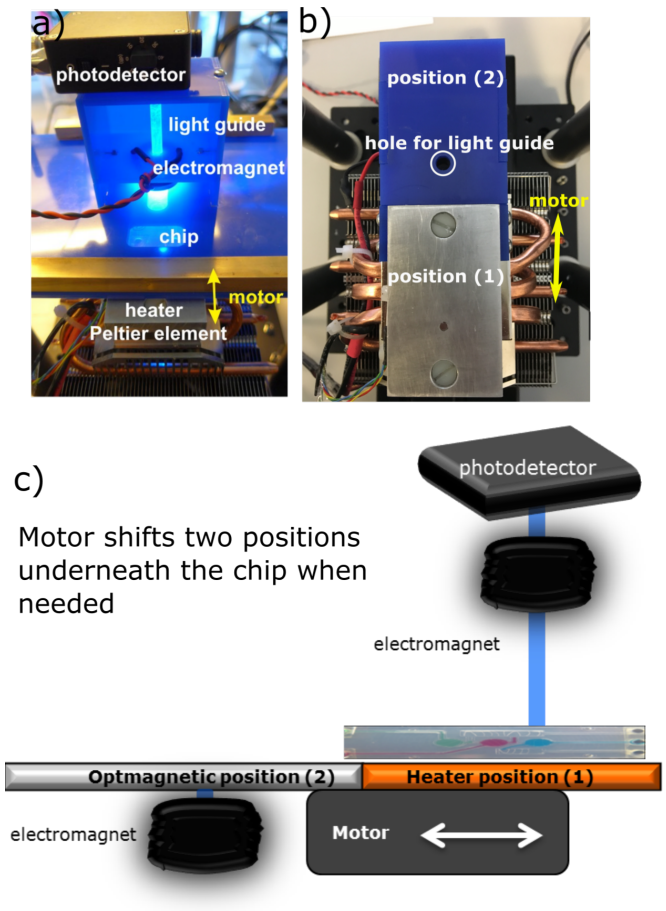

Figure 5.2: (a) Section of the front view of the setup, showing the main features. (b) Top view of the setup, once the photodetector and top electromagnet part are removed, showing the two positions allowed. (c) Sketch of the setup from a side view, showing the two possible positions allowed.

5.2.5 Bioassay

Bioassay Design Experiments were carried out using synthetic target DNA for the type-B influenza virus (IDT, 81 oligonucleotide bases). The synthetic target DNA was designed to have a 5'-biotin, in order to be able to directly link to the magnetic nanoparticles (MNPs).

The padlock probe (PLP) was composed of 90 nt and was designed to match a sequence of the DNA target. The padlock probe was modified with a 5'-phosphate group. PLPs were added in 3-fold excess (1.5-24 nM) to minimise the number of unreacted probes (targets without circles).
All information regarding sequences can be found in Table 5.1, and buffers in Table 5.2.

Table 5.1: Sequences of influenza target and PLP. The target-specific 'arms' of the PLPs as well as their binding sites in the target sequences are underlined.

DNA Tag	DNA sequence (5′-3′)	Modification
Target	AGACCTGTTACATCTGGGTGCT TTCCTATAATGCACGACAGAA CAAAAATTAGACAGCTGCCC AACCTTCTCCGAGGATAC	5′-biotin
PLP	GGGCAGCTGTCTAATTTTTGAGT CGGAAGTACTACTCTCTGTGTAT GCAGCTCCTCAGTAATAGTGTCT TACGTATCCTCGGAGAAGGTT	5′-phosphate

Table 5.2: Buffers and reagents composition (final concentration).

Buffer name	Composition
Ligation buffer	0.2 mg/ml BSA (New England Biolabs), 20 mM Tris-HCl (pH 8.3), 25 mM KCl, 10 mM $MgCl_2$, 0.5 mM NAD, and 0.01% Triton X-100 (Illumina)
RCA and detection buffer	66 mM Tris-acetate (pH 7.9 at 37°C), 25 mM Mg-acetate, 132 mM K-acetate, 0,2% (v/v) Tween 20, 2 mM DTT, BSA 0.2 mg/mL, 190 μM dNTPs (New England Biolabs)

Bioassay performance The objective was to create an automated isothermal RCA assay on a chip. The assay comprised three steps, of which the latter two where performed on-chip: (1) ligation, (2) RCA and (3) detection. The entire process is shown in Fig. 5.3.

The first step was performed in tubes using a thermostat (Grant PHMT Thermoshaker, Cambridge, UK). The reaction, depicted in Fig. 5.3, would occur according to the following procedure:

I Ligation: eppendorf tube in thermostat at 55°C for 20 min.

II Capture of biotinylated target on MNPs[1]: inserted in eppendorf and kept at 55°C for another 20 min.

III RCA: solution was inserted in the chip, on the setup, at temperature T_{RCA} for 20 min.

IV Detection: chip on setup, at 25°C for 5 min.

In brief, the ligation step would allow DNA Target and PLPs to get joined into circles, which acted as template for the isothermal amplification. Several circles were then

[1]The magnetic nanoparticles (⌀100nm, MNPs - BNF-Starch streptavidin, prod. code 10-19-102, Micromod Partikeltechnologie GmbH, Germany).

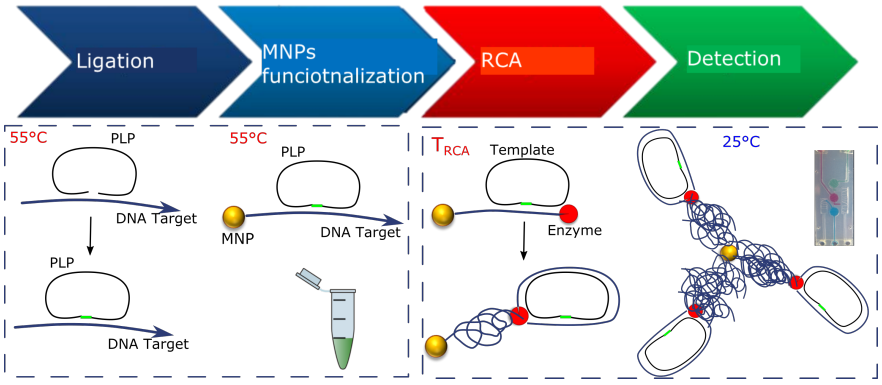

Figure 5.3: Process flow for assay on chip, with cartoon-like features explaining the entire process.

captured on MNPs to saturate them, via direct-link to avoid complexity. As a result, long rolling circle products (RCPs), repeating the sequence complementary to the circle, were created during RCA [105]. The RCPs attached to single MNPs, were then detected with the optomagnetic detection technique. The amount of target density affects the outcome of the OM spectra, as we observed in unpublished data, with low percentages creating double peaks or shoulders in the spectra. The efficiency of the amplification is sensitive to the RCA temperature. Therefore we studied the spectra after RCA took place for 20 min, for T_{RCA} ranging from 20 to 44°C. These results were of key importance for the complete integration of the bioassay on chip, since it probes the efficiency of the isothermal amplification.

5.3 Results

5.3.1 Optimization of RCA temperature

The results of the temperature optimization study are shown in Fig. 5.4. For a better understanding, it is important to remember that in the optomagnetic spectra, a peak is centered at a frequency, which is inversely proportional to the hydrodynamic volume of the MNPs [49]. This is due to the Brownian relaxation frequency f_{B} (Eq. 2.25). Due to the high probe density, the RCPs interlock into each other, forming a sponge-like structure that hinders the rotation of the MNPs, which results in a peak shift, as shown in Fig. 5.4(a), and a growth of hydrodynamic diameter D_{h} as shown in Fig. 5.4(b). This means we are looking for the most efficient RCA in terms of RCP size, where the largest RCP (and D_{h}) corresponds to the lowest peak frequency.
In Fig. 5.4, it is clearly possible to distinguish between different peaks positioned at different frequencies.

The outcome can be linked to the enzyme activity which changes at different temperatures, allowing to divide the results in:

- extremely low enzyme activity ($T_{\mathrm{RCA}} = 20$°C).

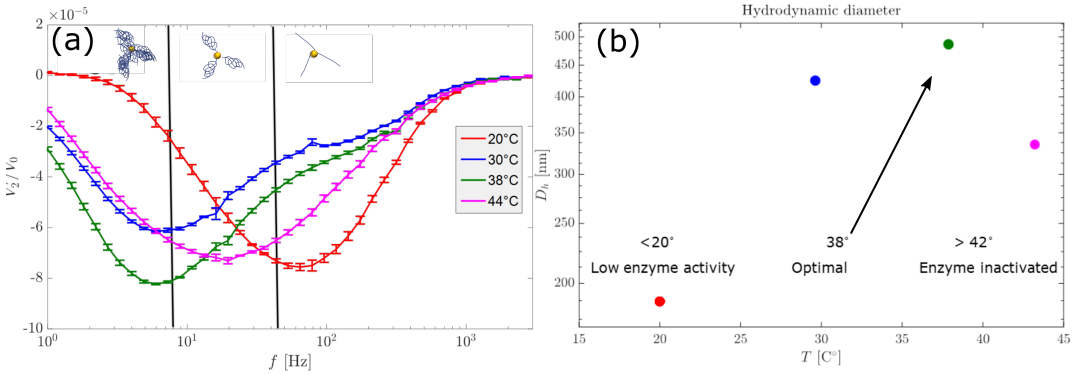

Figure 5.4: (a) Optomagnetic spectra of suspensions of MNPs with attached targets/RCPs measured at 25°C after 20 min of RCA for a concentration of DNA Target c=8nM. The figure shows four representative results obtained for T_{RCA} = 20, 30, 38 and 44°C, together with small schematic illustrations indicating the RCP size. (b) Graph of the hydrodynamic diameter D_{h} size change at the different T_{RCA}. Image adapted from [122].

- deactivation of enzyme activity ($T_{\mathrm{RCA}} \geq 42$°C).
- optimal temperature conditions resulting in the longest RCPs ($T_{\mathrm{RCA}} = 38$°C).

The graph also shows a schematic illustration of the presented interpretation. The optimal temperature ($T_{\mathrm{RCA}} = 38$°C) was a major step in the integration of the assay on chip, and will be used in the next chapters as the optimal RCA temperature.

5.4 Discussion

The initial integration of the assay on chip, was found to work well when the conditions remained the same: ligation in tubes and RCA and detection inside the chip. In our case the final goal was to transfer the entire assay on chip, with no need for external manipulation by a technician. The ideal chip should have larger chambers, with a larger optical path. To obtain larger volumes, the milled shim, which featured the counterpart of the actual chip design, would need to have higher walls than the 200 μm allowed (see section 3.2.3 on micromilling). Moreover, the use of PP as material to make chips should be avoided due to its opaqueness.
For these reasons, in order to advance to the final goal of the chip, there was a need for a similar low-cost fabrication method, which would not have constraints regarding thickness. The availability at our department included the use of deposition and electrodeposition, etching, bonding, CO_2 laser machining, injection molding, embossing and soft lithography. Most of the techniques listed, required the use of a cleanroom, which would counterbalance the initial aim of a "low-cost" chip. It was therefore decided to use the CO_2 laser machining, by creating chips using three different layers.

5.5 Summary

We created an injection moulded and ultrasonically welded polymer chip, suitable for integration of an isothermal amplification assay. The multichamber chip granted controlled filling of liquid, thanks to the use of capillary forces and phaseguide structures. Moreover, the experiments were run on a custom-made setup with temperature control, motor positioning and optomagnetic detection. The measurements demonstrated the most efficient temperature for the bioassay on MNPs (38°C). The study was carried out as a pre-investigation for the use of magnetic microbeads, which will be introduced in the subsequent chapter, as means of transport of DNA.
The knowledge obtained from this study, was of great importance in the development of a single-use polymer chip for the integration of the entire bioassay.

Chapter 6

Integrated bioassay with optomagnetic detection

This chapter discusses in detail the process of integrating the bioassay on chip. The chapter starts with an explanation on the requirements needed for the integration, from chip design to the bioassay design and magnetic microbead (MMB) handling, followed by the explanation of the setup used to carry out the experiments. Finally, the optimization process for *Influenza* is finalized in the last part of the chapter. An optimization process is started for *Tuberculosis*, shown in the last paragraph of the chapter, where initial results are shown.

6.1 Objective

The objective of this final part of the project was the creation and optimization of a lab-on-a-chip system, designed for the complete automation of an isothermal rolling circle amplification (RCA) assay. The work shows the capability of integrating DNA handling, with optomagnetic readout in an all-polymer chip. Moreover, the work shows also the possibility of changing the infectious disease under study, keeping the same chip and setup.

6.1.1 Assay approach and requirements

The assay remains similar to the previous chapter and includes sequence-specific ligation and RCA as isothermal amplification method. The methods require specific temperatures to work in optimal conditions: at least 55°C for ligation and 38°C for RCA. It was critical that the RCA chamber was not exposed to temperatures above room temperature prior to the amplification, as the enzyme polymerase would be inactivated in such conditions. Therefore there was a need to keep some parts of the chip colder than others. Another important aspect to keep in mind for the development of the assay, is the use of magnetic microbeads (MMBs) as a mean of transport. In our case, the choice was to use Dynabeads MyOne streptavidin microbeads (ThermoFisher Scientific, Germany) [90].

6.1.2 Chip requirements

The bioassay needed three different steps: (1) ligation, (2) RCA and (3) detection to be carried out on-chip. Therefore it was necessary to develop a 3-chambered chip, where each reaction would take place in a separate chamber (as illustrated in Fig. 6.1). Interconnection between chambers was essential, since MMBs together with an external magnet were used as a mean of transport of DNA from one chamber to another. On the other hand, it was essential to keep liquids from diffusing from one chamber to another, and therefore capillary stops were added at the end of each channel to stop liquid diffusion (depicted in Fig. 6.1). It was also decided to keep the chip of similar size as a microscope slide (26×70 mm^2), to be able to shift back to injection moulding if needed.

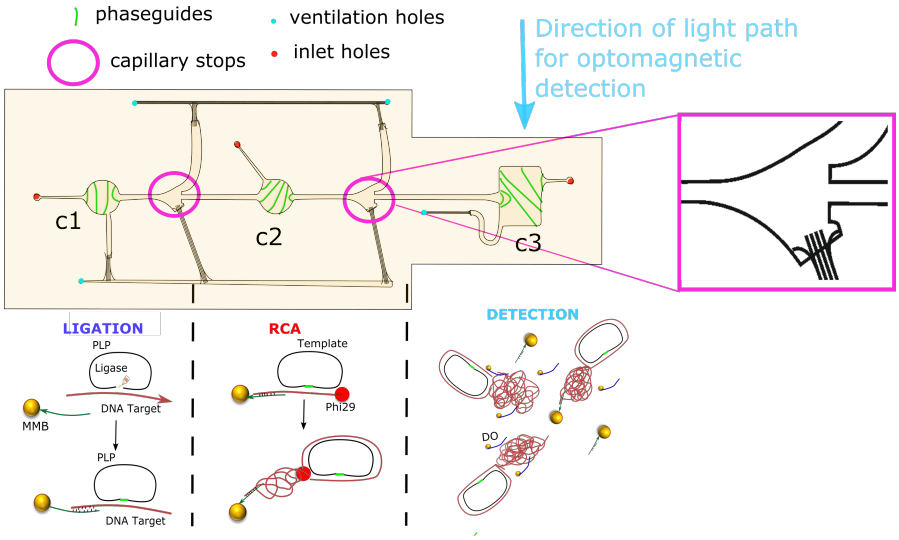

Figure 6.1: Schematic view of the final (design 2) chip design with details on capillary stops, phaseguides, ventilation holes and inlet holes, together with the reactions happening in each chamber. Image adapted from Paper III.

6.2 Chronology of process

This section illustrates the different steps that were taken to finalize the chip design (developed together with MSc student Gada Violo under my supervision), the bioassay design and the microbead handling (also developed together with MSc student Gada Violo under my supervision).

6.2.1 Chip designs and testing

The chip design, in particular its ventilation channels, changed over time, improving its features in regards of liquid filling and air bubbles formation. The chip main body had consistent design feautirng two smaller chambers (c1 and c2 , ⌀4.08 mm, in Fig. 6.1 and

in Fig. 6.2) and a bigger one (c3, 5×7 mm^2), linked through 0.7 mm wide channels with heart-shaped capillary stops (cs1 and cs2), that helped avoiding diffusion between liquids inside the different chambers. The capillary stops were designed and tested in order to stop the fluid at the desired location, with the design of an abrupt expansion of the channel width at the desired location. In this way a pressure change was required to push the liquid across the capillary stop. These parts were done as vector cut in the CO_2 laser, cutting through the entire middle layer (part 3 in Fig. 3.1). Phaseguides of height 40 μm were designed for every chamber, in order to have a control over the filling of the liquid inside them. The fabrication of the phaseguides was done by engraving the 0.5 mm thick layer, so that the polymer surrounding the phaseguides was ablated.

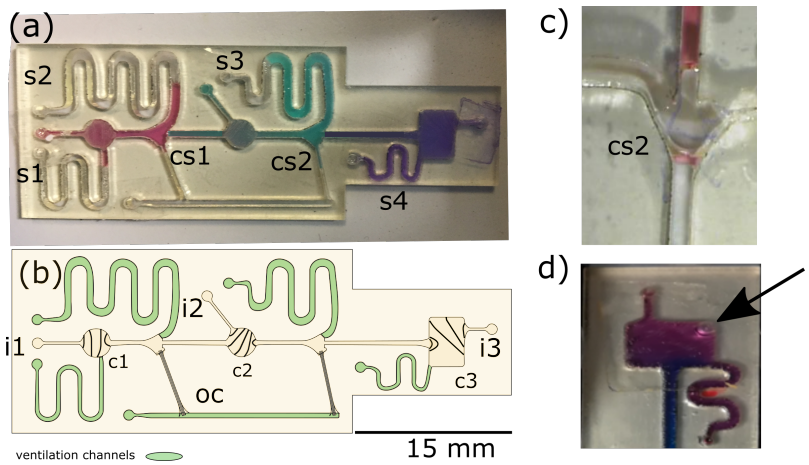

Figure 6.2: (a) Real picture and (b) schematic view of the first chip design (c) liquid movement in capillary stop valve cs2 (d) air bubble trapped in chamber c3.

Design 1 As illustrated in Fig. 6.2, initially the ventilation channels had a serpentine design with outlet holes at their end to allow liquid movement (s1, s2, s3 and s4). The serpentine design was chosen to create longer waste chambers, in order to be able to withheld higher liquid volumes. The fabrication method of these serpetines matched the creation of the chambers: vector cut through the entire middle layer (1.5 mm). An overload channel (oc) next to c2 was created for excess liquid flow. Inlets (i1, i2 and i3) and outlets holes, were ⌀2 mm in order to match the width of the pipette used to fill liquid inside them. The filling process was the following:

- fill c3 until the capillary stop (cs2) and s4. Seal i3.
- fill c2 until both cs1 and cs2, slightly pushing liquid in s4 and s3. Seal i2.
- fill c1 until cs1, slightly pushing even more liquid in s3, s2 and s1. Seal i1 and all outlet holes at the end of the serpentine channels (s1, s2, s3 and s4).

In Fig. 6.2 it is possible to clearly distinguish the three different liquids inserted in the chip thanks to a dye added to each buffer. It shows almost no diffusion or liquid intermixing between chambers, which is due to well designed capillary stops.
The first experiments run on this chip showed a technical problem: air bubble formation and its enlargement (as illustrated in Fig. 6.2(c) and (d)). The problem rose once we started filling and heating the chip on the setup, at *Influenza* protocol temperatures (above 55°C for ligation, 38°C for RCA and 56°C for detection). The main disadvantage in the formation of air bubbles, was the consequence of a built-up pressure inside the chip which would cause liquid movement and consequently leakage, emptying the capillary stops or chambers, as shown in Fig. 6.2(c). This would also cause interference with transport of beads between the chambers. Another disadvantage was that bubbles would create an obstacle for the LED light path in the detection chamber (c3 in the figures).

The issues encountered with Design 1 can be summarized as:

- Air bubble formation at the corners of chamber c3.
- Built-up pressure in channels and chambers of the chip, when heated, causing leakage.
- Spilling of liquid out of the inlets holes i1, i2 and i3, when filling the chip.

Built-up pressure The built-up pressure derived from air-bubbles can be explained using the Ideal gas law, which represents the equation of state of a hypothetical ideal gas. The law is:

$$pV_{\mathrm{G}} = n_{\mathrm{G}} R_{\mathrm{G}} T. \tag{6.1}$$

where p is the pressure of the gas, V_{G} is the volume, n_{G} is the number of moles, R_{G} is the ideal gas constant and T is the temperature of the gas. Once the T increases, the pressure p will also increase accordingly. Similarly, if a liquid is heated in a closed container, it will expand following its thermal expansion coefficient, causing leakage if the sealing is not perfect.

Design 2 - final chip In order to fix the above mentioned problems, a new design was needed. While it was decided to keep the main part (chambers and capillary stops) the same, the ventilation channels were re-designed in order to block the liquid movement from the capillary stops to the ventilation/waste channels. To accomplish this task, the waste channels were engraved rather than completely cut of from the PMMA layer [109]. The optimal engraving parameters would create 0.17 mm wide and 0.77 mm deep channels (checked on cross-sections with the use of a LEICA MZFLIII Stereomicroscope, equipped with a Sony DFW-X710 camera), which would allow less liquid movement in respect to 0.90 mm wide and 1.5 mm deep serpentines of the previous chip. This method was used to change all the serpentines to engraved channels (as shown in Fig. 6.3), which were connected to the same overload channel (oc) as before and an engraved waste chamber (ewc - 0.17 mm wide and 0.90 mm deep) placed on the left side of the central channel, to allow enough space for the built-up pressure during heating parts of the experiments.

In order to avoid the air bubble formation in c3, a new phaseguide was introduced in the chamber, in order to push the liquid to fill the top right angle of the chamber before filling the rest of c3. Inlet holes were decreased from ⌀2 mm to ⌀0.8 mm, and outlet holes were decreased to ⌀0.5 mm. The latter ones where not sealed anymore when filling the chip, in order to prevent built-up pressure in the chip. Fig. 6.3 shows the new and improved final design.

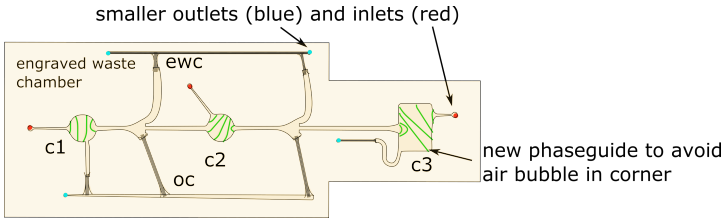

Figure 6.3: Schematic view of the new and improved design. Image adapted from Paper III.

The changes made to overcome the issues encountered with Design 1 can be summerized in the following list:

- Introduction of a new phaseguide to avoid bubble formation in the angles of chamber c3.
- Creation of an engraved channel instead of vector cut serpentines, to allow less liquid movement and therefore less trapped air that could expand.
- Decrease of inlet hole size down to ⌀0.8 mm, to prevent spills during filling of liquid.
- Decrease of outlet hole size down to ⌀0.5 mm, no sealing of outlet holes.

6.2.2 Bioassay design - *Influenza*

The *Influenza* bioassay design is very similar to the one described in the previous chapter (section 5.2.5). New oligonucleotides sequences were introduced to try to boost the opto-magnetic signal.
The target DNA was the type-B influenza virus (IDT, 81 oligonucleotide bases), with padlock probe (PLP - 90 nt) designed to match sequence of DNA target. The padlock probe was modified with a 5'-phosphate group. PLPs were added in 3-fold excess (1.5-24 nM) to minimise the number of unreacted probes (targets without circles).
In this part of the project, additional sequences were used to try to boost the optomagnetic signal. Detection oligonucleotides (DO, 20 bases, 3'-biotin) were designed to be complementary to RCPs and were attached to MNPs for OM detection.
Capture oligonucleotides (CO, 15 bases, 3'-biotin group) were linked to the MMBs to bridge DNA target and MMBs for efficient magnetic handling of sequential DNA processing steps. The length of CO was adjusted to be sensitive at moderate/elevated temperature (above 53°C) to enhance the detection signal. CO was complementary to the 5' terminal

part of the DNA target to not interfere with binding of PLPs. All information regarding sequences can be found in Table 6.1.

Table 6.1: Sequences of *Influenza* target, PLP, detection oligo (DO) and capture oligo (CO). The target-specific 'arms' of the PLPs as well as their binding sites in the target sequences are underlined.

DNA Tag	DNA sequence (5′-3′)	Modification
Target	AGACCTGTTACATCTGGGTGCT TTCCTATAATGCACGACAGAA CAAAAATTAGACAGCTGCCC AACCTTCTCCGAGGATAC	—
PLP	GGGCAGCTGTCTAATTTTTGAGT CGGAAGTACTACTCTCTGTGTAT GCAGCTCCTCAGTAATAGTGTCT TACGTATCCTCGGAGAAGGTT	5′-phosphate
DO	GTGTATGCAGCTCCTCAGTA	3′-biotin
CO	GAAAGCACCCAGATG-TTTTT	3′-biotin

Reagents and Buffers Table 6.2 shows all components that have been used in the experiments.

Table 6.2: Buffers and reagents composition (final concentration).

Buffer name	Composition
Binding buffer	8 mM tris, 4 mM EDTA, 0.1 % Tween-20, and 0.8 M NaCl (pH 8)
Ligation buffer	0.2 mg/ml BSA (New England Biolabs), 20 mM Tris-HCl (pH 8.3), 25 mM KCl, 10 mM $MgCl_2$, 0.5 mM NAD, and 0.01% Triton X-100 (Illumina)
RCA buffer	66 mM Tris-acetate (pH 7.9 at 37°C), 25 mM Mg-acetate, 132 mM K-acetate, 0,2% (v/v) Tween 20, 2 mM DTT, BSA 0.2 mg/mL, 190 μM dNTPs (New England Biolabs)
Detection buffer	20mM Tris-HCL (pH 8.0 at 25°C), 140mM NaCl, 5 mM KCl, 50 mM EDTA, 0,1% BSA, 0,01% Tween20

6.3 Setup for integrated amplification and detection

The first version of the setup used in this project was invented and designed by former Post-Doc of our group Giovanni Rizzi and was later modified by me. This section will give a detailed explanation of each of the parts portrayed in Fig. 6.4.

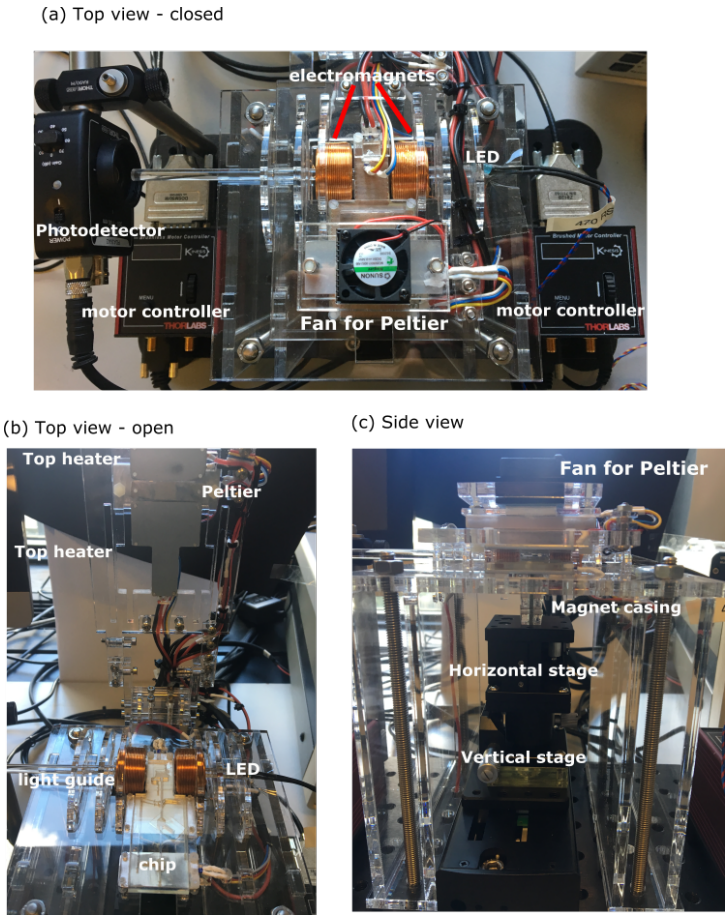

Figure 6.4: Setup used in the experiments. (a) Top view with the lid closed. The LED shines the light from the right, passes through the electromagnets and arrives to the photodetector thanks to a light guide. (b) Top-view with open lid and a chip in experimental position. (c) Side view showing the horizontal stage on the top of the vertical one. Image adapted from ESI of Paper III.

Stages The OM setup consisted of two motorized stages from Thorlabs creating a two-axis (xz) stage, a KBD101 Brushless DC Servo Driver attached to a Single-Axis Flexure Translation Stages for horizontal positioning and a KDC101 Brushed DC Servo Motor Controller attached to T40Z-10A Minimum Vertical Z Axis Translation Stage (MPositioning) , with a 12 mm Motorized Actuator, 3/8" Barrel Fitting for vertical positioning (12 mm range). On the top of the upper stage a plastic casing containing the external magnets was screwed, allowing the top magnet to be positioned 1 mm far from the bottom heaters. The magnets were used to move MMBs inside the chip from one chamber to another.

Temperature control The stages were placed underneath tailor-made "sandwich - heaters" (2 mm thick) with temperature monitoring using Pt100 elements and controlled using a Stanford Research Systems PTC10 unit, inside which we placed a disposable chip (see Fig. 6.4(b) and Fig. 6.5). Between the two heaters on the top, to keep the RCA chamber (c2) cold while performing ligation in c1, it was placed an aluminum strip which was regulated with the use of a thermoelectict (TE) element also controlled by the PTC10 unit. Heaters were custom-built for our setup on aluminum printed circuit boards (PCBs), by designing the printed circuit board on EAGLE software and then fabricate them on aluminum/copper plate through exposition of the design to UV light.

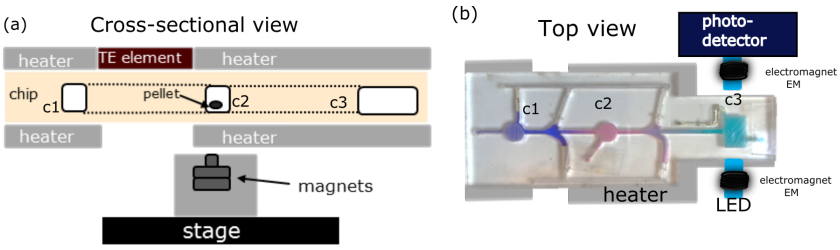

Figure 6.5: Schematic of setup used in experiments: (a) shows a cross-sectional view of the setup, showing the sandwich-heaters with the chip and the magnet and motors underneath. (b) shows a top view of the setup (removing the top heaters) with electromagnets, LED and photodetector.

Optomagnetic detection Detection took place in the last chamber of the chip (c3 in Fig. 6.5). PMMA rods guided light from a light emitting diode (wavelength of 470 nm) to the side of the chip, and from the other side of the chip to the photodetector (Thorlabs PDA-36A-EC) as shown in Fig. 6.5(b). The electromagnets were driven by a custom-built voltage to current converter controlled by a data acquisition card (National Instruments, NI-6211) that also collected the signal from the photodetector.
The optomagnetic technique is explained in section 2.5.

6.3.1 On-chip MMB handling strategy

MMB transportation Streptavidin coated magnetic microbeads were used as carriers of DNA on chip. A custom plastic casing including permanent magnets was used to carry the beads around and was screwed on the top of the horizontal stage. The stack consisted of four axially aligned cylindrical magnets (top to bottom): two N48, NdFeB, ⌀3 mm, 1 mm high magnets (S-03-01-N, Supermagnete, Gottmadingen, Germany) and two N45, NdFeB, ⌀6 mm, 3 mm high magnets (S-06-03-N, Supermagnete, Gottmadingen, Germany) [123] [90]. Transportation was performed by moving the stages between chambers at 0.3 mm/s with 5 s stops every 5 mm, to ensure the majority of the MMBs would be dragged along by the magnet.

MMB mixing On-chip mixing was achieved by moving the stages back and forth along the diameter of the chamber (4 mm) at a constant speed of 2 mm/s. These movements were useful to increase the sample solution-MMBs interaction for the entire duration of each reaction.

MMB flattening The use of MMBs caused problems in c3, for the detection signal, since their bigger hydrodynamic diameter would interfere with the results obtained from MNPs, as depicted in Fig. 6.6, where the dark green curve shows a shoulder at the lower frequencies due to the presence of MMBs. Since MMBs have a ten-fold larger diameter than MNPs, the parameter D_{h} of equation 2.25 would be influenced by their size. This would result in the appearance of another peak at lower frequencies of the real component of the spectra. It was therefore important to find a way to minimize this effect, which was done by introducing a vertical stage in the setup (already introduced in section 6.3). The vertical stage was always kept at its highest position, apart at the very end of the experiment just before detection started. The retraction of the stage under c3, by lowering it to its lowest position with a speed of 0.3 mm/s, had the outcome of creating a sedimented MMB pellet at the bottom of the detection chamber c3, hence out of light path not interfering with the MNP signal.

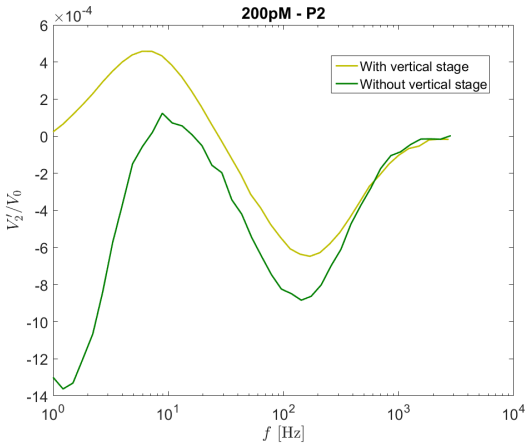

Figure 6.6: OM signal curves related to experiments carried out with (light green) or without (dark green) vertical stage. Image adapted from ESI of Paper III.

6.4 RCA assay performance - *influenza*

6.4.1 Investigation of different protocols for LOD optimization

This section considers the steps used to optimize the *influenza* assay protocol. The following sections have been discussed in Paper II and/or Paper III and will therefore only be summarized.

Enzyme concentration and addition of EDTA The enzyme concentration was optimized balancing assay efficiency and costs. In Fig. 6.7, we present the results of different enzyme concentrations (referred as unit/mL) (P1 (150 u/mL), P2 (300 u/mL), P4 (600 u/mL)) and addition of Ethylenediaminetetraacetic acid (EDTA) (P2-E) at the stage of detection (addition only in c3), along with corresponding scaling of other reagents (1×, 2×, and 4×). The graph shows histograms for c= 40 and 200pM, where a higher B_{MNP} means higher depletion and therefore better results. We used the sequences stated in Table 6.1, except that the target was biotinylated at the 5'-end and thus directly linked to the MMBs rather than via the CO probe. Ligation took place off-chip in a thermoshaker at 55°C for 20 min, followed by incubation of the obtained DNA target-PLP hybrids with streptavidin coated MMBs (0.2 mg/mL) for additional 20 min at 55°C (upon rotary mixing 1000 rpm). The obtained ligated products on-MMBs (60 μL) were further diluted in the RCA buffer to 120 μL and loaded into chamber c2 for on-chip RCA (45 min, 38.5°C). The first chamber (c1) contained 1x ligation buffer and the third chamber (c3) contained 0.05 mg/mL MNPs in the detection buffer. Because of a direct biotin-streptavidin link between target DNA and MMB, the obtained system represented a robust prototype of the experiments implemented using capture probes on MMBs in the later stage.

It is possible to notice a higher depletion for P4 concentration, but due to the high cost of the polymerase enzyme, it was decided to use the P2 concentration, equal to 30 units of polymerase enzyme. The addition of EDTA in the detection chamber was necessary to boost depletion of the chosen concentration P2 to a higher value, since its capacity of removing Mg^{+} from RCPs allowed them to open more freely and therefore be more attractive for detection probes. In Fig. 6.7, the histogram related to the addition of EDTA (P2-E) shows an increase in the signal almost comparable to P4 for both concentrations tested.

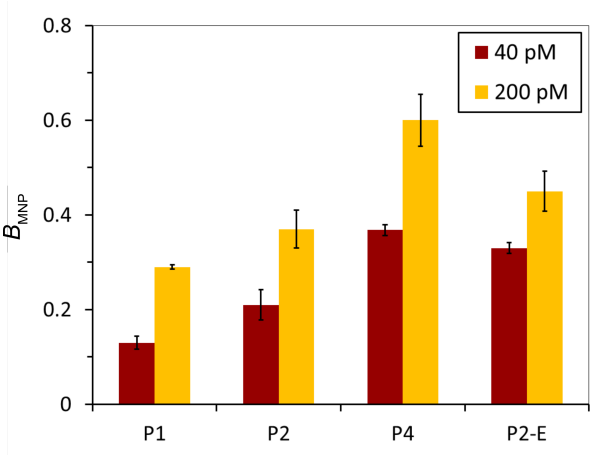

Figure 6.7: Histogram showing the amount of depleted MNPs for three different concentrations of enzyme (P1 (150 u/mL), P2 (300 u/mL), P4 (600 u/mL)) and one with the addition of EDTA (P2-E), $n = 3$. Image adapted from ESI of Paper III.

MMB concentration optimization Microbead concentration (0.1 , 0.3 mg/mL) was studied in Paper II, in a setup from now on called "4-chip setup" that allowed four simultaneous measurements, in order to investigate CO-MMBs interference on the detection of MNPs, in relation to the measurements of the limit of detection (LOD) for a dose-response curve (a thorough explanation of the setup can be found in [79]). The LOD was found to be:

- 4pM, with a linear dynamic range of 4-100pM for 0.1 mg/ml MMBs
- 20pM, with a linear dynamic range of 20-60pM for 0.3 mg/ml MMBs

Results indicate a trend of increasing LOD and narrowing dynamic range for higher amount of CO-MMBs. We speculate that a large excess of MMBs (0.3 mg/ml) and consequently excess of capture probes led to an increasing melting temperature of the CO-DNA bridges at target concentration $c \leq 20$ pM. That would be enough to compromise the discussed mechanism of temperature-dependent release of RCPs from MMBs during OM detection. Similarly, the same concentrations were studied from a physical point of view, to investigate their ability to transport beads from one chamber to another, resulting a large amount of beads lost at the capillary stops for concentrations 0.3 mg/mL and almost no bead loss for 0.1 and 0.2 mg/mL . The final concentration chosen was 0.2 mg/mL.

Boosting the optomagnetic signal The first optimization study included an investigation of the use of biotin-DNA target-PLP hybrids, attached to the streptavidin MMBs. The result (dotted brown curve in Fig. 6.8(a)), showed a poor depletion compared to similar studies without MMBs (as illustrated in Paper II). The reason behind this result was the reduced diffusion of the RCPs, which were still attached to the sedimented MMBs. In this perspective, it was necessary to find a method to release the RCPs from the MMBs, so that DOs could more easily attach to the complementary parts of the RCPs for the detection (as illustrated in the higher depletion of the green solid curve of Fig. 6.8(a) and in the cartoon-like sketch of Fig. 6.8(b)).

In order to overcome diffusion of DOs to RCA products linked to MMBs and reduce interference of MMBs with the assay, a heat-labile capture probe (CO) was employed to link DNA target to MMBs, as explained later in this chapter.
In this way, captured targets with amplification products (RCPs) could be released at certain temperatures in the detection step to achieve a more efficient readout. On the other hand, it was fundamental that the detection oligo (DO) - RCP hybrids should be stable at $T_{\text{detection}}$ to allow detection of the binding of MNPs to RCPs.
We therefore optimized the CO sequence and characterized the melting of CO-target hybrids and DO-MNPs hybrids (illustrated in Fig. 6.8(b) and (c)).
The procedure implied optomagnetic measurements to characterize the effective hydrodynamic size of the MNP-RCP, thorugh an experiment in which the temperature was increased at 0.01°C/s while OM spectra of the hydrodynamic size D_{h} of CO-RCPs and DO-RCPs were continuously recorded. The measurements were carried out on the "4-chip

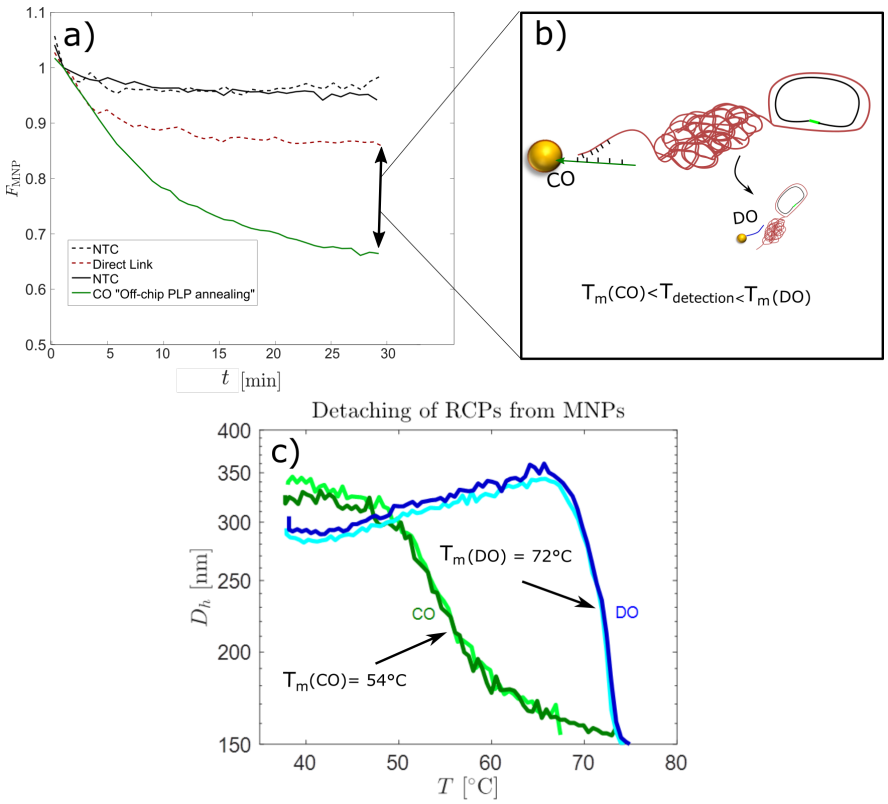

Figure 6.8: (a) Depletion signal over time for a concentration c=200pM. The red dashed line refers to direct link between MMB and target DNA and the solid green line refers to the introduction of COs, for the "Off-chip PLP annealing" case. (b) The cartoon shows the detachment of the CO-MMB from the RCP and the consequent attachment of the DO-MNP for the detection. (c) The graph shows the melting curves of DOs (blue curves) and COs (green curves), more particularly the detaching of RCPs from MNPs linked via CO and DO. Image adapted from Paper II and III.

setup". The hydrodynamic diameter D_h was extracted from the peak position in the V_2'/V_0 spectra, as described in section 2.5. The results are depicted in Fig. 6.8(b), showing:

- clear decrease of the D_h at about 54°C for the capture oligonucleotide CO.
- clear decrease of the D_h at about 72°C for the detection oligonucleotide DO.

Detection of MNP depletion was performed at 56°C, meaning no interference with the DO-RCP bond since melting CO-RCP $< T_\mathrm{detection} <$ melting DO-RCP. In Fig. 6.8(a) it is possible to notice the moment (at around 5 min) in which the CO-MMBs supposedly detach from the target DNA, allowing more DOs to penetrate into the RCPs.

Pre-ligation steps: On- and Off-chip PLP annealing Sequence-specific ligation is the process of joining together two nucleic acid fragments. The action requires circular

padlock probes to specifically recognize target DNA and get joint into circles. In order to boost the LOD, two different types of pre-ligations steps were tested: On- and Off-chip PLP-annealing. The idea behind these steps was the annealing of ligating arms of the padlock probes on the target DNA.

"Off-chip annealing" implied a pre-ligation step performed outside the chip, in a thermoshaker, after which the bioassay was inserted on chip, see process flow in Fig. 6.9.

In the experiments, a solution containing DNA target in ligation buffer was placed in a thermoshaker at 55°C for 20 min, and then lowered to 30°C which required 30 min. Afterward, Ampligase enzyme and MMBs were added to the solution, which was then inserted in the chip. Ligation was then performed on chip at 58°C for 20 min followed by cooling to 35°C over 5 min, in the presence of MMBs, under continuous MMB mixing to complete the ligation and target capture on the CO-functionalized MMBs.

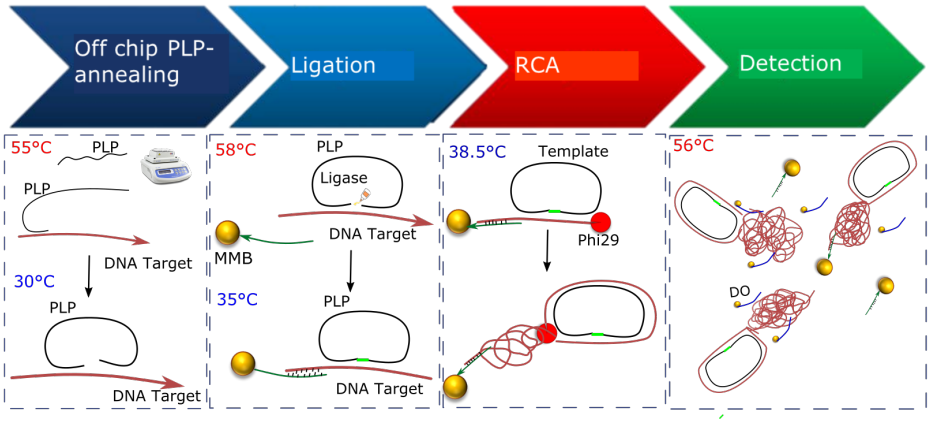

Figure 6.9: Process flow for OFF chip PLP-annealing, with cartoon-like sketches to show each step of the process.

"On-chip annealing" started directly with ligation on chip, see Fig. 6.10 for the process flow.

In this case, to mimic annealing of DNA target and PLPs, the MMBs were placed in the second chamber for the entire duration of the ligation (carried out in the first chamber, 20 min at 58°C). The beads were then taken back from the second chamber to the first one. They were annealed for 2 min at 58°C and then temperature was dropped to 30°C for 15 min as functionalization step occurred. Similarly, the capture protocol pursued the same mode of annealing between CO and DNA target.

Fig. 6.11 illustrates the results obtained from studying the two different annealing steps and compares them to the biotin-DNA target-PLP hybrids depletion results, for a DNA concentration c=200pM. The histogram shows the amount of depleted MNPs B_{MNP} for three different protocols. As already mentioned, the direct-link histogram bar (red) shows the lowest depletion, due to the reduced diffusion of the RCPs still attached to the MMBs. "On-chip PLP annealing" shows a slightly higher depletion but "Off-chip PLP annealing"

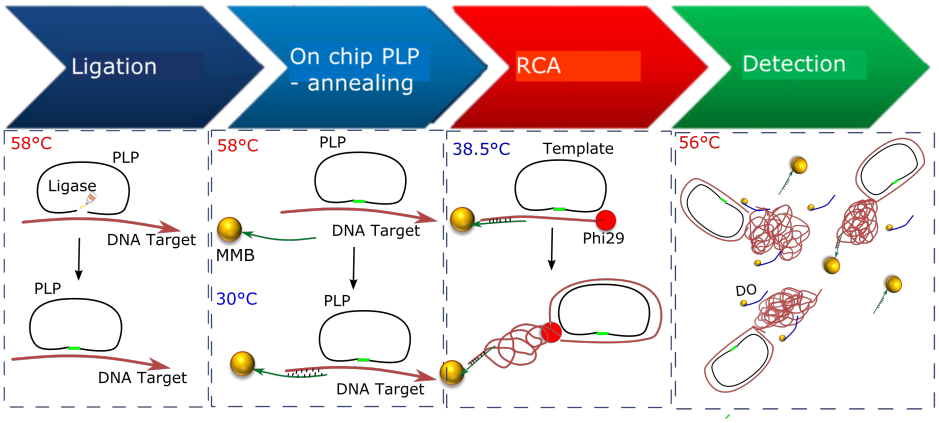

Figure 6.10: Process flow for ON chip PLP-annealing. with cartoon-like sketches to show each step of the process.

is defined as the best result.

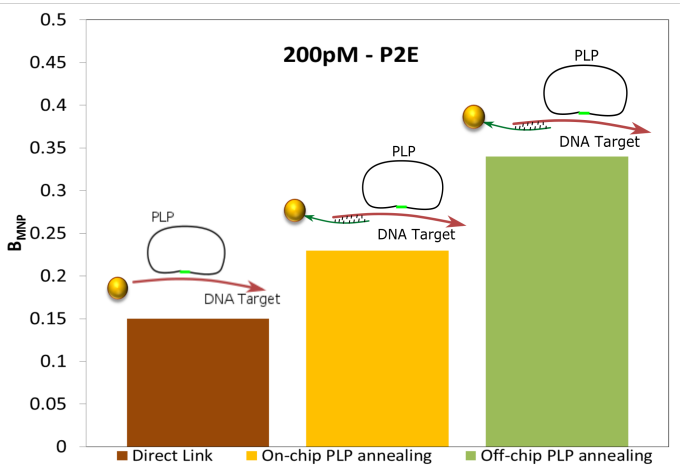

Figure 6.11: Histogram showing the amount of depleted MNPs B_{MNP} for three different protocols: dark red for direct link, yellow for "On-chip PLP annealing" and green for "Off-chip PLP annealing". All experiments were done for c=200pM DNA Target concentration and with the P2-EDTA enzyme concentration.

Rolling circle amplification. In both protocols RCA was carried out in the same way. The MMBs were transported from the ligation chamber (c1) to the RCA chamber (c2) containing the RCA buffer and 30 units of phi29 polymerase enzyme. Amplification took place at 38.5°C for 45 min under continuous MMBs mixing. From each ligated PLP-Target-CO attached to an MMB, the RCA produced a single-stranded concatamer with nominally $\sim$ 750 copies of the sequence complementary to that of the PLP.

Optomagnetic readout. Once RCA reaction was completed, the temperature of chambers c2 and c3 was ramped towards the detection temperature of 56°C, while beads were carried to chamber c3, which contained the DO-functionalized MNPs in the detection buffer. The MMBs entered the detection chamber (c3) when the heater temperature was around 50°C. Once the temperature stabilized at 56°C, the z-stage was automatically lowered to the home position (the lowest possible position) at 0.3 mm/s. Subsequently the x-stage was quickly moved to its home position farthest away from the detection chamber and the optomagnetic detection was started.

6.5 Results

6.5.1 Dose response curve

The final goal of this part of the project was to demonstrate the possibility of integrating an automated bioassay on chip. In order to evaluate this capability, the study focused on obtaining a dose-response analysis for the two methods explained in the previous section. The results can be seen in Fig. 6.12. The graph shows two dose response curves obtained from the two different methods previously mentioned, "On-chip PLP annealing" (red circles) and "Off-chip PLP annealing" (black squares) chip. The solid lines are fits to the Hill equation $B_{\mathrm{MNP}}(c) = B(0) + [B(\infty) - B(0)] \,/\, [1 + (K_{\mathrm{A}}/c)^{n_{\mathrm{H}}}]$ with the association constant K_{A} and Hill coefficients n_{H}.

Results: off-chip PLP annealing Experiments were carried out for 10 different concentrations c: 1, 2, 4, 10, 20, 40, 100, 200, 400, 800, 2000 pM. For each concentration, three experiments were done. The cutoff (black dotted line in the graph) was measured as the average of the repeated negative control experiments with the addition of standard deviation multiplied by a factor of 3. The LOD obtained was estimated to be 2pM, with parameters of the Hill fitting as the following: $K_{\mathrm{A}} = 145.55$ pM and $n_{\mathrm{H}} = 1.10$. It is clearly visible saturation both at low (before 10 pM) and high (after 800 pM) concentrations, the dynamic range is the considered in between those two concentrations.

Results: on-chip PLP annealing Experiments were carried out for 7 different concentrations c: 10, 20, 40, 100, 200, 400, 800, 2000 pM. For each concentration, three experiments have been done. The cutoff (red dotted line in the graph) was measured as the average of the repeated negative control experiments with the the addition of standard deviation multiplied by a factor of 3. The LOD obtained was estimated to be 20pM, with parameters of the Hill fitting as the following: $K_{\mathrm{A}} = 292.67$ pM and $n_{\mathrm{H}} = 1.28$. In this case saturation is visible at high concentrations (above 800 pM), but not at lower ones.

6.6 Discussion

Results show a linear trend for the dynamic range of both curves, with "Off-chip PLP annealing" showing a lower limit of detection (LOD) of 2pM than "On-chip PLP annealing"

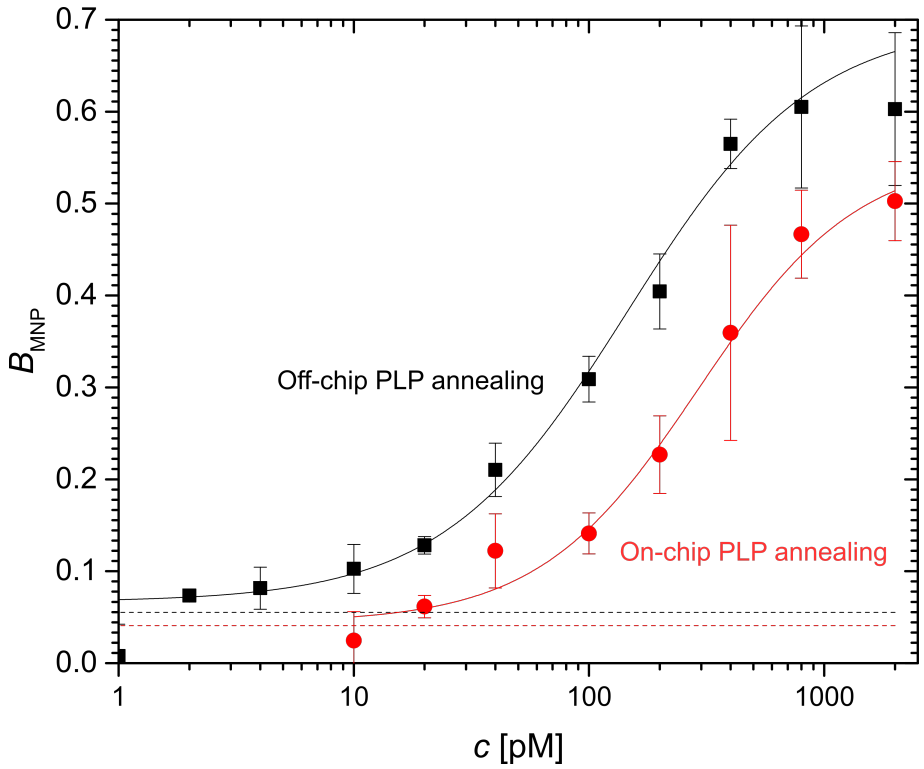

Figure 6.12: Dose response curve for single MNPs. The black dots refer to "Off-chip PLP annealing" and the red ones to "on-chip PLP annealing" ($n = 3$.). Same colours have been used for showing the cutoff line for both methods, measuring LOD=2pM for "Off-chip PLP annealing" and LOD=20pM for "On-chip PLP annealing". The cutoff (black and red dotted lines in the graph) were measured in both scenarios as the average of the repeated negative control experiments with the addition of standard deviation multiplied by a factor of 3. The two solid lines are Hill fits of the data. Image adapted from Paper III.

(20pM). The trend is similar in both cases, with "On-chip PLP annealing" being shifted of 0.1 towards lower values, meaning less depleted MNPs, with respect to "Off-chip PLP annealing". We speculate that the reason behind this difference lies in different efficiency of the MMBs in capturing ligated DNA circles. For "Off-chip PLP annealing" the MMBs were inserted in the solution containing target-PLP complexes prior to on-chip capture and ligation, having more chance to capture the DNA targets compared to "On-chip PLP annealing". In this latter case, it was necessary to leave the CO-MMBs in the c2 chamber until ligation was carried out in chamber c1. The prolonged stay in chamber c2 in the form of a pellet and without mixing, was most likely the cause of the creation of irreversible forming a clumps of MMBs. As a consequence, once the MMBs are brought back to chamber c1 for annealing and capture, they had a reduced surface for the capture of ligated PLP-Target.

6.7 Discrimination of single-base mutation for *Tuberculosis*

In order to demonstrate the creation of a scalable assay device, it was decided to test it with another infectious disease: *Mycobacterium tuberculosis*. This multi-drug resistant strain becomes resistant to antibiotics via acquisition of a point mutation in the genome. Sequence-specific ligation can be used to distinguish the single-nucleotide variation, as demonstrated in the next paragraphs. Part of these results were presented at a conference and refer to conference contribution V.

Bioassay design The *tuberculosis* bioassay was designed with *katG* 315 (A**G**C/A**C**C) mutation (107 oligonucleotide bases). The padlock probe (PLP - 89 bases) was designed to match sequence of DNA target, and was modified with a 5'-phosphate group.
The same detection oligonucleotides (DO, 20 bases, 3'-biotin) used for *Influenza* were implemented also in this bioassay. Capture oligonucleotides were also used (CO, 16 bases, 3'-biotin group). The length of CO was adjusted to be sensitive at moderate/elevated temperature (above 60°C) to enhance the detection signal. CO was complementary to the 5' terminal part of the DNA target to not interfere with binding of PLPs. All information regarding sequences can be found in Table 6.3. Buffers and reagents were the same as the ones used for *Influenza* and can be found in Table 6.2.

Table 6.3: Sequences of *Tuberculosis* wild and mutant target, mutant PLP, DO and CO. The target-specific 'arms' of the PLPs as well as their binding sites in the target sequences are underlined, whereas the point mutation is underlined and bold.

DNA Tag	DNA sequence (5′-3′)	Modification
Wild Target	GAACCCGAGGCTGCTCCGCTGGAGCAGATGG GCTTGGGCTGGAAGAGCTCGTATG GCACCGGAACCGGTAAGGACGCGATCACCA **C**CGGCATCGAGGTCGTATGGAC	—
Mutant Target	GAACCCGAGGCTGCTCCGCTGGAGCAGATGG GCTTGGGCTGGAAGAGCTCGTATG GCACCGGAACCGGTAAGGACGCGATCACCA **G**CGGCATCGAGGTCGTATGGAC	—
Mutant PLP	TGGTGATCGCGTCCTTACCGAGTAGCCTT CCCGAGCATTGTGTATGCAGCTCCTCAGTA ATAGTGTCTTACATACGACCTCGATGCCGG	5′-phosphate
DO	GTGTATGCAGCTCCTCAGTA	3′-biotin
CO	CAAGCCCATCTGCTCC-TTT	3′-biotin

Specificity - Discrimination of single base mutation Due to the limited time available before the end of the PhD project, we decided to study the specificity measurements in the "4-chip setup" presented earlier in this chapter (Section 6.4.1). This setup does not

allow automated experiments, and therefore ligation and RCA were carried out outside of the setup in an eppendorf tube. The detection method remained the same. The main reason for this choice lies in the possibility of running four different experiments in parallel rather than only one like in the setup presented in this thesis.

The assay is based on rolling circle amplification (RCA) with mutant (MT) and wild (WT) specific DNA Targets, shown in Table 6.3. For sequence-specific ligation to work properly, the DNA Target and PLP have to be complementary. In this case we wanted to show the ability of this method to discriminate between a one-point mutation in the DNA Target, keeping the same mutant PLP. Once the ampligase enzyme is added to the solution, the PLPs on matching targets are enzymatically joined to form circles, whereas those on mismatching targets remain open. Subsequently, during amplification, targets on circular ligated PLPs are extended to form a long concatemer of the sequence complementary to the PLP, whereas non-circular PLPs are not extended (as shown in Fig. 6.13(a)). The resulting rolling circle products (RCPs) are detected using 100 nm MNPs functionalized with DOs. Neither COs, nor MMBs were used in this first single base discrimination step. Fig. 6.13(b) shows the signal from depleted MNPs vs. time after mixing for a concentration c=100pM. In the case of matching mutant Target-PLP, a depletion of free MNPs of more than 80% was observed. On the other hand, the mismatching combination showed a signal decrease of about 4%, which is comparable to the observation for the no target control sample. This demonstrated the ability of the assay with on-chip OM readout to detect *Mycobacterium tuberculosis* and the mutation responsible for rifampicin antibiotic resistance with high specificity.

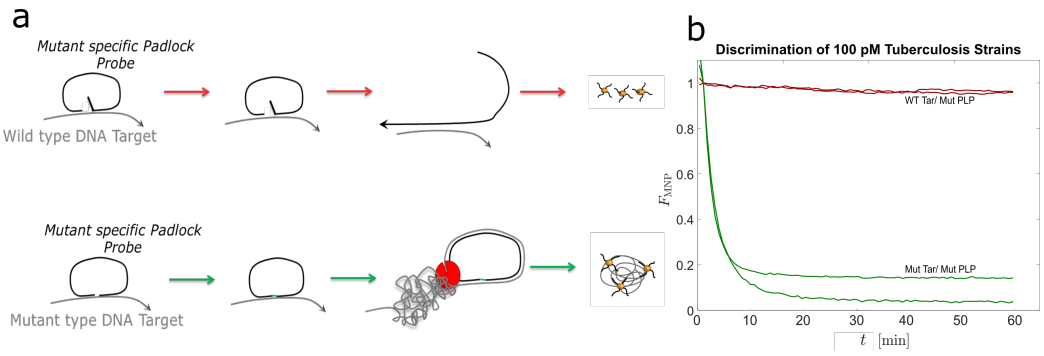

Figure 6.13: (a) RCA assay for detection of target with single nucleotide discrimination. Matching PLP-target pairs produce an RCA product, whereas mismatching pairs do not. (b) Signal from depleted MNPs vs. time. Image adapted from [124].

RCA assay performance After obtaining the results on the single nucleotide discrimination, we moved on with the optimization process on the automated setup, with the help of master student Elisabeta Tefiku under my co-supervision. In this thesis, only the initial part of the process will be shown, in a dose-response analysis.
The optimized process to boost the OM signal for *influenza* was the starting point for the

optimization process for *tuberculosis*. Therefore the experiments were carried out with:

- Use of COs.
- 0.2 mg/mL MMB concentration.
- P2 enzyme concentration with the addition of EDTA.

The assay was designed in order to perform ligation outside of the chip, the protocol will be then referred as "On-chip CO-Target capture". In the experiments, a solution containing mutant DNA target, fully matching mutant PLPs and Ampligase enzyme in ligation buffer was placed in a thermoshaker at 60°C for 20 min to perform ligation, and then lowered to 30°C which required 30 min. Afterward, MMBs were added to the solution, which was then inserted in the chip in chamber c1. Capture was then performed on chip in the presence of MMBs, with continuous movements of the external magnet to improve accessibility of the DNA circles to the COs. It was carried out by heating c1 at 60°C for 2 min and then lowering the temperature to 30°C to complete the CO-MMB functionalization step. Subsequently the external magnet was moved to the following chamber (c2) to perform RCA at 38.5°C for 45 min. Finally the MMB pellet was moved to the detection chamber (c3), and after the homing of the vertical and the horizontal stages, detection was started at 62°C for 30 min. The process flow can be seen in Fig. 6.14.

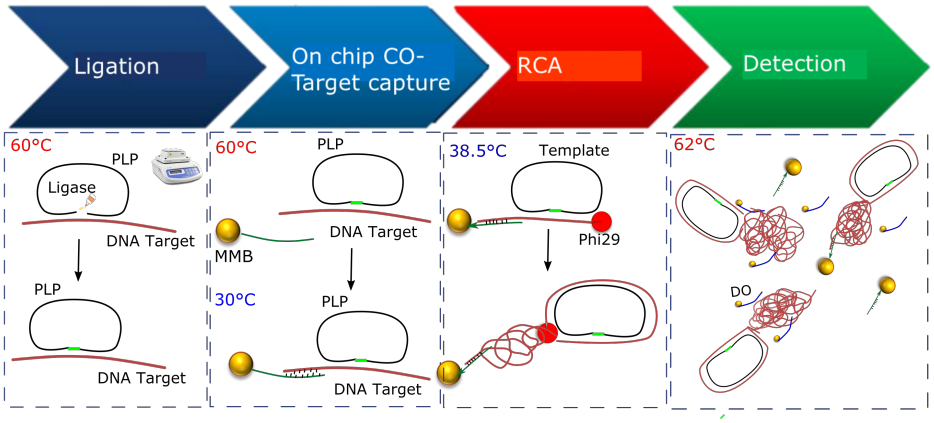

Figure 6.14: Process flow for the tuberculosis bioassay. Ligation was performed outside of the chip in a thermoshaker. The solution was then inserted in the chip for on-chip CO-Target capture, RCA and detection.

Results - Dose response curve The results can be seen in Fig. 6.15. The graph shows the dose response curve obtained for "On-chip CO-Target capture" carried out for *tuberculosis*. The solid line is a fit to the Hill equation $B_{\mathrm{MNP}}(c) = B(0)+[B(\infty) - B(0)] \,/\, [1 + (K_{\mathrm{A}}/c)^{n_{\mathrm{H}}}]$ with the association constant K_{A} and Hill coefficients n_{H}.

Experiments were carried out for 7 different concentrations c: 4, 10, 20, 30, 40, 60, 100 pM. For each concentrations, three experiments were done. The cutoff (black dotted line

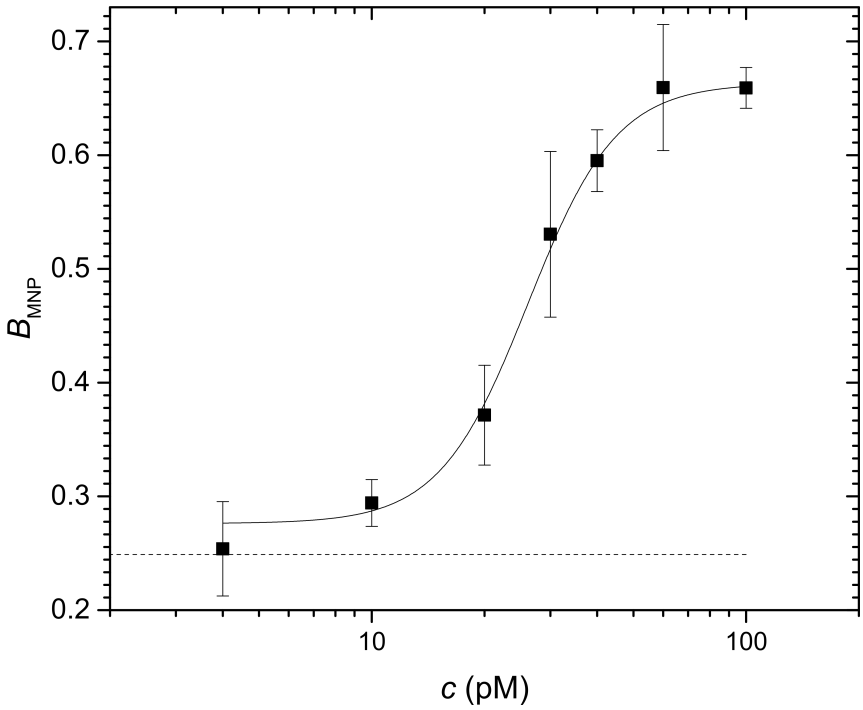

Figure 6.15: Dose response curve for single MNPs. The black dots refer to the different concentrations for the "On-chip CO-Target capture" protocol ($n = 3.$), with an LOD of 10pM. The cutoff was measured as the average of the repeated negative control experiments with the addition of standard deviation multiplied by a factor of 3. The solid line is Hill fit of the data.

in the graph) was measured as the average of the repeated negative control experiments with the addition of standard deviation multiplied by a factor of 3. The LOD obtained was estimated to be 10pM, with parameters of the Hill fitting as the following: $K_{\mathrm{A}} = 26.15$pM and $n_{\mathrm{H}} = 3.66$. Saturation is visible for high concentrations (above 60 pM), but not at lower ones. The dynamic range can be considered between 10pM and 60pM.

6.8 Discussion

The cutoff value is consistently higher than compared with previous experiments with *Influenza* strand, assessing to 20% of depletion. This high depletion of the NTC can be in part explained by the higher self-complementarity of the DOs with the COs for the *tuberculosis* strand (4 bases) compared to the *Influenza* one (3 bases). Therefore, we can speculate that some DOs get attracted and attached to the COs, causing a constant measured depletion even without the presence of DNA.

6.9 Summary

We created a laser ablated chip, suitable for integration of an isothermal amplification assay. The multichamber chip granted controlled filling of liquid, thanks to the use of capillary forces and phaseguide structures. Moreover, the experiments were run on a custom-made fully automated setup with temperature control, motor positioning of DNA through the use of magnetic beads and optomagnetic detection. The results demonstrated the feasibility of performing an isothermal amplification assay on an automated lab-on-a-chip device for two different respiratory infectious diseases such as Influenza and Tuberculosis. The knowledge obtained from this study, was of great importance in the development of a single-use mass-producible injection moulded polymer chip for the integration of the entire bioassay.

Chapter 7

Conclusions and outlook

The main goals of this PhD project were the optimization of a manufacturing process for the mass-production of a low-cost all-polymer chip, the creation of a microfluidic multichamber chip with capillary structures for liquid handling, and the development of a protocol for the integration of a molecular diagnostic assay on the multichamber chip.

The injection moulding fabrication technology used for the manufacturing process had been previously studied by Kasper Kistrup, a former PhD of our group and all the equipment was already present at DTU Nanotech. The established fabrication process required the use of micro-milling for the realization of the milling insert and a picosecond laser for the creation of energy directors, which are necessary to ensure bonding. Moreover, the process required also an injection moulding machine for the mass-production of chip parts and finally an ultrasonic welding machine for the direct bonding of the chip parts. This entire process, including the finalization of the design on CAD, was performed as a 2-day process. The manufacturing method was successfully used to fabricate different injection moulded chips throughout the development of the project.

The first part of the project was carried out on the study of capillarity and liquid filling. One of the major risks when handling a microfluidic platform, is the creation of air bubbles during the filling process. It is important to avoid them not only to avoid liquid expansion if the platform is heated up, but also because they could interfere with the reactions occurring inside the different chambers. In addition, air bubbles would interfere also with the optical detection needed in the final step of the assay. To avoid them, phaseguide structures were created and tested with the development of a COC Luer chip. The manufacturing process used was the one mentioned above, with the phaseguides micromilled on the milling insert with the use of an engraving tool. The characterization showed that the liquid would systematically pin at the border of the phaseguides, until a burst pressure was reached with an increase in filling pressure. This result proved the reliability of the injection moulding manufacturing method for the creation of capillary structures to control liquid filling inside the chip. The same manufacturing method was used to create a multichamber microfluidic system with phaseguides structures to enable controlled liquid filling. The final goal for this device was the implementation of the assay on-chip. In this case polypropylene was used for the fabrication of the chips. After

several reference experiments had been run in our lab on a single-chamber chip, it was finally possible to start testing the bioassay on the multichamber chip. Initially only one chamber was used, and experiments matching the reference experiments were run. In this way it was possible to prove the feasibility of the bioassay integration on-chip. Due to height limitation of the injection moulding at our department, it was then decided to shift to a second manufacturing technique, the CO_2 laser machining combined with adhesive bonding. Its high flexibility together with the possibility of changing the design several times per day made this method attractive for the prototype development in the project. The chip layout was kept the same as before, in order to be able to shift back to the injection moulding later in the project, to be able to asses a mass-production process. The multichamber chip design included phaseguide structures and capillary stop valves to enable the controlled liquid filling of the connected chambers with no liquid intermixing. In parallel to the integration of the assay on-chip, the mechanical department at DTU was contacted to fabricate an entire mould and tool for the creation of the finalized chip using injection moulding. The multichamber chip allowed for the implementation of the three-step assay entirely on-chip, with the use of a custom-made setup. The setup was designed to be fully automated and with the integration of temperature control, magnetic bead handling and optomagnetic detection through the use of LabVIEW software. Optimization steps were carried out both on the single-chamber and three-chamber chips, such as the study of enzyme or MMB concentrations. Once the optimal protocol was found, it was finally possible to start running systematic experiments entirely on the three-chamber chip. We compared two different assay strategies, for the implementation of ligation on-chip for the Influenza target. The results were illustrated with the inclusion of the two corresponding dose-response curves in the thesis. To demonstrate the scalability of the microfluidic chip and of the automated setup, Tuberculosis was studied at the very end of the project. In this case we demonstrated the specificity of ligation to point mutations though reference experiments on the single-chamber chip with wild and mutant type tuberculosis. Moreover an initial dose-response curve of the optimized protocol, with ligation performed off-chip, was shown.

Further development and optimization of the microfluidic chip insert and of the bioassay protocol for the study of Tuberculosis is underway with the help of a master student under my co-supervision and will be continued in a planned postdoc project in the same group. The main focus will be on the implementation of ligation on-chip, to be able to perform a fully automated assay on-chip. An optimization of the on-chip MMB mixing is under study, to create, e.g, a more efficient CO-MMB mixing in the first step of the bioassay. Furthermore, the sensitivity of the presented study can be further improved by implementing more RCA cycles on-chip, boosting the current limit of detection. Moreover, it would be interesting to demonstrate the reliability of the setup not only for the study of particle depletion (turn-off signal), but also the study of the agglutination of particles (turn-on signal), to show the different detection possibilities of the optomagnetic readout. The chip layout in its current form needs some minor revisiting before it is ready to be injection moulded at the mechanical department. The final aim is to be able to obtain a finalized optimization protocol for the tuberculosis target and to implement it in a low-cost mass producible and disposable chip.

Bibliography

[1] United Nations, "The Sustainable Development Goals Report 2018", United Nations, Nwe York, Tech. Rep., 2018, p. 38. [Online]. Available: https://unstats.un.org/sdgs/files/report/2018/thesustainabledevelopmentgoalsreport2018.pdf (visited on 10/22/2018).

[2] World Health Organization, "SEVENTY-FIRST WORLD HEALTH ASSEMBLY A71/4 Provisional agenda item 11.1", WHO, New York, Tech. Rep., 2018, p. 50. [Online]. Available: http://apps.who.int/gb/ebwha/pdf%7B%5C_%7Dfiles/WHA71/A71%7B%5C_%7D4-en.pdf?ua=1 (visited on 10/22/2018).

[3] ——, "World report on Ageing and Health", WHO, New York, Tech. Rep., 2015, p. 60. [Online]. Available: www.who.int.

[4] S. R. B. L. Shrivastava, P. S. Shrivastava, and J. Ramasamy, "Health-care of Elderly: Determinants, Needs and Services.", *International journal of preventive medicine*, vol. 4, no. 10, pp. 1224–5, Oct. 2013.

[5] World Health Organization, *Ageing and health*, 2018. [Online]. Available: http://www.who.int/news-room/fact-sheets/detail/ageing-and-health (visited on 10/22/2018).

[6] A. St John and C. P. Price, "Existing and Emerging Technologies for Point-of-Care Testing.", *The Clinical biochemist. Reviews*, vol. 35, no. 3, pp. 155–67, Aug. 2014.

[7] A. Manz, N. Graber, and H. M. Widmer, "Miniaturized Total Chemical Analysis Systems: a Novel Concept for Chemical Sensing", *Sensors and Actuators*, vol. 1, no. 6, pp. 244–248, 1990. DOI: 10.1016/0925-4005(90)80209-I.

[8] O. Geschke, H. Klank, P. Telleman, O. Geschke, H. Klank, and P. Telleman, *Microsystem Engineering of Lab-on-a-chip Devices*, Wiley-VCH, Ed. Weinheim, 2004, p. 200.

[9] M. L. Metzker, "Emerging technologies in DNA sequencing", *Genome Research*, vol. 15, no. 12, pp. 1767–1776, 2005. DOI: 10.1101/gr.3770505.

[10] J. Wang, A. Ibáñez, and M. P. Chatrathi, "On-chip integration of enzyme and immunoassays: Simultaneous measurements of insulin and glucose", *Journal of the American Chemical Society*, vol. 125, no. 28, pp. 8444–8445, 2003. DOI: 10.1021/ja036067e.

[11] R. B. Schasfoort, "Proteomics-on-a-chip: The challenge to couple lab-on-a-chip unit operations", *Expert Review of Proteomics*, vol. 1, no. 1, pp. 123–132, 2004. DOI: 10.1586/14789450.1.1.123.

[12] J. Wang, "From DNA biosensors to gene chips", *Nucleic Acids Research*, vol. 28, no. 16, pp. 3011–3016, 2000. DOI: 10.1093/nar/28.16.3011.

[13] D. Huh, W. Gu, Y. Kamotani, J. B. Grotberg, and S. Takayama, "Microfluidics for flow cytometric analysis of cells and particles", *Physiological Measurement*, vol. 26, no. 3, R73–R98, 2005. DOI: 10.1088/0967-3334/26/3/R02.

[14] S. Mouradian, "Lab-on-a-chip: applications in proteomics", Caliper Technologies, Tech. Rep., 2001, pp. 51–55. DOI: 10.1016/S1367-5931(01)00280-0.

[15] P. S. Dittrich and A. Manz, "Lab-on-a-chip: microfluidics in drug discovery", *Nature Reviews Drug Discoveries*, vol. 5, no. 3, pp. 210–218, 2006. DOI: 10.1038/nrd1985.

[16] C. D. Chin, V. Linder, and S. K. Sia, "Lab-on-a-chip devices for global health: Past studies and future opportunities", *Lab on a Chip*, vol. 7, no. 1, pp. 41–57, 2006. DOI: 10.1039/b611455e.

[17] L. Chen, A. Manz, and P. J. R. Day, "Total nucleic acid analysis integrated on microfluidic devices", *Lab on a Chip*, vol. 7, no. 11, pp. 1413–1423, 2007. DOI: 10.1039/b708362a.

[18] V. Gubala, L. F. Harris, A. J. Ricco, M. X. Tan, and D. E. Williams, "Point of Care Diagnostics: Status and Future", *Analytical Chemistry*, vol. 84, no. 2, pp. 487–515, 2012. DOI: 10.1021/ac2030199.

[19] N. Ramalingam, Z. Rui, H. B. Liu, C. C. Dai, R. Kaushik, B. Ratnaharika, and H. Q. Gong, "Real-time PCR-based microfluidic array chip for simultaneous detection of multiple waterborne pathogens", *Sensors and Actuators, B: Chemical*, vol. 145, pp. 543–552, 2010. DOI: 10.1016/j.snb.2009.11.025.

[20] M. Hillmering, "Polymer microfluidic systems for sample preparation for bacterial detection", PhD thesis, KTH, 2014, p. 300.

[21] D. Mark, S. Haeberle, G. Roth, A. Felix Von Stetten, and R. Zengerle, "Microfluidic lab-on-a-chip platforms: requirements, characteristics and applications", *Chemical Society Reviews*, vol. 39, pp. 1153–1182, 2010. DOI: 10.1039/b820557b.

[22] J. Daviaud, D. Fournet, C. Ballongue, G. P. Guillem, A. Leblanc, C. Casellas, and B. Pau, "Reliability and feasibility of pregnancy home-use tests: Laboratory validation and diagnostic evaluation by 638 volunteers", *Clinical Chemistry*, vol. 39, no. 1, pp. 53–59, 1993.

[23] D. J. Litman, R. H. Lee, H. J. Jeong, H. K. Tom, S. Stiso, N. C. Siztzo, and E. F. Ullman, "An Internally Referenced Test Strip Immunoassay for Morphine", *Clinical Chemistry*, vol. 29, no. 6, pp. 1598–1603, 1983.

[24] A. H. B. Wu, "Recent advances in point-of-care diagnostics for cardiac markerscare diagnostics for cardiac markers", *The Journal of the International Federation of Clinical Chemistry and Laboratory Medicine*, vol. 25, no. 2, pp. 170–177, 2014.

[25] M. P. Hudson, R. H. Christenson, L. K. Newby, A. L. Kaplan, and E. M. Ohman, "Cardiac markers: point of care testing", *Clinica Chimica Acta*, vol. 284, pp. 223–237, 1999. DOI: 10.1039/b403341h.

[26] US National Library of Medicine, *Blood Glucose Self-Monitoring*, 2015. [Online]. Available: https://meshb.nlm.nih.gov/record/ui?ui=D015190 (visited on 10/23/2018).

[27] PregnancyStore, *Pregnancy Midstream Tests Instruction - www.early-pregnancy-tests.com*, 2018. [Online]. Available: https://www.early-pregnancy-tests.com/inpregmidtes (visited on 10/23/2018).

[28] B. Yılmaz and F. Yılmaz, "Chapter 8. Lab-on-a-Chip Technology and Its Applications", in *OMICS TECHNOLOGIES AND BIO-ENGINEERING*, Ankara: Academic Press, 2017, ch. 8, pp. 145–153. DOI: 10.1016/B978-0-12-804659-3.00008-7.

[29] L. Spielman and S. L. Goren, "Improving resolution in coulter counting by hydrodynamic focusing", *Journal of Colloid And Interface Science*, vol. 26, pp. 175–182, 1968. DOI: 10.1016/0021-9797(68)90310-X.

[30] G. Valet, "Past and present concepts in flow cytometry: A European perspective", *Journal of Biological Regulators and Homeostatic Agents*, vol. 17, no. 3, pp. 213–222, 2003.

[31] M. Yamada and M. Seki, "Microfluidic particle sorter employing flow splitting and recombining", *Analytical Chemistry*, vol. 78, no. 4, pp. 1357–1362, 2006. DOI: 10.1021/ac0520083.

[32] H. Cho, H. Kim, J. Kang, and T. Kim, "Capillary passive valve in microfluidic systems", in *Technical proceedings of the NSTI nanotechnology conference and trade show—NSTI Nanotech 2004*, vol. 1, Boston, Massachussets, 2004, pp. 263–266.

[33] P. Vulto, S. Podszun, P. Meyer, C. Hermann, A. Manz, and G. a. Urban, "Phaseguides: a paradigm shift in microfluidic priming and emptying.", *Lab on a chip*, vol. 11, no. 9, pp. 1596–1602, 2011. DOI: 10.1039/c0lc00643b.

[34] A. Van Reenen, A. M. De Jong, J. M. Den Toonder, and M. W. Prins, "Integrated lab-on-chip biosensing systems based on magnetic particle actuation-a comprehensive review", *Lab on a Chip*, vol. 14, pp. 1966–1986, 2014. DOI: 10.1039/c3lc51454d.

[35] M. A. Gijs, F. Lacharme, and U. Lehmann, "Microfluidic applications of magnetic particles for biological analysis and catalysis", *Chemical Reviews*, vol. 110, pp. 1518–1563, 2010. DOI: 10.1021/cr9001929.

[36] D. Horák, M. Babič, H. Macková, and M. J. Beneš, "Preparation and properties of magnetic nano- and microsized particles for biological and environmental separations", *Journal of Separation Science*, vol. 30, pp. 1751–1772, 2007. DOI: 10.1002/jssc.200700088.

[37] R. Raiteri, M. Grattarola, H. J. Butt, and P. Sklådal, "Micromechanical cantilever-based biosensors", *Sensors and Actuators, B: Chemical*, vol. 79, no. 2-3, pp. 115–116, 2001. DOI: 10.1016/S0925-4005(01)00856-5.

[38] J. Wang, "Electrochemical biosensors: Towards point-of-care cancer diagnostics", *Biosensors and Bioelectronics*, vol. 21, no. 10, pp. 1887–1892, 2006. DOI: 10.1016/j.bios.2005.10.027.

[39] K. B. Nuriman, J. Huskens, and W. Verboom, "Optical sensing systems for microfluidic devices: A review", *Analytica Chimica Acta*, vol. 601, pp. 141–155, 2007. DOI: 10.1016/j.aca.2007.08.046.

[40] N. M. M. Pires, T. Dong, U. Hanke, and N. Hoivik, "Recent Developments in Optical Detection Technologies in Lab-on-a-Chip Devices for Biosensing Applications", *Sensors*, vol. 14, pp. 15 458–15 479, 2014.

[41] S. Mehrabani, A. J. Maker, and A. M. Armani, "Hybrid integrated label-free chemical and biological sensors", *Sensors (Switzerland)*, vol. 14, pp. 5890–5928, 2014. DOI: 10.3390/s140405890.

[42] D. M. Vykoukal, G. P. Stone, P. R. Gascoyne, E. U. Alt, and J. Vykoukal, "Quantitative detection of bioassays with a low-cost image-sensor array for integrated microsystems", *Angewandte Chemie - International Edition*, vol. 121, pp. 7785–7790, 2009. DOI: 10.1002/anie.200901814.

[43] S. Wang, X. Zhao, I. Khimji, R. Akbas, W. Qiu, D. Edwards, D. W. Cramer, B. Ye, and U. Demirci, "Integration of cell phone imaging with microchip ELISA to detect ovarian cancer HE4 biomarker in urine at the point-of-care", *Lab on a Chip*, vol. 11, pp. 3411–3418, 2011. DOI: 10.1039/c1lc20479c.

[44] J. C. Jokerst, J. A. Adkins, B. Bisha, M. M. Mentele, L. D. Goodridge, and C. S. Henry, "Development of a paper-based analytical device for colorimetric detection of select foodborne pathogens", *Analytical Chemistry*, vol. 84, pp. 2900–2907, 2012. DOI: 10.1021/ac203466y.

[45] J. B. Lee, J. Hong, D. K. Bonner, Z. Poon, and P. T. Hammond, "Self-assembled RNA interference microsponges for efficient siRNA delivery", *Nature Materials*, vol. 11, pp. 316–322, 2012. DOI: 10.1038/nmat3253.

[46] N. Yildirim, F. Long, C. Gao, M. He, H. C. Shi, and A. Z. Gu, "Aptamer-based optical biosensor for rapid and sensitive detection of estradiol in water samples", *Environmental Science and Technology*, vol. 46, pp. 3288–3294, 2012. DOI: 10.1021/es203624w.

[47] E. Ouellet, C. Lausted, T. Lin, C. W. T. Yang, L. Hood, and E. T. Lagally, "Parallel microfluidic surface plasmon resonance imaging arrays", *Lab on a Chip*, vol. 10, pp. 581–588, 2010. DOI: 10.1039/b920589f.

[48] A. M. Foudeh, J. T. Daoud, S. P. Faucher, T. Veres, and M. Tabrizian, "Sub-femtomole detection of 16s rRNA from Legionella pneumophila using surface plasmon resonance imaging", *Biosensors and Bioelectronics*, vol. 52, pp. 129–135, 2014. DOI: 10.1016/j.bios.2013.08.032.

[49] J. Fock, C. Jonasson, C. Johansson, and M. F. Hansen, "Characterization of fine particles using optomagnetic measurements", *Physical Chemistry Chemical Physics*, vol. 19, no. 13, pp. 8802–8814, 2017. DOI: 10.1039/c6cp08749c.

[50] J. Fock, C. Balceris, R. Costo, L. Zeng, F. Ludwig, and M. F. Hansen, "Field-dependent dynamic responses from dilute magnetic nanoparticle dispersions †", *Nanoscale*, vol. 10, p. 2052, 2018. DOI: 10.1039/c7nr07602a.

[51] M. Donolato, P. Antunes, R. S. Bejhed, T. Zardán, Z. Gómez De La Torre, F. W. Østerberg, M. Strömberg, M. Nilsson, M. Strømme, P. Svedlindh, M. F. Hansen, and P. Vavassori, "Novel Readout Method for Molecular Diagnostic Assays Based on Optical Measurements of Magnetic Nanobead Dynamics", *Analytical Chemistry*, vol. 87, pp. 1622–1629, 2015. DOI: 10.1021/ac503191v.

[52] H. Becker and L. E. Locascio, "Polymer microfluidic devices", *Talanta*, vol. 56, pp. 267–287, 2002. DOI: 10.1016/S0039-9140(01)00594-X.

[53] C. W. Tsao, "Polymer microfluidics: Simple, low-cost fabrication process bridging academic lab research to commercialized production", *Micromachines*, vol. 7, no. 12, pp. 255–266, 2016. DOI: 10.3390/mi7120225.

[54] D. J. Guckenberger, T. E. De Groot, A. M. Wan, D. J. Beebe, and E. W. Young, "Micromilling: A method for ultra-rapid prototyping of plastic microfluidic devices", *Lab on a Chip*, vol. 15, no. 11, pp. 2364–2378, 2015. DOI: 10.1039/c5lc00234f.

[55] R. Suriano, A. Kuznetsov, S. M. Eaton, R. Kiyan, G. Cerullo, R. Osellame, B. N. Chichkov, M. Levi, and S. Turri, "Femtosecond laser ablation of polymeric substrates for the fabrication of microfluidic channels", *Applied Surface Science*, vol. 257, pp. 6243–6250, 2011. DOI: 10.1016/j.apsusc.2011.02.053.

[56] P. Abgrall, L. N. Low, and N. T. Nguyen, "Fabrication of planar nanofluidic channels in a thermoplastic by hot-embossing and thermal bonding", *Lab on a Chip*, vol. 7, pp. 520–522, 2007. DOI: 10.1039/b616134k.

[57] M. Focke, D. Kosse, C. Müller, H. Reinecke, R. Zengerle, and F. Von Stetten, "Lab-on-a-Foil: Microfluidics on thin and flexible films", *Lab on a Chip*, vol. 10, pp. 1365–1386, 2010. DOI: 10.1039/c001195a.

[58] D. A. Mair, E. Geiger, A. P. Pisano, J. M. Fréchet, and F. Svec, "Injection molded microfluidic chips featuring integrated interconnects", *Lab on a Chip*, vol. 6, pp. 1346–1354, 2006. DOI: 10.1039/b605911b.

[59] K. Kistrup, C. E. Poulsen, M. F. Hansen, and A. Wolff, "Ultrasonic welding for fast bonding of self-aligned structures in lab-on-a-chip systems", *Lab on a Chip*, vol. 15, no. 9, pp. 1998–2001, 2015. DOI: 10.1039/C5LC00174A.

[60] C. M. Koellner, K. A. Mensink, and W. E. Highsmith, "Basic Concepts in Human Molecular Genetics", in *Molecular Pathology The Molecular Basis of Human Disease*, William B. Coleman Gregory J. Tsongalis, Ed., Second, Academic Press, 2018, ch. 5, pp. 99–120. DOI: 10.1016/B978-0-12-802761-5.00005-5.

[61] A. J. Atkinson, W. A. Colburn, V. G. DeGruttola, D. L. DeMets, G. J. Downing, D. F. Hoth, J. A. Oates, C. C. Peck, R. T. Schooley, B. A. Spilker, J. Woodcock, and S. L. Zeger, "Biomarkers and surrogate endpoints: Preferred definitions and conceptual framework", *Clinical Pharmacology and Therapeutics*, vol. 69, no. 3, pp. 89–95, 2001. DOI: 10.1067/mcp.2001.113989.

[62] Y. Peng and C. M. Croce, "The role of MicroRNAs in human cancer", *Signal Transduction and Targeted Therapy*, vol. 1, p. 15 004, 2016.

[63] L. N. Cella, D. Blackstock, M. a. Yates, A. Mulchandani, and W. Chen, "Detection of RNA viruses: current technologies and future perspectives", *Critical reviews in eukaryotic gene expression*, vol. 23, no. 2, pp. 125–137, 2013. DOI: 10.1615/CritRevEukaryotGeneExpr.2013006974.

[64] A. R. Pavankumar, A. Engström, J. Liu, D. Herthnek, and M. Nilsson, "Proficient Detection of Multi-Drug-Resistant Mycobacterium tuberculosis by Padlock Probes and Lateral Flow Nucleic Acid Biosensors", *Analytical Chemistry*, vol. 88, no. 8, pp. 4277–4284, Apr. 2016. DOI: 10.1021/acs.analchem.5b04312.

[65] G. Shipp, "Ultra-sensitive measurement of protein and nucleic acid biomarkers may enable earlier disease detection and more effective therapies", *Drug Discovery World*, vol. 3, no. 2, pp. 35–40, 2007.

[66] R. Howie and J. Thorsen, "An Enzyme-linked Immunosorbent Assay Infectious Bursal Disease Virus", *The Canadian Journal of Comparative Medicine*, vol. 45, pp. 51–55, 1981.

[67] M. P. Richard Mcpherson, *Henry's Clinical Diagnosis and Management by Laboratory Methods*. Elsevier/Saunders, 2011, p. 155. DOI: 10.1002/pi.2967.

[68] J. Mairhofer, K. Roppert, and P. Ertl, "Microfluidic systems for pathogen sensing: A review", *Sensors (Switzerland)*, vol. 9, no. 6, pp. 4804–4823, 2009. DOI: 10.3390/s90604804.

[69] E. M. Burd, "Validation of Laboratory-Developed Molecular Assays for Infectious Diseases", *CLINICAL MICROBIOLOGY REVIEWS*, vol. 23, no. 3, pp. 550–576, 2010. DOI: 10.1128/CMR.00074-09.

[70] J. Wu, R. Kodzius, W. Cao, and W. Wen, "Extraction, amplification and detection of DNA in microfluidic chip-based assays", *Microchimica Acta*, vol. 181, pp. 1611–1631, 2014. DOI: 10.1007/s00604-013-1140-2.

[71] L. Van Heirstraeten, P. Spang, C. Schwind, K. S. Drese, M. Ritzi-Lehnert, B. Nieto, M. Camps, B. Landgraf, F. Guasch, A. H. Corbera, J. Samitier, H. Goossens, S. Malhotra-Kumar, and T. Roeser, "Integrated DNA and RNA extraction and purifi cation on an automated microfl uidic cassette from bacterial and viral pathogens causing community-acquired lower respiratory tract infections.", *Lab Chip*, vol. 14, p. 1519, 2014. DOI: 10.1039/c3lc51339d.

[72] X. Mao, T. J. Huang, and C.-M. Ho, "The Lab-on-a-Chip Approach for Molecular Diagnostics", in *Molecular Diagnostics*, Academic Press, 2010, ch. 3, pp. 21–34.

[73] P. S. Lu, "Early diagnosis of avian influenza", *Science*, vol. 312, no. 5772, p. 337, 2006. DOI: 10.1126/science.1128199.

[74] A. García-Basteiro, A. DiNardo, B. Saavedra, D. Silva, D. Palmero, M. Gegia, G. Migliori, R. Duarte, E. Mambuque, R. Centis, L. Cuevas, S. Izco, and G. Theron, "Point of care diagnostics for tuberculosis", *Pulmonology*, vol. 24, no. 2, pp. 73–85, Mar. 2018. DOI: 10.1016/J.RPPNEN.2017.12.002.

[75] W. Johnson, "The polymerase chain reaction: AN overview and development of diagnostic PCR protocols at the LDCD", Centre for Disease Control, Ottawa, Tech. Rep., 1991, p. 4. [Online]. Available: https://www.ncbi.nlm.nih.gov/pmc/articles/PMC3327995/pdf/idmm02089.pdf.

[76] R. K. Saiki, S. Scharf, F. Faloona, K. B. Mullis, G. T. Horn, H. A. Erlich, and N. Arnheim, "Enzymatic amplification of β-globin genomic sequences and restriction site analysis for diagnosis of sickle cell anemia", *Science*, vol. 230, pp. 1350–1354, 1985. DOI: 10.1126/science.2999980.

[77] G. T. Walker, M. C. Little, J. G. Nadeau, and D. D. Shank, "Isothermal in vitro amplification of DNA by a restriction enzyme/DNA polymerase system (nucleic acid amplification/strand displacement/Mycobacterium tuberculosis)", *Applied Biological Sciences*, vol. 89, pp. 392–396, 1992.

[78] O. Piepenburg, C. H. Williams, D. L. Stemple, and N. A. Armes, "DNA detection using recombination proteins", *PLoS Biology*, vol. 4, no. 7, pp. 1115–1121, 2006. DOI: 10.1371/journal.pbio.0040204.

[79] G. A. S. Minero, C. Nogueira, G. Rizzi, B. Tian, J. Fock, M. Donolato, M. Strömberg, and M. F. Hansen, "Sequence-specific validation of LAMP amplicons in real-time optomagnetic detection of Dengue serotype 2 synthetic DNA ", *Analyst*, vol. 142, p. 3441, 2017. DOI: 10.1039/c7an01023k.

[80] M. M. Ali, F. Li, Z. Zhang, K. Zhang, D. K. Kang, J. A. Ankrum, X. C. Le, and W. Zhao, "Rolling circle amplification: A versatile tool for chemical biology, materials science and medicine", *Chemical Society Reviews*, vol. 43, pp. 3324–3341, 2014. DOI: 10.1039/c3cs60439j.

[81] M. Nilsson, M. Gullberg, F. Dahl, K. Szuhai, and A. K. Raap, "Real-time monitoring of rolling-circle amplification using a modified molecular beacon design.", *Nucleic Acids Research*, vol. 30, no. 14, pp. 1–7, Jul. 2002.

[82] J. Tank, *Rolling circle amplification mechanism.jpg - Wikimedia Commons*, 2017. [Online]. Available: https://commons.wikimedia.org/wiki/File:Rolling%7B%5C_%7Dcircle%7B%5C_%7Damplification%7B%5C_%7Dmechanism.jpg%7B%5C#%7Dmetadata (visited on 10/26/2018).

[83] H. Bruus, *Theoretical microfluidics*. Oxford University Press, 2008, p. 346. DOI: 10.1111/j.1574-6968.2009.01808.x.

[84] J. Gillis, *File:Contact angle.svg - Wikimedia Commons*, 2006. [Online]. Available: https://commons.wikimedia.org/wiki/File:Contact%7B%5C_%7Dangle.svg (visited on 11/06/2018).

[85] J. Berthier, *Microdrops and digital microfluidics.* William Andrew, Norwich, NY, 2008, p. 500. DOI: 10.1016/B978-1-4557-2550-2.00012-2.

[86] T. S. Meiron, A. Marmur, and I. S. Saguy, "Contact angle measurement on rough surfaces", *Journal of Colloid and Interface Science*, vol. 274, pp. 637–644, 2004. DOI: 10.1016/j.jcis.2004.02.036.

[87] B. Sahoo, K. Yoon, J. Seo, and T. Lee, "Chemical and Physical Pathways for Fabricating Flexible Superamphiphobic Surfaces with High Transparency", *Coatings*, vol. 8, no. 2, p. 47, 2018. DOI: 10.3390/coatings8020047.

[88] C. Hansang Cho a, H.-Y. K. B, J. Y. K. C, and Tae Song Kim c, "How the capillary burst microvalve works", *Journal of Colloid and Interface Science*, vol. 306, no. 2, pp. 379–385, 2007. DOI: 10.1016/j.jcis.2006.10.077.

[89] K. Kistrup, C. E. Poulsen, P. F. Østergaard, K. B. Haugshøj, R. Taboryski, A. Wolff, and M. F. Hansen, "Fabrication and modelling of injection moulded all-polymer capillary microvalves for passive microfluidic control", *Journal of Micromechanics and Microengineering*, vol. 24, no. 12, p. 125 007, Dec. 2014. DOI: 10.1088/0960-1317/24/12/125007.

[90] K. Kistrup, "Development of injection moulded, ultrasonically welded immiscible phase filtration devices", PhD thesis, Department of Micro-and Nanotechnology. Technical University of Denmark, 2015.

[91] P. Vulto, G. Medoro, L. Altomare, G. a. Urban, M. Tartagni, R. Guerrieri, and N. Manaresi, "Selective sample recovery of DEP-separated cells and particles by phaseguide-controlled laminar flow", *Journal of Micromechanics and Microengineering*, vol. 16, pp. 1847–1853, 2006. DOI: 10.1088/0960-1317/16/9/013.

[92] F. Garbarino, K. Kistrup, G. Rizzi, and M. F. Hansen, "Burst pressure of phaseguide structures of different heights in all-polymer microfluidic channels", *Journal of Micromechanics and Microengineering*, vol. 27, no. 12, aa97b7, 2017. DOI: 10.1088/1361-6439/aa97b7.

[93] M. Price Ball, *DNA chemical structure.svg - Wikimedia Commons*, 2016. [Online]. Available: https://commons.wikimedia.org/wiki/File:DNA%7B%5C_%7Dchemical%7B%5C_%7Dstructure.svg (visited on 10/02/2018).

[94] B. Alberts, A. Johnson, J. Lewis, M. Raff, K. Roberts, and P. Walter, *Molecular biology of the cell.* Garland Science, 2002, p. 400.

[95] V. Sergerie, *POPULATION D ADN COMPLEXE - ADN génomique ou - copie d ARNm = CDNA - PDF*, 2015. [Online]. Available: https://docplayer.fr/3787763-Population-d-adn-complexe-adn-genomique-ou-copie-d-arnm-cdna.html (visited on 10/02/2018).

[96] G. Felsenfeld and H. T. Miles, *THE PHYSICAL AND CHEMICAL PROPERTIES 648 OF NUCLEIC ACIDS1,lI.* Annual Review of Biochemistry, 1967, p. 36.

[97] S. C. Edberg, "Principles of nucleic acid hybridization and comparison with monoclonal antibody technology for the diagnosis of infectious diseases.", *The Yale Journal of Biology and Medicine*, vol. 58, no. 5, pp. 425–42, 1985.

[98] T. E. Ouldridge, P. Šulc, F. Romano, J. P. Doye, and A. A. Louis, "DNA hybridization kinetics: Zippering, internal displacement and sequence dependence", *Nucleic Acids Research*, vol. 41, no. 19, pp. 8886–8895, 2013. DOI: 10.1093/nar/gkt687.

[99] H. Clausen-Schaumann, M. Rief, C. Tolksdorf, and H. E. Gaub, "Mechanical Stability of Single DNA Molecules", *Biophysical Journal*, vol. 78, pp. 1997–2000, 2000.

[100] M. M. Senior, R. A. Jones, and K. J. Breslauer, "Influence of loop residues on the relative stabilities of DNA hairpin structures", *Proceedings of the National Academy of Sciences of the United States of America*, vol. 85, no. 17, pp. 6242–6246, 1988. DOI: 10.1073/pnas.85.17.6242.

[101] K. B. Cederquist and C. D. Keating, "Hybridization efficiency of molecular beacons bound to gold nanowires: Effect of surface coverage and target length", *Langmuir*, vol. 26, no. 23, pp. 18 273–18 280, 2010. DOI: 10.1021/la1031703.

[102] J. H. Reif and T. H. LaBean, "Engineering Natural Computation by Autonomous DNA-Based Biomolecular Devices", in *Handbook of Natural Computing*, Berlin, Heidelberg: Springer Berlin Heidelberg, 2012, pp. 1319–1353. DOI: 10.1007/978-3-540-92910-9_39.

[103] Y. Gao, L. K. Wolf, and R. M. Georgiadis, "Secondary structure effects on DNA hybridization kinetics: a solution versus surface comparison", *Nucleic Acids Research*, vol. 34, no. 11, pp. 3370–3377, 2006. DOI: 10.1093/nar/gkl422.

[104] G. A. S. Minero, P. F. Wagler, A. A. Oughli, and J. S. Mccaskill, "Electronic pH switching of DNA triplex reactions †", *RSC Advances*, vol. 5, p. 27 313, 2015. DOI: 10.1039/c5ra02628h.

[105] M. Nilsson, H. Malmgren, M. Samiotaki, M. Kwiatkowski, B. P. Chowdhary, and U. Landegren, "Padlock probes: Circularizing oligonucleotides for localized DNA detection", *Science*, vol. 265, no. 5181, pp. 2085–2088, 1994. DOI: 10.1126/science.7522346.

[106] G. Lohman, *Substrate specificity and mismatch discrimination in DNA ligases — NEB*, 2017. [Online]. Available: https://international.neb.com/tools-and-resources/feature-articles/substrate-specificity-and-mismatch--discrimination-in-dna-ligases (visited on 09/19/2018).

[107] IDT Integrated DNA Technologies, *IDT Oligo Analyzer*, 2017. [Online]. Available: https://eu.idtdna.com/site/account/login?returnurl=/calc/analyzer (visited on 10/02/2018).

[108] D. Snakenborg, H. Klank, and J. P. Kutter, "Microstructure fabrication with a CO2 laser system", *Journal of Micromechanics and Microengineering*, vol. 14, no. 2, pp. 182–189, Feb. 2004. DOI: 10.1088/0960-1317/14/2/003.

[109] F. E. Gabriel Moreira, W. Karlos, T. Coltro, and C. D. Garcia, "Fast and Versatile Fabrication of PMMA Microchip Electrophoretic Devices by Laser Engraving", *Electrophoresis*, vol. 35, no. 16, pp. 2325–2332, 2014. DOI: 10.1002/elps.201470140.

[110] D. A. Mair, E. Geiger, A. P. Pisano, J. M. Fréchet, and F. Svec, "Injection molded microfluidic chips featuring integrated interconnects", *Lab on a Chip*, vol. 6, no. 10, pp. 1346–1354, 2006. DOI: 10.1039/b605911b.

[111] H. A. Maddah, "Polypropylene as a Promising Plastic: A Review", *American Journal of Polymer Science*, vol. 6, no. 1, pp. 1–11, 2016. DOI: 10.5923/j.ajps.20160601.01.

[112] C. E. Poulsen, "All-polymer microfluidic systems for droplet based sample analysis Bringing droplet technologies to life: Bridging the gap between academia and industry", PhD thesis, Department of Micro-and Nanotechnology. Technical University of Denmark, 2015.

[113] S. Ebnesajjad and S. Ebnesajjad, "PART II 7 Injection Molding", in *Melt Processible Fluoroplastics*, William Andrew Publishing, 2003, pp. 151–193. DOI: 10.1016/B978-1-884207-96-9.50010-2.

[114] XCENTRIC Mold and Engineering, *Injection Molding Service - Custom Molds & Plastic Parts - U.S. Company*, 2018. [Online]. Available: https://www.xcentricmold.com/injection-molding-process/ (visited on 10/04/2018).

[115] S. Li, G. Zhao, and J. Wang, "A method to improve dimensional accuracy and mechanical properties of injection molded polypropylene parts", *Journal of Polymer Engineering*, vol. 37, no. 4, pp. 334–340, 2017. DOI: 10.1515/polyeng-2015-0526.

[116] K. Ø. Andresen, M. Hansen, M. Matschuk, S. T. Jepsen, H. S. Sørensen, P. Utko, D. Selmeczi, T. S. Hansen, N. B. Larsen, N. Rozlosnik, and R. Taboryski, "Injection molded chips with integrated conducting polymer electrodes for electroporation of cells", *Journal of Micromechanics and Microengineering*, vol. 20, no. 5, p. 055 010, May 2010. DOI: 10.1088/0960-1317/20/5/055010.

[117] D. McNally, *How to Injection Mold Cyclic Olefin Copolymers : Plastics Technology*, 2010. [Online]. Available: https://www.ptonline.com/articles/how-to-injection-mold-cyclic-olefin-copolymers (visited on 09/28/2018).

[118] M. J. Troughton, *Handbook of plastics joining : a practical guide*. William Andrew, 2008, p. 590.

[119] S. J. Trietsch, W. Rauwé, G. a. Urban, A. Manz, T. Hankemeier, H. J. V. D. Linden, and P. Vulto, "The Phaseguide Paradigm : Priming and Emptying of Monolithic Polymer Chips", in *The 15th International Conference on Miniaturized Systems for Chemistry and Life Sciences*, 2011, pp. 942–944.

[120] E. Yildirim, S. J. Trietsch, J. Joore, A. van den Berg, T. Hankemeier, and P. Vulto, "Phaseguides as tunable passive microvalves for liquid routing in complex microfluidic networks.", *Lab on a Chip*, vol. 14, pp. 3334–40, 2014. DOI: 10.1039/c4lc00261j.

[121] C. E. Poulsen, K. Kistrup, N. K. Andersen, R. Taboryski, M. F. Hansen, and A. Wolff, "Laser ablated micropillar energy directors for ultrasonic welding of microfluidic systems", *Journal of Micromechanics and Microengineering*, vol. 26, no. 6, 2016. DOI: 10.1088/0960-1317/26/6/067001.

[122] F. ; Garbarino, G. A. S. Minero, J. ; Fock, G. ; Rizzi, F. ; Neumann, N. Madaboosi, and M. F. Hansen, "Automated rolling circle amplification and optomagnetic product detection in an injection molded all-polymer chip-optimization of amplification temperature", in *MNE — 2017 – 43rd International Conference on Micro and Nano Enigneering*, APA, 2017, p. 1.

[123] O. Strohmeier, A. Emperle, G. Roth, D. Mark, R. Zengerle, and F. Von Stetten, "Centrifugal gas-phase transition magnetophoresis (GTM)-a generic method for automation of magnetic bead based assays on the centrifugal microfluidic platform and application to DNA purification", *Lab on a Chip*, vol. 13, pp. 146–155, 2013. DOI: 10.1039/c2lc40866j.

[124] F. Garbarino, G. Khose Antonio, and M. Fougt Hansen, "On-chip optomagnetic detection and discrimination of single base mutation in Mycobacterium tuberculosis", in *Abstract from 3rd Functional DNA Nanotechnology Workshop, Rome, Italy.*, Rome, 2018, p. 1.

Appendix A

Conference Proceeding

BURST PRESSURE OF ALL-POLYMER PHASEGUIDE STRUCTURES OF DIFFERENT HEIGHTS

F. Garbarino*, K. Kistrup, G. Rizzi and M. F. Hansen*
DTU Nanotech, Technical University of Denmark, Denmark

ABSTRACT
Microfluidic platforms rely on the ability to guide and spread liquids in channel and chamber structures. Phaseguides – ridges protruding from the channel bottom or top – have proven successful to achieve controlled filling and can also be used for passive valving. We present an experimental investigation of the burst/overflow pressure of water in 90° phaseguide in an injection moulded polymer chip as function of the phaseguide height, *h*. Phaseguide structures without and with branches of angles α = 45°, 60° and 75° were studied. The knowledge obtained in this study provides a set of systematic experimental data to compare with simulations/theory.

KEYWORDS: phaseguide, injection moulding, ultrasonic welding, hydrostatic burst pressure

INTRODUCTION
Passive valves have attracted significant interest in the last years [1], mainly for their ability to support controlled liquid handling in Lab-on-a-Chip systems [2]. A key issue in microfluidic systems is the ability to fill channels and chambers in a controllable manner without trapping air bubbles and also to use structures for passive valving. Phaseguides, which are protrusions or ridges extending from the channel bottom or top, have been demonstrated to solve many of these challenges [3,4]. The burst pressure of a phaseguide structure is determined by the phaseguide geometry and its angle to the channel sidewalls. Furthermore, it can be modified by inclusion of kinks or branches [2,4]. However, the dependence of the burst pressure of a phase guide structure on its height has not been studied systematically in the literature. Here, we present an experimental analysis of the burst pressure of phaseguides structures in injection moulded polymer chips without or with a centre branch as a function of their height, *h*.

EXPERIMENTAL
The polymer chip consisted of two parts: a main part of injection moulded cyclic olefin-copolymer (COC) polymer (TOPAS grade 5013L-10) and a 0.254 mm COC sheet (TOPAS grade 5013S-04) ultrasonically welded to the main part [5].

The channel layout featured four 1 mm wide and three 3 mm wide channels (Fig. 1b and 1c) of height H = 200 μm with a sequence of phaseguides of heights increasing from h = 20 μm to 100 μm (Fig. 1a, Table 1). In six of the seven channels, the phaseguides were designed as 90° structures with branches, V-shaped grooves also called supporting phaseguides, starting from the middle of the phaseguide at angles α = 45°, 60° and 75° (see Fig. 1a). The 1 mm wide channel also included phaseguide structures without a branch.

Hydrostatic burst pressures were measured for Milli-Q water using the setup shown in Figure 2. The setup consisted of a Thorlabs LTS150 motorized stage (Thorlabs, Newton, NJ, USA) fitted with a peroxide cured silicon tube (OD=10mm, ID=6mm) connected through the other end to the chip. Measurements were done by filling the tube with Milli-Q water and raising one end of the tube to a height Δz above chip level. Experiments were performed in triplicate by first adjusting Δz to zero. Then, the tubing was raised at 1 mm/s while carefully monitoring the position of the liquid meniscus in the chip. The pressure at the meniscus was

$$p = \rho g \Delta z + (2\gamma / H)\cos\theta \qquad (1)$$

where ρ = 998 kg/m^3 is the density of the liquid, g = 9.82m/s^2 is the gravitational acceleration. In the second term accounting for the capillary filling pressure of the channel leading to the phaseguide, γ is the liquid-air surface tension and θ is the contact angle of the liquid with the channel surface.

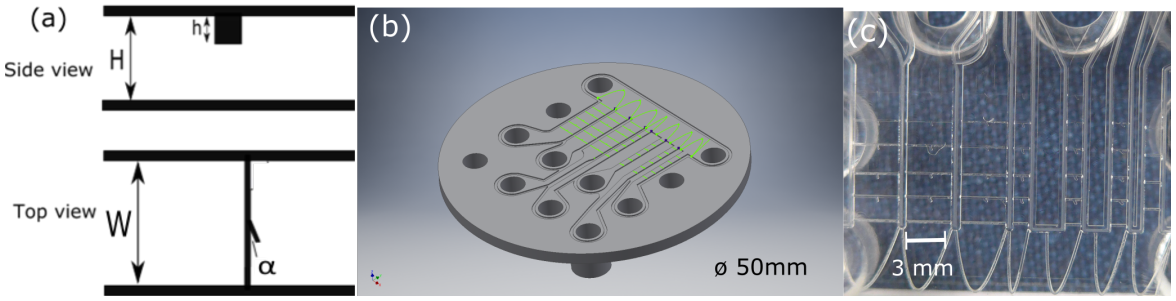

Figure 1: (a) Side and top views of phaseguide structure. (b) layout of injection moulded chip with integrated Luer connectors. (c) photograph of the fabricated chip prior to ultrasonic welding showing the parallel layout of the channels containing the phaseguides with branches (first six channels from left) and one without branches (last channel on the right).

Table 1. Geometrical parameters of channel and phaseguide structures. Values are also given for the contact angle and surface tension measured for water.

Parameter	Values
Channel height (*H*)	200 µm
Phaseguide height (*h*)	20,40,60,80,100 µm
Channel width (*W*)	1, 3 mm
Phaseguide-wall angle	90°
Branch angle α	45°, 60°, 75°
Contact angle θ	96°
Surface tension γ	72 mN/m

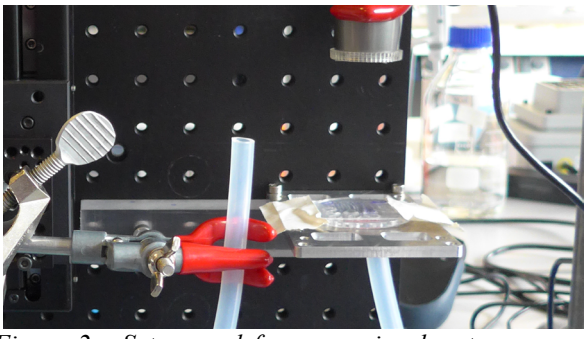

Figure 2: Setup used for measuring burst pressures. Water is filled in the tube which is then lifted at constant velocity (1 mm/s) using the motorized stage until the meniscus is observed to burst through a phaseguide.

RESULTS and DISCUSSION

Figure 3a shows the results for 1 mm wide channels. The presented burst pressure for a phaseguide structure, p_{burst}, is the values of p given by Eq. (1) where the liquid meniscus advanced past the structure. The results can clearly be divided into two groups, α = 45°/60° and α = 75°/no branches. The first group had a lower and better-defined values of p_{burst} compared to the other group, having smaller error bars. The results for W = 3 mm in Fig. 3b show a similar but less pronounced grouping, but the phaseguides with α=75° still show slightly higher values of p_{burst}, although the tendency is not as pronounced as for W = 1 mm.

The data obtained for W = 1 mm (Fig. 3a) and W = 3 mm (Fig. 3b) are identical within the experimental uncertainty. A comparison of the two graphs shows that differences are negligible: at the lowest phaseguide (h = 20 µm) the burst pressures in both channels are around 100 Pa, at the highest phaseguide (h = 100µm) the burst pressures for the two channels differ only slightly being around 375 Pa for W = 1 mm and 400 Pa for W = 3 mm.

In both cases it is also important to notice the approximately linear dependence of p_{burst} on h/H and that no significant dependence on α can be observed except for the above mentioned grouping. The water was observed to always overflow at the weakest point, i.e., at the lowest angle between the supporting phaseguide and the phaseguide. This is in line with previous work showing that the branch defines a point of controlled overflow [2,3].

In the present study we observed that the phaseguide without branches, which are straight 90° phaseguides, had almost the same burst pressure as those with branches. This differs from the predictions of Vulto *et al.* [3] that straight 90° phaseguides should be significantly more stable than those with a branch. It must be underlined though, that they only considered phaseguides that were about 30 µm wide and high, made using lithography techniques. The differennce in fabrication techniques and materials employed by Vulto *et al.* and in the present study may influence the ability to observe this effect.

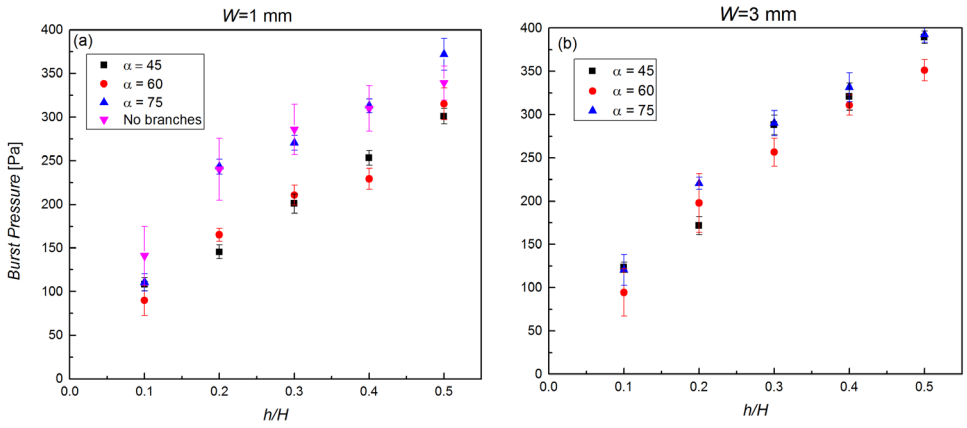

Figure 3: Pressures, p_{burst}, where water burst through a phaseguide structure as function of its relative height h/H for phaseguides with branches of the indicated angles. Results are shown for (a) W=1 mm and (b) W= 3 mm. Error bars in both graphs refer to the standard error of the mean for three sets of repeated experiments on three different chips (n=9).

Another important observation relates to the similar results obtained for the two investigated channel widths. Previous work [4] suggests an analytical model in which the pinning behaviour is dominated by the horizontal geometry of the channel/phaseguide and mainly by the angle of the phaseguide to the channel wall. Consistent with this, we observe almost identical burst pressures for the two channel widths. There is a continued need for researchers to reconsider limitations in the present models and develop new models that include the influence of a wider variety of parameter, e.g., wetting properties of the liquid, the physical/chemical properties of the materials, the complete geometry of the phaseguide, the impact of branches and other supporting structures, and the fabrication technique.

CONCLUSION

We investigated the applied pressures required to advance the meniscus of Milli-Q water past phaseguides of varying heights fabricated in injection moulded microfluidic channels of widths of 1 mm and 3 mm. Moreover, we investigated the effect of including a branch to the phaseguide. The fabrication via micro milling and injection moulding allowed for the creation of an all-polymer chip that easily combined features of different heights. The data presented in this study showed that the height of a phaseguide could be used to tune the burst pressure in a reproducible and controllable manner with well-defined points of overflow. In our further work, we will use such phaseguides as key ingredients to form multi-chamber microfluidic systems for health diagnostics.

ACKNOWLEDGEMENTS

This work was supported by DFF projects 4005-00116 and 4184-00121. Thanks to Carl Esben Poulsen for help with the fabrication of energy directors and for help on ultrasonic welding.

REFERENCES

[1] Vulto *et al*, Proc 15th International Conference on Solid-State Sensors, Actuators and Microsystems, 2009, Denver, Colorado, USA, pp. 409-412.
[2] S. J. Trietsch et al., Proc 15th International Conference on miniaturized systems for chemistry and life sciences, 2011, Seattle Washington, USA, pp. 942-944
[3] P. Vulto et al., Lab Chip, **11**, 1561 (2011).
[4] E. Yildirim et al., Lab Chip **14**, 3334 (2014).
[5] K. Kistrup et al, Lab Chip, **15**, 1998 (2015)

CONTACT

*E-mail: (F.G.) Franga@nanotech.dtu.dk, (M.F.H.) Mikkel.hansen@nanotech.dtu.dk

Appendix B

Paper I

IOP Publishing Journal of Micromechanics and Microengineering

J. Micromech. Microeng. **27** (2017) 125015 (9pp) https://doi.org/10.1088/1361-6439/aa97b7

Burst pressure of phaseguide structures of different heights in all-polymer microfluidic channels

Francesca Garbarino, Kasper Kistrup, Giovanni Rizzi and Mikkel Fougt Hansen

Department of Micro- and Nanotechnology, DTU Nanotech, Technical University of Denmark, Building 345B, DK-2800 Kongens Lyngby, Denmark

E-mail: Mikkel.hansen@nanotech.dtu.dk

Received 9 August 2017, revised 25 October 2017
Accepted for publication 2 November 2017
Published 16 November 2017

Abstract

We present an experimental investigation of the burst/overflow pressure of water and a representative surfactant-containing buffer in microfluidic channels with phaseguide structures oriented at an angle of 90° to the channel length as a function of their height, h. The all-polymer chips were fabricated by injection moulding and sealed by ultrasonic welding. Channels with a height of 200 μm and widths of 1 mm or 3 mm were investigated for five values of h between 8 μm and 82 μm. Phaseguide structures without branches and with branches at angles $\alpha = 45°$, 60° and 75° were studied. All phaseguide structures were found able to pin both liquids and the burst pressure was found to increase approximately linearly with the height of the phaseguide from about 100–350 Pa for water and from about 25–200 Pa for the buffer. The burst pressure was found not to depend on the channel width and it was only weakly influenced by the presence of a branch on the phaseguide. For phaseguides with a branch, the liquid was always found to burst at the branch location. The measured burst pressures were compared to those estimated using a simple theory. The knowledge obtained in this study enables simple tuning of liquid spreading and overflow in microfluidic channels by use of phaseguide structures with different heights and it also provides a set of systematic experimental data to be compared with simulations/theory.

Keywords: all-polymer chip, phaseguide, injection moulding, ultrasonic welding, hydrostatic burst pressure, topas

(Some figures may appear in colour only in the online journal)

1. Introduction

Portable microfluidic devices have attracted significant interest for point-of-care (POC) testing during the last two decades due to their potential of producing fast results at reduced cost. Traditionally, such devices were developed using rapid prototyping techniques, such as casting of polydimethylsiloxane (PDMS) and/or cleanroom micromachining; however, neither technique is well suited for low-cost mass-production (Becker 2010). Within the last few years, focus has changed to develop devices using techniques and materials that can be directly transferred to an industrial mass-production setting (Mukhopadhyay 2009).

Recently, we demonstrated rapid shim prototyping and injection moulding of polymer lab-on-a-chip systems that were sealed using ultrasonic welding (Kistrup *et al* 2015, Poulsen *et al* 2016). In these, the inverse microchannel structures were defined in the shims using micromilling and energy director structures for ultrasonic welding were defined using laser machining. Both injection moulding and ultrasonic welding are widely used techniques for low-cost industrial mass-production and joining of polymer components. In our

setting, the injection moulding of a single chip took about 1 min and ultrasonic welding could be completed (including mounting) in about 30 s per chip. The combination of a shim made by rapid prototyping with injection moulding and ultrasonic welding enabled us to go from design to a 'bag of sealed chips' in as little as 1–2 d (Kistrup *et al* 2015).

The advantage but also the curse of lab-on-a-chip systems is the high surface-to-volume ratio that enables fast reactions but also has as a consequence that capillary forces dominate over inertial forces. A well-known issue in lab-on-a-chip systems is the occurrence and trapping of air bubbles at undesired locations. Another challenge in lab-on-a-chip systems has been the integration of valves and pumps to enable multi-chamber microfluidic operations. The advent of phaseguide structures by Vulto *et al* presented an attractive approach to the controlled wetting and filling of microfluidic structures to solve these challenges (Vulto *et al* 2006). The phaseguide structures are ridges extending from the channel bottom or top which pin the liquid meniscus until the pressure exceeds the burst pressure defined by the geometry of the structure and the wetting properties of the liquid. The burst pressure could be tuned by varying the angle between the phaseguide ridge and the sidewall of the channel or by introducing kinks or branches in the phaseguide structure (Trietsch *et al* 2011,Yildirim *et al* 2014). By use of phaseguide structures, passive liquid valving and the controlled and bubble-free liquid filling of microfluidic chambers of arbitrary shape was demonstrated (Vulto *et al* 2011). Trietsch *et al* showed controlled filling and emptying of a non-hydrophilic monolithic chip with dead angle sections by use of supporting phaseguides (Trietsch *et al* 2011). Vulto demonstrated the spatially and sequentially controlled phaseguide overflow using a passive valve approach (Vulto *et al* 2011). Yildirim presented liquid routing using a hierarchy of phaseguides with different burst pressures (Yildirim *et al* 2014). Moreover, Phurimsak *et al* demonstrated the use of phaseguides to layer different liquids in a single chamber to facilitate an enzyme-linked immunosorbent assay (Phurimsak *et al* 2014). Finally, Gottheil *et al* demonstrated the use of phaseguide structures and capillary valves in an injection moulded polymer chip to form a four-chamber microfluidic device for a sandwich immunoassay (Gottheil *et al* 2014).

The chips in all of the above studies except for Gottheil *et al* (2014) were fabricated using photolithography, which leads to highly well-defined phaseguides of the same height to keep the fabrication simple. When structures are defined by milling and fabricated by injection moulding, it is easy to modify the height of the structures while maintaining a constant geometry; however this has not yet been studied systematically in the literature. Here, we present a systematic experimental analysis of the burst pressure of phaseguide structures in polymer chips, fabricated by injection moulding using a micromilled shim, as function of their height, h, and we study the dependence on the channel width and the effect of including branches to the phaseguides.

2. Theory

Burst pressure measurements are used to determine when the liquid will overflow the phaseguides and propagate through the chip. These pressures can be estimated analytically for simple geometries. Below, we briefly consider the dominant forces in microfluidic systems. The Young–Laplace equation, equation (1), expresses the pressure difference over an interface between two phases (here liquid–gas) with surface tension γ characterized by radii of curvature R_1 and R_2 as

$$\Delta p = \gamma \left(\frac{1}{R_1} + \frac{1}{R_2} \right). \tag{1}$$

Note, that with this definition, the pressure is higher in the medium in which the centers of the radii of curvature are placed (the convex side of the interface). For a channel with a rectangular cross-section of width W and height H and which is formed by a structured moulded part sealed by a flat foil, equation (1) can be written in terms of the contact angles θ_m and θ_f of the liquid to the moulded part (m) and the foil (f), respectively, as

$$\Delta p_{cap}(H) = \gamma \left(\frac{2\cos\theta_m}{W} + \frac{\cos\theta_m + \cos\theta_f}{H} \right) \approx \gamma \frac{\cos\theta_m + \cos\theta_f}{H}, \tag{2}$$

where the latter expression is valid for $W \gg H$. Note, that Δp_{cap} in equation (2) denotes the *increase* in pressure upon passing through the liquid–gas interface, i.e. $\Delta p_{cap} > 0$ drives capillary filling of the channel whereas $\Delta p_{cap} < 0$ does not. Consequently, depending on whether $\cos\theta_m + \cos\theta_f > 0$ (wetting) or <0 (non-wetting), the capillary pressure in equation (2) may assist or hinder the filling of the microfluidic channel. The phaseguide of height h first defines a contraction of the channel and subsequently an expansion (figure 1). Above a wide phaseguide, a non-wetting liquid will experience a higher capillary pressure, $\Delta p_{cap}(H-h)$, which may prevent the liquid from reaching the back edge of the phaseguide. When the liquid–gas interface has passed the phaseguide, the liquid will again experience the capillary pressure $\Delta p_{cap}(H)$. In the experimental studies below, the interface was observed to pin at the back edge of the phaseguide in all experiments.

When the liquid–gas interface has proceeded to the back edge of the phaseguide, it may be pinned. At this edge, the phaseguide defines an abrupt expansion of the channel with an angle β to horizontal (side-view in figure 1). Following the arguments of Cho *et al* (2007) the interface contact angle to the expanded region, ϕ, at the expansion is smaller than the advancing contact angle, θ_m, of the expanded region and the interface is pinned if $\phi \leqslant \theta_m + \beta$. For the structure in figure 1, the pressure that we need to apply to overcome the pinning at the edge of the expansion is

$$p_{pin} = -\gamma \left(\frac{2\cos\theta_m}{W} + \frac{\cos\left(\min\left\{\theta_m + \beta, 180^\circ\right\}\right) + \cos\theta_f}{H-h} \right). \tag{3}$$

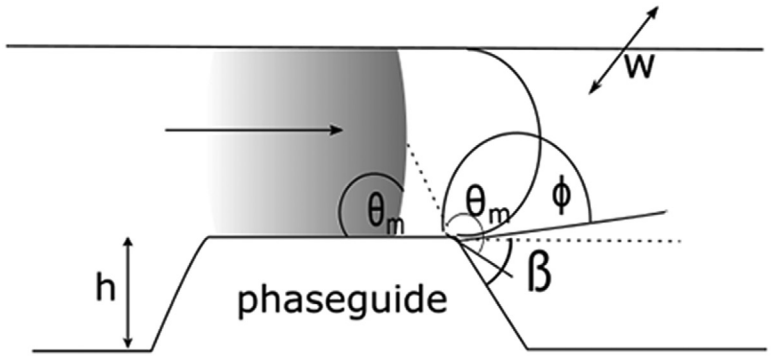

Figure 1. Side-view sketch of channel cross-section with a liquid passing over a phaseguide (left to right), where pinning is achieved through a sudden expansion of the geometry in the moulded part (top in figure). The parameters θ_m, α, and ϕ describe the liquid contact angle to the moulded part, the expansion angle, and the effective contact angle, respectively. W and h denote the width of the channel and height of the phaseguide.

Equation (3) determines the calculated burst pressure of the structure. A value of $p_{pin} > 0$ indicates that the liquid–gas interface is pinned at the edge (pinning condition), whereas $p_{pin} < 0$ indicates that the liquid–gas interface will pass the edge without being pinned. In the devices investigated in the present work, the nominal expansion angle was $\beta = 75°$. For $W \gg H - h$, it can be observed by inspection of equation (3) for $\theta_m < 105°$ that a pinning requirement is that $\cos(\theta_m + 75°) + \cos\theta_f < 0$. If this is no longer fulfilled, the sidewall contribution will reduce p_{pin} for $\theta_m < 90°$ and increase p_{pin} for $\theta_m > 90°$. The full equation (3) was used in all calculations below.

3. Methods

3.1. Chip fabrication and design

The all-polymer chip consisted of two parts: a main part in cyclic olefin-copolymer (COC) polymer (TOPAS grade 5013L-10), fabricated by injection moulding and a 0.254 mm COC foil (TOPAS grade 5013S-04) both polymers from TOPAS Advanced Polymers GmbH, Frankfurt-Höchst, Germany. Injection moulding was conducted on an Engel Victory 80/45 Tech injection moulder (ENGEL, Schwertberg, Austria), featuring the negative counter-part of the channel layout on one side of the injection moulding tool and a luer-layout counter-part with through-holes on the other (Andresen *et al* 2010). The machine was set to run an isothermal program with injection and mould temperatures of 270 °C and 120 °C, respectively. During injection moulding, a pressure of 1766 bar was applied for 5 s and finally the chip was cooled for 30 s.

The mould insert/negative counterpart, designed with Autocad Inventor 2016, was micro-milled with a three-axis Mini-Mill/3 mill frame fitted with a Nakanishi E3000C spindle and controller (MinitechMachinery, Norcross, Georgia) on a 2 mm thick sheet of aluminum alloy 2017. Phaseguides were fabricated in a final milling step using an engraving tool (DIXI polytool 7009, art 976370, 30°, $D1 = 50$ μm). This tool is conical with an angle of each of its sides to vertical of 15° and it has a flat tip with a diameter of 50 μm. The last step before injection moulding was the creation of energy directors, special protrusions that allow localizing the vibrations of the sonotrode of the ultrasonic welder to the areas were welding is required, via the use of a microSTRUCT vario picosecond laser (3D-Micromac AG, Chemnitz, Germany) as described by Poulsen *et al* (2016). To complete the chip, the injection moulded top part was bonded to the bottom COC sheet using a Telsonic USP4700 ultrasonic welder (Telsonic, Erlangen, Germany) as described previously (Poulsen *et al* 2016).

The main part featured the chip layout with seven channels in parallel, each with its own luer-fitted inlet. Each channel had a height of $H = 200$ μm and contained a sequence of five phaseguides of increasing nominal heights $h_{nom} = 20$ μm, 40 μm, 60 μm, 80 μm and 100 μm. All phaseguides were straight and orthogonal to the channel length (90°). One channel had a width of $W = 1$ mm and did not feature any branches on the phaseguides. The remaining six channels consisted of three channels with $W = 1$ mm and three channels with $W = 3$ mm. The phaseguides in each of these channels had a centrally placed branch forming an angle of $\alpha = 45°$, 60° or 75° (see figure 2(a)). It was decided not to study a 90° branch, due to the similarity to the 'no branch' one with 90° angle to the sidewalls. The overall chip structure, including the luer inlets, is illustrated in figure 2(b).

3.2. Test liquids

Two different liquids were used in experiments: (1) water obtained from a Millipore MilliQ lab water system, and (2) a mixture of phosphate buffer saline containing 0.01% (V/V) of surfactant Tween 20 and 0.1% (V/V) of protein bovine serum albumin (referred to as PBST-BSA). The latter liquid was used as a representative buffer for analysis of biological samples. To facilitate visualization of the liquid in the channels, Brilliant Blue R dye was added to both solutions. The PBST-BSA reagents and the dye were purchased from Sigma-Aldrich. Densities of the dyed solutions were measured at room temperature to $\rho_{water} = 998\,kg\,m^{-3}$, $\rho_{PBST\text{-}BSA} = 1005\,kg\,m^{-3}$.

3.3. Contact angle and interfacial tension measurements

All measurements were performed on a Krüss DSA10 Contact Angle Measuring System (Krüss GmbH, Hamburg, Germany) with the associated DSA1 v1.9 software. Measurements,

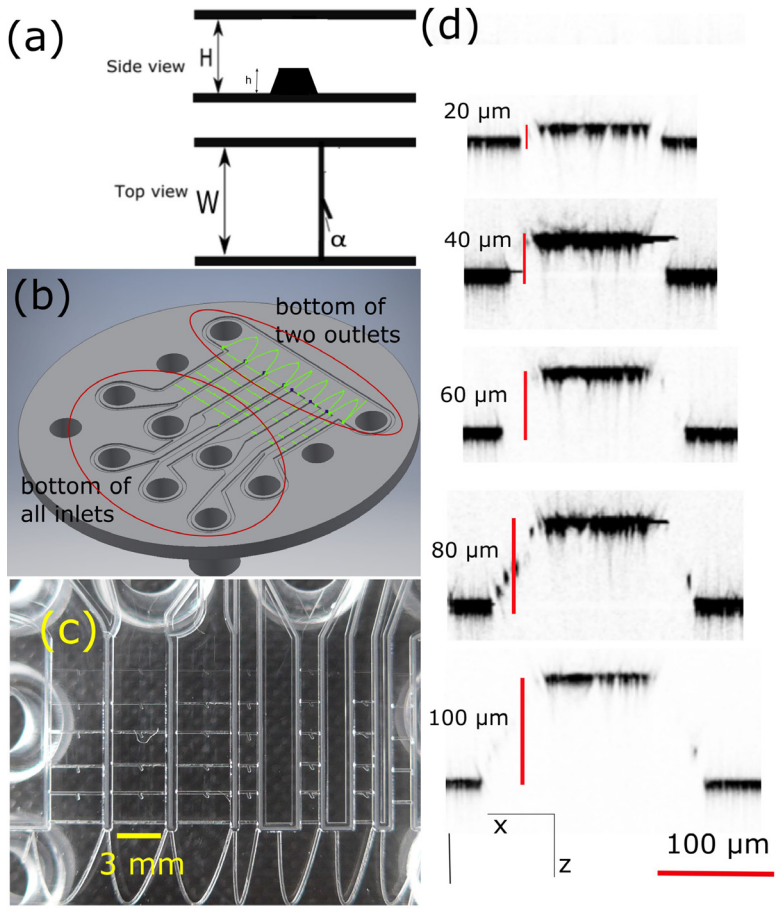

Figure 2. (a) Side and top views of a channel (height H, width W) with 90° phaseguide structure (height h) including a branch placed centrally at an angle α. (b) Layout of seven-channel injection moulded chip with integrated luer connectors and a common waste chamber. (c) Photograph of the fabricated chip prior to ultrasonic welding showing the parallel layout of the channels containing the phaseguides with branches (first six channels from left) and one without branches (last channel on the right), (d) cross-sections of all phaseguide profiles indicating the measured heights as obtained by confocal microscopy.

including both advancing and static contact angles, were performed using the 'sessile drop' method and fitting the obtained images using the 'tangent 2' method in the instrument software. Liquid–air interfacial tension measurements were performed using the 'pendant drop' method.

3.4. Burst pressure measurements

Hydrostatic burst pressures were determined by raising one end of a peroxide cured silicone tubing ($OD = 10$ mm, $ID = 6$ mm), filled with the test liquid, connected through the other end to the chip to a height Δz above chip level using a Thorlabs LTS150 motorized stage (Thorlabs, Newton, NJ, USA) (schematic in figure 3(a) and picture in figure S1, ESI). In the experiments, the chips were mounted with the luer connectors facing downwards. An experiment was performed by first adjusting Δz to zero. Then, the tubing was raised at 1 mm s^{-1} while carefully monitoring the position of the liquid meniscus in the channel. When the meniscus advanced in the channel, the stage was paused and the meniscus was allowed to pin at the next phaseguide (figure 3(b)) after which the stage motion continued. Measurements were performed on three different chips, which were rinsed and dried before conducting another set of measurements. The applied burst pressure was determined as

$$p_{\text{burst}} = \rho g z \tag{4}$$

where ρ is the density of the liquid, $g = 9.82$ m s^{-2} is the gravitational acceleration.

3.5. Microscopy

The geometries of the fabricated chips and phaseguides were investigated using a Zeiss LSM 700 confocal microscope (20×/0.5, z-stack images, and 1.590 μm sections). Images were analysed using ImageJ v. 1.47 and geometrical parameters of the relevant chip cross-sections in the z-direction were obtained from cross-sections of the stacked images.

The quality of the bonding of the channel lid was investigated using a standard stereo microscope (MZ FLIII, Leica Microsystems GmbH, Wetzler, Germany) equipped with a CCD camera (DFW-X710, Sony, Tokyo, Japan). In the experiments, the chips were filled with PBST-BSA with added Brilliant Blue R dye. The quality of the bonding was investigated by visual inspection of the colour transition from the channel to the area just outside the channel.

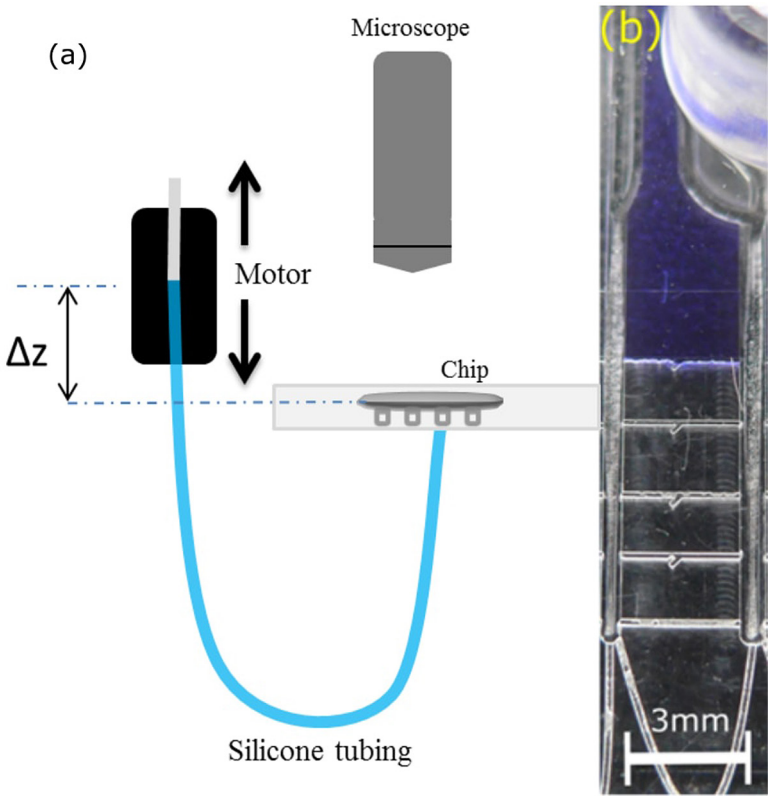

Figure 3. (a) Schematic of the setup, with the chip (and luer connectors) facing downwards and attached to the tubing. The other end of the liquid filled tube was mounted in a linear motor stage such that its height could be changed at constant velocity. In an experiment, the tube was first raised to fill the chip until the liquid meniscus pinned at the first phaseguide. Then, the position of the stage was adjusted to make the height of the liquid–air interface in the open end of the tube coincide with the top of the injection moulded part (top of the channel) defining $\Delta z = 0$. Subsequently, the motor stage was set in motion at constant velocity and the time at which the liquid meniscus burst and reached the next phaseguide was recorded. This continued for all phaseguides in a channel. (b) Picture of the liquid meniscus pinned at the second phaseguide ($h_{\mathrm{nom}} = 40$ μm) in a 3 mm wide channel.

4. Results

4.1. Physical characterization

The advancing contact angles were found to differ for the foil (θ_{f}) and the injection moulded part (θ_{m}) in which the channels were defined. For the dyed water, we measured $\theta_{\mathrm{m}} = 96 \pm 2°$ and $\theta_{\mathrm{f}} = 74 \pm 4°$ and for the PBST-BSA solution we measured $\theta_{\mathrm{m}} = 83 \pm 2°$ and $\theta_{\mathrm{f}} = 76 \pm 6°$, where the stated uncertainties indicate the standard deviation on the mean ($n = 10$). The results for the foil showed a larger variability due to inhomogeneity of the surface and were generally lower than those for the moulded part. We speculate that this could be due to residues on the foil from the fabrication. The liquid–air surface tension γ was measured to 73 mN m^{-1} for the dyed water and 35 mN m^{-1} for the PBST-BSA, respectively. These values are consistent with those reported in the literature for similar solutions (Niño and Patino 1998). The contact angle for PBST-BSA was further investigated, due to its modification of the surface wettability, once a chip had been exposed to BSA. This hypothesis was verified by contact angle measurements on substrates given an overnight exposure to PBST-BSA, where we found a reduction of the contact angle from 83° to around 65°.

Figure 2(c) shows an optical image (top view) of the channels with phaseguide taken prior to ultrasonic welding of the channel lid. All channel and phaseguide geometries were investigated by confocal microscopy to verify the channel and phaseguide dimensions. It was found that the channel width W and height H corresponded to their nominal values and also that the geometries of the phaseguide branches matched those on the design. The angle of the phaseguide sidewall to horizontal was measured to β=75° as expected from the opening angle of the engraving tool (15° to vertical). Figure 2(d) shows cross-sections of the phaseguide ridges as determined by confocal microscopy. A 3D view of a phaseguide is given in section S2, ESI. The heights of the phaseguide ridges were also investigated by scanning probe profilometry. Analysis of the profiles (section S3, ESI) showed that the measured values of h were systematically 12 μm lower than their nominal values h_{nom}, such that the actual five values of h in the sequence of phaseguides were $h = 8$ μm, 28 μm, 48 μm, 68 μm and 88 μm. This deviation is attributed to an offset in the z-zeroing of the engraving tool during the micromilling fabrication of the shim. The measured values will be used in the plots and the analysis below. The investigation also indicated that one of the structures was not realized as expected due to left-over particles in the smallest phaseguide cavities in the master insert used for the injection moulding (section S1, ESI). The results for this structure were discarded in the analysis.

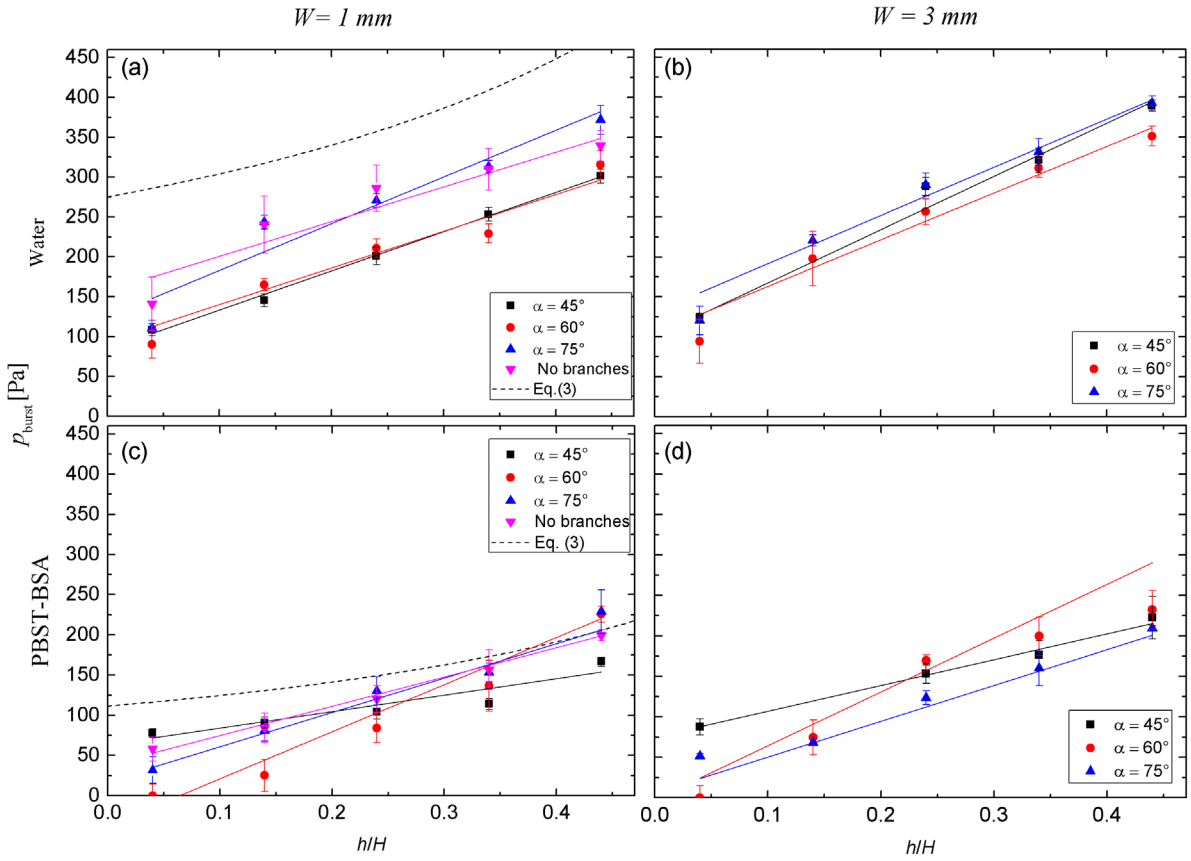

Figure 4. Burst pressure p_{burst} measured as function of h/H for phaseguides with branches at the indicated angles and the indicated channel widths. Results for $W = 1$ μm also include a channel without a branch on the phaseguide. Panels (a) and (b) show results obtained for water and panels (c) and (d) show results obtained for the PBST-BSA solution. Error bars in all graphs refer to the standard deviation of the mean ($n = 3$ for PBST-BSA and $n = 9$ for water). Solid lines are linear fits of each dataset with the parameters given in table 1. The dashed lines are plots of equation (3) using the measured values of contact angles and liquid–air surface tension given in the text.

Standard microscopy of chips filled with dyed PBST-BSA was used to study the quality of the channel sealing. Due to fabrication tolerances, the approximately 10 μm high energy directors were defined as lines surrounding the channels with a lateral spacing to the channel of 205 μm. In the images (section S4, ESI), we observed a sharp transition in colour between the channel and the region outside the channel with no detectable colouring in the narrow region between the channel and the welded energy directors. These observations are consistent with those of Poulsen *et al* by confocal fluorescence imaging of a fluorescent dye filled into channels using the same energy directors and ultrasonic welding procedure. This indicates that the ultrasonic welding provided a leak-tight sealing of the channels and also that the gap between the moulded part and the foil after welding was negligible.

4.2. Burst pressure measurements

Insertion of the measured contact angles and surface tension in equation (2) reveals capillary pressures of $\Delta p_{cap}(H)$ of 62 ± 2 Pa for water and 63 ± 2 Pa for PBST-BSA and thus the channels are expected to fill spontaneously with the liquid. This was in agreement with the experimental observations. Further, we find by insertion of the dimensions and contact angles in the expression for p_{pin} in equation (3) that both liquids fulfill the requirement for pinning of the liquid meniscus. Again, this was found to agree with experimental observations and it is therefore meaningful to determine the burst pressures for the phaseguides.

The burst pressure p_{burst} at which the pinned liquid meniscus moved to the next phaseguide structure was determined experimentally as function of the relative height h/H of phaseguides with the indicated angles α of the branch for channels with $W = 1$ mm and $W = 3$ mm for water and PBST-BSA, respectively.

Figure 4(a) shows measured values of p_{burst} for water in a channel with $W = 1$ mm as function of h/H for a phaseguide without a branch and for phaseguides with branches with the indicated values of α. Note, that a pressure of 100 Pa corresponds to a liquid column with a height of about 10 mm. Error bars were determined as the standard deviation on the mean from three repeated experiments on three separate chips ($n = 9$). The values of p_{burst} were observed to increase systematically with h/H in an approximately linear fashion from about 100 Pa ($\approx$10 mm H_2O) for $h = 8$ μm to about 350 Pa for $h = 88$ μm. Below, we describe them in terms of a simple empirical linear model and compare later to the expectations based on the theory presented in section 2. The results could be divided into two groups corresponding to phaseguides with low-angle branches ($\alpha = 45°$ and 60°) or phaseguides

Table 1. Values of p_0 and p_{slope} obtained from fits of $p_{burst} = p_0 + p_{slope} \cdot (h/H)$ to the values measured for the conditions indicated below. The stated uncertainties indicate the standard deviations obtained from the fits.

Geometry		Water		PBST-BSA	
W (mm)	Phaseguide branch	p_0 (Pa)	p_{slope} (Pa)	p_0 (Pa)	p_{slope} (Pa)
1	$\alpha = 45°$	84 ± 5	492 ± 17	63 ± 12	205 ± 42
1	$\alpha = 60°$	94 ± 17	460 ± 71	-38 ± 15	586 ± 46
1	$\alpha = 75°$	124 ± 30	586 ± 120	18 ± 11	427 ± 43
1	No branch	158 ± 25	435 ± 75	63 ± 12	205 ± 42
3	$\alpha = 45°$	100 ± 11	667 ± 42	74 ± 5	318 ± 22
3	$\alpha = 60°$	104 ± 23	584 ± 66	-2 ± 31	665 ± 129
3	$\alpha = 75°$	131 ± 13	603 ± 46	6 ± 7	443 ± 53

with no branch or a high-angle branch ($\alpha = 75°$). The results within each of these groups were found to be identical (one-way ANOVA F(1132) = 3.51, $p = .06$ for the first grouping and one-way ANOVA F(1132) = 2.87, $p = .07$ for the second grouping) and the results for the low-angle branches were found to be systematically lower than those for the other group. The solid lines in figure 4(a) are linear fits to

$$p_{burst} = p_0 + p_{slope} \cdot (h/H). \quad (5)$$

The parameters obtained from fits of equation (5) to the separate series of data for the different phaseguide branch types are given in table 1. It should be noted that the experiment to experiment variation (and hence the error bars) was larger for the phaseguide with no branches than for those with branches. Moreover, in all experiments on phaseguides with branches, the liquid interface was observed to always overflow a phaseguide at the branch location.

Figure 4(b) depicts the corresponding results for water in a channel with $W = 3$ mm. For this channel width, a phaseguide without a branch was not fabricated. The burst pressures showed values and a behaviour similar to that for $W = 1$ mm, but the values were found to be slightly larger for the low-angle branches ($\alpha = 45°$ and 60°), whereas the burst pressures for the high-angle branch ($\alpha = 75°$) were very similar to those obtained for $W = 1$ mm. The solid lines are linear fits of equation (5) to the data. The chip geometry and measured burst pressures were found to be reproducible and no systematic variation between burst pressures measured repeatedly on the same chip ($n = 3$) and on different chips ($n = 3$) was observed (see section S5, ESI). Thus, the observed variation between repeated experiments is likely due to the experimental reproducibility of the burst pressure measurements.

Figures 4(c) and (d) show the corresponding results for PBST-BSA for $W = 1$ mm and $W = 3$ mm, respectively. In both cases, the behaviour was similar to that obtained for water, but the burst pressures were lower and a possible grouping of the results was less obvious. The burst pressures were found to either slightly depend or not depend at all on the channel width. For both channel widths, the slope for $\alpha = 45°$ was observed to be lower than for phaseguides with $\alpha > 45°$. The lines are linear fits of equation (5) to the data. It should be noted that the PBST-BSA measurements were performed on three different chips ($n = 3$), and that the behaviour changed irreversibly once a channel had been primed with the PBST-BSA solution. For this reason, repeated measurements on the same chip were not performed for PBST-BSA.

5. Discussion

5.1. Reproducibility of burst pressures and effect of phaseguide branch

The studies of the fabricated chip geometries revealed that the channel and phaseguide geometries could be fabricated consistently with dimensions identical to their nominal values, except for the phaseguide height, where values were systematically 12 μm lower than their nominal values due to an offset in the zeroing of the engraving tool. Moreover, we found that the chips could be sealed without leaks using ultrasonic welding. The measured burst pressures were generally found to be reproducible and for water no systematic variation was observed between repeated experiments, on the same chip, and between nominally identical chips (see section S5, ESI). Therefore, the presented method allowed for the fabrication of a large number of single-use chips within a few days with burst pressures that were reproducible within the experimental uncertainty.

The branches on the phaseguide were found to have only a modest impact on the measured burst pressures, which was most pronounced for water in channels with $W = 1$ mm. Their main function was to define a specific point of overflow to provide a reproducible and well-defined continued filling of the channel. A related observation from figure 4 is that phaseguides with branches with $\alpha = 45°$ (in particular) and $\alpha = 60°$ generally produced results with lower variation compared to phaseguides with no branches or branches with $\alpha = 75°$. In our work, this indicates that phaseguides with branches with $\alpha = 45°$ provided the best control and reproducibility of the liquid overflow.

The measurements using PBST-BSA were also found to be reproducible from chip-to-chip on a level comparable to those obtained with water. However, repeated measurements on the same chip were not reproducible, due to the decrease in contact angle as explained in the results part.

5.2. Comparison to analytical modelling

The analytical model presented in section 2 only concerns the phaseguide structures without branches and we therefore restrict the comparison to the results obtained for channels $W = 1$ mm. It is noted, however, that as $W \gg H$ for both channel widths, the theory predicts a minimal dependence on the channel width in agreement with the experimental observations. The dashed lines in figures 4(a) and (c) show the pinning pressure p_{pin} versus h/H calculated by insertion of the measured values of the surface tension and contact angles in equation (3) for the two liquids. In both cases, the calculated pinning pressure is found to be comparable to (but somewhat overestimating) the measured burst pressures and

it shows an increase with h/H comparable to that observed experimentally. Moreover, the change in pinning pressure with the change of liquid is comparable to (but slightly underestimating) that observed experimentally. However, it is clear that the pinning pressure calculated from the measured parameters does not provide a quantitative description of the measured values. It is noted that it was found to be an ill-defined problem to fit equation (3) to the available measured data and this option was therefore not further pursued.

Generally, we observed that the theory tended to overestimate p_{burst} at low values of h/H and thus underestimated the slope of p_{burst} versus h/H. Several factors could contribute to the observed deviations:

First, we note that the roughness of the channel introduced during the milling process of the shim may cause a variability in the effective contact angle. As both liquids were observed to wet the substrate (Wenzel wetting state), a roughness will enhance the already existing wetting properties and thus make a wetting liquid more wetting (reduction of contact angle) and a non-wetting liquid less wetting (increase of contact angle). The contact angle measurements on the injection moulded part, however, were performed on an area where the shim had been subject to milling and thus we expect that the measured values are representative for those of the fluid channels.

Second, we note a lowering of the contact angle and surface tension could in principle contribute to the observed deviation. However, great care was taken in the experiments to use different tubing for the water and PBST-BSA such that the values for the contact angle and surface tension measured for water were valid also for the on-chip experiments.

Third, the actual profile of the phaseguide could deviate from the ideal profile assumed in the calculations, for example by the edge being more rounded or by having a variation in the height created by milling burrs left in the cavity in the shim, which is the inverse of the phaseguide structure (section S2, ESI). This could weaken the pinning ability of the phaseguide and thus reduce the measured burst pressure compared to the calculated one. This effect is random in nature but reproducible for the same phaseguide from chip to chip as they are made from the same shim. The systematic variation of the results with phaseguide geometry indicates that the effect is small as we would otherwise anticipate a substantial random variation of the results with the phaseguide geometry.

Finally, the theory considers a liquid meniscus that can bulge freely near the pinning point of the phaseguide when the liquid is non-wetting. This requires that the height of the phaseguide is sufficient to avoid contact between the liquid-air interface and the channel bottom after the phaseguide. When the height of the phaseguide is low, however, this may not be fulfilled in practice and this may cause a reduction of the measured burst pressure compared to the calculated one.

At this point, we therefore simply note that the simple theory in equation (3) is able to predict the magnitude of the burst pressure and the trends of the burst pressure with changing liquid/wetting properties and the channel geometry, but also that for the determined experimental parameters the agreement between equation (3) and the experimentally determined burst pressures is not quantitative.

5.3. Comparison to literature

We generally observed that the burst pressures for the investigated straight 90° phaseguides without a branch were close to those with a branch for $\alpha = 75°$ and higher than those for phaseguides with lower angle branches ($\alpha = 45°$ and 60°). Moreover, the branches were found to define the point at which the liquid meniscus burst through the phaseguide. These results are qualitatively consistent with those obtained by Vulto *et al* (2011) on lithographically defined phaseguides with a width and height of about 30 μm and $\beta \approx 90°$, but the effect of the branch on the phaseguide is less pronounced in our study. A possible cause of this can be the different fabrication methods and materials where the cleanroom fabrication provides structures with a sharper and a better controlled geometry.

Yildirim *et al* presented an analytical model for the pinning behaviour of a liquid in a channel with a highly hydrophilic top on phaseguides with a square cross-section with focus on the effect of the angle of the phaseguide to the channel sidewall (Yildirim *et al* 2014). Based on their more elaborate model, they concluded that the pinning behaviour was dominated by the horizontal geometry of the phaseguide. They found good agreement between their model and an experimental study in which the phaseguide angle to the channel sidewall was varied from 50° to 90°, but only a single channel width was investigated. The present study differs from their study in the respect that we have used a fixed angle of the phaseguide to the sidewall of 90°, our phaseguides have a non-square cross-section and the materials used by us have similar wetting properties in the entire channel. Moreover, we investigated the phaseguide burst pressure as function of the phaseguide height rather than its angle to the sidewall. In our studies, we found that the width of the channel had minimal influence on the result. Further studies are needed to shed more light onto whether these observations are in agreement or in conflict.

Considering previous literature, there is a need for further systematic theoretical studies of the burst pressure of phaseguides in order to reconsider limitations in the present models and develop new models which include the influence of a wider variety of parameters to cover different fabrication techniques. These parameters include the wetting properties of the liquid (wetting/non-wetting), the properties of the materials and the complete geometry of the phaseguide as well as the impact of branches and other supporting structures.

5.4. Consequences for applications

Micromilling and injection moulding allow for the creation of phaseguides of different heights keeping all other geometries constant as an alternative or supplement to varying the angle between the phaseguide structure to the channel sidewall. This can be recognized as a step in the creation of an all-polymer chip with different chambers for clinical diagnostics and can be used to tailor a sequence of burst pressures to suit a given application. For example, the phaseguides can be used to provide a controlled sequential filling of chambers with a significantly reduced risk of trapping of air bubbles (Phurimsak *et al* 2014, Yildirim *et al* 2014).

6. Conclusion

We have presented the fabrication of an all-polymer microfluidic chip with integrated straight capillary stop phaseguide structures forming an angle of 90° to the channel sidewalls. Single-use chips were fabricated by injection moulding of a part with structures defined in a micromilled shim combined with chip sealing by ultrasonic welding. Both techniques are compatible with low-cost mass production. We measured the burst pressures of the phaseguides as a function of their height for phaseguides without and with branches at different angles in channels of two different widths for water and for a representative buffer (PBST-BSA). The results were found to be reproducible and showed a burst pressure that increased approximately linearly with the height of the phaseguide. It was determined that the channel width does not affect significantly the burst pressure. A branch on the phaseguide was found to provide a well-defined burst point and phaseguides with a low-angle branch generally had slightly lower burst pressures than those without a branch or with a branch at a high angle. Results were found to be of the same magnitude but somewhat lower than the predictions of a simple analytical model.

The present work addressed a hitherto not studied parameter, the height of the phaseguide, which can easily be varied in chips made by injection moulding from a shim fabricated by milling. Most of the past studies of phaseguides in the literature were based on cleanroom fabricated structures where each layer requires a new mask and thus makes it tedious to vary the height of the phaseguide within a microfluidic chip. Moreover, the phaseguides in the present study also differ from the past literature by having a non-square cross-section with slanted sides. Thus, in addition to presenting an alternative approach to controlling the burst pressure by varying the height of the phaseguide in a mass-producible microfluidic system, the present work also fills a gap in the experimental data in the literature on phaseguides that may inspire to further theoretical work on the burst pressure of phaseguides. Our own further work will focus on using phaseguides to form multichamber microfluidic systems for health diagnostics.

Acknowledgments

This work was supported by DFF projects 4005-00116 and 4184-00121.

ORCID iDs

Mikkel Fougt Hansen https://orcid.org/0000-0003-3333-2856

References

Andresen K O Ø *et al* 2010 Injection molded chips with integrated conducting polymer electrodes for electroporation of cells *J. Micromech. Microeng.* **20** 55010

Becker H 2010 Mind the gap! *Lab Chip* **10** 271–3

Cho H, Kim H Y, Kang J Y and Kim T S 2007 How the capillary burst microvalve works *J. Colloid Interface Sci.* **306** 379–85

Gottheil R, Baur N, Becker H, Link G, Maier D, Schneiderhan-Marra N and Stelzle M 2014 Moving the solid phase: a platform technology for cartridge based sandwich immunoassays *Biomed. Microdevices* **16** 163–72

Kistrup K, Poulsen C E, Hansen M and Wolff A 2015 Ultrasonic welding for fast bonding of self-aligned structures in lab-on-a-chip systems *Lab Chip* **15** 1998–2001

Mukhopadhyay R 2009 Microfluidics: on the slope of enlightenment *Anal. Chem.* **81** 4169–73

Niño M R R and Patino J M R 1998 Surface tension of bovine serum albumin and tween 20 at the air-aqueous interface *J. Am. Oil Chem. Soc.* **75** 1241–8

Phurimsak C, Yildirim E, Tarn M D, Trietsch S J, Hankemeier T, Pamme N and Vulto P 2014 Phaseguide assisted liquid lamination for magnetic particle-based assays *Lab Chip* **14** 2334–43

Poulsen C E, Kistrup K, Andersen N K, Taboryski R, Hansen M F and Wolff A 2016 Laser ablated micropillar energy directors for ultrasonic welding of microfluidic systems *J. Micromech. Microeng.* **26** 67001

Trietsch S J, Rauwé W, Urban G A, Manz A, Hankemeier T, Linden H J and Van Der Vulto P 2011 The phaseguide paradigm : priming and emptying of monolithic polymer chips *Proc. 15th Int. Conf. on Miniaturized Systems for Chemistry and Life Sciences (μTAS) (Seattle, Washington, USA, 2–6 October 2011)* pp 942–4

Vulto P, Medoro G, Altomare L, Urban G A, Tartagni M, Guerrieri R and Manaresi N 2006 Selective sample recovery of DEP-separated cells and particles by phaseguide-controlled laminar flow *J. Micromech. Microeng.* **16** 1847–53

Vulto P, Podszun S, Meyer P, Hermann C, Manz A and Urban G A 2011 Phaseguides: a paradigm shift in microfluidic priming and emptying *Lab Chip* **11** 1596–602

Yildirim E, Trietsch S J, Joore J, van den Berg A, Hankemeier T and Vulto P 2014 Phaseguides as tunable passive microvalves for liquid routing in complex microfluidic networks *Lab Chip* **14** 3334–40

Electronic supplementary information

Burst pressure of phaseguide structures of different heights in all-polymer microfluidic channels

Francesca Garbarino, Kasper Kistrup, Giovanni Rizzi, and Mikkel Fougt Hansen*

Department of Micro- and Nanotechnology, DTU Nanotech, Building 345B, Technical University of Denmark, DK-2800 Kongens Lyngby, Denmark

*E-mail: Mikkel.hansen@nanotech.dtu.dk

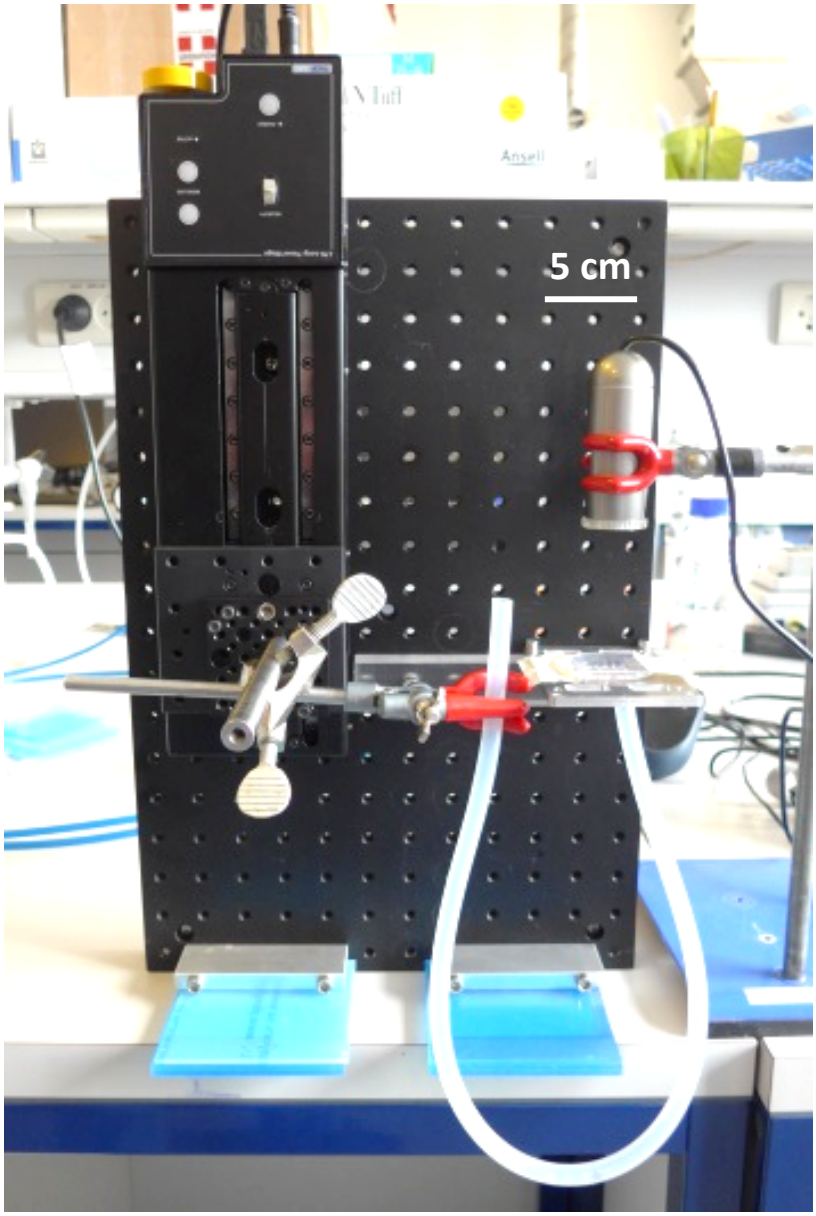

Figure S1: Setup used for the experiments. The chip was mounted with the luer connectors facing downwards with one end of a tube attached to the luer. The other end of the tube was attached to a motorized stage, which can move in the vertical direction. At the beginning of an experiment, the tube was filled with liquid and the height was adjusted so that the liquid level in the open end of the tube matched the top of the channel. Experiments were performed by increasing the height of the open end of the tube at 1 mm/s while monitoring the position of the liquid meniscus in the chip. When the liquid burst through a phaseguide, the stage was immediately paused and the position noted. Subsequently, the stage motion was re-engaged to study the burst pressure of the next phaseguide and so on.

S1. Fabrication issues

Once chips were fabricated in the injection moulder, confocal images were taken to confirm the fabrication fidelity. Figure S2a shows the typical successful outcome of an injection moulded channel containing a phaseguide with a branch. Figure S2b shows a worst-case failure in the fabrication that was found to be reproduced in every injection moulded part, meaning that it was not a problem of the injection moulder. Investigations of the micro milled aluminum master insert, the shim, (Figure S2c) showed that some particles were left in the groove defining the phaseguide (see white ellipse) whereas most other parts were clean. This indicates that dust/burrs from the milling process on some occasions could cause a deviation of the shape of the phaseguide from the ideal one. Sonication of the shim prior to injection moulding was found to reduce the problem. The results for the phaseguide presented in Figure S2b were discarded in the analysis.

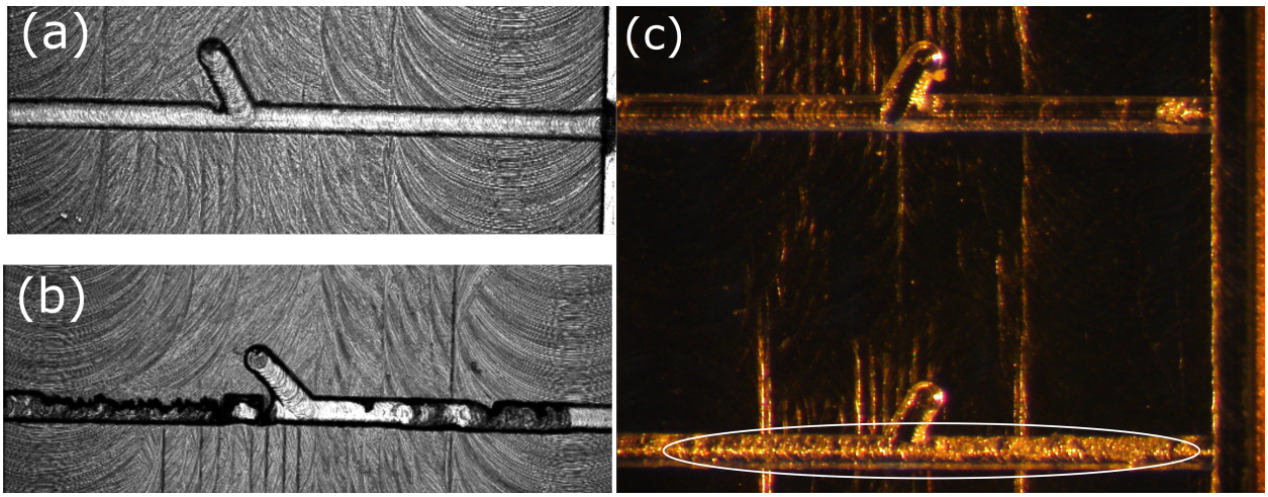

Figure S2: (a) Confocal image of a well-defined phaseguide in an injection moulded channel ($W = 3$ mm, $\alpha = 60°$, $h = 28$ μm). (b) Confocal image of a phaseguide with fabrication defects in an injection moulded channel ($W = 3$ mm, $\alpha = 45°$, $h = 28$ μm). (c) Micrograph of the master used for injection moulding of the structure from (b) ($W = 3$ mm, $\alpha = 45°$, $h = 28$ μm). The white ellipse indicates left-over particles/burrs from the milling in the cavity defining the phaseguide.

S2. 3D structure of phaseguide

Figure S3 shows a 3D picture of the central section of one of the phaseguides, with a branch pointing downwards.

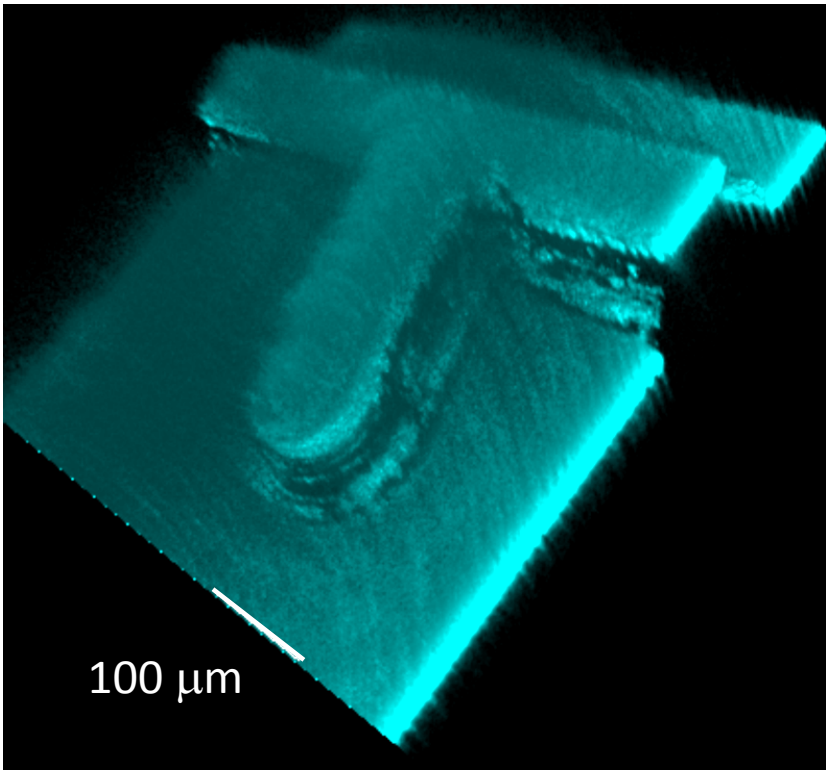

Figure S3: 3D image of injection moulded phase guide with h=88 µm and $\alpha = 75°$ in a 1 mm wide channel. Colours were changed to cyan to enhance contrast to the background.

S3. Heights of phaseguides determined by scanning profilometry

To verify the actual height of the phaseguides, an analysis with a stylus profilometer (Stylus profiler – Tencor alpha step) was conducted. Stylus profilometer use a probe to detect the surface of the sample, physically moving the probe along the surface of the sample to acquire its surface height. Figure S4 shows the result of a scan in which the peaks from left to right correspond to the phaseguides without a branch and with nominal heights of h_{nom} =100 μm, 80 μm, 60 μm, 40 μm, and 20 μm in a channel with W = 1 μm. The height of the phaseguides was for all phaseguides found to be 12 μm lower than the nominal value. This was attributed to an offset in the z-zeroing of the engraving tool used to define the phaseguides. The measured values were used in all reported results.

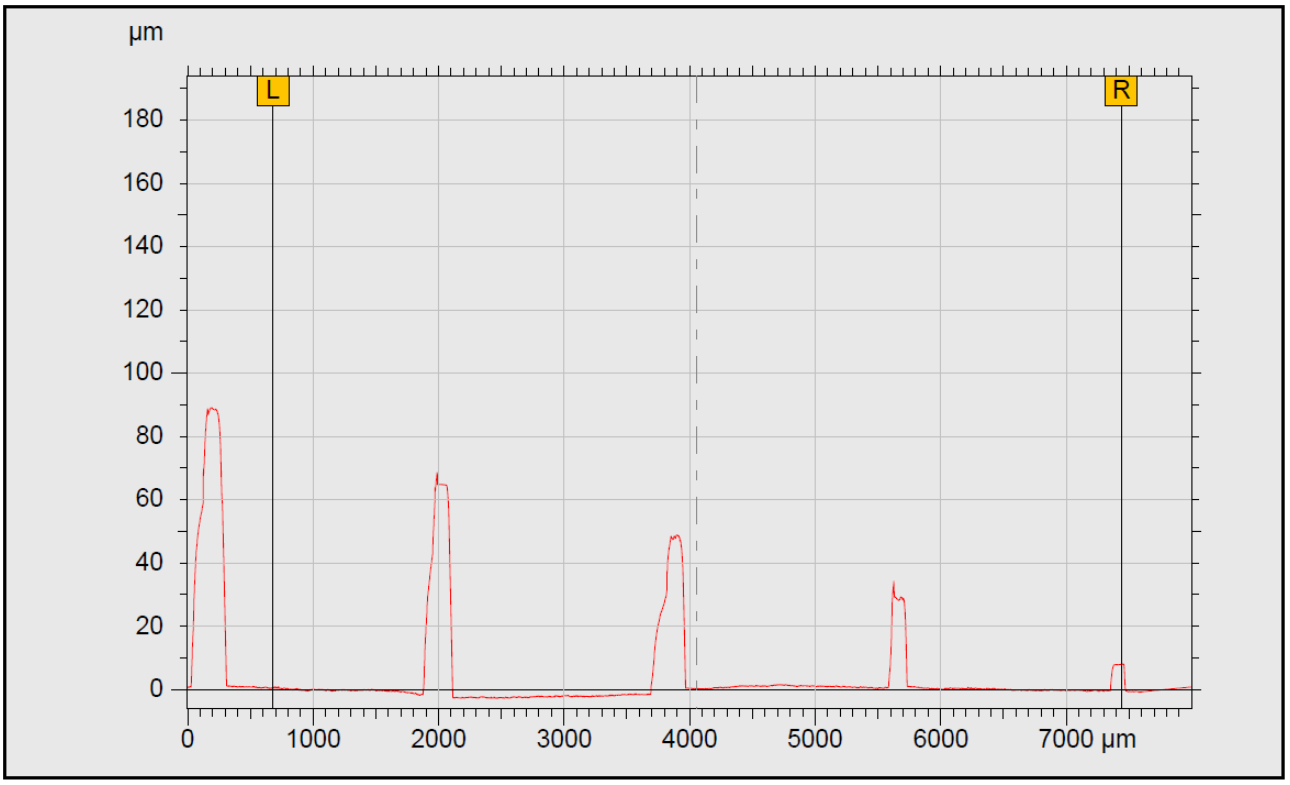

Figure S4: Result of stylus profilometer scan along injection moulded channel with W = 1 μm over phaseguides without a branch and nominal heights of of h_{nom} =100 μm, 80 μm, 60 μm, 40 μm, and 20 μm. The measured values are found to be offset by –12 μm due to an offset in the z-zeroing of the engraving tool used for the fabrication.

S4. Channel sealing by ultrasonic welding

The injection moulded and bonded chips were filled with PBST-BSA with added blue dye (to aid visualization) and investigated using microscopy. PBST-BSA was chosen as liquid because it would (with added detergent) spontaneously fill any gaps by capillary forces. Figure S5a shows an overview of a series of 1 mm wide channels with various phaseguide structures. The channels are observed to show no leakage. Figure S5b shows a representative zoom-in on one of the 1 mm wide channels. The welded energy directors can be observed as approximately 200 μm wide bands along either side of the channel that have a small spacing to the channel. A sharp transition between inside and outside the channel is observed with no blue colouring of the region between the welding and the channel. This indicates that the welding has left either no gap or a gap of negligible size in the region between the channel and the welded energy directors in agreement with a previous study of energy directors and ultrasonic welding made by the same method (Poulsen *et al*., 2016).

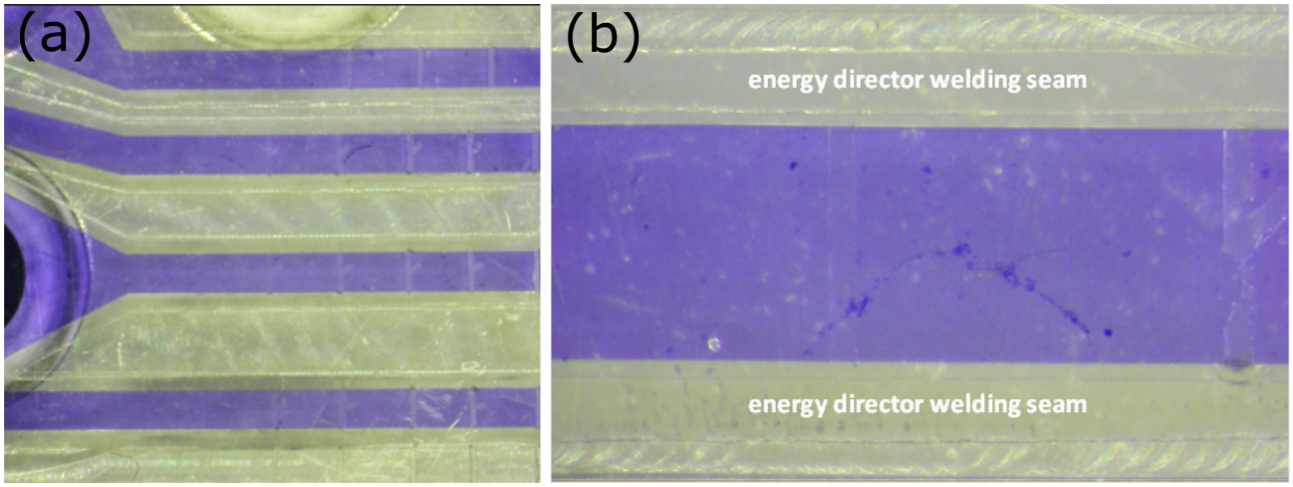

Figure S5: Micrographs of injection moulded chip sealed by ultrasonic welding filled with blue-dyed PBST-BSA in the 1 mm wide channels. Panel (a) shows an overview of four 1 mm wide channels showing that the channels are sealed. Panel (b) shows a zoom-in on one of the 1 mm wide channels showing a sharp transition in color between the channel and the surrounding plastic. The energy director welding seams are visible as bands along the channel.

S5. Reproducibility of measured burst pressures

For length considerations, we only present the reproducibility results for the phaseguides with a branch at $\alpha = 45°$ branch for both widths of channel. Figures S6 (W=1 mm) and S7 (W=3 mm) depict the experimentally determined burst pressures for measurements on separate chips ('Fabrication reproducibility') and for repeated measurements on the same chip ('Experimental reproducibility') to illustrate the chip-to-chip and experiment-to-experiment variation of the results, respectively. The experiments were performed on three separate days. No systematic variation was observed between the results obtained for different chips or on different days. This indicates that the chip fabrication resulted in chips with properties that were reproducible from chip-to-chip within the experimental uncertainty and that experimental results were reproducible on separate days. Values obtained in this study are shown fig. S6 and S7 and in table S1.

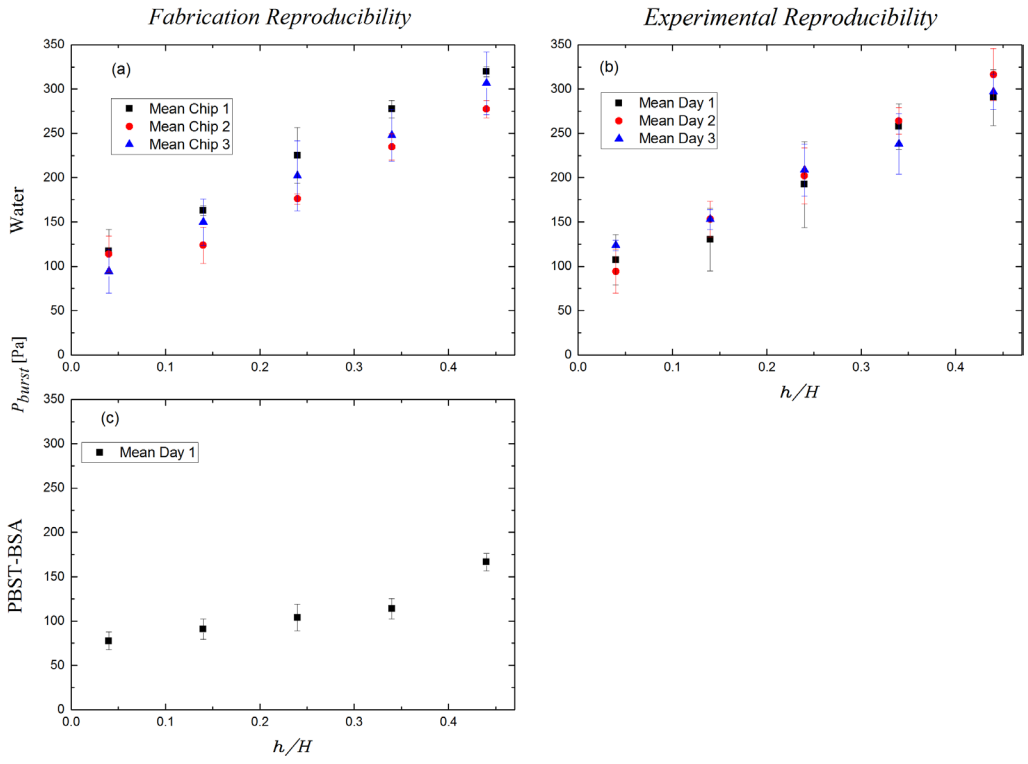

Figure S6: Measured burst pressure vs. h/H for a phaseguide with a central branch at $\alpha = 45°$ in a channel with W = 1 mm. Panels (a) and (b) show average results obtained for water on (a) three separate chips and (b) on three separate days. Panel (c) shows the results obtained for PBST-BSA on three separate chips.

.

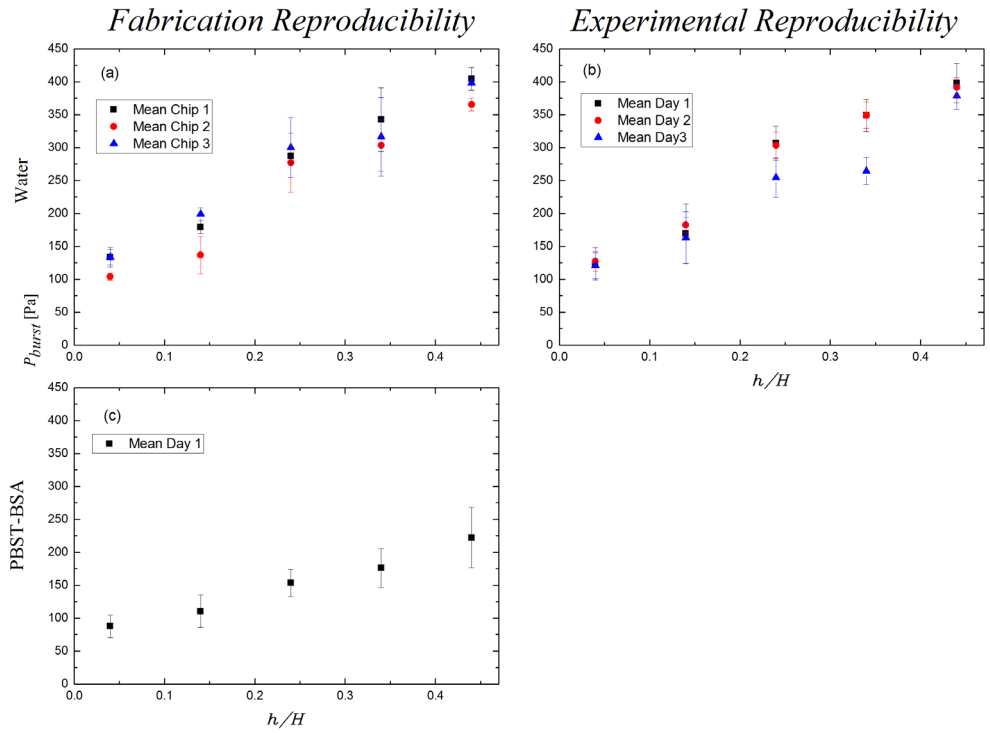

Figure S7: Measured burst pressure vs. h/H for a phaseguide with a central branch at $\alpha = 45°$ in a channel with $W = 3$ mm. Panels (a) and (b) show average results obtained for water on (a) three separate chips and (b) on three separate days. Panel (c) shows the results obtained for PBST-BSA on three separate chips.

Table S1: Values of *fabrication* and *experimental reproducibility* obtained from measurement data for phaseguides with a 45° branch. The stated uncertainties are standard deviation on the mean (n=9 (water), n=3 (PBST-BSA)).

Geometry		Water		PBST-BSA	
W[mm]	h [μm]	Fabrication	Experimental	Fabrication	Experimental
1	8	108±11	108±11	77±9	-
1	28	144±15	144±18	90±11	-
1	48	200±6	167±35	103±11	-
1	68	253±12	252±12	113±11	-
1	88	300±15	300±17	166±9	-
3	8	123±3	123±10	87±15	-
3	28	176±23	171±20	110±24	-
3	48	287±23	288±13	153±18	-
3	68	320±20	320±10	176±20	-
3	88	389±10	388±15	222±35	-

References

Poulsen, C.E., Kistrup, K., Andersen, N.K., Taboryski, R., Hansen, M.F., Wolff, A., 2016. Laser ablated micropillar energy directors for ultrasonic welding of microfluidic systems. J. Micromechanics Microengineering 26, 67001. doi:10.1088/0960-1317/26/6/067001

Appendix C

Paper II

DNA handling on magnetic microbeads in RCA assay with optomagnetic detection

Gabriel Antonio S. Minero,[*,†] Valentina Cangiano,[†] Francesca Garbarino,[†] Jeppe Fock,[†,‡] and Mikkel Fougt Hansen[*,†]

†*Department of Micro- and Nanotechnology, Technical University of Denmark, DTU Nanotech, Building 345C, DK-2800 Kongens Lyngby, Denmark*

‡*Blusense Diagnostics, Fruebjergvej 3, DK-2100 Copenhagen, Denmark*

E-mail: gant@nanotech.dtu.dk; mfha@dtu.dk

Phone: +45 45 25 63 16

Abstract

Rolling circle amplification (RCA) is a linear isothermal amplification technique, which is attractive for molecular diagnostics due to its high specificity. There is a continued need to automate and integrate the operations of RCA. Handling of a target sample using magnetic microbeads (MMBs) in a multi-step assay is appealing as the MMBs enable separation and transportation using an external magnet. Detection of amplicons using optomagnetic measurements of the rotational diffusion properties of magnetic nanoparticles (MNPs) is also appealing as it can be performed on a low-cost transparent sample container. Here, we investigated a reference strategy without MMB sample handling and two strategies using MMB sample handling for the integration of the steps of RCA of a DNA target with optomagnetic detection. The first MMB handling strategy relied on selective irreversible release of the amplicons from the MMBs so that the binding of functionalized MNPs to the amplicons could be detected optomagnetically. The second MMB handling strategy relied on capture of MNPs on

RCA products on MMBs, separation of the MMBs with attached RCA products, and subsequent optomagnetic detection of MNPs released from the RCA products. For the homogeneous reference strategy, we found a limit of detection (LOD) of 200 fM with a total assay time of 1.5 h (45 min RCA). For the heterogeneous MMB-using strategies, we found LODs between 4-20 pM with assay times between 2 and 2.5 h. The results demonstrate general strategies to handling of DNA on MMBs and present significant steps towards automation and integration of a complete RCA assay on a chip platform.

Introduction

Isothermal amplification of nucleic acid targets is an attractive approach to fast and simple diagnostics of different pathogens at an early stage and a great variety of techniques with exponential or linear amplification over time have been proposed.[1] Among these techniques is rolling circle amplification (RCA).[2] In RCA, a circular template is formed by annealing and ligation of a padlock probe (PLP) onto the target. The 3′-end of DNA targets on circular PLPs is extended by the phi29 polymerase, which displaces newly synthesized DNA to continue the "rolling circle" amplification. This leads to formation of a long single-stranded DNA concatemer containing repeated copies of the DNA sequence complementary to the PLP. Typically, 1000 copies of the approximately 100 nt long PLP are produced in 1 h. By proper design, the PLP recognition step is highly specific and it can be sensitive to single point mutations with up to 100% specificity.[3] The RCA takes place at 30-40°C and due to the high processivity of the phi29 polymerase, linear amplification can continue for up to 20 h. Compared to exponential isothermal amplification methods, RCA has the advantage of providing a more specific and precise target quantification and the disadvantage of being slower. The assay can be extended to detect protein biomarkers, such as bacterial spores, via circle-to-circle amplification (C2CA) coupled with a proximity ligation mechanism to form the circular target for RCA.[4]

After about 30-60 min of RCA, RCA products (RCPs) are coils of DNA with a size of 0.2-1

μm that can be labelled with fluorescent tags and visualized using fluorescence microscopy.[5] The fluorescence of molecular beacons has been used to detect RCP concentrations from 10 pM to 10 nM where the results also revealed a strong sensitivity to intra- as well as inter-molecular loops in the RCPs that caused self-quenching of the beacons.[6] Furthermore RCPs can be directly visualized using confocal microscopy with a limit of detection (LOD) falling between 3 and 30 fM.[7] Recently, the Nilsson group established that individual RCA products (RCPs) could be discriminated and precisely quantified by a mobile-phone-based microscope over a 4-log dynamic range (1 fM to 10 pM) after an RCA time of 3 h.[8] The RCPs can also hybridize to capture sequences, for example immobilized on an electrode, to provide thousands of sites for intercalation of sensing molecules, such as electroactive methylene blue. By this means, Zhang *et al.* demonstrated electrochemical detection of a synthetic DNA target with an LOD of 100 pM.[9] Using a microarray readout format, an LOD of 480 fM was obtained for detection on a DNA microarray after 4 h RCA and a total assay time of 8 h.[10]

Capture sequences targeting one or several separated regions of the RCPs can also be grafted onto micro- or nanoparticles to provide a dose-dependent readout upon hybridization. The binding of functionalized magnetic nanoparticles (MNPs) to RCPs has been detected via the resulting change in the hydrodynamic size of the MNPs using magnetic susceptibility or optomagnetic measurements with LODs of 10 pM for 1 h of RCA.[11,12] Alternatively, the RCPs could be cleaved into monomers (the repeating unit complementary to the PLP) using a restriction enzyme and the monomers could be used to link two populations of functionalized nanoparticles to obtain a more sensitive readout. A monomer LOD of 30 pM was demonstrated using an optomagnetic readout with a detection time that was reduced to 7 min by use of magnetic incubation.[13] This monomer LOD corresponded to a predicted RCP detection LOD of about 30 fM for 1 h of RCA. Using gold nanoparticles and a colorimetric readout, a target LOD of 70 fM was obtained after 2 h of RCA.[14]

Magnetic microbeads (MMBs) have proven highly useful as solid substrates for multi-

step sample processing in automated laboratory equipment as well as in microfluidic systems as they can be simply manipulated using an external magnet.[15–18] It is therefore attractive to implement them in an RCA-based detection scheme. Although there are advantages of bead-based multi-step nucleic acid processing, the MMBs may interfere with enzymatic amplification and potentially also the detection.[19,20] In multi-round circle-to-circle RCA (C2CA), a step of particular importance is the separation of unreacted PLPs from PLPs ligated onto targets as PLPs remaining from the previous ligation will interfere with re-circularization of monomers made of the complementary sequence. This step has usually been achieved using MMBs functionalized to capture the target with attached RCPs.[4,21] Although some work has been undertaken to further integrate RCA on an automated platform,[22–25] there is still a need for integration and automation of the RCA processing and detection steps to enable use of this technique in a high-throughput or lab-on-a-chip setting.

In the present work, we investigate strategies for the integration of multi-step amplification reaction including (1) DNA ligation, (2) RCA performed on MMBs, and (3) optomagnetic readout of the RCPs. Two new strategies to enable the optomagnetic readout of RCPs are introduced and demonstrated: (i) selective release of RCPs from MMBs to enhance subsequent binding of functionalized MNPs, (ii) capture of MNPs on RCPs during RCA and a subsequent pH-induced MNP release. These strategies are compared to a reference assay without MMB handling where the optomagnetic detection is performed on RCPs directly mixed with functionalized MNPs.

Results

The padlock probe was designed to match a synthetic DNA target containing the hemagglutinin gene of Victoria, a type-B influenza virus strain.[21] The magnetic MMBs were functionalized with a 15 nt capture oligo (CO) targeting a section of the target outside the binding region of the PLP. To perform the detection, MNPs were functionalized with a 20 nt de-

tection oligo (DO) identical to a section of the user-chosen region on the non-target specific backbone of the PLP. The DNA sequences are given in the ESI†, Table S1.

Each single-stranded RCP has many potential binding sites for the DO-functionalized MNPs. The binding of MNPs to RCPs was detected using optomagnetic (OM) measurements. These were carried out in a transparent chip with a 5×5 mm^2 measurement chamber with a height of 2 mm. During measurements, the chip was mounted horizontally and sandwiched between two heaters and a light path through the measurement chamber was formed in the horizontal direction.[26] The optomagnetic technique measures the modulation of the intensity of light transmitted through the MNP suspension in response to a magnetic field applied along the light path as function of the frequency f of the magnetic field. The ability of the MNPs to rotate in response to the applied field depends on their hydrodynamic size such that smaller MNPs can follow the field up to higher f than large MNPs. For a magnetic field excitation of $B(t) = B_0 \sin(2\pi f t)$ we have previously shown that the real 2nd harmonic photodetector voltage (indicating the $\sin(4\pi f t)$-component of the signal) normalized by 0th harmonic voltage, V_2'/V_0, shows a characteristic peak at a frequency f_p, which is proportional to the Brownian relaxation frequency $f_\mathrm{B} = k_\mathrm{B}T/(\pi^2 \eta D_\mathrm{h})$, where $k_\mathrm{B}T$ is the thermal energy, η is the viscosity and D_h is the average hydrodynamic diameter of the MNPs.[27] When MNPs bind to RCPs, their size increases substantially from that of the free MNPs ($\approx$ 100 nm). The signal at high frequencies can therefore be used to quantify the amount of free MNPs for a given target concentration. Here, we detect RCPs as a 'turn-off' signal detecting the depletion of free MNPs as they bind to the RCPs or as a 'turn-on' signal when MNPs are released from RCPs.

We compared three detection strategies - a reference strategy performed without MMB sample handling (Strategy 1) and two strategies (Strategy 2 and 3) where MMBs were used to capture and transport the DNA target complex from ligation through RCA to detection using two different OM readout strategies. All experiments were carried out with a combined PLP annealing and ligation at 55°C for 20 min and RCA at 38°C for 45 min. The OM spectra

were obtained as function of time (one spectrum every 45 s). Error bars indicate the sample standard deviation (SD) obtained from triplicate or quadruplicate experiments. The LOD was estimated from the no template control (NTC) signal plus three SD. Dose-response curves, $f(c)$ vs. DNA target concentration c, were analyzed in terms of the Hill equation, $f(c) = f(0) + [f(\infty) - f(0)] \,/\, [1 + (K_{\mathrm{A}}/c)^{n_{\mathrm{H}}}]$, where K_{A} is the association constant and n_{H} is the Hill coefficient.

Strategy 1: Direct MNP turn-off signal detection (reference)

We benchmarked our results obtained using MMB sample handling with reference measurements in which DO-functionalized MNPs were spiked directly into a solution of RCPs after RCA was carried out for 45 min without physical mixing unless otherwise stated. Compared to previous studies,[11,28–30] the detection buffer and temperature were optimized to minimize self-annealing of the RCPs. Moreover, during detection the depletion of MNPs due to binding to RCPs was monitored in real time at 54°C in a low-stringency buffer.

Figure 1A shows OM spectra measured for samples with target concentrations of $c = 0$ pM (NTC), 10 pM, and 40 pM approximately 20 min after initiation of detection. The spectra show a negative peak at high frequencies near 200 Hz, which is attributed to free MNPs, and features below about 10 Hz, which are attributed to MNPs bound to RCPs. We detected the binding of MNPs to the RCPs via the depletion of free MNPs. As a measure of the signal from free MNPs in spectrum number n, we took the average normalized signal

$$\langle V_2'/V_0 \rangle(n) \equiv N^{-1} \sum_f V_2'(f,n)/V_0(f,n), \tag{1}$$

where the sum was taken over N frequencies between 40 Hz and 1 kHz indicated by the vertical dashed lines in Fig. 1A. Taking the initial amount of free MNPs as that measured in the first spectrum measured after temperature equilibration of the chip, we define the fractions F_{MNP} and B_{MNP} of free and bound MNPs, respectively, in the n'th spectrum in a

series of measurements as

$$F_{\mathrm{MNP}} = 1 - B_{\mathrm{MNP}} = \langle V_2'/V_0 \rangle(n)/\langle V_2'/V_0 \rangle(1). \tag{2}$$

Figure 1B shows F_{MNP} vs. time for the indicated target concentrations. It is observed that a higher target concentration led to a lower signal from free MNPs as more MNPs were bound to RCPs, and that as time progressed more MNPs were bound to RCPs. For the NTC sample, F_{MNP} was found to decrease by about 2% due to unspecific interactions. As a compromise between signal and speed of measurement, we chose to quantify results after a measurement time of $\approx$ 20 min ($n = 30$). Figure 1C reports the fraction of bound MNPs after 20 min of detection as function of the target concentration c. The NTC had a signal $B_{\mathrm{MNP}} \pm$ SD=0.0182±0.0007. From the dose-response curve, we found an LOD of 200 fM.

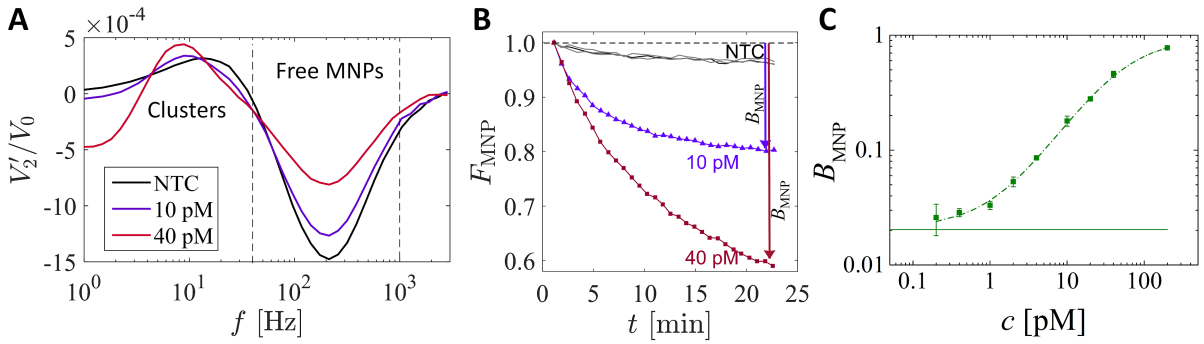

Figure 1: Strategy 1: 'Turn-off' OM detection without MMB handling where functionalized MNPs were mixed directly with RCPs after 45 min of RCA for the indicated target concentrations, c. (A) OM spectra measured 20 min after mixing. The vertical dashed lines indicate the frequency windows used to quantify the signal from free MNPs. (B) Time evolution of the fraction of free MNPs, F_{MNP}, in the n'th spectrum during OM detection (45 s/spectrum). (C) Fraction of MNPs bound to RCPs after 20 min, B_{MNP}, vs. c obtained from quadruplicate experiments. The horizontal line indicates the signal cut-off (NTC signal+3×SD). The dashed line is a Hill equation fit with $K_{\mathrm{A}} = 48$ pM and $c_{\mathrm{H}} = 1.03$.

Strategy 2: Microbead sample handling with turn-off MNP signal detection

Next, we considered an assay in which the DNA target was captured on CO-functionalized MMBs that were used as a handle to transport the DNA target complex through amplification to OM detection. To perform the multi-step processing of DNA using MMBs, we required that the capture oligo (CO)-target hybrid was stable in all buffers and temperatures used for the RCA assay. Moreover, to reduce diffusion limitations, we required that the RCPs could be released from the MMBs in the detection step. Under the same conditions, the detection oligo (DO)-RCP hybrids should be stable to enable 'turn-off' detection of the binding of CO-functionalized MNPs to RCPs. We therefore characterized the melting of CO-target hybrids for the CO sequence, which was chosen to have a 15 nt sequence matching the target (Fig. 2A).

For the melting assays, RCPs (45 min of RCA) were grown on target-PLPs that were pre-attached to MNPs (Fig. 2B). Subsequently, we used OM measurements during a melting experiment in the detection buffer to characterize the effective hydrodynamic size D_{h} of the MNP-RCPs, which was extracted from the peak position in the V_2'/V_0 spectra as described in our previous work.[26]

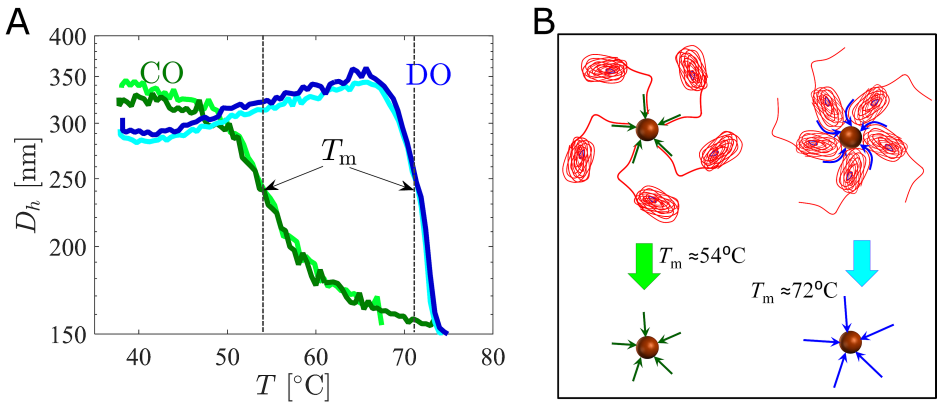

Figure 2: (A) Hydrodynamic diameter D_h vs. temperature obtained from peaks of OM spectra in two repeated experiments on individual MNPs with attached RCPs as illustrated in panel (B). In CO experiments, RCPs were grown on targets captured on CO-functionalized MNPs. In DO experiments, DO-functionalized MNPs were saturated with RCPs. The melting temperatures T_m, corresponding to the release of RCPs from the MNPs, are indicated.

The melting temperature for the CO-target hybrids was estimated to 54°C. We note that this temperature is close to the temperature used for ligation (55°C) and well above the RCA temperature (38°C). The DO-labelled curves in Fig. 2A reveal more abrupt decrease in D_h corresponding to a melting temperature of 71°C.

We further note that once the RCPs were formed, the release of the target from the CO was essentially irreversible with virtually no recapture as the single target sequence was buried within the DNA cloud of the RCP. The release of the RCPs from the DO-functionalized MNPs was partly reversible as the RCPs exposed many binding sites for the DO (ESI†, Section S2).

We now return to the assay in which the CO-functionalized MMBs were used as solid support for targets with pre-ligated PLPs during (1) target capture, (2) RCA, and (3) release of RCPs from MMBs and simultaneous detection of the turn-off signal from free MNPs upon binding of DO-functionalized MNPs to the RCPs in the detection buffer (Fig. 3A). We chose to perform detection at 54°C, which is the melting temperature of the CO-target hybrids and well below the melting temperature of the DO-RCP hybrids. The MMBs with attached target complexes were subject to magnetic separation between the above three steps.

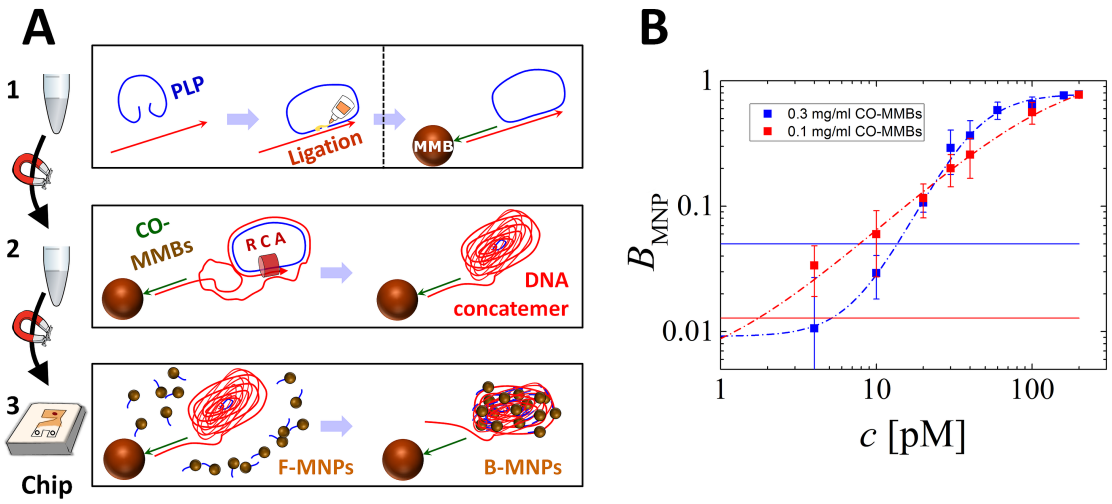

Figure 3: Strategy 2: 'Turn-off' OM detection with MMB handling for the indicated MMB concentrations. (A) Schematic of assay steps: (1) PLP annealing and ligation on targets in tube followed by target capture by CO-functionalized MMBs and magnetic separation; (2) 45 min of RCA in tube followed by magnetic separation; (3) on-chip OM detection of MNP turn-off signal. (B) Fraction B_{MNP} of MNPs bound to RCPs after 20 min of detection at 54°C. Error bars indicate SDs of quadruplicate experiments. Horizontal lines indicate signal cutoff (NTC+3×SD) and the dashed lines are Hill equation fits with $K_{\mathrm{A}} = 74$ pM and $c_{\mathrm{H}} = 1.33$ ($c_{\mathrm{MMB}} = 0.1$ mg/mL) and $K_{\mathrm{A}} = 42$ pM and $c_{\mathrm{H}} = 2.54$ ($c_{\mathrm{MMB}} = 0.3$ mg/mL), respectively.

PLP ligation (55°C, 20 min) was performed prior to the capture on MMBs. The reacted hybrids were spiked into a solution of MMBs to obtain final concentrations of DNA target in the range of 2-200 pM (Fig. 3A). We found that the target capture in step 1 was sensitive to time, temperature and mixing and used the following two-step procedure: (1) heating of target-PLP hybrids and MMBs to 55°C for 3 min followed by temperature ramping to 35°C over 30 min under constant rotation mixing at 1000 rpm in a thermoshaker; (2) end-over-end mixing at room temperature for 30 min. By ramping up the temperature, we avoided formation of unwanted secondary structures and dimers.[31]

The RCA reaction in step 2 was performed after resuspension of the MMB pellet by gentle mixing in the RCA buffer. Shaking of MMBs at 1000 rpm was maintained also during RCA in order to prevent sedimentation of MMBs, which would be detrimental for the results. The rotation mixing was found to somewhat reduce the efficiency of the phi29 polymerase

(ESI†, Section S3). After RCA (38°C, 45 min), the reaction was terminated by magnetic separation of the MMBs with attached RCPs followed by suspension in the detection buffer in which the phi29 polymerase was inactive due to the absence of Mg ions.

The detection buffer containing the resuspended MMB-RCPs and DO-labelled MNPs was subsequently injected into the chip. The MMBs were captured at the bottom of the detection chamber to a diffuse pancake-like pellet using an external magnet to avoid interference of the MMBs with the subsequent OM measurements of the MNPs. The temperature during OM detection was kept at 54°C (ESI†, Fig. S4). The OM spectra (ESI†, Fig. S4) had features similar to those shown for Strategy 1 in Fig. 1A and B, and we therefore analyzed the free MNP turn-off signal, B_{MNP}, using the same approach. In these studies, we investigated the importance of the MMB concentration as it could potentially impact the assay performance. Fig. 3B shows B_{MNP} vs. c for two investigated MMB concentrations c_{MMB} of 0.1 mg/mL and 0.3 mg/mL. For c_{MMB}=0.1 mg/mL and 0.3 mg/mL, respectively, we found NTC signals $B_{\mathrm{MNP}}\pm$ SD=-0.030±0.014 and 0.000±0.017 and LODs of 4 pM and 20 pM.

To verify that RCPs were indeed released from MMBs during detection and that DO-functionalized MNPs bound specifically to the RCPs, we subjected selected samples (c[pM] = 40, 100, 160, and 200) to further investigations after the detection step. First, the MMBs were selectively captured and removed using a magnetic separator with a low field gradient and the MMB-free supernatant was studied in a temperature melting experiment. This experiment revealed clusters of MNPs with signal features at frequencies below 40 Hz that underwent a melting transition to free MNPs at a temperature of about 72°C (ESI†, Section S5). This confirmed that the RCPs were released from the MMBs during the detection step and the sharpness as well as temperature of the transition confirmed that the binding of the MNPs to the RCPs was mediated by specific interactions.

Strategy 3: Microbead sample handling with turn-on MNP signal detection

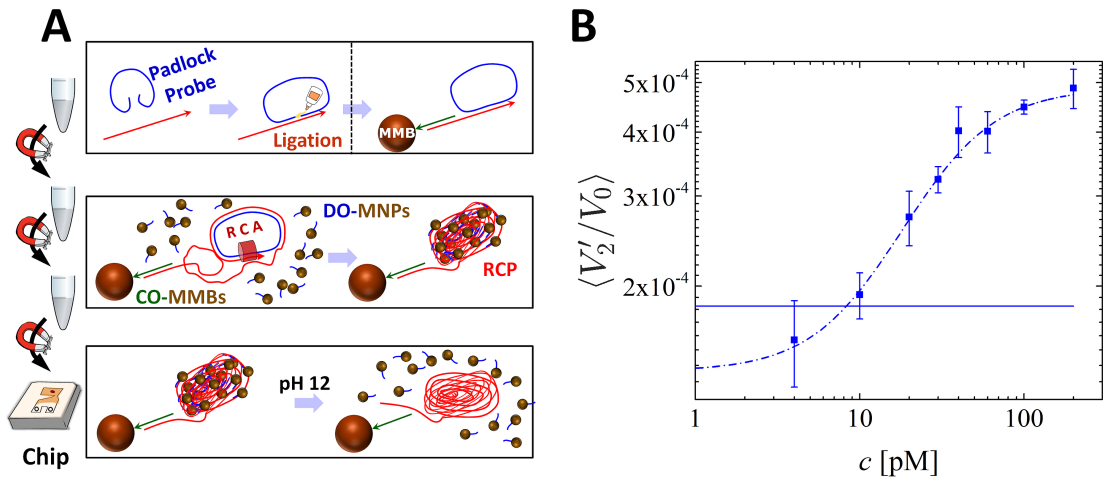

Figure 4: Strategy 3: 'Turn-on' OM detection with MMB handling for the indicated MMB concentrations. (A) Schematic of assay steps: (1) PLP annealing and ligation on targets in tube followed by target capture by CO-functionalized MMBs and magnetic separation; (2) 45 min of RCA in tube with DO-functionalized MNPs followed by magnetic separation; (3) on-chip OM detection of MNP turn-on signal upon release from RCPs in high-pH buffer. (B) Signal from free MNPs after 2 min of OM detection at 38°C, $\langle V_2'/V_0 \rangle$. The corresponding OM spectra V_2'/V_0 (ESI, section S6) were analyzed in the range of 40-1000 Hz. Error bars indicate SDs of triplicate experiments. Horizontal lines indicate signal cutoff (NTC+3×SD) and the dashed line is a Hill equation fit with $K_A = 27$ pM and $c_H = 1.6$.

Finally, we considered an assay in which the DNA target was captured on CO-functionalized MMBs that were used as solid support for the target with pre-ligated PLPs during (1) target capture and (2) RCA in the presence of DO-functionalized MNPs. This was followed by magnetic separation of MMBs with attached RCP-MNP complexes and washing to remove unbound MNPs. Finally, (3) the separate was resuspended in a high-pH detection buffer (pH 12) and the turn-on signal from released MNPs detected (Fig. 4A). Except for the addition of DO-functionalized MNPs during RCA, all steps until detection in step (3) were carried out as described for Strategy 2. Upon resuspension in the high-pH buffer, the DNA hybrids denatured[18] and the MNPs were released from the RCPs. As for Strategy 2, the MMBs were captured at the chip bottom using a permanent magnet to minimize interference with the

subsequent quantification of the released MNPs, which took place at 38°C. To better enable visual verification of the capture of MMBs during magnetic separation from non-incorporated MNPs, all experiments were carried out for $c_{\mathrm{MMB}} = 0.3$ mg/mL. This protocol required only stability of the CO-target and DO-RCP hybrids until the final magnetic separation step.

The resulting OM spectra showed only features from free MNPs and MMBs with only a very weak signal from the NTC (ESI†, Section S6). Moreover, the signal from free MNPs reached a stable level within 2 min. In the dose-response analysis, we therefore considered the turn-on signal $\langle V_2'/V_0 \rangle$ from free MNPs measured after 2 min, which is shown as function of c in Fig. 4B. We found an NTC signal $B_{\mathrm{MNP}} \pm$ SD$= (1.33 \pm 0.16) \times 10^{-4}$ and an LOD of 10 pM.

Discussion

The reference assay showed an LOD of 200 fM for 45 min of RCA, which is significantly lower than previously reported values of $5 - 10$ pM using OM or magnetic susceptibility readouts based on binding of functionalized MNPs to RCPs.[11,12] The reduced LOD is likely due to that the detection took place in the presence of only 140 mM NaCl at $T = 54$°C without prior cooling. In contrast to Strömberg *et al.*,[11] we did not heat above T_{m} for the DO-RCP hybrids and we therefore avoided the signal loss arising from the need to re-capture DO-labelled MNPs on the RCPs (ESI†, Section S2).

Our results also clearly indicate that the MMB handling reduced the assay performance as indicated by the comparison of the 200 fM LOD for the turn-off signal in the reference assay to the 4-20 pM LODs found in the assays with MMB handling. Comparing the B_{MNP} signal cut-offs, we observe that the cut-offs for Strategy 1 (Fig. 1C) and Strategy 2 with $c_{\mathrm{MBB}} = 0.1$ mg/mL (Fig. 3B) assume nearly the same value, which is only about one third of the value found for Strategy 2 with $c_{\mathrm{MBB}} = 0.3$ mg/mL (Fig. 3B). This is likely caused by the higher amount of MMBs in the measurement chamber interfering with the measurement

on the MNP suspension. This interference could be of physical origin, for example if a variable amount of MMBs entered the light path through the chip or affected the MNPs magnetically in the applied measurement field, or of biochemical origin as a higher amount of MMBs increased the probability to form short DO-CO hybrids. In Strategy 3, the signal variation was primarily due to a background from MNPs even in the NTC after washing (ESI†, Section S6). This could indicate that also for that case, some unspecific binding occurred. Comparing the CO and DO sequences, we find that they form an overlap of three matching bases (ESI†, Section S1), which due to cooperative binding of several DO-CO hybrids could produce an unspecific signal background that would become more pronounced for a higher MMB concentration. This hypothesis is supported by the observation of a significantly higher Hill coefficient n_{H} of 2.33 in Strategy 2 for $c_{\mathrm{MMB}} = 0.3$ mg/mL compared to 1.33 for $c_{\mathrm{MMB}} = 0.1$ mg/mL (Fig. 3B). Further investigations of this hypothesis and on how to reduce the effect of it will be topics of our future work.

Comparing the slopes and centre points of the dose-response curves determined by the Hill coefficient n_{H} and the association constant K_{A}, respectively, we also observe a dependence on both the assay strategy and the MMB concentration with a general shift of the dose-response curves to higher concentrations when MMB handling is used. A significant difference between the MMB-free Strategy 1 and the MMB-using Strategies 2 and 3 is that all steps in Strategy 1 prior to detection take place in solution (homogeneous assay), whereas the amplification in the two latter strategies takes place on the MMB solid phase (heterogeneous assay). In the MMB-based strategies, the target is essentially immobile on the MMBs and the reaction rate is therefore to a higher degree limited by diffusion of the other reactants to the surface of the MMBs where the template concentration is potentially also high. Moreover, the exchange of liquid between MMBs in an MMB pellet is limited and if the MMBs are not fully re-dispersed after magnetic separation, this will reduce the output of the reaction. Diffusion limitations could also reduce the signal in Strategy 2 and increase the time needed to reach a signal steady-state during the detection as RCPs released from the MMBs are initially

at the bottom of the detection chamber. In contrast, the MNPs and RCPs were initially a homogeneous mixture in Strategy 1.

Finally, the activity of the phi29 polymerase may be affected by the presence of the MMBs[20] and by crowding due to other RCPs on the same MMB. Moreover, to avoid sedimentation of the MMBs during the RCA reaction, it was performed in a thermoshaker at 1000 rpm. This vigorous mechanical agitation was found to reduce the polymerase activity (ESI†, Section S3). Yet, the overall assay performance was similar or better compared to heterogeneous linear RCA assays reported by others.[9,19,20,32,33] Our results indicate that MMB mixing significantly impacts the results and can cause a variation of the obtained signal.[25] It is likely that a higher reproducibility can be obtained when the mixing and sample processing are automated. In perspective, the sensitivity of RCA can be further increased by implementing C2CA,[4,25] in which first round of amplification takes place on MMBs followed by digestion and a second round of MMB-free PLP ligation and amplification.

Conclusion

We studied and compared strategies for the capture, transportation and selective release of DNA target for an assay based on rolling circle amplification integrated with an optomagnetic readout of the amplification products. The overall assay time, including 45 min of RCA, was in all cases at most 2.5 h.

In a reference assay without microbead sample handling and direct detection of the binding of magnetic nanoparticles to rolling circle amplification products, we found a limit of detection of 200 fM. We implemented a strategy for the selective and irreversible release of rolling circle products from the microbeads during the detection step that facilitated detection of the binding of magnetic nanoparticles with limits of detection of 4-20 pM. Moreover, we tested a strategy to first capture magnetic nanoparticles on rolling circle products on microbeads during amplification followed by detection of their subsequent release in a high-pH

buffer with a limit of detection of 10 pM obtained with a 2 h assay time.

The higher limits of detection found for the assays with microbead sample handling were due to a combination of the increased variability of the results introduced by using the microbeads and the reduced diffusion and reduced polymerase activity when the targets are bound to the solid surface of the microbeads.

The presented DNA-handling strategies are useful for any assay strategies where there is a need for the selective capture, transportation and non-destructive release of a DNA target and are also amenable for integration in robotic sample handling or in lab-on-a-chip systems. Our future work aims to automate the assay handling and implement a mild microbead mixing procedure and to transfer the assay to a lab-on-a-chip platform.

Experimental

Optomagnetic detection

The OM setup, made for parallel detection of four assays in disposable plastic chips, was described previously in Minero *et al.*[26] In brief, each chip was placed between two custom-made heaters with a temperature controlled using a Stanford Research Systems PTC10 unit and monitored using Pt100 elements. Light (wavelength of 405 nm) was guided from a light emitting diode to the side of the chip, and from the other side of the chip to a photodetector (Thorlabs PDA-36A-EC). The optical path length within the detection chamber of the chip was 5 mm. A sinusoidal homogeneous magnetic field of amplitude 1 mT on the detection chamber was produced by two coils supplied by a custom-built voltage-to-current converter. Measurements of OM spectra comprising 41 logarithmically spaced frequencies between $f =$ 1 and 2800 Hz were initiated immediately after temperature equilibration ($\approx$1 min) and allowed to continue with one spectrum every 45 s for up to 100 sweeps ($\approx$ 75 min).

Reagents and buffers

Ampligase, BSA, dNTP mix and *Ligation buffer* (10×) (200 mM Tris-HCl, 250 mM KCl, 100 mM $MgCl_2$, 5 mM NAD, 0.1% Triton X-100, pH 8.3) were purchased from Nordic Biolabs. phi29 polymerase and *RCA buffer* (10×) (330 mM Tris-CH_3COOH, 100 mM $Mg(CH_3COO)_2$, 660 mM K-CH_3COOH, 1.0% Tween 20, 10 mM DTT, pH 7.9) were purchased from Thermo Fischer. Additionally, the following buffers were used (reagents from Sigma-Aldrich): *Binding buffer* (1×): 8 mM tris, 4 mM EDTA, 0.1 Tween-20, and 0.8 M NaCl (pH 8); *pH 8/12 detection buffer* (1×): 20 mM Tris-HCL, 140 mM NaCl, 5 mM KCl, 50 mM EDTA, 0.1% BSA, 0.01% Tween20, pH adjusted to 8 using HCl or to 12 using NaOH.

Magnetic nanoparticles

The 100 nm MNPs (BNF-Starch streptavidin, prod. code 10-19-102, Micromod Partikeltechnologie GmbH, Germany) were functionalized by biotinylated DO-probes that were complementary to the repeating sequence of RCPs (ESI†, Table S1) with approximately 40 DO probes per MNP as previously described.[34] Briefly, 10 μL stock MNP solution (10 mg/mL) was mixed with 8 μL DO (1 μM) and 82 μL binding buffer (1×) to obtain a final volume of 100 μL. After incubation for 30 min at room temperature to allow the DO probes to bind to the MNPs, the MNPs were washed 3 times and resuspended to 100 μL in binding buffer (1×).

PLP annealing and ligation on target

A 60 μL volume of the target DNA with three-fold excess of PLP was prepared in ligation buffer (1×) with 0.2 mg/mL BSA and 250 u/mL ampligase. Sequence-specific annealing and PLP ligation was performed for 20 min at 55°C.

Strategy 1: Reference RCA assay without MMBs

To maintain an approximately constant carry-over volume of the ligation buffer, three stock solutions of the target DNA-PLP hybrids with DNA concentrations of 2 nM, 200 pM and 20 pM were prepared as described above. 50 μL of each of the three ligated target-PLP stocks was mixed with 10 μL RCA buffer (10×), 10 μL BSA (2 mg/mL), 1.12 μL dNTP (10 mM), and 3.6 μL phi29 polymerase (10 u/μL) to obtain final volume 100 μL. A no template control was prepared in the same manner with 50 μL of milliQ water instead of DNA.

Unless otherwise specified, tubes with the solutions were placed in the thermoshaker without shaking at 38°C and RCA was run for 45 min. Subsequently, tubes were placed on ice until the thermoshaker reached 65°C after which the tubes were moved to the thermoshaker and amplification was terminated by heat inactivation of the phi29 polymerase.

Different volumes of the three RCP stocks were mixed with DO-MNPs in pH 8 detection buffer (1×) to obtain a final MNP concentration of 0.05 mg/mL and final target-PLP concentrations c [pM] of 200, 40, 30, 20, 10, 4, 2, 1, 0.4, 0.2, and 0. The samples were subsequently mounted in chips in the OM setup pre-heated to 54°C. The fraction of depleted MNPs in the samples was determined after 20 min of the detection to obtain the dose-dependent turn-off OM signal.

Preparation of MMBs with ligated targets (Strategy 2 and 3)

MyOne Streptavidin C1 microbeads from Thermo Fisher Scientific with a diameter of 1 μm were functionalized with biotinylated CO-probes (ESI†, Table S1) complementary to the non-amplified part of the DNA target as follows: 36 μL stock MMBs (10 mg/mL) was mixed with 90 μL CO (1 μM) and 174 μL binding buffer (1×). After 30 min incubation at room temperature with end-over-end mixing, MMBs were washed 3 times in binding buffer (1×) and finally resuspended in 300 μL ligation buffer (1×) with 0.2 mg/mL BSA.

A stock solution of the target DNA-PLP hybrids with DNA concentrations of 16 nM was prepared as described in the DNA ligation section followed by serial dilution to 1.6 nM and

160 pM.

To probe the dose-dependence of the RCA assay on MMBs for DNA concentrations 2 pM - 200 pM, we mixed 1.25-12.5 μL of the 1.6 nM DNA stock as well as 1.25-12.5 μL of the 0.16 nM DNA stock with 10 μL ligation buffer (1×), 10 μL BSA (2 mg/ml), and either 25 μL or 8.3 μL MMBs (1.2 mg/mL). For the NTC, no DNA was added.

Unless otherwise specified, the obtained cocktail of CO-MMBs (0.3 mg/mL or 0.1 mg/mL) was placed in thermoshaker at 1000 rpm at 55°C for 3 min followed by cooling to $\approx$ 35°C over 30 min. Four tubes were processed simultaneously. The tubes were subsequently placed for additional 30 min of end-over-end mixing at room temperature after which magnetic separation was carried out to remove unreacted PLPs. The subsequent steps were different for Strategy 2 and 3.

Strategy 2: MMB sample handling with turn-off MNP signal detection

After the magnetic separation, the MMBs were resuspended in 20 μL RCA buffer (10×), 2.25 μL dNTP mix (10 mM), 20 μL BSA (2 mg/mL), 3.6 μL phi29 polymerase (10 u/μL), and 54.15 μL milliQ water. The resulting solutions in tubes were placed in the thermoshaker at 38°C for 45 min (1000 rpm). We note that phi29 polymerase concentration was kept constant in all strategies whereas the concentrations of BSA, phi29 and dNTPs were doubled in Strategy 2 and 3 to improve diffusion of reagents to the MMBs.

Magnetic separation was carried out to remove phi29 polymerase (terminate RCA) and resuspend the MMBs in 100 μL of pH 8 detection buffer (1×) with 0.05 mg/mL DO-MNPs prior to on-chip OM detection. The amount of depleted MNPs in the NTC and in the samples containing RCPs was calculated after 20 min of detection to obtain a dose-dependent turn-off OM signal.

Strategy 3: MMB sample handling with turn-on MNP signal detection

After the magnetic separation, the MMBs were resuspended in 20 μL RCA buffer (10×), 2.25 μL dNTP mix (10 mM), 20 μL BSA (2 mg/mL), 3.6 μL phi29 polymerase (10 u/μL), 5 μL DO-functionalized MNPs (10 mg/mL) and 49.15 μL milliQ water. The resulting solutions in tubes were placed in the thermoshaker at 38°C for 45 min (1000 rpm).

Magnetic separation was carried out to remove phi29 polymerase (terminate RCA) and wash out unbound DO-MNPs in the detection buffer. The MMBs were subsequently resuspended in pH 12 detection buffer (1×) prior to on-chip OM detection, where the amount of released MNPs in the samples was calculated after 2 min of the detection to obtain a dose-dependent turn-on OM signal.

Acknowledgement

We thank Mats Nilsson (SciLifeLab, Stockholm) for design of Influenza target and probes as well as for the routine protocols of MMB-free circularization and rolling circle amplification

The work was supported by DFF project (4184-00121B). VC thanks Erasmus+ Program (Key action 1 A.Y. 2017-18) and Roberto Raiteri the sponsoring of the Erasmus program. JF acknowledges MUDP for support (MST-141-01415).

Supporting Information Available

The following files are available free of charge.

- ESI-ACS Anal Chem-Minero et al: The enclosed content does not add further novelty to the manuscript and can be used only as supporting material for the research presented in the current manuscript.

References

(1) Zhao, Y.; Chen, F.; Li, Q.; Wang, L.; Fan, C. *Chemical Reviews* **2015**, *115*, 12491–12545.

(2) Ali, M. M.; Li, F.; Zhang, Z.; Zhang, K.; Kang, D. K.; Ankrum, J. A.; Le, X. C.; Zhao, W. *Chemical Society Reviews* **2014**, *43*, 3324–3341.

(3) Pavankumar, A. R.; Engström, A.; Liu, J.; Herthnek, D.; Nilsson, M. *Analytical Chemistry* **2016**, *88*, 4277–4284.

(4) Göransson, J.; Ke, R.; Nong, R. Y.; Howell, W. M.; Karman, A.; Grawé, J.; Stenberg, J.; Granberg, M.; Elgh, M.; Herthnek, D.; Wikström, P.; Jarvius, J.; Nilsson, M. *PLoS ONE* **2012**, *7*, e31068.

(5) Clausson, C.-M.; Arngården, L.; Ishaq, O.; Klaesson, A.; Kühnemund, M.; Grannas, K.; Koos, B.; Qian, X.; Ranefall, P.; Krzywkowski, T.; Brismar, H.; Nilsson, M.; Wählby, C.; Söderberg, O. *Scientific Reports* **2015**, *5*, 12317.

(6) Nilsson, M.; Gullberg, M.; Dahl, F.; Szuhai, K.; Raap, A. K. *Nucleic Acids Research* **2002**, *30*, e66.

(7) Jarvius, J.; Melin, J.; Göransson, J.; Stenberg, J.; Fredriksson, S.; Gonzalez-Rey, C.; Bertilsson, S.; Nilsson, M. *Nature Methods* **2006**, *3*, 725–727.

(8) Kühnemund, M.; Wei, Q.; Darai, E.; Wang, Y.; Iván, H. N.; Yang, Z.; Tseng, D.; Ahlford, A.; Mathot, L.; Sjöblom, T.; Ozcan, A.; Nilsson, M. *Nature Communications* **2017**, *8*, 13913.

(9) Zhang, S.; Wu, Z.; Shen, G.; Yu, R. *Biosensors and Bioelectronics* **2009**, *24*, 3201–3207.

(10) Nallur, G. *Nucleic Acids Research* **2001**, *29*, e118.

(11) Strömberg, M.; Göransson, J.; Gunnarsson, K.; Nilsson, M.; Svedlindh, P.; Strømme, M. *Nano Letters* **2008**, *8*, 816–821.

(12) Donolato, M.; Antunes, P.; de la Torre, T. Z. G.; Hwu, E. T.; Chen, C. H.; Burger, R.; Rizzi, G.; Bosco, F. G.; Strømme, M.; Boisen, A.; Hansen, M. F. *Biosensors and Bioelectronics* **2015**, *67*, 649–655.

(13) Mezger, A.; Fock, J.; Antunes, P.; Østerberg, F. W.; Boisen, A.; Nilsson, M.; Hansen, M. F.; Ahlford, A.; Donolato, M. *ACS Nano* **2015**, *9*, 7374–7382.

(14) Li, J.; Deng, T.; Chu, X.; Yang, R.; Jiang, J.; Shen, G.; Yu, R. *Analytical Chemistry* **2010**, *82*, 2811–16.

(15) Gijs, M. A.; Lacharme, F.; Lehmann, U. *Chemical Reviews* **2010**, *110*, 1518–1563.

(16) Van Reenen, A.; De Jong, A. M.; Den Toonder, J. M.; Prins, M. W. *Lab on a Chip* **2014**, *14*, 1966–1986.

(17) Rödiger, S.; Liebsch, C.; Schmidt, C.; Lehmann, W.; Resch-Genger, U.; Schedler, U.; Schierack, P. *Microchimica Acta* **2014**, *181*, 1151–1168.

(18) Oishi, M. *Analytical and Bioanalytical Chemistry* **2015**, *407*, 4165–72.

(19) Schopf, E.; Fischer, N. O.; Chen, Y.; Tok, J. B. *Bioorganic and Medicinal Chemistry Letters* **2008**, *18*, 5871–5874.

(20) Sato, K.; Ishii, R.; Sasaki, N.; Sato, K.; Nilsson, M. *Analytical Biochemistry* **2013**, *437*, 43–45.

(21) Neumann, F.; Hernández-Neuta, I.; Grabbe, M.; Madaboosi, N.; Albert, J.; Nilsson, M. *Clinical chemistry* **2018**, *64*, e12.

(22) Sato, K.; Tachihara, A.; Renberg, B.; Mawatari, K.; Sato, K.; Tanaka, Y.; Jarvius, J.; Nilsson, M.; Kitamori, T. *Lab on a Chip* **2010**, *10*, 1262–1266.

(23) Ahlford, A.; Conde, A.; Sabourin, D.; Kutter, J.; Nilsson, M.; Dufva, M.; Brivio, M. *15th International Conference on Miniaturized Systems for Chemistry and Life Sciences 2011 (MicroTAS 2011)* **2011**, 61–63.

(24) Kühnemund, M.; Witters, D.; Nilsson, M.; Lammertyn, J. *Lab on a Chip* **2014**, *14*, 2983.

(25) Hernández-Neuta, I.; Pereiro, I.; Ahlford, A.; Ferraro, D.; Zhang, Q.; Viovy, J. L.; Descroix, S.; Nilsson, M. *Biosensors and Bioelectronics* **2018**, *102*, 531–539.

(26) Minero, G. A. S.; Nogueira, C.; Rizzi, G.; Tian, B.; Fock, J.; Donolato, M.; Strömberg, M.; Hansen, M. F. *The Analyst* **2017**, *142*, 3441–3450.

(27) Fock, J.; Balceris, C.; Costo, R.; Zeng, L.; Ludwig, F.; Hansen, M. F. *Nanoscale* **2017**, *10*, 2052–2066.

(28) Strömberg, M.; Zardán Gómez de la Torre, T.; Göransson, J.; Gunnarsson, K.; Nilsson, M.; Strømme, M.; Svedlindh, P. *Biosensors and Bioelectronics* **2008**, *24*, 696–703.

(29) Strömberg, M.; Zardán Gómez De La Torre, T.; Göransson, J.; Gunnarsson, K.; Nilsson, M.; Svedlindh, P.; Strømme, M. *Analytical Chemistry* **2009**, *81*, 3398–3406.

(30) Zardán Gómez De La Torre, T.; Strömberg, M.; Russell, C.; Göransson, J.; Nilsson, M.; Svedlindh, P.; Strømme, M. *Journal of Physical Chemistry B* **2010**, *114*, 3707–3713.

(31) Schopf, E.; Liu, Y.; Deng, J. C.; Yang, S.; Cheng, G.; Chen, Y. *Analytical Methods* **2011**, *3*, 267–273.

(32) Schopf, E.; Chen, Y. *Analytical Biochemistry* **2010**, *397*, 115–117.

(33) Yang, X.; Yang, K.; Zhao, X.; Lin, Z.; Liu, Z.; Luo, S.; Zhang, Y.; Wang, Y.; Fu, W. *The Analyst* **2017**, *142*, 4661–4669.

(34) Minero, G. A. S.; Fock, J.; McCaskill, J. S.; Hansen, M. F. *The Analyst* **2017**, *142*, 582–585.

Graphical TOC Entry

Some journals require a graphical entry for the Table of Contents. This should be laid out "print ready" so that the sizing of the text is correct.
Inside the `tocentry` environment, the font used is Helvetica 8 pt, as required by *Journal of the American Chemical Society*.
The surrounding frame is 9 cm by 3.5 cm, which is the maximum permitted for *Journal of the American Chemical Society* graphical table of content entries. The box will not resize if the content is too big: instead it will overflow the edge of the box.
This box and the associated title will always be printed on a separate page at the end of the document.

Electronic Supplementary Information

DNA handling on magnetic microbeads in RCA assay with optomagnetic detection

Gabriel Antonio S. Minero[a], Valentina Cangiano[a], Francesca Garbarino[a], Jeppe Fock[a,b], and Mikkel F. Hansen[a]

[a]Department of Micro- and Nanotechnology, Technical University of Denmark, DTU Nanotech, Building 345C, DK-2800 Kongens Lyngby, Denmark
[b]BluSense Diagnostics, Fruebjergvej 3, DK-2100 Copenhagen, Denmark

Contents

S1 DNA target and PLP sequences and secondary structures

The DNA sequence design for padlock probe (PLP) recognition and rolling circle amplification (RCA) of Influenza synthetic target DNA was adapted from Neumann *et al.*[1] and sequences are given in Table S1. Melting points were calculated using the IDT Oligoanalyzer tool. The melting points of the PLP ligating arms were 62°C (5'-terminal) and 60°C (3'-terminal) in the ligation buffer. Ampligase was used to join 3'- and 5'-ends of the PLP at the ligation temperature that was chosen to be 5°C below the melting temperature of the PLP ligating arms (underlined), i.e. 55°C. Note that the 5'-end of the PLP is phosphorylated. Phi29 polymerase was used to displace newly synthesized copies of PLP in course of RCA. Besides, this enzyme possesses 3'-5' exonuclease activity and is therefore capable of digesting protruding 3'-ends of the DNA target.

Table S1. DNA sequences of the synthetic target, PLPs, detection oligonucleotide (DO) and capture probes (CO) given in the 5'→3' direction. The target sequence matching the arms of the PLP is underlined. The part of the target matching the CO is marked in bold and by green color. The sequence on the PLP identical to that of the DO is marked in bold by blue color.

	DNA sequence (5' to 3')	Modification
Target	AGACCTGTTA**CATCTGGGTGCTTTC**CTATAATGCACGACAGAA CAAAAATTAGACAGCTGCCCAACCTTCTCCGAGGATAC	-------
PLP	GGGCAGCTGTCTAATTTTTGAGTCGGAAGTACTACTCTCT**GTGTAT** **GCAGCTCCTCAGTA**ATAGTGTCTTACGTATCCTCGGAGAAGGTT	-------
DO	**GTGTATGCAGCTCCTCAGTA**	3'-biotin
CO	**GAAAGCACCCAGATG-TTTTT**	3'-biotin

The detection oligonucleotide sequence was designed to match the sequence of DNA product of rolling amplification (RCP). As a consequence, the DO sequence is just a 20 nucleotide long subsequence of the PLP. The capture oligonucleotide was designed to match a 15 nt region of the target sequence (beyond the two sites of PLP recognition).

A simple screening for possible secondary structures of both DNA target and PLP sequences revealed multiple self-annealing sub-sequences of 3-4 nt (Fig. S1). The melting point of the CO-target hybrid was calculated to be about 56°C in the ligation and RCA buffers and about 53°C in the Mg-free detection buffer (20 mM Tris-HCl, 140 mM NaCl, 5 mM KCl, 0.1% BSA, 0.01% Tween-20). The DNA target revealed a competing intramolecular folding in the CO binding site (Fig. S1 A) with a melting point of about 52.5°C (in the ligation buffer). On MMBs, cooperativity of DNA hybridization could play a role, such that the actual melting point of the CO-target hybrids could be higher depending on the excess of COs.

For most efficient capture of the target-PLP conjugates on the CO-linked magnetic microbeads, both the conjugates and CO-MMBs were annealed in the ligation buffer at 55°C. At this temperature, the binding site of CO was unlocked and the CO could successfully bind to the DNA target upon annealing of the complementary DNA strands. Slow cooling of the mixture in a thermoshaker to 35°C over 30 min was important for CO bridges to form, whereas rapid cooling of denatured DNA molecules to 23°C significantly reduced the CO-target hybridization.

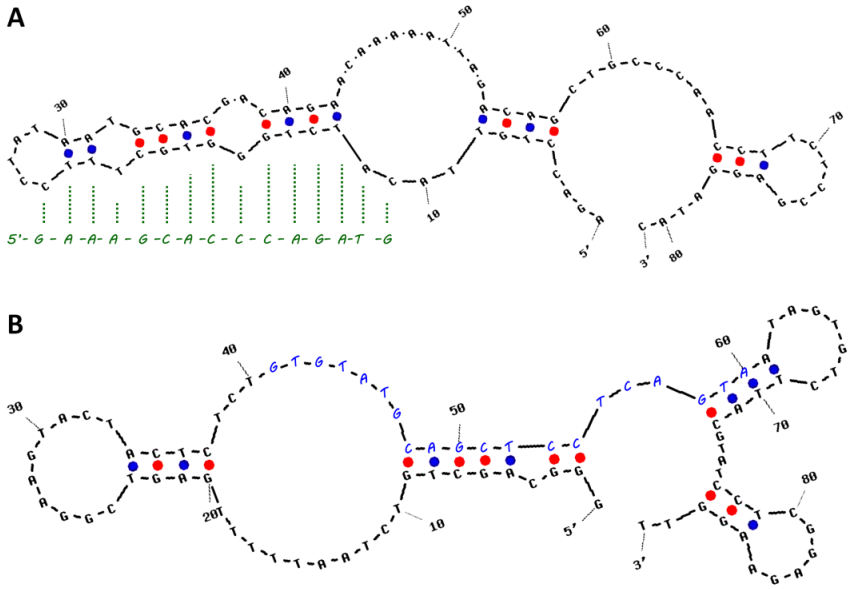

Fig. S1 Secondary structures of DNA target (A) and padlock probe (B). (A) Competition between intra-molecular folding of DNA target vs. inter-molecular hybridization between the target and capture oligonucleotide (green). The CO was designed to match 5'-terminal part of the DNA target (nt #11-25). The PLP matching sequence of the DNA target is encoded at nt #45-61. (B) Intramolecular folding of the PLP. Two ligating arms of PLP are located at nt #1-21 and nt #73-90t at the 5'- and 3'-terminal, respectively. The DO matches nt #41-60.

The sequences of CO and DO were also screened for formation of self- as well as hetero-dimers (Table S2).

Table S2. Self- as well as hetero-dimers predicted using IDT Oligoanalyzer tool.

CO-CO	CO-DO	DO-DO
Delta G: -3.14 kcal/mole **Base Pairs:** 2 5' GAAAGCACCCAGATG : || : 3' GTAGACCCACGAAAG	**Delta G:** -5.09 kcal/mole **Base Pairs:** 3 5' GAAAGCACCCAGATG ||| :: 3' ATGACTCCTCGACGTATGTG	**Delta G:** -7.05 kcal/mole **Base Pairs:** 4 5' GTGTATGCAGCTCCTCAGTA : |||| : 3' ATGACTCCTCGACGTATGTG
Delta G: -1.95 kcal/mole **Base Pairs:** 2 5' GAAAGCACCCAGATG || : : :: 3' GTAGACCCACGAAAG	**Delta G:** -4.74 kcal/mole **Base Pairs:** 3 5' GAAAGCACCCAGATG ||| : 3' ATGACTCCTCGACGTATGTG	**Delta G:** -6.34 kcal/mole **Base Pairs:** 4 5' GTGTATGCAGCTCCTCAGTA : : |||| : : 3' ATGACTCCTCGACGTATGTG
Delta G: -1.95 kcal/mole **Base Pairs:** 2 5' GAAAGCACCCAGATG || :: 3' GTAGACCCACGAAAG	**Delta G:** -3.3 kcal/mole **Base Pairs:** 3 5' GAAAGCACCCAGATG : : ||| 3' ATGACTCCTCGACGTATGTG	**Delta G:** -3.14 kcal/mole **Base Pairs:** 2 5' GTGTATGCAGCTCCTCAGTA || :: 3' ATGACTCCTCGACGTATGTG
Provided for ligation buffer	Provided for detection buffer	

S2 Melting studies (Strategy 2)

We used OM measurements to characterize the effective hydrodynamic size of the RCPs captured on MNPs via CO and DO during melting experiments in the detection buffer following our previous report.[2] In CO experiments, RCPs were grown on targets captured on CO-functionalized MNPs. In DO experiments, DO-functionalized MNPs were saturated with RCPs (RCA 45 min). Consequently, the temperature was increased at 0.01°C/s while OM spectra were continuously recorded. The CO and DO-labelled curves in Fig. S2 show D_{h} obtained from two such melting experiments. For CO-target hybrids, the drop in D_{h} was found to be reproducible and was taken as indication of a melting of the corresponding DNA bridges, which resulted in release of RCPs from the MNPs. The melting temperature for the CO-target hybrids, taken as the temperature where the value of D_{h} had decreased half-way to its final value, was estimated to 54°C. For DO-RCP hybrids, the melting temperature was significantly dependent on the length and compaction of the RCPs and could therefore vary (70±2°C). In the experiment below, it was estimated to 68°C (Fig. S2).

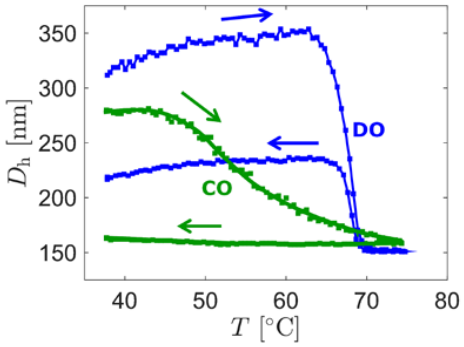

Fig S2 Hydrodynamic size D_{h} determined from peak of OM spectra during heating and cooling cycle experiment for RCPs initially bound to MNPs via CO (green) or DO (blue) probes. The temperature was cycled 38°C → 75°C → 38°C at 0.01°C/s with a spectrum measured every 45 s, where the arrows indicate the results obtained for increasing and decreasing temperature.

As the ligation and RCA buffers had higher ionic strengths than the detection buffer, the CO-target hybrids were stable under the conditions used for ligation and RCA. These results show that the CO and DO sequences could be chosen to allow for MMB handling of the target complex combined with a selective irreversible release of RCPs from the MMBs while still maintaining efficient binding of DO-labelled MNPs to the intact RCPs.

S3 Impact of tube shaking on RCP production

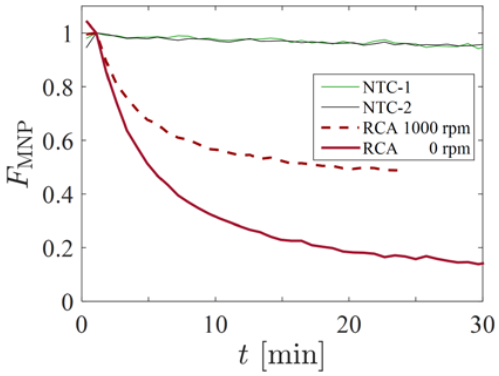

Fig S3 Time evolution of MNP depletion through hybridization of DO-MNPs with RCPs prepared for c = 100 pM with and without 1000 rpm shaking during 45 min of RCA at 38°C (procedure as in Strategy 1).

S4 Detection temperature optimization (Strategy 2)

Based on the capture oligonucleotide melting data, we investigated the release of RCPs from magnetic microbeads at temperatures for T_m between 52°C and 56°C (around the slope) to identify the optimum temperature for detection. The OM spectra were analyzed using the turn-off signal of the free MNPs.

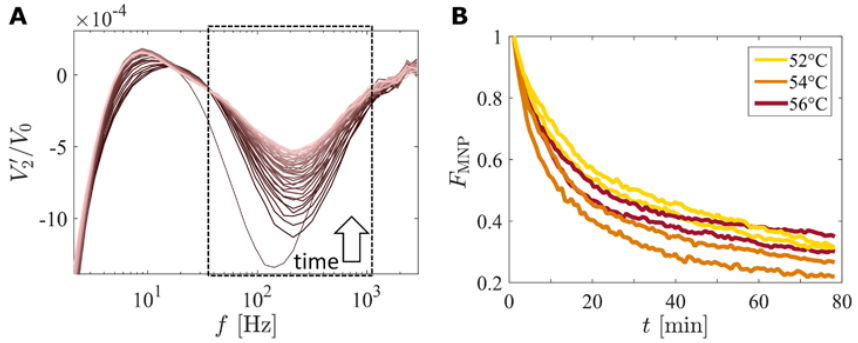

Fig S4 Detection of RCPs released from MMBs (c_{MMB}=0.3 mg/mL). (A) Real-time optomagnetic spectra vs. time at 56°C. Depletion of free MNPs is observed in the range $40\ \text{Hz} < f < 1000\ \text{Hz}$. (B) Results obtained in two repeated experiments at the indicated detection temperatures of which 54°C was found optimal.

S5 RCP release from microbeads (Strategy 2)

A quick check was made on selected samples post-RCA post-detection (75 min at 54°C) samples of 200 pM, 160 pM, 100pM and 40 pM. The supernatants revealed large clusters of MNPs (signals at f<40 Hz), which were gradually heated 75°C at 0.01°C/s while measuring OM spectra (1 spectrum every 45 s) to quantify the amount of released MNPs due to melting of DO-RCP bridges (see Fig. S2 for supporting melting analysis of DO-MNPs).

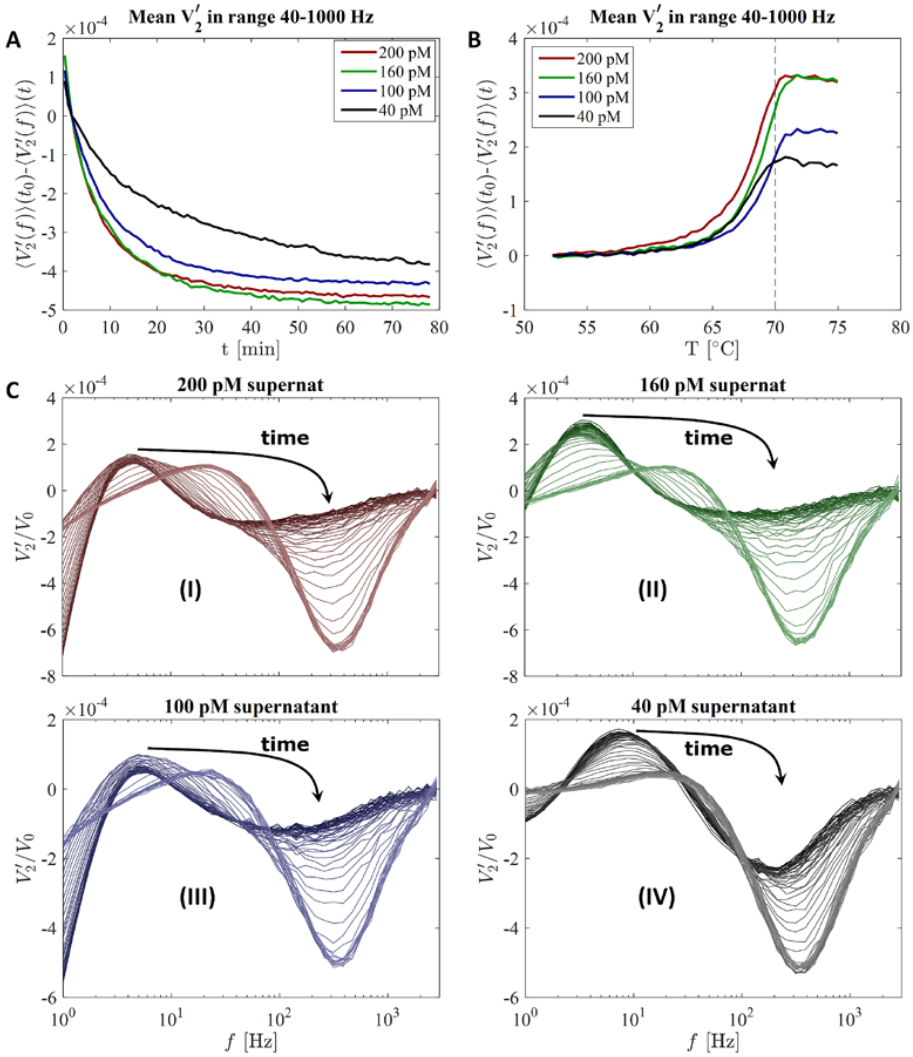

Fig S5 Analysis of supernatants after RCA and detection for 75 min at 54°C for Strategy 2. (A) Depletion of free MNPs upon mixing with MMB-RCPs after 45 min of RCA. (B) Profiles of MNP release from RCPs vs. increasing temperature (0.01°C/s) measured after removal of MMBs. (C) Optomagnetic spectra of the MNPs in the supernatants during the annealing experiments presented in (B). The arrows indicate the direction of time from low to high temperatures.

S6 Optomagnetic spectra (Strategy 3)

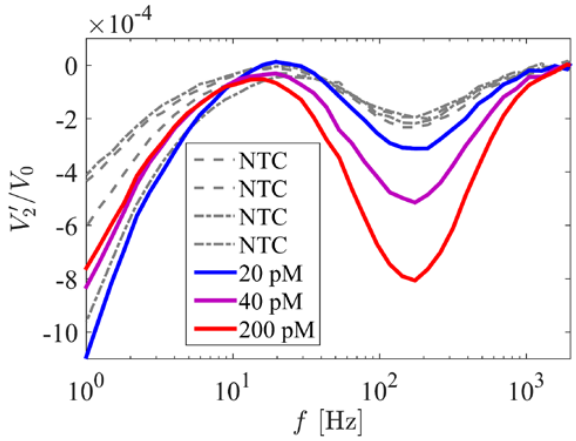

Fig S6 Detection of MNPs released from RCPs-on-MMBs 2 min after mixing with high-pH buffer (Strategy 3).

References

1 F. Neumann, I. Hernández-Neuta, M. Grabbe, N. Madaboosi, J. Albert and M. Nilsson, *Clin. Chem.*, **2018**, 64, e12.

2 G. A. S. Minero, C. Nogueira, G. Rizzi, B. Tian, J. Fock, M. Donolato, M. Strömberg and M. F. Hansen, *Analyst*, **2017**, 142, 3441–3450.

Appendix D

Paper III

Journal Name

ARTICLE TYPE

Cite this: DOI: 10.1039/xxxxxxxxxx

Rolling circle amplification and optomagnetic detection integrated on a low-cost polymer chip†

Francesca Garbarino,[a] Gabriel Antonio S. Minero,[a] Giovanni Rizzi,[a] Giada Violo,[a] Jeppe Fock,[a,b] and Mikkel Fougt Hansen*[a]

Received Date
Accepted Date

DOI: 10.1039/xxxxxxxxxx

www.rsc.org/journalname

Rolling circle amplification (RCA) of circular templates formed on a DNA target by annealing and ligation of a padlock probe is attractive for molecular diagnostics due to its high specificity. Here, we report on a chip and setup for integrated RCA analysis. The disposable polymer chip, made by three layers of laser-machined PMMA assembled by pressure sensitive adhesives, contains three interconnected chambers filled with the reagents for the three automated assay steps comprising (i) padlock probe annealing and ligation, (ii) rolling circle amplification, and (iii) detection. The liquids in the three chambers were separated using passive microfluidic structures and sequential filling. Magnetic microbeads actuated by an external motorized magnet were used as solid substrates to transport the target DNA complex between reaction chambers and for mixing within a chamber. Detection was achieved using non-contact optomagnetic measurements that detected the binding of functionalized magnetic nanoparticles to the amplification products. We compared results obtained when the first step of padlock probe annealing was performed off-chip to the case when the entire assay is performed on-chip and found corresponding limits of detection of 2 pM and 20 pM, respectively, after 45 min of RCA. The higher LOD in the latter case was due to a reduced target capture efficiency on the MMBs when the entire protocol was carried out on-chip. The results demonstrate the feasibility of the integration and automation of a multi-step molecular assay in a low-cost polymer chip.

1 Introduction

Since the early 1990s lab-on-a-chip devices have received much attention due to their promise of miniaturization and automation of laboratory techniques.[1–3] Over this period, materials for microfluidic chip fabrication have gradually shifted from silicon and glass to polymers such as polydimethylsiloxane (PDMS) and poly(methyl methacrylate) (PMMA) due to their promise of lower cost production.[4,5] Moreover, new passive approaches to liquid handling have greatly reduced the complexity and increased the robustness of microfluidic devices. Among these are capillary-stop valves based on sudden channel expansions[6,7] and phaseguide structures used to control the liquid spreading in liquid chambers to avoid trapping of air-bubbles.[8]

An important target for microfluidic devices is point-of-care (POC) detection of nucleic acid targets.[1] Polymerase chain reaction (PCR) has become an essential tool for *in vitro* amplification of nucleic acid sequences,[9,10] but the fast temperature cycling needed for the reaction is demanding in a low-cost lab-on-a-chip setting.[11] Therefore, there has been significant interest in alternative isothermal molecular amplification strategies.[12] These methods include recombinase polymerase amplification (RPA),[13] loop-mediated isothermal amplification (LAMP),[14] and rolling circle amplification (RCA).[15]

High specificity and sensitivity are key requirements for DNA detection in molecular diagnostics. Exponential amplification techniques such as LAMP and RPA can detect few copies of DNA molecules, but they are also prone to false-positive results that can be particularly difficult to control in an out-of-lab setting.[16] In contrast, linear amplification by RCA can amplify the DNA target sequence a thousand fold in 1 h, making it ideal for many applications that require reliable analysis at the expense of a higher limit of detection (LOD).[15] In RCA, a circular template is formed

[a] *Department of Micro- and Nanotechnology, Technical University of Denmark, DTU Nanotech, Building 345C, DK-2800 Kongens Lyngby, Denmark; E-mail: mikkel.hansen@nanotech.dtu.dk*

[b] *BluSense Diagnostics, Fruebjergvej 3, DK-2100 Copenhagen, Denmark*

† Electronic Supplementary Information (ESI) available: Section S1 Pictures of experimental setup; Section S2 Optimization of RCA and detection protocols; Section S3 Comparison of MMB handling strategies; Section S4 Optimization of MMB concentration; S5 Signals vs. time for off-chip and on-chip PLP annealing. See DOI: 10.1039/b000000x/

‡ Additional footnotes to the title and authors can be included *e.g.* 'Present address:' or 'These authors contributed equally to this work' as above using the symbols: ‡, §, and ¶. Please place the appropriate symbol next to the author's name and include a `\footnotetext` entry in the the correct place in the list.

by annealing and ligation of a padlock probe (PLP) on the target.[17] Subsequently, the 3′-end of the DNA target is continuously extended on the PLP by phi29 polymerase to create a long single-stranded DNA concatamer containing repeated copies of the sequence complementary to the PLP. The formation of the circular template is highly sensitive to sequence mismatches near the point where the PLP is joined and has been demonstrated to have up to 100% specificity for point mutations.[17,18]

In the past decade, magnetic microbeads (MMBs) have been used in nucleic acid assays for purification, amplification and detection.[19–23] For example, solid-phase capture of DNA was used to concentrate the target and enable washing cycles in an RCA assay with an LOD of 3 pM after 75 min of RCA.[26] Morever, magnetic separation of RCA products constitutes a key step in so-called circle-to-circle (C2CA) amplification, which is one or several extra RCA cycles used to increase sensitivity of RCA.[19,24,25] Hernández-Neuta *et al.* recently presented an on-chip RCA assay combining a fluidized bed of MMBs with detection on a polymer microarray with an LOD of 1 pM after RCA for 20 min followed by C2CA for 60 min.[27]

RCA products (RCPs) were also detected in a so-called volume amplified magnetic nanobead detection assay, where the increase in hydrodynamic size of magnetic nanoparticles (MNPs) upon binding to RCPs was detected using end-point magnetic susceptibility measurements with an LOD of 10 pM after about 1 h of RCA.[28–30] We have previously achieved a similar LOD using a simpler optomagnetic (OM) readout method.[31,32] The optomagnetic method probes the second harmonic modulation of light transmitted through a suspension of magnetic nanoparticles in response to a magnetic field of frequency f applied along the light path.[33,34] The resulting spectra reflect the ability of the particles to rotate in response to the field, which is inversely proportional to their hydrodynamic size. When MNPs bind to the RCPs, their hydrodynamic size increases significantly and spectral features shift to lower frequencies.[32] Mezger *et al.* detected changes in the OM signal when two populations of functionalized MNPs were linked by single copies of the sequence complementary to the PLP (the RCP monomer) and found a monomer LOD of 30 pM,[35] which ideally would correspond to 30 fM RCPs after 1 h of RCA.

Here, we present the integration and automation of a multi-step RCA assay on an all-polymer chip, with phaseguides and capillary stop valves for controlled filling of liquids, temperature control and MMB sample handling. The on-chip operations comprise (1) PLP ligation, (2) RCA, and (3) optomagnetic detection. The quantitative results for two strategies for PLP annealing are presented and compared.

2 Materials and methods

2.1 Assay requirements

The PLP ligation, RCA and optomagnetic detection steps of the complete RCA assay carried out in this work required specific temperatures and buffers to work optimally. The optimal temperature for ligation is typically 5-10°C below the melting points of the arms of the PLP-target hybrid where lower or higher temperatures result in unspecific PLP annealing or no PLP annealing, respectively, in both cases producing no template for RCA. In the present study, we used a ligation temperature of 58°C. The RCA took place at 38.5°C, but it was critical that the phi29 polymerase was not exposed to temperatures above room temperature prior to RCA as the free polymerase would be rapidly inactivated under such conditions. In the present study, optomagnetic detection of the RCPs took place after RCA, where again a specific temperature and buffer were needed to produce optimum results.

To integrate and carry out the above assay on a chip, we therefore needed three separate chambers filled with different buffers and with different temperature requirements. As a key point, the chambers should be connected to enable transportation of the DNA target complex on MMBs between the chambers but with negligible liquid mixing between them. To fulfill these requirements, we developed the chip design presented in Fig. 1 and the instrumentation and experimental protocol described below.

2.2 Chip design and fabrication

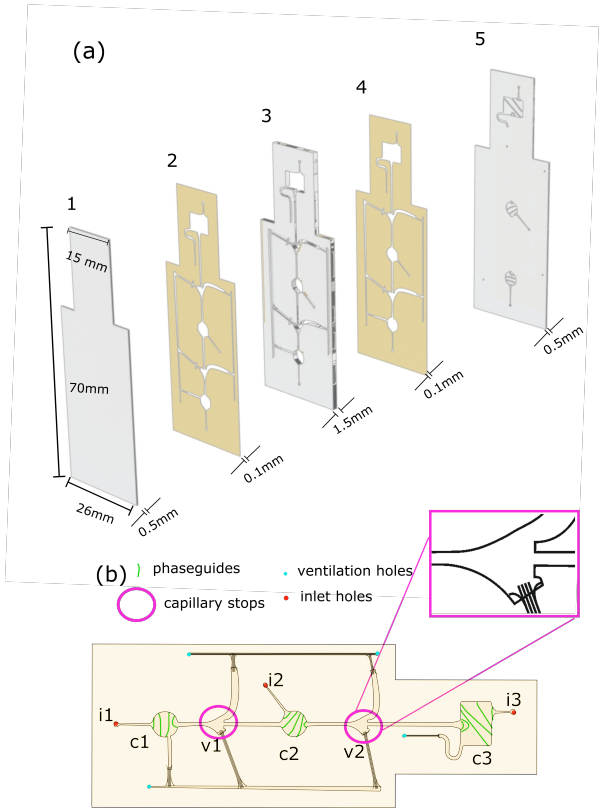

Fig. 1 (a) Bottom-to-top exploded view of the chip where parts 1 (bottom), 3 (middle), and 5 (top) are the PMMA layers of the chip and parts 2 and 4 are pressure sensitive adhesive foils mounted on the middle PMMA layer (part 3) during fabrication. (b) Schematic view of the design of the chip with labelled chambers (c1-c3), capillary valves (v1,v2), and inlets (i1-i3). The inset shows a zoom-in on the capillary valve.

The chip design, shown in Fig. 1, was inspired by the design introduced by Gottheil *et al.*[7] The chip device consisted of five different parts (Fig. 1a), forming a three-chambered path

(Fig. 1b). Two circular chambers (c1 and c2, ⌀4.08 mm) and a rectangular chamber (c3, 5×7 mm^2) were connected by 0.7 mm wide channels with heart-shaped capillary stop valves (v1 and v2) with an abrupt expansion of the channel width (Fig. 1b, inset).[6] These were further connected to pressure ventilation and overflow channels placed at the chip sides. The chambers contained phaseguide structures,[8] ridges protruding from the top of the chip (part 5 in Fig. 1a), to ensure controlled liquid filling without trapping of air bubbles.

Parts 1, 3 and 5 in PMMA defined the microfluidic structures and the lid of the chip in bottom-to-top order (Fig. 1a). Parts 2 and 4 were the 0.15 mm thick pressure sensitive adhesive (PSA) foils (ARcare 90106, Adhesive Research, Limerick, Ireland) placed on both sides of part 3 prior to fabrication of the structures. All layers were structured by CO_2 laser ablation (Epilog Mini 18 10 W system) using vector cutting and engraving modes. Part 5 was also processed in raster mode, a "bi-directional" engraving removing material pixel by pixel to create a cavity with 40 μm high phaseguides[36] to enable a controlled liquid filling in the chambers.

The chip was loaded with the three different liquids in the three chambers by a c3-c2-c1 loading sequence (Fig. 1b). First, chamber c3 was loaded with liquid through inlet i3 using a pipette until the liquid reached valve v2. Excess liquid flowed into the overload channel just next to chamber c3. Then, inlet i3 was sealed using tape. Next, chamber c2 was loaded with liquid through inlet i2. Due to the design of the phaseguide structures, the liquid first filled the channel to valve v1 and then the channel connecting to valve v2. When it reached valve v2, the liquid continued to flow into the overflow channel (above v2 in Fig. 1b) and gas trapped in valve v2 could be released through a shallow pressure ventilation channel (below v2 in Fig. 1b). Then, inlet i2 was sealed using tape. Finally, chamber c1 was filled with liquid in the same manner and inlet i1 and the pressure ventilation holes were sealed using tape.

Figure 2a shows the result of this loading sequence performed with dyed liquids. It is observed that the chambers are filled with the three different liquids with no mixing and that the regions where the liquids meet are separated from the chambers by at least 5 mm. This was sufficient to ensure that no mixing between the chambers take place during reactions due to diffusion. The heating of the different sections of the chip during the assay was found not to produce any significant shifting of the liquids.

2.3 Setup for integrated amplification and detection

Top and cross-sectional schematic views of the setup are given in Fig. 2. Pictures of the setup are given in Fig. S1†.

Magnetic manipulator. The setup consisted of two motorized stages from Thorlabs creating a two-axis (xz) stage, a KBD101 Brushless DC Servo Driver attached to a Single-Axis Flexure Translation Stages for horizontal positioning and a KDC101 Brushed DC Servo Motor Controller attached to T40Z-10A Minimum Vertical Z Axis Translation Stage (MPositioning), with a 12 mm Motorized Actuator, 3/8" Barrel Fitting for vertical positioning (12 mm range). A custom milled aluminum magnet casing was placed on the top of the upper stage. The casing included a stack consisting of four axially aligned cylindrical magnets (top to bottom): two N48, NdFeB, ⌀3 mm, 1 mm high magnets (S-03-01-N, Supermagnete, Gottmadingen, Germany) and two N45, NdFeB, ⌀6 mm, 3 mm high magnets (S-06-03-N, Supermagnete, Gottmadingen, Germany).[37] The magnets were used to manipulate the MMBs along the channel connecting the three chambers.

Temperature control The stages were placed underneath two custom-built 2 mm thick resistive heaters where one set covered chamber c1 and the other covered chambers c2 and c3. Another identical set of heaters was placed on top to enable heating of the chip from both sides to ensure a faster and more precise temperature equilibration (Fig. 2b). The heaters were fabricated on aluminum printed circuit boards (PCBs) by defining the resistive heater wire as meandering circuits in the Cu layer. The temperature of each heater was monitored using Pt100 elements and controlled using a Stanford Research Systems PTC10 unit.

To avoid heating of chamber c2 with the temperature-sensitive phi29 polymerase above room temperature while heating chamber c1 during on-chip ligation, we placed a 9 mm wide aluminum strip between the two heaters on the top of the chip (Fig. 2b). The temperature of the aluminum strip was regulated and maintained at 25°C using a thermoelectric (TE) element that was also controlled by the PTC10 unit. In subsequent assay steps, the temperature of this aluminum strip was set to the same temperature as the heater of chambers c2 and c3.

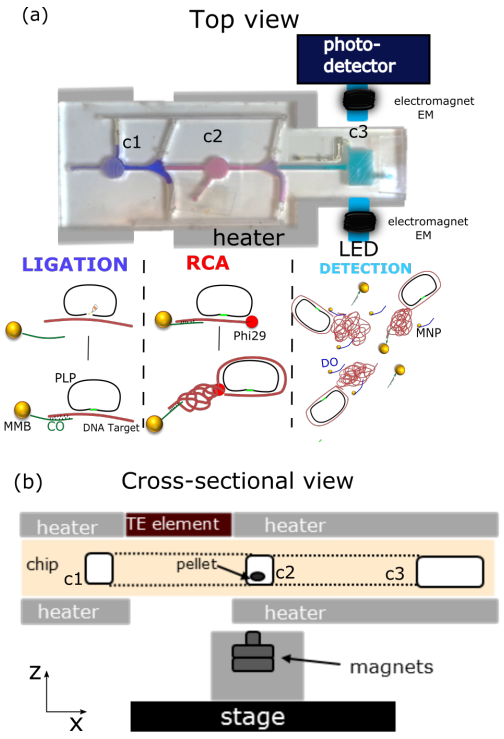

Fig. 2 (a) Top schematic view of the setup indicating the chambers and assay step taking place in each chamber and a schematic of the opto-magnetic setup. (b) Cross-sectional schematic view of setup indicating the positions of heaters, the three chambers and the external magnet.

OM detection setup. The OM detection took place in chamber c3 (Fig. 2a and b). Light from a light emitting diode ($\lambda = 470$ nm) was guided to the chip side and from the other side of the chip to a photodetector (Thorlabs PDA-36A-EC) using PMMA rods. Two electromagnetic coils placed symmetrically on either side of the detection chamber (c3) were used to produce a homogeneous oscillating magnetic field $B(t) = B_0 \sin(2\pi f t)$ applied along the light path with an amplitude of $B_0 = 1$ mT. The coils were driven by a custom-built voltage-to-current converter controlled by a data acquisition card (National Instruments, NI-6211) that also collected the signal from the photodetector.

2.4 Rolling circle amplification assay and detection

DNA sequences All DNA oligonucleotides were purchased from Integrated DNA Technologies, Belgium, and sequences are reported in Table 1. Experiments were carried out using a synthetic target DNA for type-B influenza virus (81 bases).[25] The padlock probe (PLP, 90 bases, 5′-phosphate) was designed to match a specific sequence of the DNA target. A detection oligonucleotide (DO, 20 bases, 3′-biotin) was designed to be complementary to the RCPs and was attached to MNPs for OM detection. A capture oligonucleotide (CO, 15 bases of the recognition sequence, 3′-biotin) was attached to MMBs to enable capture and handling of the DNA target on the MMBs. The sequence was chosen to be outside the region targeted by the PLP. The length of the CO was adjusted so that the CO-target hybrid denatured in the detection buffer at temperatures above 54°C.

Table 1 Sequences of Influenza target, PLP, detection oligo (DO) and capture oligo (CO). The target-specific 'arms' of the PLP as well as their binding sites in the target sequence are underlined.

DNA Tag	DNA sequence (5′-3′)	Modification
Target	AGACCTGTTACATCTGGGTGCT TTCCTATAATGCACGACAGAA CAAAAATTAGACAGCTGCCC AACCTTCTCCGAGGATAC	-
PLP	GGGCAGCTGTCTAATTTTTGAGT CGGAAGTACTACTCTCTGTGTAT GCAGCTCCTCAGTAATAGTGTCT TACGTATCCTCGGAGAAGGTT	5′-phosphate
DO	GTGTATGCAGCTCCTCAGTA	3′-biotin
CO	GAAAGCACCCAGATG-TTTTT	3′-biotin

Buffers and reagents Ampligase, BSA, dNTP mix and the 10× *Ligation buffer* (200 mM Tris-HCl (pH 8.3), 250 mM KCl, 100 mM $MgCl_2$, 5 mM NAD, and 0.1% Triton X-100) were purchased from Nordic Biolabs. phi29 polymerase and 10× *RCA buffer* (330 mM Tris-acetate (pH 7.9), 100 mM Mg-acetate, 660 mM K-acetate, 1.0% (v/v) Tween 20, 10 mM DTT) were purchased from Thermo Fischer. Additionally, we used the following buffers made from reagents from Sigma-Aldrich: *Binding buffer* (8 mM Tris-HCl (pH ≈ 8), 4 mM EDTA, 0.1 % Tween-20, and 0.8 M NaCl) and *Detection buffer* (20 mM Tris-HCL (≈ 8), 140 mM NaCl, 5 mM KCl, 50 mM EDTA, 0.1% BSA, 0.01% Tween20).

Magnetic particles MyOne Streptavidin C1 magnetic microbeads (MMBs) from Thermo Fisher with a diameter of 1 μm were used for the the capture and transportation of the DNA target complexes. Functionalization of the MMBs with CO probes was performed in a volume of 100 μL containing 12 μL MMB stock solution (10 mg/mL), 30 μL CO probes (1 μM) and 58 μL binding buffer. The suspension was end-over-end mixed for 30 min at room temperature. After 3 times washing and magnetic separation, the functionalized MMBs were resuspended in a solution containing 80 μL MilliQ water, 10 μL ligation buffer (10×) and 10 μL BSA (2 mg/mL).

The OM detection was carried out using multicore MNPs with a nominal diameter of 100 nm and a streptavidin surface (BNF-Starch streptavidin, prod. code 10-19-102, Micromod Partikeltechnologie GmbH, Germany). These MNPs have a remanent magnetic moment with a linked optical anisotropy.[33] A 50 μL volume of MNPs was prepared by addition of 5 μL MNP stock solution (10 mg/mL) and 4 μL DO probes (1 μM) to 41 μL binding buffer. The suspension was placed in a tray for 30 min followed by 3 times magnetic separation and washing and finally resuspension in the detection buffer to a final MNP concentration of 0.05 mg/mL used for OM detection.

On-chip MMB handling. The MMBs were captured and manipulated on-chip using the motorized magnet assembly that could move the magnets along the fluid channel connecting the three chambers as well as in the height direction.

The z-stage was used in two positions, 'high' and 'low', with magnet-to-channel bottom separations of 3.5 and 15.5 mm, respectively. The 'high' position was used at all times except when the magnets should be moved away without dragging the MMBs along.

The x-stage was used to mix MMBs with the sample within a chamber and to transport MMBs between chambers. Mixing was performed by moving the stage back and forth between the edges of a chamber at alternating constant velocities ± 2 mm/s (7 s in each direction) and served to increase the sample-MMB interaction and to minimize the risk of MMBs sticking to the bottom of the chamber. Mixing was performed during all incubation steps in the assay. Transportation was performed by moving the stage between chambers at 0.3 mm/s with brief stops every 5 mm. This low velocity was chosen to ensure that all MMBs were dragged along the moving magnet.

Padlock probe annealing and ligation. The PLP annealing and ligation consisted of (1) annealing of the PLP to the target to form the padlock, and (2) enzymatic ligation of PLPs on matching targets to form circles using ampligase. The PLP was added in 3-fold excess to the target (1.5-24 nM) to minimize the number of unreacted probes (targets without circles). The PLPs were covalently joined in ligation buffer doped with BSA to 0.2 mg/mL and Ampligase to 250 u/mL.

The temperature and time used for the PLP annealing has a significant impact on the result as the PLP arms bind unspecifically to the target if the temperature is too low and not at all to the target if the temperature is too high, in both cases producing no circular PLP templates upon ligation. The optimum temperature

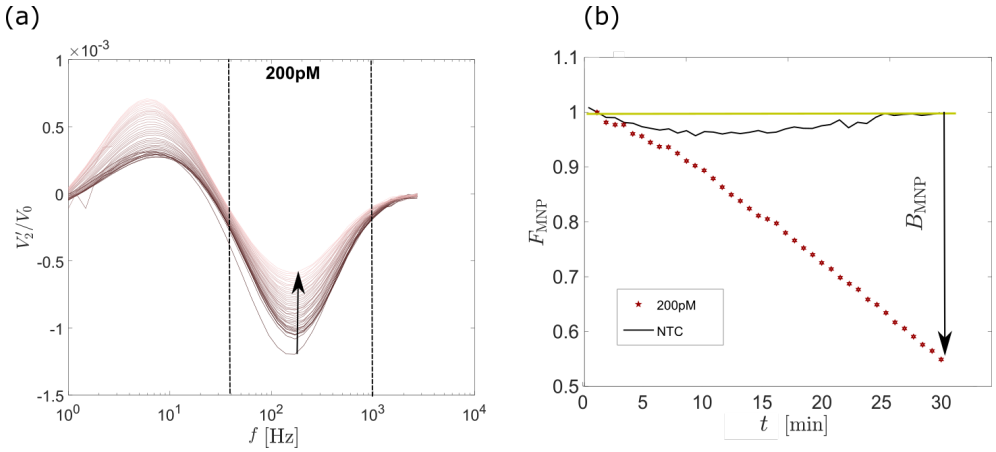

Fig. 3 (a) Time evolution of optomagnetic spectra measured during detection at 56°C for $c = 200$ pM in an experiment with off-chip PLP annealing. One spectrum was obtained every 45 s (increasing time indicated by arrow). The vertical dashed lines indicate the frequency range used to quantify the signal from free MNPs. (b) Relative change in signal from free MNPs, F_{MNP} vs. detection time for the same sample and an NTC. The arrow indicates the fraction of bound MNPs, B_{MNP}, after 30 min of detection.

is typically 5-10°C below the melting point of the PLP arm - target hybrids. The annealing temperature was therefore optimized experimentally.

Furthermore, in our initial studies we found a significant reduction in the number of produced RCPs if the MMBs were present during the annealing of PLPs on the DNA target.[38] This could be due to the reduced diffusion of targets when they were bound to MMBs or that the two ends of a PLP could bind to two targets on the same MMB resulting in no PLP ligation. We therefore pursued experimental approaches, where the MMBs were not present during the target annealing.

Prior to the optimized protocols presented below, chamber c3 of the chip was loaded with the detection buffer with DO-functionalized MNPs, chamber c2 was loaded with the RCA buffer containing the phi29 polymerase, and chamber c1 was loaded with ligation buffer containing DNA target and PLPs (see two protocols below). During the steps below, the heater of chambers c2 and c3 was off and the aluminum strip between c1 and c2 was kept at 25°C to prevent heating of the temperature-sensitive phi29 polymerase above room temperature.

Two different protocols were used and compared in the studies:

'Off-chip PLP annealing': The PLP was added to the target in the ligation buffer and placed in a thermoshaker without mixing at 55°C for 20 min followed by cooling to 30°C over 30 min. Ampligase and MMBs were added and the suspension was immediately loaded into chamber c1 on the chip. Under continuous MMB mixing, the temperature was kept at 58°C for 20 min followed by cooling to 35°C over 5 min to complete the ligation and target capture on the CO-functionalized MMBs.

'On-chip PLP annealing': The MMBs were loaded in the RCA buffer and initially parked in chamber c2 and kept above the external magnet at the 'low' position. The PLP, target and ampligase were added to the ligation buffer and loaded in chamber c1 on the chip where the solution was incubated at 58°C for 20 min. Then, the MMBs were transported to chamber c1 where they were kept under constant mixing at 58°C for 2 min followed by cooling to 30°C over 15 min to complete the ligation and target capture on the CO-functionalized MMBs.

Rolling circle amplification. The MMBs were transported from the ligation chamber (c1) to the RCA chamber (c2). The RCA chamber was filled with 20 μL RCA buffer (10×), 20 μL BSA (0.4 mg/mL), 1.9 μL dNTPs (10 mM), 3 μL phi29 polymerase (10 units/μL), and 55.1 μL milliQ water. The RCA reaction took place at 38.5°C for 45 min with continuous mixing of the MMBs. From each ligated PLP attached to an MMB, the RCA produced a single-stranded concatamer with nominally ~ 750 copies of the sequence complementary to that of the PLP. The RCA product remained attached to the MMBs.

Optomagnetic readout. Upon completion of the RCA reaction, the temperature of chambers c2 and c3 was ramped towards the detection temperature of 56°C. This temperature was chosen to be above the denaturation temperature of the CO-target hybrids but below the denaturation temperature of the DO-RCP hybrids to enable release of the RCPs.[39] During the temperature ramping, the MMBs with attached RCPs were transported to the detection chamber (c3) containing the DO-functionalized MNPs in the detection buffer such that the MMBs entered the detection chamber (c3) when the heater temperature was about 50°C. When the temperature stabilized at 56°C, the z-stage was slowly lowered to the 'low' position at 0.3 mm/s. Then the x-stage was quickly moved to its home position furthest away from the detection chamber and the optomagnetic measurements were initiated.

The optomagnetic technique probed the second harmonic modulation of light transmitted through the MNP suspension the magnetic field $B(t) = B_0 \sin(2\pi f t)$ applied along the light path. The signal from the photodetector was collected and the sine and cosine components of the signal at $2f$, denoted V_2' and V_2'', respectively, were found in LabView using a fast Fourier transformation algorithm. All measurements were normalized by the zero'th harmonic photodetector signal V_0 to compensate for possible variations of the incoming light intensity. A single OM frequency spec-

trum was obtained in 45 s by measuring the response at 41 logarithmically equidistant frequency points between 1 Hz and 2800 Hz.[33] The evolution of the OM spectra was studied over a detection period of 30 min corresponding to 40 measured spectra.

3 Results

3.1 Assay integrated with optomagnetic readout

Figure 3a shows a series of OM spectra (V_2'/V_0 vs. f) obtained during detection after a complete experiment with off-chip PLP annealing for a target concentration of 200 pM. The arrows indicate the time evolution of the spectra. The spectra show a negative peak centered at $f_{\text{peak}} \approx 150$ Hz and a positive peak at $f_{\text{peak}} \approx 5$ Hz. The OM method measures the ability of the MNPs to perform a small-angle rotation in response to the applied oscillating magnetic field, which is characterized by the Brownian relaxation frequency

$$f_{\text{B}} = \frac{k_{\text{B}}T}{\pi^2 \eta(T) D_{\text{h}}^3}. \quad (1)$$

Here, $k_{\text{B}}T$ is the thermal energy, $\eta(T)$ is the temperature-dependent viscosity of the liquid (=0.50 mPa s for water at 56°C), and D_{h} is the apparent hydrodynamic MNP diameter. It has previously been established that the Brownian relaxation at low B_0-values gives rise to a peak in the V_2'-response at $f_{\text{peak}} = 1.21 f_{\text{B}}/\sqrt{3} \approx 0.70 f_{\text{B}}$.[34] Inserting the values of f_{peak} found above, we estimate that the two peaks correspond to D_{h}-values of about 160 nm and 500 nm, respectively. The peak at high frequencies is attributed to free MNPs, whereas that at low frequencies is attributed to multiple MNPs bound to RCPs. In the latter case, the peak has a positive sign due to optical interference phenomena appearing for clusters of MNPs.[40] As the detection time progressed in Fig. 3a, the peak from free MNPs decreased whereas that from bound MNPs increased as more and more MNPs bound to the released RCPs. Taking the first spectrum as representative for the initial suspension of MNPs, we define the relative signals F_{MNP} and B_{MNP} from free and bound MNPs, respectively, in spectrum number n as

$$F_{\text{MNP}} = 1 - B_{\text{MNP}} = \frac{\sum_f V_2'(f,n)/V_0(f,n)}{\sum_f V_2'(f,1)/V_0(f,1)}. \quad (2)$$

where the sum is taken over frequencies f between 50 Hz and 1 kHz marked by the vertical lines in Fig. 3a.

Figure 3b shows F_{MNP} vs. time for the experimental data presented in Fig. 3a as well as for a no template control (NTC), where no target was added but the remaining procedure was the same. The arrow indicates the signal B_{MNP} due to bound MNPs (or depleted free MNPs) obtained in the last spectrum after 30 min of detection that we will take as the binding signal in the following. For the 200 pM target concentration, we found $F_{\text{MNP}} \approx 0.55$, i.e., about 45% of the free MNPs were depleted from solution during the 30 min detection.

In contrast, the NTC experiment in Fig. 3b had values of F_{MNP}, which deviated less than 3% from the nominal value of 1 during the detection and ended at a value after 30 min that was indistinguishable from 1, i.e., in this sample, virtually no free MNPs were depleted from solution during the 30 min detection.

3.2 Optimization of assay protocol

Here, we describe the optimization of the assay protocol that led to the final protocol described in Materials and Methods.

RCA protocol For the RCA protocol, the concentration of phi29 polymerase, dNTPs, BSA and RCA buffer was optimized (Section S2†). Three final phi29 concentrations were investigated: P1 (150 u/mL), P2 (300 u/mL), and P4 (600 u/mL). We found significantly higher values of B_{MNP} for higher phi29 concentrations (Fig. S2†). As a compromise between performance and cost of the phi29 polymerase, we proceeded with the P2 concentration.

EDTA in detection buffer The effect of adding ethylenediaminetetraacetic acid (EDTA) in the detection buffer was investigated as EDTA is known to sequest magnesium from magnesium pyrophosphate crystals formed as a biproduct of the RCA that may reduce the ability of the DO-probes to bind to the RCPs. The effect was investigated following for the P2 phi29 concentration during RCA, where EDTA was found to increase the B_{MNP}-values (Fig. S2†). We therefore used EDTA in the detection buffer.

MMB sample handling strategy During the initial work, we found that the MMBs could interfere with the OM measurements on the MNPs in the detection chamber as MMBs in the light path produced a significant low-frequency signal with a tail that extended up to the frequency window used to quantify free MNPs (Fig. S3.1†). It was therefore important to remove the MMBs from the light path. We found that the MMB pellet spread-out to a pancake-like shape when the magnet array was slowly moved away from the chip. Introducing the z-stage in the setup we found that lowering the magnet array to the 'low' position at 0.3 mm/s resulted in a flat, spread out distribution of MMBs that no longer interfered with the OM measurements on the MNPs. The MMB spreading also had the positive effect that it was easier to release the RCPs bound to the MMBs.

Further, to improve the binding of DO-functionalized MNPs to the RCPs, we designed the CO to have a melting point below the detection temperature such that the RCPs were released from the MMBs in the detection chamber.[39] This approach significantly increased the B_{MNP}-value compared to a protocol where the RCPs were directly linked to the MMBs using a biotinylated DNA target (Fig. S3.2†) and it was therefore used in subsequent studies.

MMB concentration Three MMB concentrations of 0.1, 0.2, and 0.3 mg/mL were investigated to find the value that produced the best results with minimum loss of MMBs during transportation in the chip. For 0.3 mg/mL MMB concentration, a higher variability of the results was found for the NTC (Fig. S4†) and slightly higher values of B_{MNP}-values were found for the two lower MMB concentrations. Moreover, for the 0.3 mg/mL MMB concentration we found that a significant fraction of the MMBs was lost in the capillary valves during the transportation. As a compromise between binding capacity and robustness, we therefore chose to use a 0.2 mg/mL MMB concentration.

3.3 Optimized assay results

Triplicate experiments were performed for DNA target concentrations of c [pM] = 0, 1, 2, 4, 10, 20, 40, 100, 200, 400, 800

and 2000 for off-chip PLP ligation and c [pM] = 0, 10, 20, 40, 100, 200, 400, and 2000 for on-chip PLP ligation. Fig. 4 shows the fraction of bound MNPs after 30 min of detection, B_{MNP}, for the two experiment series (examples of F_{MNP} signals vs. time are given in Fig. S5[†]). Error bars indicate the sample standard deviations (SD). The horizontal signal cut-off lines indicate the NTC signal plus three SD. The first target concentration for which the signal was higher than the cut-off line was taken as the limit of detection (LOD). The solid lines are fits to the Hill equation $B_{\mathrm{MNP}}(c) = B_{\mathrm{MNP}}(0) + [B_{\mathrm{MNP}}(\infty) - B_{\mathrm{MNP}}(0)] / [1 + (K_{\mathrm{A}}/c)^{n_{\mathrm{H}}}]$ with the association constant K_{A} and Hill coefficient n_{H}.

For off-chip PLP annealing, we found an NTC signal of $B_{\mathrm{MNP}} = 0.007 \pm 0.016$, an LOD of 2 pM, $K_{\mathrm{A}} = 146$ pM and $n_{\mathrm{H}} = 1.10$. For on-chip PLP annealing, we found an an NTC signal of $B_{\mathrm{MNP}} = 0.004 \pm 0.012$, an LOD of 20 pM, $K_{\mathrm{A}} = 293$ pM and $n_{\mathrm{H}} = 1.28$.

The two dose-response curves had similar cut-off values. The ten times higher LOD obtained for on-chip PLP annealing was therefore mainly due to the observation that the B_{MNP}-values for on-chip PLP annealing were generally about 0.1 lower than those obtained for off-chip PLP annealing. Thus, for the latter case, more MNPs were bound to RCPs. For the investigated concentrations, both dose-response curves were observed to approach saturation with a slightly higher B_{MNP}-value of 0.6 for off-chip PLP annealing compared to that of 0.5 for on-chip PLP annealing.

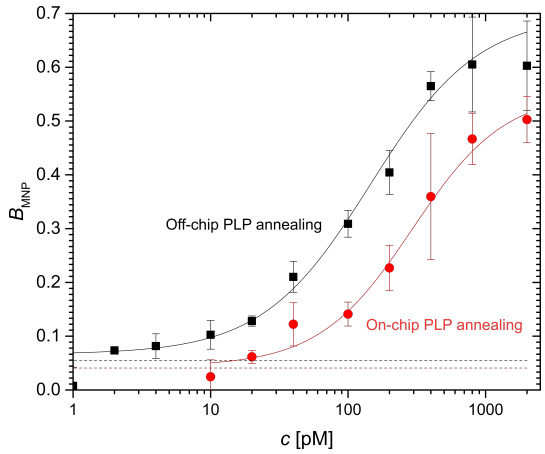

Fig. 4 Fraction of MNPs depleted from solution after OM detection for 30 min as function of DNA target concentration in experiments with off-chip PLP annealing (black squares) and on-chip PLP annealing (red circles). Horizontal lines indicate the signal cut-off taken as the NTC signal plus three SD. Solid lines are the fits to the Hill equation described in the text.

4 Discussion

In the above results, off-chip PLP annealing produced significantly higher signals than on-chip PLP annealing. This indicated that more RCPs formed in the latter case, which could be due to a lower output of successful annealing and ligation or simply that fewer targets with ligated PLPs were captured. The PLP annealing and ligation were performed sequentially for off-chip annealing and simultaneously for on-chip annealing, in both cases followed by capture on MMBs. In standard RCA, however, these steps are usually performed simultaneously, so the fact that the steps were performed sequentially for the off-chip annealing should not affect the outcome. The reason is more likely to be found in the MMB handling. For off-chip annealing, the MMBs were mixed with the target-PLP complexes prior to on-chip capture and ligation. Therefore the MMBs could have a higher chance of capturing the DNA targets compared to the on-chip case where the MMBs were only mixed with the DNA targets using the motion of the magnet. This agrees with the findings of Hernández-Neuta *et al.*,[27] who found that mixing using an actuated magnet was less efficient than their fluidized MMB bed. Moreover, for the on-chip annealing, the MMBs were parked (with the magnet under the second chamber at low position) in the RCA buffer with the phi29 polymerase during the 20 min annealing at 58°C. This procedure could result in some clustering of the MMBs, which could also make them less efficient to capture the target DNA in the subsequent capture step. The on-chip MMB mixing is a topic for further optimization in our future work.

Hernández-Neuta *et al.* optimized the on-chip MMB mixing but used external pressure-driven liquid supplies to regulate the flow and liquid composition in a single-chamber continuous-flow system to achieve an LOD of the integrated system of 1 pM after two cycles of RCA.[27] We, instead performed an initial loading of our chip with reagents and sample after which the assay ran automatically with no enrichment step or need for extra supply of liquids. For our approach with off-chip annealing, our LOD of 2 pM was comparable to that obtained by Hernández-Neuta *et al.* and the 3 pM LOD reported by Sato *et al.* for a microchannel column assay.[26] In the past, linear RCA assays or their readouts were adapted to, for example, discs (LOD ≈100 pM, 90 min RCA),[41] bioactive paper strips (LOD 100 pM, 60 min RCA),[42] and microarrays (LOD 480 fM, 4 h RCA).[43] Considering the RCA times, the LODs obtained in the present work compare well with those reported for less integrated systems.

The sensitivity of the presented proof-of-concept can be further improved by implementing several cycles of RCA in a circle-to-circle amplification scheme. In this way, the sensitivity and risk of false positive results can be balanced to satisfy the need for a given application.

5 Conclusion

We presented and demonstrated an automated on-chip RCA assay on a multi-chamber polymer chip with external chip temperature control and integrated capture, transportation and release of a DNA target complex by use of magnetic microbeads. The target was taken through ligation and rolling circle amplification to detection. The optomagnetic readout was based on measurements of the immobilization of functionalized magnetic nanoparticles on the rolling circle amplification products. Robust liquid handling was achieved using sequential filling of the three reaction chambers combined with capillary stops and phaseguide structures. Assay conditions, such as polymerase concentration, detection buffer and microbead concentration and handling, were optimized. Significant improvement in successful capture of target-ligated PLP complexes was found when targets were pre-annealed off-chip and were introduced on the chip after mixing with the MMBs. The dose-response curves were determined for assay pro-

tocols with off-chip or on-chip padlock probe annealing with limits of detection of 2 pM and 20 pM, respectively. These values obtained in a one-chip assay compare favorably to those obtained in similar but less integrated linear assays as well as MNP-based readout formats in previous studies.

The microbead mixing can be further optimized to improve the LOD beyond the present results. The presented system has the advantage that it does not rely on external pumps and valves and the disadvantage that it requires manual filling of reagents prior to initiation of an experiment and only runs a single-plex experiment. The developed microfluidic chips require no additional processing steps such as biomolecule spotting, sensor integration or functionalization and are suited for fabrication by a low-cost mass-production method such as injection moulding. The setup is currently a laboratory prototype built from high-end off-the-shelf components, which has a significant potential to be made in a more compact and portable format. The microfluidic chip and setup can be readily adapted to other RCA-assay targets, such as urinary tract infections[35] and antibiotic resistance in tuberculosis.[44] Moreover, its design and operation is flexible such that it has the potential to be adapted to other multi-step isothermal assays.[12]

Conflicts of interest

There are no conflicts to declare.

Acknowledgements

This work was supported by DFF project 4184-00121. G.V. thanks Erasmus+ Program (Key action 1 A.Y. 2017-18) and Roberto Raiteri, University of Genova, for the sponsoring of the exchange program. J.F. acknowledges MUDP for support (MST-141-01415). We thank Mats Nilsson (SciLifeLab, Stockholm) for design of influenza target and probes, for routine protocols for MMB-free circularization and rolling circle amplification and for discussions on the assay strategy.

References

1 A. Manz, N. Graber and H. M. Widmer, *Sensors and Actuators: B. Chemical*, 1990, **1**, 244–248.

2 S. Shoji and M. Esashi, *Journal of Micromechanics and Microengineering*, 1994, **4**, 157–171.

3 T. Thorsen, S. J. Maerkl and S. R. Quake, *Science*, 2002, **298**, 0–584.

4 C. W. Tsao, *Micromachines*, 2016, **7**, 255–266.

5 H. Becker and C. Gärtner, *Analytical and Bioanalytical Chemistry*, 2008, **390**, 89–111.

6 H. Cho, H. Y. Kim, J. Y. Kang and T. S. Kim, *Journal of Colloid and Interface Science*, 2007, **306**, 379–385.

7 R. Gottheil, N. Baur, H. Becker, G. Link, D. Maier, N. Schneiderhan-Marra and M. Stelzle, *Biomedical Microdevices*, 2014, **16**, 163–172.

8 P. Vulto, S. Podszun, P. Meyer, C. Hermann, A. Manz and G. a. Urban, *Lab on a chip*, 2011, **11**, 1596–1602.

9 R. K. Saiki, S. Scharf, F. Faloona, K. B. Mullis, G. T. Horn, H. A. Erlich and N. Arnheim, *Science*, 1985, **230**, 1350–1354.

10 W. Johnson, *The polymerase chain reaction: AN overview and development of diagnostic PCR protocols at the LDCD*, Centre for disease control technical report, 1991.

11 C. Zhang, J. Xu, W. Ma and W. Zheng, *Biotechnology Advances*, 2006, **24**, 243–284.

12 Y. Zhao, F. Chen, Q. Li, L. Wang and C. Fan, *Chemical Reviews*, 2015, **115**, 12491–12545.

13 O. Piepenburg, C. H. Williams, D. L. Stemple and N. A. Armes, *PLoS Biology*, 2006, **4**, 1115–1121.

14 N. Tomita, Y. Mori, H. Kanda and T. Notomi, *Nature Protocols*, 2008, **3**, 877–882.

15 M. M. Ali, F. Li, Z. Zhang, K. Zhang, D. K. Kang, J. A. Ankrum, X. C. Le and W. Zhao, *Chemical Society Reviews*, 2014, **43**, 3324–3341.

16 G. A. S. Minero, C. Nogueira, G. Rizzi, B. Tian, J. Fock, M. Donolato, M. Strömberg and M. F. Hansen, *Analyst*, 2017, **142**, 3441–3450.

17 A. R. Pavankumar, A. Engström, J. Liu, D. Herthnek and M. Nilsson, *Analytical Chemistry*, 2016, **88**, 4277–4284.

18 M. Nilsson, M. Gullberg, F. Dahl, K. Szuhai and A. K. Raap, *Nucleic Acids Research*, 2002, **30**, e66.

19 F. Dahl, J. Baner, M. Gullberg, M. Mendel-Hartvig, U. Landegren and M. Nilsson, *Proceedings of the National Academy of Sciences*, 2004, **101**, 4548–4553.

20 S. Berensmeier, *Applied Microbiology and Biotechnology*, 2006, **73**, 495–504.

21 C. R. Tamanaha, S. P. Mulvaney, J. C. Rife and L. J. Whitman, *Biosensors and Bioelectronics*, 2008, **24**, 1–13.

22 M. A. Gijs, F. Lacharme and U. Lehmann, *Chemical Reviews*, 2010, **110**, 1518–1563.

23 A. Van Reenen, A. M. De Jong, J. M. Den Toonder and M. W. Prins, *Lab on a Chip*, 2014, **14**, 1966–1986.

24 J. Göransson, R. Ke, R. Y. Nong, W. M. Howell, A. Karman, J. Grawé, J. Stenberg, M. Granberg, M. Elgh, D. Herthnek, P. Wikström, J. Jarvius and M. Nilsson, *PLoS ONE*, 2012, **7**, 1–9.

25 F. Neumann, I. Hernández-Neuta, M. Grabbe, N. Madaboosi, J. Albert and M. Nilsson, *Clinical chemistry*, 2018, **64**, 1–9.

26 K. Sato, A. Tachihara, B. Renberg, K. Mawatari, K. Sato, Y. Tanaka, J. Jarvius, M. Nilsson and T. Kitamori, *Lab on a Chip*, 2010, **10**, 1262–1266.

27 I. Hernández-Neuta, I. Pereiro, A. Ahlford, D. Ferraro, Q. Zhang, J. L. Viovy, S. Descroix and M. Nilsson, *Biosensors and Bioelectronics*, 2018, **102**, 531–539.

28 M. Strömberg, T. Zardán Gómez de la Torre, J. Göransson, K. Gunnarsson, M. Nilsson, M. Strømme and P. Svedlindh, *Biosensors and Bioelectronics*, 2008, **24**, 696–703.

29 M. Strömberg, T. Zardán Gómez De La Torre, J. Göransson, K. Gunnarsson, M. Nilsson, P. Svedlindh and M. Strømme, *Analytical Chemistry*, 2009, **81**, 3398–3406.

30 T. Zardán Gómez De La Torre, M. Strömberg, C. Russell, J. Göransson, M. Nilsson, P. Svedlindh and M. Strømme, *Journal of Physical Chemistry B*, 2010, **114**, 3707–3713.

31 R. S. Bejhed, T. Zardán Gómez De La Torre, M. Donolato,

M. F. Hansen, P. Svedlindh and M. Strömberg, *Biosensors and Bioelectronics*, 2015, **66**, 405–411.

32 M. Donolato, P. Antunes, T. Z. G. de la Torre, E. T. Hwu, C. H. Chen, R. Burger, G. Rizzi, F. G. Bosco, M. Strømme, A. Boisen and M. F. Hansen, *Biosensors and Bioelectronics*, 2015, **67**, 649–655.

33 J. Fock, C. Jonasson, C. Johansson and M. F. Hansen, *Phys. Chem. Chem. Phys.*, 2017, **19**, 8802–8814.

34 J. Fock, C. Balceris, R. Costo, L. Zeng, F. Ludwig and M. F. Hansen, *Nanoscale*, 2018, **10**, 2052–2066.

35 A. Mezger, J. Fock, P. Antunes, F. W. Østerberg, A. Boisen, M. Nilsson, M. F. Hansen, A. Ahlford and M. Donolato, *ACS Nano*, 2015, **9**, 7374–7382.

36 F. Garbarino, K. Kistrup, G. Rizzi and M. F. Hansen, *Journal of Micromechanics and Microengineering*, 2017, **27**, aa97b7.

37 O. Strohmeier, A. Emperle, G. Roth, D. Mark, R. Zengerle and F. Von Stetten, *Lab on a Chip*, 2013, **13**, 146–155.

38 G. A. S. Minero, F. Garbarino, J. Fock, M. Nilsson and M. F. Hansen, 12th International Conference on the Scientific and Clinical Applications of Magnetic Carriers, Poster 251.

39 G. A. S. Minero, V. Cangiano, F. Garbarino, J. Fock and M. F. Hansen, "DNA handling on magnetic microbeads in RCA assay with optomagnetic detection", submitted.

40 J. Fock, M. Parmvi, M. Strömberg, P. Svedlindh, M. Donolato and M. F. Hansen, *Biosensors and Bioelectronics*, 2017, **88**, 94–100.

41 H. Y. Heo, S. Chung, Y. T. Kim, D. H. Kim and T. S. Seo, *Biosensors and Bioelectronics*, 2016, **78**, 140–146.

42 M. M. Ali, S. D. Aguirre, Y. Xu, C. D. M. Filipe, R. Pelton and Y. Li, *Chemical Communications*, 2009, **43**, 6640–6642.

43 G. Nallur, C. Luo, L. Fang, S. Cooley, V. Dave, J. Lambert, K. Kukanskis, S. Kingsmore, R. Lasken and B. Schweitzer, *Nucleic Acids Research*, 2001, **29**, e118.

44 A. Engström, T. Zardán Gómez de la Torre, M. Strømme, M. Nilsson and D. Herthnek, *PLoS ONE*, 2013, **8**, e62015.

Electronic Supplementary Information

Rolling circle amplification and optomagnetic detection integrated on a low-cost polymer chip

Francesca Garbarino [a], Gabriel Antonio S. Minero,[a] Giovanni Rizzi,[a] Giada Violo,[a] Jeppe Fock,[a,b] and Mikkel F. Hansen[a]

[a]Department of Micro- and Nanotechnology,Technical University of Denmark, DTU Nanotech, Building 345B, DK-2800 Kongens Lyngby, Denmark
[b]BluSense Diagnostics, Fruebjergvej 3, DK-2100 Copenhagen, Denmark

S1 Pictures of experimental setup

(a) Top view - closed

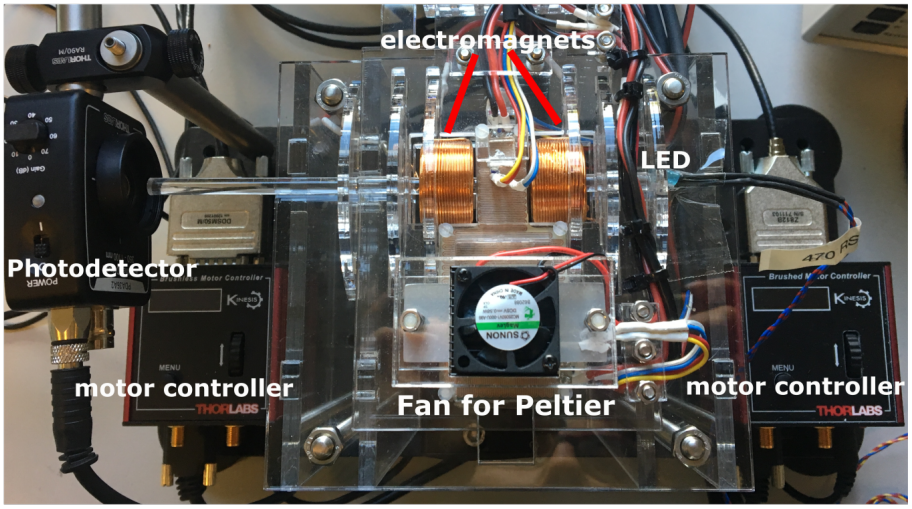

(b) Top view - open

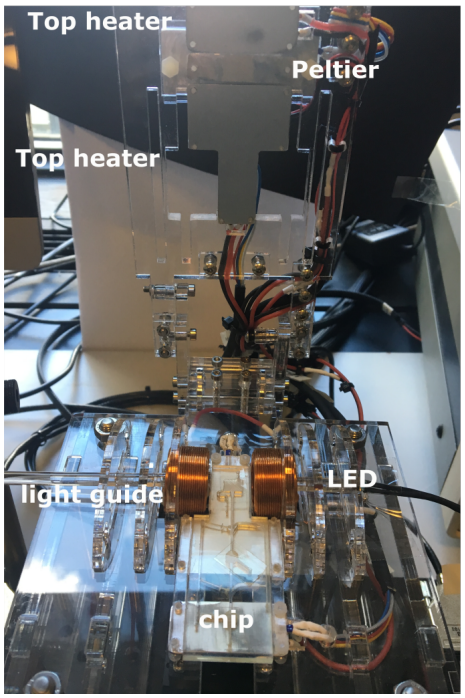

(c) Side view

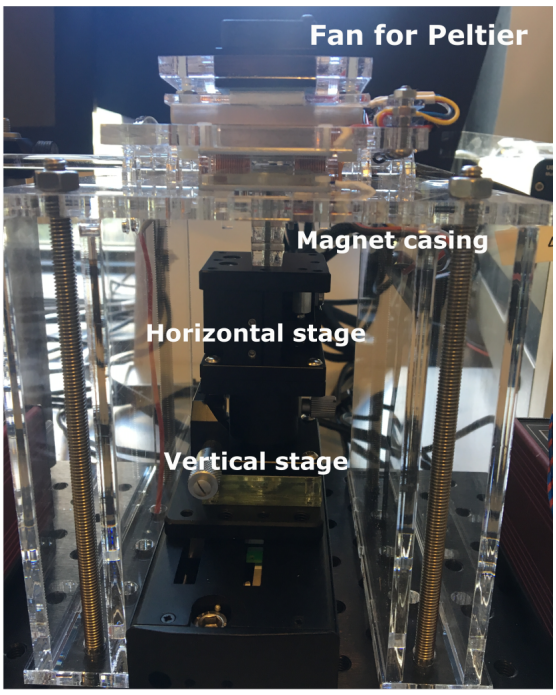

Fig. S1 Setup used in the experiments. The three pictures show the setup from different angles: (a) Top view with the lid closed. The LED shines the light from the right, passes through the electromagnets and arrives to the photodetector thanks to a light guide. (b) Top-view with open lid and a chip in experimental position. (c) Side view showing the horizontal stage on the top of the vertical one.

S2 Optimization RCA and detection protocols

In Fig. S2 we demonstrate impact of different concentrations of the phi29 polymerase (P1 (150 u/mL), P2 (300 u/mL), and P4 (600 u/mL)) along with the same scaling of the final concentrations of RCA buffer (1x, 2x, and 4x), dNTPs (95 µM, 190 µM, and 380 µM) and BSA (0.2 mg/mL, 0.4 mg/mL, and 0.8 mg/mL) in the on-chip RCA assay.

For the optimization of the protocol, we used the sequences stated in Table 1 in the main text, except that the target was biotinylated at the 5'-end and thus directly linked to the MMBs rather than via the CO probe. Ligation took place at 55°C for 20 min in Eppendorf tube (1x ligation buffer, 0.2 mg/mL BSA, 250 u/mL Ampligase) followed by incubation of the obtained DNA target-PLP hybrids with spiked streptavidin coated magnetic microbeads to 0.2 mg/mL (MyOne C1, MMBs) for additional 20 min at 55°C (upon rotary mixing 1000 rpm). The obtained complexes-on-MMBs (60 µL) were further diluted with RCA buffer, BSA, dNTPs and water (the volumes varied for protocols P2-P4) to 120 µL and loaded into chamber c2 for on-chip RCA (45 min, 38.5 °C). The first chamber contained 1x ligation buffer with 0.2 mg/mL BSA and the third chamber contained 0.05 mg/mL MNPs in the detection buffer. Because of a direct biotin-streptavidin link between target DNA and MMB, the obtained system represented a robust prototype of the experiments implemented using capture probes on MMBs in the later stage.

The histogram in Fig. S2 shows the fraction of bound MNPs, B_{MNP}, for both c = 40 and 200 pM for each of the above mentioned cases (n=3). P4 appears to be the most depleted case, but the cost of phi29 enzyme was substantial. We therefore chose the P2 protocol as a compromise between cost and performance of the assay.

We furthermore investigated the impact of Ethylenediaminetetraacetic acid (EDTA) onto the end-point optomagnetic (OM) detection that followed the RCA protocol for the P2 enzyme concentration (P2-E). EDTA was added in the detection chamber to remove Mg+ cations and the Mg pyrophosphates that were potentially carried over with RCPs (on magnetic microbeads) from the RCA chamber. Compared to the P2 protocol, we note that addition of EDTA led to increased values of B_{MNP}, particularly for the 40 pM target concentration, and we therefore continued with the P2-E protocol.

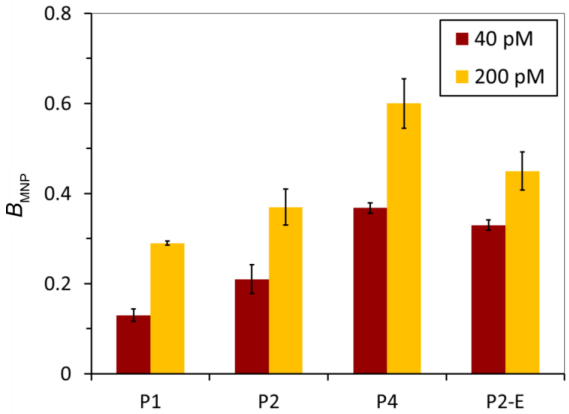

Fig. S2 Histogram of fraction of bound MNPs for the enzyme concentrations P1, P2 and P4 (see text) and for the P2 concentration with addition of EDTA (P2-E). All experiments were carried out in the same way: ligation was performed in the thermoshaker at 55°C , then slowly cooled down to 35°C. MMBs were then added to the solution together with the RCA buffer. The solution was then inserted in the chip to perform RCA at 38.5°C for 45 min. Detection was carried out for 40 min.

S3 Comparison of MMB sample handling strategies

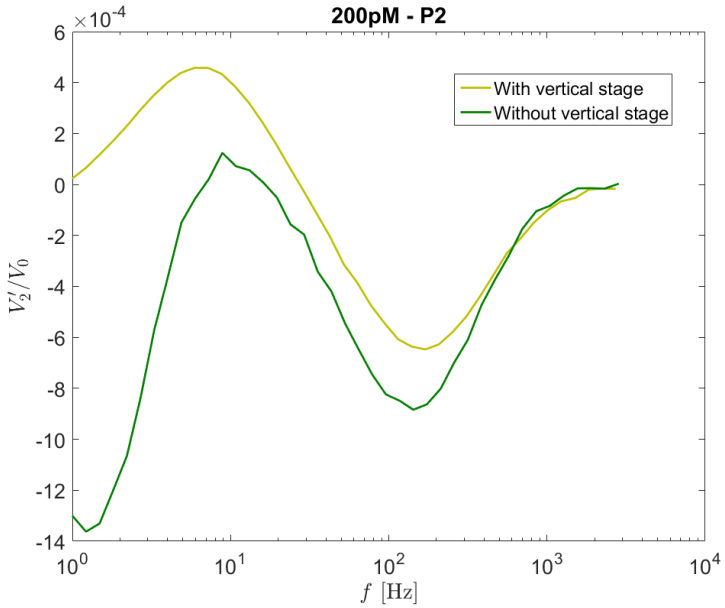

Fig. S3.1 Optomagnetic spectra obtained for *c* = 200 pM (P2-E protocol). The dark green curve was obtained in an experiment in which the MMB pellet was compact (magnet quickly withdrawn manually). The shoulder at low frequencies extending up to above 100 Hz is due to MMB interference. The light green curve was carried out with a slow withdrawal of the magnet using the vertical stage. The shoulder in the spectrum is clearly removed.

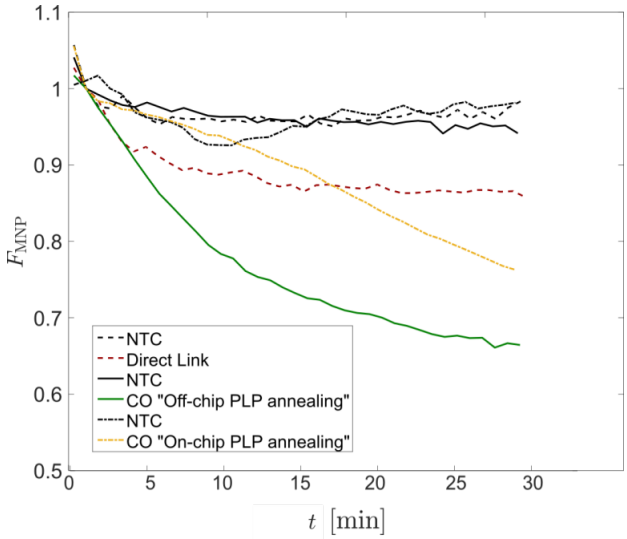

Fig. S3.2 Signal from free MNPs, F_{MNP}, vs. time for *c*=200 pM. Curves obtained from each step of the optimization carried out to boost the OM signal. The red dashed line refers to direct link between MMB and a biotinylated target DNA. The orange dotted line refers to the "on-chip PLP annealing" case and the solid green line refers to the "off-chip PLP annealing" case.

S4 Optimization of MMB concentration

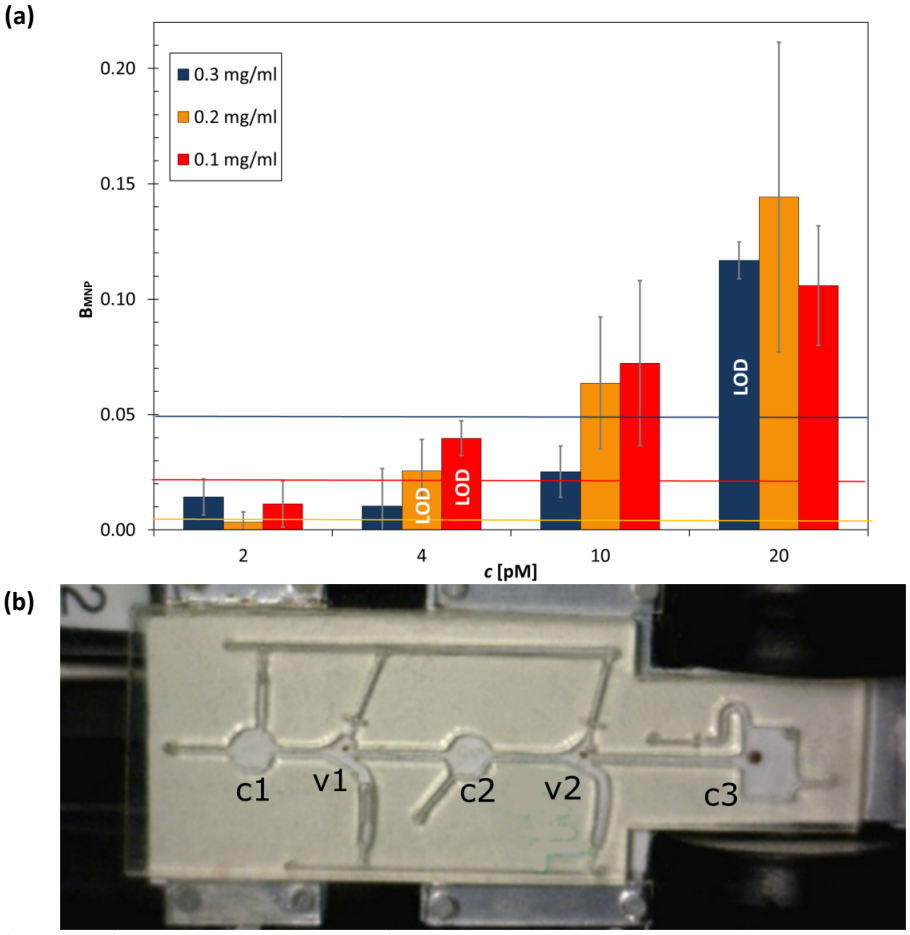

Fig. S4 (a) Fraction of bound MNPs, B_{MNP}, obtained for the indicated DNA target concentrations, *c*, and MMB concentrations (n=3). The studies were performed following the protocol for off-chip PLP annealing after a detection time of 30 min. (b) Picture of chip loaded with 0.2 mg/mL MMB concentration after MMB transportation to the detection chamber (c3). The main MMB pellet is located in the detection chamber, but leftover beads can be observed in both capillary stops (v1 and v2). This concentration allowed us to transport beads efficiently from ligation chamber to the detection one, with a very low amount of MMB loss, and it was therefore chosen as the final concentration of MMBs.

S5 Signals vs. time for off-chip and on-chip PLP annealing

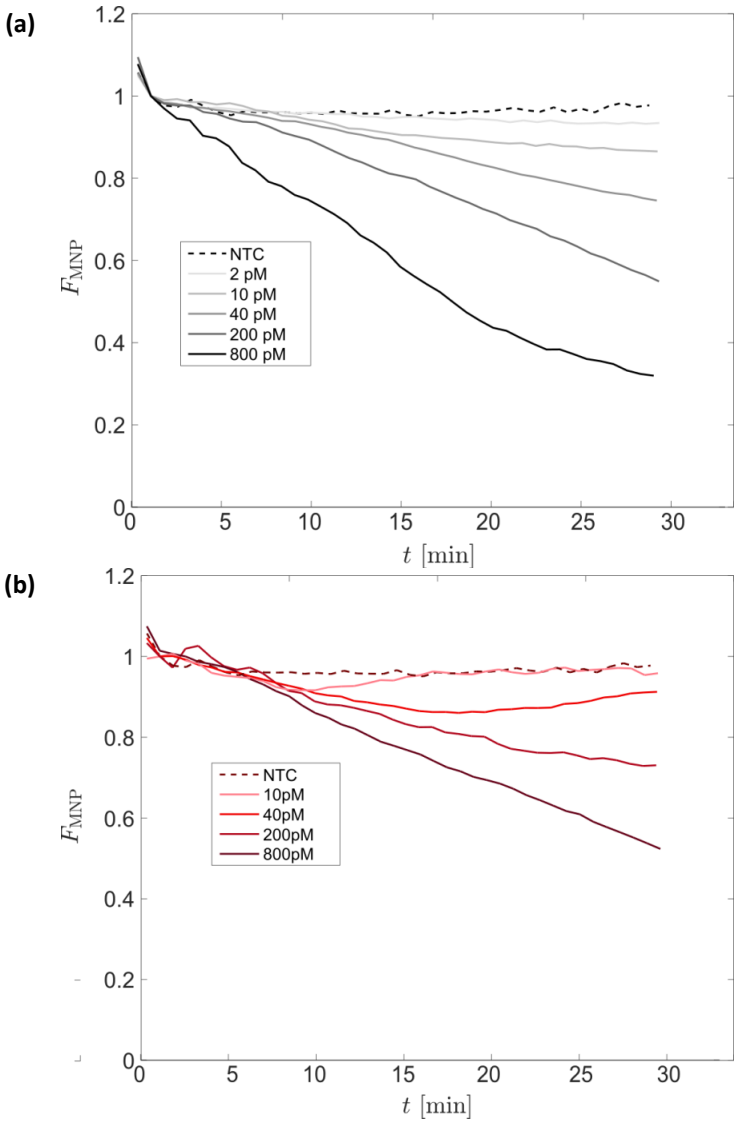

Fig. S5 Fraction of free MNPs, F_{MNP}, measured vs. time during detection for the protocols for (a) off-chip PLP annealing and (b) on-chip PLP annealing for the indicated target DNA concentrations and the no template control (NTC). The first spectrum in the plot was measured during the temperature equilibration and was not used in the analysis.